Modelling of sorption hysteresis and its effect on moisture transport within cementitious materials

Zhidong Zhang

THÈSE présentée pour obtenir le grade de

DOCTEUR DE L'UNIVERSITÉ PARIS–EST

Spécialité : **Structures et Matériaux**

préparée à l'**IFSTTAR**
dans le cadre de l'Ecole Doctorale **SIE**

Présentée par :

Zhidong ZHANG

The title of the thesis:

Modelling of sorption hysteresis and its effect on moisture transport within cementitious materials

Sujet de la thèse :

Modélisation de l'hystérésis hydrique dans les matériaux cimentaires et de son effet sur les transferts d'humidité

Thèse soutenue le 13 mai 2014 devant le jury composé de :

Prof. Alain Sellier	INSA de Toulouse, France	Rapporteur
Prof. Jan Carmeliet	ETHZ, Switzerland	Rapporteur
Prof. Lars-Olof Nilsson	Lund University, Sweden	Examinateur
Prof. Peter McDonald	The University of Surrey, UK	Examinateur
Dr. Bruno Huet	Lafarge, LCR, France	Examinateur
Dr. Jean-Michel Torrenti	IFSTTAR, France	Examinateur
Dr. Mickaël Thiéry	IFSTTAR, France	Conseiller d'études
Dr. Véronique Baroghel-Bouny	IFSTTAR, France	Directrice de thèse

Abstract

The durability of reinforced concrete structures and their service life are closely related to the simultaneous occurrence of many physical and chemical phenomena. These phenomena are diverse in nature, but in common they are dependent on the moisture properties of the material. Therefore, the prediction of the potential degradation of cementitious materials requires the study of the movement of liquid-water and gas-phase transport in the material which is considered as a porous medium. In natural environment, structures are always affected by periodic variations of external relative humidity (RH). However, most moisture transport models in the literature only focus on the drying process. There are few studies considering both drying and wetting, although these conditions represent natural RH variations. Much less studies take into account hysteresis in moisture transport. Therefore, this work is devoted to a better understanding of how the moisture behaviour within cementiitous materials responds to the ambient RH changes through both experimental investigations and numerical modelling. In particular, the consideration of hysteresis will be included in numerical modelling.

In the research, a multiphase continuum model was recalled firstly. According to a theoretical analysis and experimental verifications, a simplified model was obtained for the case that the intrinsic permeability to liquid-water is much smaller than the intrinsic permeability to gas-phase. The review of commonly-used hysteresis models enabled to conclude a set of best models for the prediction of water vapour sorption isotherms and their hysteresis. The simplified model was coupled with the selected hysteresis models to simulate moisture transport under drying and wetting cycles. Compared with experimental data, numerical simulations revealed that modelling with hysteretic effects provided much better results than non-hysteresis modelling. Among different hysteresis models, the use of the conceptual hysteresis model, which presents closed form of scanning loops, showed more accuracy predictions. Further simulations for different scenarios were also performed. All comparisons and investigations enhanced the necessity of considering

hysteresis to model moisture transport for varying RH at the boundary. The investigation of moisture penetration depth could provide a better understanding of how deep moisture as well as ions can move into the material. Furthermore, this research investigated different methods to determine the liquid-water intrinsic permeability, including the inverse analysis with different boundary conditions and fitting measured apparent diffusivity values for different equations to calculate relative permeabilities.

Keywords: Cementitious materials; Moisture transport; Hysteresis; Water vapour sorption isotherms; Drying and wetting cycles; Numerical simulation; Experimental investigations; Gas pressure variations; Transport modes; Knudsen effect; Apparent diffusivity; Mass boundary region

Résumé

La durabilité des structures en béton armé ainsi que leur durée de vie sont étroitement liées à la mise en œuvre simultanée de nombreux phénomènes physiques et chimiques. Ceux-ci sont de diverses natures mais restent, en général, fonction des propriétés hydriques du matériaux étudiés. Ainsi, la prédiction des dégradations potentielles d'un matériau cimentaire requiert l'étude du transport de l'eau liquide et des phases gazeuses à travers ce dernier, considéré comme un milieu poreux. En milieu naturel, les structures subissent des variations périodiques de l'humidité relative extérieure (HR). Cependant, la plupart des modèles de transfert hydrique préexistants dans la littérature, s'intéresse uniquement au processus de séchage. Il existe peu de modèles décrivant à la fois l'humidification et le séchage du matériau (ces deux phénomènes se produisent dans le matériau en condition naturelle d'humidité relative (HR)). Tenir compte des phénomènes d'hystérésis dans les transferts hydriques réduit à nouveau le nombre de modèles à disposition. Ainsi, cette thèse s'attache à proposer une meilleure compréhension de l'état hydrique du béton en fonction des variations d'humidité relative extérieure, sur la base d'une nouvelle campagne expérimentale et de modélisations numériques. Un soin sera apporté afin de tenir compte dans les modèles numériques des effets d'hystérésis. Dans ce travail, nous détaillerons, tout d'abord, un modèle multi-phasiques complet. Un modèle simplifié est obtenu, sur la base de considérations théoriques et de vérifications expérimentales dans le cas où la perméabilité intrinsèque à l'eau liquide reste très inférieure à la perméabilité intrinsèque au gaz. Une étude comparative des modèles d'hystérésis couramment utilisés permet d'obtenir un jeu de modèles proposant les meilleures prédictions d'isothermes de sorption d'eau et de leurs hystérésis. Par la suite, le modèle de transport simplifié est couplé avec les modèles d'hystérésis sélectionnés afin de simuler les transferts hydriques dans des bétons soumis à des cycles d'humidification-séchage. La comparaison avec des données expérimentales révèle que la prise en compte de l'hystérésis de l'isotherme de sorption d'eau ne peut pas être négligé. De plus, il est montré que les prédictions obtenues

avec des modèles d'hystérésis théoriques, sont les plus cohérentes avec les résultats expérimentaux, en particulier, pour des chemins secondaires d'hystérésis. Plusieurs scénarios (conditions environnementales, bétons différents) sont également simulés. Les résultats obtenus pointent à nouveau la nécessité de tenir compte de l'hystérésis lors de la modélisation des transferts hydriques à travers des matériaux cimentaires soumis à des variations d'humidité relative. La définition d'une profondeur pour laquelle le profil hydrique du béton est modifié par les variations périodiques d'humidité relative permet de mieux comprendre comment la modélisation de la pénétration des espèces ioniques est influencée par les cycles d'humidification-séchage. Par ailleurs, notre analyse révèle qu'il est pertinent de considérer l'effet de Knudsen pour la diffusion de la vapeur afin d'améliorer la prédiction de la diffusivité apparente.

Mots clefs : Matériaux cimentaires ; Transferts hydriques ; Hystérésis ; Isothermes de sorption de vapeur d'eau ; Cycles d'humidification-séchage ; Simulation numérique ; Investigations expérimentales ; Variation de pression de gaz ; Modes de transports ; effets de Knusen ; Diffusion apparente ; Couche limite massique.

Acknowledgements

Many people were involved in this PhD work and I would like to express all my gratitude.

First, I am obliged to all members of the jury. Professor Alain Sellier and Professor Jan Carmeliet agreed to be reviewers of my thesis and provided important and valuable suggestions, which let me improve my thesis a lot. I also express my sincere thanks to Professor Lars-Olof Nilsson, Professor Peter McDonald, Dr. Jean-Michel Torrent and Dr. Bruno Huet to be interested in my work and the discussion during the defense also provides numerous ideas for my future work.

Most of the work in this thesis was conducted at IFSTTAR, within the research group FM^2D (Formulation, microstructure, modélisation et durabilité des matériaux de construction) at Department of MAST (Département Matériaux et Structures), whereas a short period of the work was conducted at Division of Building Materials, Faculty of Engineering of Lund University (Sweden). The supervisors of this thesis are Véronique BAROGHEL-BOUNY and Mickaël THIERY. Guidance provided by both supervisors has been of great importance and influence to the work conducted. I would like to express my deepest gratitude to them. Even though at the beginning of my PhD I have very limited knowledge about moisture transport in cementitious material, they had the patience to teach me and let me can learn step by step. Especially, Mickaël helped me more in details about experiments, writing up my thesis, etc. He is not only a goo colleague in research but also a dear friend. Besides, I also would like to thank Dr. Jean-Michel Torrent, the deputy director of Department of MAST, who provided many suggestions during my research.

I also acknowledge the help of the co-workers at Lund University. Professor Lars Wadsö kindly accepted me to carry out the pressure plate measurements in the Building Materials Laboratory. Saiedpour Mahsa conducted the DVS measurements for me. Other co-workers provided all the necessary conditions for access to laboratory facilities when I stayed at Lund University.

This thesis is one part of the TRASCEND project, which provides the finance support. I

gratefully acknowledge the project organizers, Professor Karen Scrivener, Professor Peter McDonald, Professor Mette Geiker and Mrs. Marie-Alix Dalang-Secrétan. They organized various activities, including training courses, meetings and workshops, which not only provided me opportunities to learn new knowledge but also chances to know new researchers. Other fourteen PhD students in the TRANSCEND project are very talented and active, making a very good atmosphere for research.

Of course, without the assistance of my colleagues at IFSTTAR, I cannot finish my thesis on time. Dr. Mickaël Sailio and Mr. Sylvain Pradelle helped me to correct mistakes during the final step of the writing up. Mr. Jean-François Bouteloup and Mr. Alexandre Deman assisted me during measurements conducted at IFSTTAR. Secretaries, Miss. Pauline Huart and Mrs. Jeanne Bata, also helped me a lot, especially for dealing with the paperworks for so many travels in the past three years. A great thanks is also expressed to other former and current colleagues: Xiaomeng, Biyun, Antoine, Valérie, Guillaume, Aurélie, Nicolas, Assia, Thao, Othman, Rim, Jennifer, Héla, Patrick, Ingrid and Jean-Daniel.

Finally, I must acknowledge my family (my father and my brothers) in general for their support, particularly the love and constant support of my wife, Fei. Her persistent encouragement has enabled me to complete this dissertation. She provided the necessary strength and motivation to finish this thesis.

The research leading to these results has received funding from the European Union Seventh Framework Programme (FP7 / 2007-2013) under grant agreement 264448.

Contents

Abstract i

Résumé iii

Acknowledgements v

List of Figures xiii

List of Tables xvii

Lists of Symbols and Acronyms xix

General introduction 1

1 Review of modelling of drying and wetting cycles 7

1.1 Introduction . . . 7

1.1.1 Sources of water . . . 8

1.1.2 Water states in cementitious materials . . . 8

1.2 Moisture sorption and hysteresis . . . 10

1.2.1 Moisture sorption processes . . . 10

1.2.2 Sorption hysteresis . . . 12

1.3 Mechanisms of moisture transport . . . 13

1.3.1 Diffusion . . . 14

1.3.2 Capillary transport . . . 15

1.3.3 Evaporation-Condensation . . . 16

1.4 Continuum approach to model unsaturated moisture transport in porous media . 17

1.4.1 Mass balance equations . . . 18

1.4.2 Transport laws . . . 18

1.4.3 State equations . . . 20

1.4.4 Applications of the multiphase model for cementitious materials . . . 21

1.5 Modelling of moisture transport under varying ambient relative humidity 23
1.5.1 Cunningham's method - analytical solution 24
1.5.2 EMPD model 25
1.5.3 Kirchhoff's flow potential 26
1.5.4 Method from Li et al. 27
1.5.5 Hysteresis modelling methods 28
1.5.6 Interactions between materials and their surrounding 37
1.6 Critical review and conclusion 39

2 Modelling of isothermal drying of unsaturated cementitious materials 41
2.1 Introduction 42
2.2 Modelling of drying porous media in the case of cementitious materials 42
2.2.1 Initial and boundary conditions and geometry of the problem 42
2.2.2 Materials properties 43
2.2.3 Transport coefficients 45
2.2.4 Simulation results verified by experimental data of drying 49
2.3 Gas pressure variations during drying of unsaturated cementitious materials . . . 52
2.3.1 Mass balance equations of gas and moisture 53
2.3.2 Asymptotic analysis 54
2.3.3 Simulated gas pressure variations for cementitious materials 56
2.4 Modelling of drying cementitious materials in the case $K_l \ll K_g$ 58
2.4.1 Gas pressure variations 60
2.4.2 Simplification of moisture transport models 62
2.5 Transport modes analysis 65
2.5.1 Contribution of mass transport in the material 66
2.5.2 Contribution of mass transport by an integration at the boundary 67
2.6 Conclusion 69

3 Review of hysteresis models 71
3.1 Introduction 71
3.2 History of development of hysteresis models 73
3.3 Adopted comparison strategy 76
3.3.1 Procedure of comparisons 76
3.3.2 Experimental data collection 77
3.3.3 Comparison criteria 79
3.4 Comparisons of main isotherms fitting models 80
3.4.1 Feng and Fredlund's model (FF) 80

3.4.2 Van Genuchten's model . . . 80
3.4.3 Fredlund and Xing's model (FX) . . . 81
3.4.4 Kosugi's model . . . 81
3.4.5 Multi-modal model . . . 81
3.4.6 Comparison results and discussion . . . 82
3.5 Prediction of one main isotherm from the other main branch . . . 85
3.5.1 Models only based on the measured main desorption branch . . . 86
3.5.2 Models needing additional data besides the main desorption branch . . . 87
3.5.3 Comparison results and discussion . . . 89
3.6 Prediction of scanning isotherms . . . 91
3.6.1 Mualem Model II . . . 92
3.6.2 Mualem dependent model . . . 94
3.6.3 Incremental models . . . 96
3.6.4 Improved Rubin's empirical hysteresis model . . . 99
3.6.5 Comparison results and analysis . . . 100
3.6.6 Discussion . . . 104
3.7 Models for the proposed multi-level approach to simulate hysteresis . . . 106
3.8 A method to fit both main curves by using the fewest measured data . . . 107
3.8.1 A proposed new statistical criterion . . . 108
3.8.2 Determination of the number of points for the fitting . . . 108
3.8.3 Determination of the relevant positions of those five points . . . 109
3.8.4 Fitting results and comparisons . . . 110
3.8.5 Discussion on the proposed approach . . . 113
3.9 Conclusion and recommendations . . . 114

4 Experimental investigations **117**
4.1 Materials preparation . . . 118
4.2 Drying-wetting experiments . . . 118
4.2.1 Experimental procedure . . . 119
4.2.2 Porosity profiles . . . 120
4.2.3 Profiles of saturation . . . 123
4.2.4 Data consistency analysis . . . 123
4.2.5 Results of drying and wetting experiments . . . 124
4.3 Sorption isotherms measurements . . . 125
4.3.1 DVS method . . . 125
4.3.2 Sorption isotherms in high RH - pressure plate measurements . . . 128
4.3.3 Sorption isotherm measurements results . . . 130

4.4 Determination of the main adsorption curve . . . 131
4.5 Conclusion . . . 133

5 Modelling of moisture transport under drying-wetting cycles 135
5.1 Introduction . . . 136
5.2 Moisture transport models . . . 136
5.3 Modelling methods . . . 138
5.3.1 Modelling without hysteretic effects . . . 138
5.3.2 Modelling with hysteretic effects . . . 138
5.3.3 Numerical method . . . 140
5.4 Verification with experimental data . . . 141
5.4.1 Experimental data collection . . . 141
5.4.2 Determination of transport coefficients . . . 142
5.4.3 Verification with experimental data from the literature . . . 143
5.4.4 Verification with experimental data from the current study . . . 146
5.5 Investigation of reasons of differences between three modelling methods . . . 149
5.5.1 Differences between hysteresis and non-hysteresis modellings . . . 149
5.5.2 Differences between two hysteresis models . . . 150
5.6 Discussions about effects of different modelling conditions . . . 151
5.6.1 Effect of the drying and wetting cycle duration . . . 151
5.6.2 Effect of the boundary RH amplitude . . . 153
5.6.3 Effect of the initial step . . . 154
5.6.4 Effect of different forms of Richards' equations on hysteresis modelling . . . 156
5.6.5 Effect of hysteresis in $k_{rl}(S)$ . . . 157
5.6.6 Analysis of the moisture penetration depth . . . 159
5.7 Conclusion . . . 162

6 Investigation of the reliability of K_l determination 165
6.1 Determination of K_l by fitting measured apparent diffusivity values . . . 166
6.1.1 Basic method . . . 169
6.1.2 Experimental data and fitting results . . . 170
6.1.3 Improved method . . . 174
6.1.4 Partial conclusion . . . 179
6.2 Effect of boundary conditions on the determination of K_l by inverse analysis. . . . 180
6.2.1 Modelling of water vapour diffusion in the MBR . . . 181
6.2.2 Modelling validation . . . 182
6.2.3 Discussion about effect of the MBR on the fitting of K_l by inverse analysis 183

6.2.4 Partial conclusion 184
6.3 Comparisons of K_l values determined by different methods 185

7 Conclusion and perspectives **187**
7.1 General remarks 187
7.1.1 Modelling of isothermal drying 187
7.1.2 Modelling of drying and wetting cycles 188
7.1.3 Relevancy of the determination of the liquid-water intrinsic permeability . 190
7.2 Limitations and perspectives for future research 191

Bibliography **195**

List of Figures

1.1 Water states in cementitious material . . . 9
1.2 Schematic drawing of ink-bottle effect. . . . 12
1.3 Schematic drawing of contact effects. . . . 13
1.4 Representation of different diffusion and film flow processes . . . 14
1.5 Illustration of capillary transport and evaporation-condensation is a single pore . 16
1.6 An example for the first wetting scanning curve calculated by the hysteresis model. 30
1.7 A triangular representation of PM domain for the main desorption and adsorption curves. . . . 32
1.8 Water in pores trapped by ink-bottle necks . . . 35
1.9 Main desorption and adsorption curves calculated based on the pore size distribution. 35
1.10 Scanning curves calculated in the DuCOM . . . 36

2.1 Schematic representation of the geometry of the problem. . . . 43
2.2 Fitted desorption curves for the selected materials by using van Genuchten's equation. . . . 45
2.3 Predicted $\alpha(S)\tau$ for three materials calculated by Millington's and Thiéry's proposals. . . . 46
2.4 Comparison of k_{rl} and k_{rg} calculated by Method-1 and Method-2 for Paste3. . . . 49
2.5 Comparisons of simulated mass loss curves based on two different methods to calculate k_{rl} and k_{rg} for Paste4. . . . 50
2.6 Comparisons of calculated mass loss curves based on two methods to calculate k_{rl} and k_{rg} for Paste5. . . . 50
2.7 Comparisons of simulated saturation profiles based on two different methods to calculate k_{rl} and k_{rg} for Paste4. . . . 51
2.8 Comparisons of simulated saturation profiles based on two different methods to calculate k_{rl} and k_{rg} for Paste5. . . . 51
2.9 Comparisons of simulated mass loss curves based on two different methods to calculate k_{rl} and k_{rg} for Concrete3 and Paste3. . . . 52
2.10 Calculated saturation profiles for Concrete3 and Paste3 (Method-1 to calculate k_{rl} and k_{rg}). . . . 53
2.11 Profiles of gas pressure during drying of Paste4 with different values of initial saturation. . . . 57
2.12 The maximum and minimum gas pressure during drying of Paste4 under various external RH with two different values of initial saturation. . . . 58
2.13 Calculated mass loss curve and saturation profiles in the case $K_l \ll K_g$ based on Method-1 to calculate k_{rl} and k_{rg} for Paste5. . . . 60
2.14 Profiles of gas pressure during drying of Paste4 with initial saturation $S_0 = 0.99$. 61

2.15 Relationships of $f(\phi,S)RH(S)$ *vs.* S and $k_{rl}(S)$ *vs.* S for Paste4. 63
2.16 Mass loss curves calculated by three versions of models for Paste4. 64
2.17 Schematic representations of two moisture transport modes. 65
2.18 Ration of liquid-water flux to the total flux in the material during drying of Paste4 (RH_0 = 89% and RH^e = 53.5%). 66
2.19 Simulation results of mass loss curves, including total, liquid-water and vapour, during drying of Paste4 (RH_0 = 89% and RH^e = 53.5%). 67
2.20 Comparison of the contribution of liquid-water transport to total mass loss during drying of Paste3, Paste4 and Paste5 for initial RH_0= 90% and varying external relative humidity. 68

3.1 Schematic representation of WVSIs. 72
3.2 Schematic representation of Mualem's diagram for the main desorption and adsorption processes. 75
3.3 Comparison of R^2_{adj} and NME for fitting of the main desorption isotherms. . . . 82
3.4 Comparison of R^2_{adj} and NME for the main adsorption isotherms. 83
3.5 Fitting results for Paste2 material to compare results fitted by selected models. . 83
3.6 Main curves fitting results for Paste3 material. 84
3.7 Schematic drawing of Feng and Fredlund's model to predict the adsorption branch from the desorption branch. 87
3.8 Prediction results of the main adsorption curves for Paste2 material. 90
3.9 Comparison of the predicted main adsorption branch based on the measured main desorption branch. 91
3.10 The scanning loops simulated by Mualem's diagram. 93
3.11 An example of scanning loops calculated by Mualem Model II. 94
3.12 Schematic representation of Mualem's diagram for scanning processes described with the dependent domain model. 95
3.13 The calculation of p_d during a drying process in Mualem dependent model. . . . 96
3.14 Schematic representation of the calculation of scanning curves by Li's model. . . 97
3.15 Predicted wetting scanning curves and drying scanning curves for Paste3. 100
3.16 Comparison results for wetting scanning isotherm predicted by selected hysteresis models. 102
3.17 Predicted scanning loop for Paste3 compared with experimental data. 103
3.18 Definitions of DPE and WPE. 104
3.19 Simulated hysteresis loops by Li's model and improved Rubin's model (taking Paste3 as an example). 105
3.20 The evolution of PEs calculated based on two RH fluctuations. 106
3.21 The mean residual for all materials at each measured point. 110
3.22 Comparison of results calculated by three versions of FX model. 111
3.23 Comparison of calculated R^2 and MME for FX model. 112
3.24 Comparison of calculated R^2 and MME for VG3 model. 112
3.25 Results calculated by FX and VG3 models for Paste2 in the case of adding one more point. 114

4.1 The gamma-ray signal intensity at different positions inside materials after 1-day curing. 119
4.2 Profiles of porosity measured by gamma-ray attenuation for cement pastes. . . . 121
4.3 Examples of saturation profiles measured by gamma-ray attenuation. 123

4.4 Comparisons of mass loss curves measured by gamma-ray attenuation and by global weighing for CEMI + SF pastes. . . . 124
4.5 An example of controlled RH used in measurements (blue line) and measured mass changes (red line) at different RH. . . . 126
4.6 An example showing different extrapolation methods. . . . 127
4.7 One example of the comparison of original and extrapolated desorption curves measured by DVS. . . . 128
4.8 Pressure plate extractors used in measurements at Lund University. . . . 129
4.9 WVSIs measured by DVS and pressure plate for CEM I materials. . . . 131
4.10 Predicted main adsorption curves. . . . 132

5.1 Implementation of the hysteresis modelling. . . . 140
5.2 Schematic representation of a sample during the drying and wetting measurements. 141
5.3 Simulated sorption isotherms *vs.* experimental data for Paste3. . . . 142
5.4 Comparisons of mass loss curves simulated by non-hysteresis and hysteresis modellings for Paste3. . . . 143
5.5 Comparisons of mass loss curves during drying $RH^e = 63.2\%$ simulated by using two fitted K_l values for Paste3. . . . 144
5.6 Comparisons of simulated mass loss curves with experimental results for Paste4 and Paste5. . . . 145
5.7 Saturation profiles simulated by non-hysteresis ($\omega = 1.0$) and hysteresis modellings are compared with experimental data for Paste4 and Paste5. . . . 145
5.8 Evolutions of k_{rl} and $f(\phi, S)$ at different depths simulated by VGMa for Paste3. 146
5.9 Comparisons of simulation results with measured data for PCEMI6. . . . 147
5.10 Comparisons of simulation results with measured data for PCEMIII06. . . . 147
5.11 Comparisons of simulation results with measured data for PCEMIII06. . . . 148
5.12 The differences of boundary conditions used in non-hysteresis and hysteresis modellings. . . . 149
5.13 Simulation results performed with Mualem Model II and improved Rubin's model to investigate the PEs. . . . 150
5.14 Simulation results of different cycle durations in the cases of non-hysteresis and hysteresis modelling by taking Paste3 as an example. . . . 152
5.15 Simulation results in the case of using a 22% RH amplitude (between 64% and 86%) by taking Paste3 as an example. . . . 154
5.16 Simulation results in the case of initial wetting by taking Paste3 as an example. . 155
5.17 The differences of two forms of Richards equations (taking Paste3 as an example). 156
5.18 Evolutions of $k_{rl}(S)$ calculated by VGMb at different depths for Paste3 . . . 158
5.19 Comparisons of mass loss curves calculated in the cases of with or without hysteresis in relation S-k_{rl} for Paste3 (for the case of drying at 53.5%). . . . 159
5.20 Definitions of the undisturbed saturation S_{und} and the moisture penetration depth x_p after a number of cycles. . . . 160
5.21 Moisture penetration depth in relation with the cycle duration and the RH amplitude for the cases of non-hysteresis and hysteresis modelling by taking Paste3 as an example. . . . 161
5.22 Comparisons of x_p for different initial conditions and cycle durations calculated by using Mualem Model II. . . . 162

6.1 Methods to determine K_l which are compared in this research. . . . 166

6.2 Fitted D_a curves by four models for Paste5 in the desorption process. 171
6.3 Fitted D_a curves for Paste2 during both desorption and adsorption processes. . 173
6.4 Fitted D_a curves for Paste3 during both desorption and adsorption processes. . 174
6.5 Definition of pore radii. 175
6.6 The t_a curves. 176
6.7 The pore size distribution calculated by BJH method. 176
6.8 The calculated Knudsen effect for different materials. 177
6.9 Schematic representation of the system in case of our experimental conditions. . . 182
6.10 Comparisons of simulated mass loss curves and saturation profiles with measured ones for Paste4. 182
6.11 Effects of x_e on the mass loss curves during drying. 183
6.12 Relationship between x_e and K_l for the studied materials. 184
6.13 Comparisons of K_l values determined by different methods for the studied materials. 186

List of Tables

1.1 Classification of pores and features in concrete 8

2.1 Properties of materials. 44
2.2 Values of a_V and m_V for the selected materials fitted by Eq. (2.4). 45
2.3 The intrinsic permeabilities fitted by inverse analysis for different materials. . . . 51
2.4 The intrinsic permeabilities to liquid-water validated by experimental data for different materials. 59
2.5 The intrinsic permeabilities to liquid-water validated by experimental data for two versions of simplified models. 64

3.1 Proposed multi-level approach to model hysteresis. 77
3.2 Collected datasets of WVSIs measured by the saturated salt solution method . . 78
3.3 Proposed models for the multi-level approach to model hysteresis. 107

4.1 Materials and mix designs used in the present study. 118
4.2 RH cycles used during drying-wetting experiments. 119
4.3 The mass adsorption coefficient for studied CEM I pastes. 120
4.4 The comparison of global porosity (%) measured by weighing and gamma-ray for cement pastes. 122

5.1 Validated liquid intrinsic permeabilities ($\times 10^{-21}$m^2) for different materials. . . . 148

6.1 Fitted $K_l(\times 10^{-21}$ m$^2)$ for the desorption and adsorption processes. 172
6.2 The fitted x_D for the desorption process. 177
6.3 The fitted x_D for the adsorption process. 178
6.4 The calculated RH threshold values for using VGMa model with Knudsen effect. 178

Lists of Symbols and Acronyms

Abbreviation

DPE Drying pumping error.

DVS Dynamic vapour sorption.

ITZ Interfacial transition zone.

MIP Mercury Intrusion Porosimetry.

MME Mean multiplicative error.

MR Mean residual.

NME Normalized mean error.

NMR Nuclear Magnetic Resonance.

PEs Pumping errors.

PSD Pore Size Distribution.

RH Relative humidity.

WPE Wetting pumping error.

WVSIs Water vapour sorption isotherms.

Nomenclature

$\alpha(S)$	Relative tortuosity (unsaturated effect of tortuosity on D_0).	-
$\bar{\rho}$	Normalized radii of pore bodies.	-
$\bar{r}$	Normalized radii of pore necks.	-
η_g	Dynamic viscosity of gas.	$\mathrm{kg \cdot m^{-1} \cdot s^{-1}}$
η_l	Dynamic viscosity of liquid-water.	$\mathrm{kg \cdot m^{-1} \cdot s^{-1}}$
γ	Surface tension.	$\mathrm{N \cdot m^{-1}}$
κ	Thermal conductivity.	$\mathrm{W \cdot m^{-1} \cdot {}^{\circ} C^{-1}}$
λ	Mean free path.	m

$\mathbb{M}$	Capillary modulus.	Pa
$\mathbf{t}_D^g$	Time scale for advection of gas-phase.	-
$\mathbf{t}_D^l$	Time scale for advection of liquid-water.	-
$\mathbf{t}_F$	Time scale for vapour diffusion.	-
$\mathring{m}_{l\to v}$	Mass exchange from liquid-water to vapour.	$\mathrm{kg}\cdot\mathrm{m}^{-3}\cdot\mathrm{s}^{-1}$
μ	Gamma-ray attenuation coefficient.	$\mathrm{m}^2\cdot\mathrm{s}^{-1}$
$\omega, \omega_i, \omega_l$	Weighting factors.	-
ϕ	Porosity.	-
$\pi(S)$	Dimensionless function for sorption isotherms.	-
ψ	Kirchhoff's flow potential.	
ρ_l	Liquid-water density.	$\mathrm{kg}\cdot\mathrm{m}^{-3}$
ρ_m	Dry density of material.	$\mathrm{kg}\cdot\mathrm{m}^{-3}$
σ	Air-water interfacial energy.	$\mathrm{J}\cdot\mathrm{m}^{-2}$
σ_p	Standard deviation of log-transformed pore radii.	-
τ	Tortuosity coefficient.	-
θ	Water content.	$\mathrm{m}^3\cdot\mathrm{m}^{-3}$
$\theta^{\max}$	Maximum water content.	$\mathrm{m}^3\cdot\mathrm{m}^{-3}$
θ_r	Water content at dry reference state.	$\mathrm{m}^3\cdot\mathrm{m}^{-3}$
A	Surface or cross-section area.	m^2
C	Moisture capacity.	Pa^{-1}
C_T	Temperature energy capacity.	$\mathrm{W}\cdot{}^\circ\,\mathrm{C}^{-1}$
$c_v(_a)$	Molar fraction related to vapour (dry air).	-
D_0	Diffusion coefficient of vapour in the free air.	$\mathrm{m}^2\cdot\mathrm{s}^{-1}$
D_a	Apparent diffusivity.	$\mathrm{m}^2\cdot\mathrm{s}^{-1}$
D_l	Liquid-water diffusivity.	$\mathrm{m}^2\cdot\mathrm{s}^{-1}$
D_S	Moisture diffusion coefficient under saturation gradient.	$\mathrm{m}^2\mathrm{s}^{-1}$
D_T	Moisture diffusion coefficient under temperature gradient.	$\mathrm{kg}\cdot\mathrm{m}^{-1}\mathrm{s}^{-1}\mathrm{K}^{-1}$
D_v	Vapour diffusivity.	$\mathrm{m}^2\cdot\mathrm{s}^{-1}$
E	Mass transport coefficient between material and environment (emissivity).	$\mathrm{kg}\cdot\mathrm{Pa}^{-1}\cdot\mathrm{m}^{-2}\cdot\mathrm{s}^{-1}$

E_m	Rate of mass exchange between liquid-water and vapour.	$\mathrm{kg \cdot m^{-3} \cdot s^{-1}}$
$f(\bar{r}, \bar{\rho})$	Total pore water distribution function.	-
$f(\phi, S)$	Resistance factor.	-
F_o	Fourier number.	-
$h(\bar{r})$	Pore water distribution function related to pore necks.	-
$H(P_c)$	Cumulative pore water distribution function related to pore necks.	-
I	Transmitted photon intensity.	-
J_l, J_v, J_a	Flux of liquid-water, vapour and dry air.	$\mathrm{kg \cdot m^{-2} \cdot s^{-1}}$
k_d	Material constant for drying in the hysteresis model proposed by Johannesson et al.	-
k_m	Mass transport coefficient in the airside.	$\mathrm{kg \cdot m^{-2} \cdot s^{-1}}$
K_p	The slope of a scanning curve.	-
K_v	Vapour permeability.	$\mathrm{kg \cdot Pa^{-1} \cdot m^{-1} \cdot s^{-1}}$
k_w	Material constant for wetting in the hysteresis model proposed by Johannesson et al.	-
K_0	Intrinsic permeability.	$\mathrm{m^2}$
K_g	Gas intrinsic permeability.	$\mathrm{m^2}$
K_l	Liquid-water intrinsic permeability.	$\mathrm{m^2}$
k_{rg}	Gas relative permeability.	-
k_{rl}	Liquid-water relative permeability.	-
l	Length of the material.	m
$l(\bar{\rho})$	Pore water distribution function related to pore bodies.	-
$L(P_c)$	Cumulative pore water distribution function related to pore bodies.	-
M_v	Molar mass of water molecule.	$\mathrm{kg \cdot mol^{-1}}$
P_c	Capillary pressure.	Pa
$P_c^{\max}$	Maximum capillary pressure.	Pa
$P_c^{\min}$	Minimum capillary pressure.	Pa
p_d	Weighting factor used for the drying process in Mualem dependent model.	-
P_g	Gas pressure.	Pa
P_l	Liquid pressure.	Pa
P_v	Vapour pressure.	Pa

p_w	Weighting factor used for the wetting process in Mualem dependent model.	-
P_{atm}	Atmospheric pressure.	Pa
P_{cm}	Capillary pressure related to the medium pore radius.	Pa
P_{vs}	Saturated vapour pressure.	Pa
Q	Complementary normal distribution function.	-
Q_l	Total mass loss in liquid form.	kg
Q_v	Total mass loss in vapour form.	kg
R	Gas constant.	$\mathrm{J \cdot K^{-1} \cdot mol^{-1}}$
R^2	Coefficient of determination.	-
R^2_{adj}	Adjusted R^2.	-
RH^e	RH at the boundary.	-
RH_0	Initial RH.	-
S	Saturation.	-
S^e	Saturation at the boundary.	-
S_0	Initial saturation.	-
T	Temperature.	K
t_p	Cycle period.	s
v_g	Velocity of gas.	$\mathrm{m \cdot s^{-1}}$
v_l, v_v, v_a	Velocity of liquid-water, vapour and dry air.	$\mathrm{m \cdot s^{-1}}$
x_p	Moisture penetration depth in the surface layer.	m
x_r	Moisture penetration depth in the deeper layer.	m

Subscripts

0	Initial value or at the starting point of a curve.
105	Parameters for materials dried at 105°C.
a	Dry air.
d	Drying or desorption process.
g	Gas-phase.
l	Liquid-water.
sat	Parameters for materials at the saturated state.

v Vapour.

w Wetting or adsorption process.

Superscripts

0 Values at the surface or the boundary.

e External value or in the environment.

eq Parameters at equilibrium.

m Values in the material.

General introduction

Background

For a variety of reasons, concrete has become the mostly used build materials for centuries. In fact, for every person one ton of concrete is used annually. It is a strong and durable material that is versatile and economical. Designers of structures have been mostly interested in how to make structures more durable. One reason is that the cement industrials constitute 5-7% of man-made CO_2 emissions over the world [1, 2, 3]. More durable structures mean that less cement will be used in construction, which could be an indirect way to reduce global CO_2 emissions. Another reason is that it has been estimated that in developed countries about 40% of the total resources of the construction industry are being applied to repair and maintenance of existing structures [3]. This cost forces engineers to pay serious attention to durability issues.

Concrete structures are subjected to either biological, physical or chemical degradation processes. But in common, water, as the primary agent of both creation and destruction of the material, attributes to be central to most durability problems in concretes [4]. Indeed, liquid-water can transport chemicals such as chloride ions, alter mechanical properties, and cause freeze-thaw damage. To predict the degradation of concrete structures, it is important to better understand the moisture behaviour of the material and its responses to external ambient environment.

Hence, the European Community (Framework Programme 7) funded a Marie Curie Initial Training Network, called TRANSCEND, to carry out research aiming at understanding water transport in cementitious materials. This thesis is one part of the TRANSCEND project, which stands for "understanding *TRANS*port for *C*oncrete which is *E*co-friendly i*N*novative and *D*urable".

Natural conditions and importance of moisture transport

In the natural environment, the moisture behaviour is very complicated (e.g., tidal zone, fluctuating groundwater, weather changes), and the moisture exchanges occur continually at the interface between materials and environment. The material can lose moisture caused by low environment RH or gain water due to high external RH. In this process, moisture is able to move into or out the porous media, and this process keeps going along with the varying external conditions.

In porous solids, the cyclic changes of water content are known to be the cause of many types of chemical and physical degradation processes. The moisture movement is generally due to capillary suction, condensation, gradient of density of water vapour, etc. But one thing can be sure is that rarely pure water is involved. Water is noted for its ability to dissolve more substances than any other known liquid. When liquid-water enters the material, aggressive ions and salts will penetrate into along with water, and when moisture leaves the material, some chemical components will move out with liquid-water. During this repetitive process, salts and ions will accumulate in the zone where drying and wetting cycles frequently occur. Therefore, the repeated wetting and drying regimes can increase the risk of deteriorations of cement-based materials.

For concrete structures which are exposed to those conditions, materials are rarely in a state of full saturation. In that case, strongly capillary pressure will apply on pore walls and further induce shrinkage (during drying) or swelling (during wetting) which is able to damage the microstructure of cementitious materials. As the essential factor, moisture transport can induce many other durability issues, such as corrosions and carbonation, whose kinetics is correlated to the moisture states. Hence, it is of great importance to study moisture transport in cementitious materials under drying and wetting cycles conditions.

Modelling of drying and wetting cycles

Modelling of moisture transport under drying-wetting cycles conditions for cementitious materials has been studied more than two decades [5]. In the early studies, most moisture transport models used a simple way, which employed the same sorption curve for both drying and wetting processes; thus, sorption hysteresis between these two processes was neglected [5, 6, 7]. However, sorption hysteresis has been recognised as one main characteristic of moisture behaviour for cementitious materials [8, 9, 10, 11, 12]. Recent studies performed by Maekawa et al. [13], Johannesson and

Nyman [14, 15] and Derluyn et al. [16] have proved that this simple approach cannot provide high accurate predictions and suggested to take into account sorption hysteresis. This suggestion leads to a more complicated modelling method, which needs to couple a sorption hysteresis model with a moisture transport model.

In the literature, researchers used different ways to study modelling of sorption hysteresis. One way tried to understand reasons and mechanisms of sorption hysteresis. Espinosa and Franke [9] proposed an approach called "ink-bottle pore method", assuming "ink-bottle pores" as the reason of hysteresis, in order to predict the main desorption, main adsorption and scanning curves. However, there are more than eight undetermined parameters which have to be analysed firstly by fitting experimental data such as molecular adsorption data. Another model presented by Ranaivomanana et al. [17] was developed based on the description of the pore size distribution by considering oblong-shaped pores. Pinson et al. [18, 19] further assumed different levels of pore network connectivity to explain sorption hysteresis. These theoretical studies can present good explanations of hysteresis but they rarely provide an easy-to-use calculation method that can be combined with moisture transport model to simulate drying and wetting cycles.

Other researchers proposed most straightforward methods which are generally taken from modelling of hysteresis in soil science. These models fit the measured main desorption and main adsorption curves by using empirical models and further predict scanning loops, such as studies in [13, 14, 15, 16]. Models used in this method may lack physical interpretation, but they are very easy to couple with moisture transport models and can provide good fitting and prediction results.

Since the current research has a focus on modelling of drying and wetting cycles, it will only review and apply of hysteresis models which were developed in the second case mentioned above.

Objective, methods and chapter outline

The objective of this study is set to better understand how the moisture behaviour inside cementitious materials responds to varying relative humidity at the material boundary. In the current research, both a simple method (without sorption hysteresis) and a more complicated one (with sorption hysteresis) for modelling of drying and wetting cycles will be compared and discussed. The arrangement for each chapter is presented as follows.

For modelling of drying and wetting cycles, the first step focuses on the review of models which were initially developed to simulate moisture transport for varying relative humidity at the

boundary. Three methods can be summarized: using different transport coefficients for drying and wetting, modelling without hysteretic effects and modelling with hysteresis.

The second step focuses on understanding and simplifying a multiphase continuum model. The simplified model will be further used for modelling of drying and wetting cycles. This continuum model considers that the mass transport includes advection of liquid-water and gas-phase (dry air and vapour), and diffusion of gas-phase. The liquid intrinsic permeability is determined by fitting drying kinetics, while the gas intrinsic permeability can be either set equal to the liquid intrinsic permeability or obtained from measurements. In the latter case, the gas intrinsic permeability is normally several orders of magnitude higher than the liquid intrinsic permeability. The discussion and analysis of both cases can lead to simplified moisture transport models which will be used for the implementation of hysteresis models into moisture transport.

The third step is to find an appropriate hysteresis model. A detailed review of hysteresis models available in the literature is proposed in this chapter. Hysteresis models which have been initially developed for water transport in soils and sands are selected, including conceptual and empirical models. A comprehensive statistic comparison with experimental data is performed for cement pastes and concretes. A multi-level approach to simulate hysteresis is proposed as well. Evaluations and recommendations for use of this multi-level approach are provided for an application purpose of the compared models.

The fourth step is to prepare the input data for modelling, experimental data for calibration of the liquid intrinsic permeability and data for verification of modelling results of drying and wetting cycles. Meanwhile, experimental investigations of effects of cyclic RH at the boundary on moisture distribution within cementitious materials are also reported in this part. As the main input data, water vapour sorption isotherms for various cement pastes (made by CEM I, CEM III and CEM I + silica fume) are measured by using a dynamic vapour sorption instrument (DVS) and pressure plate. Measured mass loss curves during drying are used to determine the liquid intrinsic permeability. Mass loss curves measured in following processes or wetting and re-drying and saturation profiles measured at different times are used to verify the modelling results.

The most important part of this work is to perform modelling of moisture transport under drying and wetting cycles conditions. Modellings with and without hysteretic effects are implemented and compared based on experimental data. Simulations in various situations, such as different initial conditions, cycle durations, RH amplitudes, etc., are conducted to check the

applicability of the proposed modelling methods. In the cyclic drying and wetting regime, the moisture penetration depth, which is very useful for studies on durability issues, such as ions penetration, can be determined by modelling.

The last step introduces two research perspectives which can provide further information to understand moisture transport properties in cementitious materials, especially for the assessment of the liquid-water intrinsic permeability K_l. The first perspective is to determine K_l by fitting measured apparent diffusivity values taken from the literature [11]. The resistance factor to vapour diffusion can also be determined likewise. To improve the fitting results, Knudsen effect is taken into account for the vapour diffusion. The second perspective is to check if using different boundary conditions has an effect on moisture transport in the material under our experimental conditions. The liquid intrinsic permeabilities can be determined by inverse analysis for different boundary conditions. These K_l values are further compared with these determined by other methods (Katz-Thompson [20] and fitting apparent diffusivity values). The work in this part aims to illustrate the robustness and the reliability of using inverse analysis to determine K_l.

Declaration of modelling codes and experimental data

Numerical modellings in Chapter 2 of this thesis were conducted by using BIL, a modelling platform based on finite element/volume methods dedicated to coupled problems involved in environmental engineering, geomechanical engineering, material sciences, etc. BIL is released by Patrick Dangla (see http://perso.lcpc.fr/dangla.patrick/bil/) and distributed under the terms of the GNU General Public License (GPL). Other calculations (in Chapters 3, 5 and 6) were carried out by the authors themselves by using MATLAB, Microsoft Excel and other free softwares.

The experimental data used to feed and verify the models were either measured in the previous work by Baroghel-Bouny [21, 22, 23, 11] and Nguyen [24] performed at IFSTTAR (former LCPC) or conducted by the authors themselves at IFSTTAR and Lund University.

Chapter 1

Review of modelling of drying and wetting cycles

Summary

Cementitious materials are composite materials, with cement, sands and gravels, whose microstructure is random over wide range of length scales, which makes the major difference to other porous media such as soils and rocks. Of course, the moisture (liquid-water + vapour) states, transport properties, measurement methods, etc., are also different.

This chapter will focus on discussing "moisture" in cementitious materials, which is associated with several questions: Where is moisture from? How does moisture stay in the material? How does external moisture become internal moisture and *vice versa*? How does moisture move within the material? What are the moisture transport mechanisms? After discussions about these questions, a multiphase moisture transport model for porous media will be introduced. The most important part is the review of models initially developed for varying external RH at the boundary to predict moisture behaviour under drying and wetting cycles conditions. Then, the discussion about moisture interactions between materials and their surrounding will be presented.

1.1 Introduction

For materials like concretes, the moisture transport properties are not easy to determine because of the unpredictable sources of water and different states of water in the material.

1.1.1 Sources of water

Water is a necessary ingredient for the cement hydration reactions. As an agent, it facilitates the mixing of the components of concrete. The amount of added water is more than the amount water needed for the chemical reactions, since only a water-to-cement ratio (w/c) = 0.25 is enough for all chemical reactions in case of Portland cements [25, 26]. Besides, a cementitious material normally cannot reach a fully hydrated state, so more water beyond estimation will be left in the material and become physically-bound and free water. This is the initial source of water in hardened cement-based materials.

Gradually, depending on the ambient conditions and the size of the material, most of the evaporable water in concrete is lost, leaving empty or unsaturated pores. When the ambient relative humidity increases, the material can capture external moisture. This is the second source of moisture in the material.

1.1.2 Water states in cementitious materials

Water states and water transport are related to the microstructure of the material. It needs to know the pore size distribution to understand water states and their mobility. Owing to the complex structure and connectivity of the network, pores are in different shapes and randomly distribute which makes the quantification of the exact pores size distribution (PSD) extremely difficult. By assuming pores as cylinders, techniques can be used to measure PSD. Based on measurements using such as Scanning Electron Microscopy, Optical Microscopy, Impedance Spectroscopy and Mercury Intrusion Porosimetry (MIP), movable water in the pores in cementitious materials can be classified into different levels (see Table 1.1).

Table 1.1: Classification of pores and features in concrete (taken from [27]).

Type of pore	Description	Size	Water	Properties
Capillary pores	Large	10 μm - 50 nm	Evaporable Bulk water	Permeability, strength
	Medium	50 -10 nm	Evaporable Moderate menisci	Permeability, strength, shrinkage (high RH)
Gel pores	Small	10 - 2.5 nm	Evaporable Strong menisci	Shrinkage (up to 50% RH)
	Micro	2.5 - 0.5 nm	Non-evaporable, no-menisci, intermolecular interactions	Shrinkage, creep (35-11% RH)
Interlayer spaces	Structural	$<$ 0.5 nm	Non-evaporable, ionic/covalent bond	Shrinkage, creep ($<$11% RH)

Below interlayer water, there is some chemically-bound water which is concerned by the transport. Only in extreme conditions, this kind of water can be lost, such as drying at high temperature (e.g., 105°C).

The water states in the material are not only related to the pore size distribution but also related to other microstructure properties such as geometry shapes of pores and pores layout. Researchers create different simplistic models for hardened cement paste to represent the structure. For example, Powers' model [28] considered that a representative part of the material consists of either two or three layers of C-S-H, which could roll into fibres. Feldman and Sereda [29, 30] regarded gel as a three-dimensional assemblage of C-S-H layers, which tends to form a subparallel group with a few layers of thickness. In Munich model [31], the paste was described as a dispersed gel, together with the crystalline constituents. Jennings [32] proposed a model for the structure of C-S-H, considering roughly spherical C-S-H units, which flocculate to form larger units.

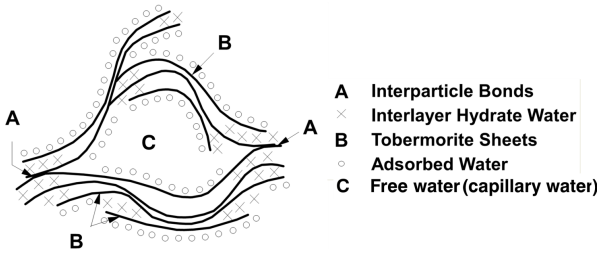

Figure 1.1: Water states in cementitious material (adapted from Feldman and Sereda [29, 30]).

The layered irregular structure of the Feldman and Sereda model [29, 30], which was developed based on studies of sorption properties, porosity and relations between water content and mechanical properties, clearly shows three types of water in the material: interlayer, adsorbed and capillary water (see Fig. 1.1). Interlayer water is highly combined to C-S-H sheets, so it needs very strong driving force to move. In atmospheric condition, this water is rarely affected by varying RH at the boundary. Adsorbed water and gel pore water can be released under low RH. Capillary water is more movable and evaporable, and is the main source of transported water. However, capillary water is generally not continuous because of the complex geometry structure. It evaporates into vapour at the menisci between liquid and vapour. Partially continuous liquid-water only exits in the high water content range. It is distributed in different locations and is locally separated by the gas-phase in the material.

1.2 Moisture sorption and hysteresis

1.2.1 Moisture sorption processes

When the pore is not fully filled by liquid-water, the material gains or releases moisture through the sorption process. Sorption, including adsorption and desorption, is the accumulation of molecules onto pore walls from the surrounding moisture [33]. The adsorption is brought about by forces acting between the solid and water molecules. These forces are of two kinds - physical and chemical - and give rise to physical sorption and chemisorption, respectively. The main mechanisms of adsorption are given as follows.

1) Exchange sorption: electrostatic interaction of ions due to the different charges between the pore walls and water molecules.

2) Physical sorption: van der Waals attraction between adsorbate (moisture) and adsorbent (pore walls). The attraction is not fixed to a specific site and the adsorbate is relatively free to move on the pore walls. This sorption is relatively weak and reversible, and can lead to a multilayer of adsorbed water.

3) Chemical sorption: some degree of chemical bonding between adsorbate and adsorbent characterized by strong attractiveness. Adsorbed molecules are not free to move on the pore walls. There is a high degree of specificity, and typically a monolayer is formed.

The adsorption and desorption of a gas on the solid surface is always accompanied by the evolution of heat. It is dependent on the adsorbent – adsorbate and adsorbate - adsorbate interactions [33]. The adsorption releases heat, while the desorption requires heat. This makes these two processes quite different.

When menisci are formed in pores, capillarity is involved. The interface between liquid-water and gas-phase is maintained due to the surface tension γ between these two phases. At equilibrium, a balance of force at this interface can be described by the Young-Laplace equation:

$$P_c = P_g - P_l = \frac{2\gamma}{r^*} \tag{1.1}$$

where P_c, P_g and P_l represent capillary pressure, gas pressure and liquid pressure, respectively. r^* denotes the mean radius of curvature.

When the concentration of vapour in gas-phase changes, vapour can condense or release from solid surfaces, and menisci appear in big or small pores. There should be a strong relationship between vapour concentration in gas-phase and water saturation in the material. At the macroscopic scale, vapour concentration in gas-phase is closely related to the external relative humidity. In physical and chemical science, the relationship between external relative humidity RH and water saturation S in the material at equilibrium is known as "sorption isotherms" or "water vapour sorption isotherms" (WVSIs) [23]. For more porous materials, such as soils, a great amount of menisci can be formed in the material, so the relationship between macroscopic capillary pressure and water saturation is also called "retention curves" [34].

$$P_c = P_c(S) \tag{1.2}$$

At equilibrium, the macroscopic capillary pressure in the material can be calculated based on the external relative humidity. Hence, for cementitious materials, sorption isotherms can be measured by exposing the material to water vapour with a definite RH and temperature. When RH changes from a high value to a low value, a desorption curve can be measured. In an inverse process, an adsorption isotherm is obtained.

In the low RH range, the sorption process plays the main role for sorption isotherms. Sorption models, such as Linear [35], Freundlich [36], Langmuir [37], BET [38], Dent [39], etc., can provide good fitting of gas sorption isotherms. Langmuir's equation is used for the adsorption of a single layer of vapour molecules (monomolecular). BET and Dent's equations are capable of accounting for multilayer molecules adsorption (polymolecular). However, comparisons performed by Kumar et al. [40] show that these models are only valid for isotherms in the low RH range, i.e., smaller than 45% [41]. In the high RH range, these models produce big errors. Nevertheless, most concrete structures suffer durability issues under moderate and high RH levels, generally between 50% and 100%. In this range, water vapour sorption isotherms not only include sorption but also is involved by capillarity. Hence, for the purpose of modelling, researchers are apt to fit measured sorption isotherms by using empirical equations, which can be widely found in soil science to fit retention curves [42, 11, 43, 44]. The review of these equations, which were initially developed for soils and sands, will be presented in Chapter 3.

1.2.2 Sorption hysteresis

In measurements, adsorption curves show different paths to desorption curves. This phenomenon, different sorption isotherms during drying and wetting, is called "sorption hysteresis". Experimental data from the literature [23] reveal that hysteresis between desorption and adsorption is found in the whole RH range. It is more significant in the middle RH range, in which the capillary condensation and evaporation is assumed to be the mechanism which governs the thermodynamic equilibrium between liquid-water and water vapour.

Actually, in different pore scales, various reasons contribute to hysteresis. For capillary pores, the main reason, known as "ink-bottle effect", results from the different shapes of connected pores. One example is shown in Figure 1.2. If considering the pore is initially filled with water, during drying, capillary pressure increases gradually from $P_c(r_5)$ to $P_c(r_4)$. At the beginning, because the meniscus at the narrow throat r_0 blocks moisture inside, at capillary pressure $P_c(r_5)$, $P_c(r_3)$ and $P_c(r_1)$, no moisture can be transported outside the pore. Until capillary pressure is larger than $P_c(r_0)$, the meniscus cannot support the same capillary pressure and moisture in r_0 and r_1 suddenly loses. The same process will happen when capillary pressure increases to $P_c(r_2)$ and $P_c(r_4)$. This kind of sudden change is called "Haines jump" [45]. During wetting, the throat will be filled by water in the sequence of r_4, r_2, r_0, r_1, r_3 and r_5. Therefore, hysteresis is observed between the drying curve and the wetting curve (see Fig. 1.2b). It is clear that the drying process depends on the narrow throats, while the wetting process is more related to the pore bodies [34].

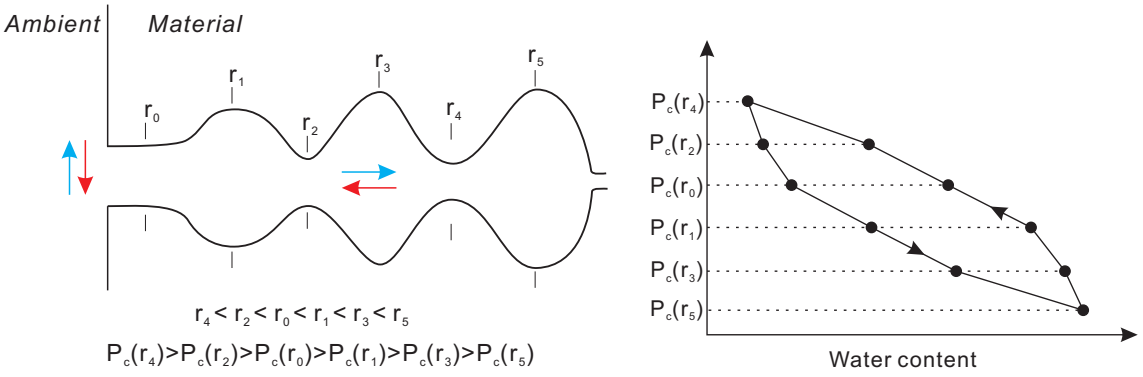

(a) Representation of moisture transport one pore. (b) The corresponding sorption isotherms.

Figure 1.2: Schematic drawing of ink-bottle effect.

The second most known reason of sorption hysteresis is the different contact angle [46, 34] which is able to affect hysteresis in various ways. Indeed, different chemical components in cementitious materials have different contact angles (see Fig. 1.3a). Hydrophobic or hydrophilic

impurities in pores also cause hysteresis (see Figs. 1.3b and 1.3c) because they make water easily or difficultly to enter pores. Besides, the polarization of water molecules is recognised as one reason. A pre-wetted material is more easily to accept water molecules while a dried material shows strong repulsion. This can also be explained by the different energy states during drying and wetting.

Theoretically, moisture in C-S-H pores induces very small hysteresis. Hence, there should be linear relationship between RH and water content in the low RH range, and no hysteresis between desorption and adsorption should be observed. However, experimental data show hysteresis when water is the adsorbate, while there is no hysteresis for nitrogen or other gas [23]. The main reason is that in room temperature moisture is in liquid form which has stronger interactions with pore walls. During drying, because the removal of interlayer water which is strongly bound to the C-S-H [29], interlayer pores collapse. During adsorption, the collapsed pores will expand again, but they cannot reach their usual size [23]. The reason of shrinkage and swelling has been explained in more detail in the literature [47].

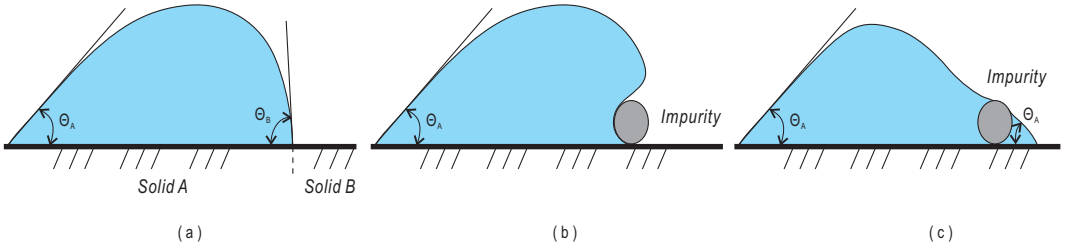

Figure 1.3: Schematic drawing of contact effects.

The existing hysteretic behaviour leads to the need of hysteresis models when performing modelling of moisture transport. Some hysteresis models, which were developed based on the conceptual theories, are known as conceptual models [48, 49, 50, 51, 52, 53, 54, 55]. Others, which were initially used to fit the measured sorption curves, are called empirical models [56, 57, 58, 59, 60, 61]. Both types of hysteresis models will be compared and discussed in Chapter 3.

1.3 Mechanisms of moisture transport

Moisture transport in cementitious materials is related to many complex mechanisms which occur more or less jointly. In porous materials, several phenomena such as permeation, diffusion, adsorption-desorption-condensation and evaporation are very important. They depend on the internal relative humidity prevailing in the material.

1.3.1 Diffusion

The diffusion processes are those of ordinary diffusion and Knudsen diffusion as put forward by Mason and Malinauskas [62] and surface diffusion as reported by Higashi et al. [63]. The different diffusion processes are illustrated in Fig. 1.4 [64].

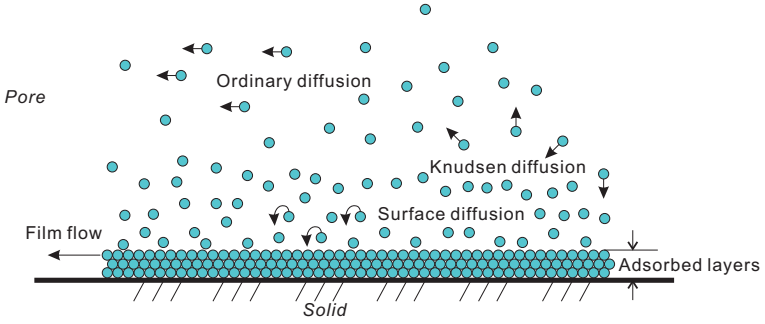

Figure 1.4: Representation of different diffusion and film flow processes (adapted from [64]).

Ordinary diffusion

Ordinary diffusion is commonly found in both low RH and high RH ranges. It is caused by the gradient of concentration, so water molecules tend to diffuse from the high concentration region to the low concentration zone. There are two main effects which can slow down ordinary diffusion. One is collisions between water molecules, which are able to offset some molecular momentum. The other one is the molecules exchange with adsorbed layer on pore walls. Water molecules adsorbed by pore walls decrease the ordinary diffusion process. When the relative humidity exceeds a threshold value, a meniscus is formed at each end of the path. In this condition, moisture transport becomes a process of condensation and evaporation at menisci. This mechanism is dominant in pores with size between 50 nm and 10 μm [65] which is typically the size of capillary pores in cementitious materials (see Table 1.1).

Knudsen diffusion

According to the definition, Knudsen diffusion occurs when the pore size is the same as or smaller than the mean free path of the water molecules. This kind of diffusion is governed by collisions against the pore walls, which are the main source of resistance to Knudsen diffusion. Knudsen diffusion can be quantified by the Knudsen number $K_n = \lambda/2r_p \geq 1$ where λ is the mean free path. For Knudsen diffusion, the value of K_n is equal to or greater than 1. The gives free path in air at atmospheric pressure and room temperature (for instance 23 °C) is around 68 nm [66].

Hence, Knudsen diffusion widely exists in gel pores and partially in capillary pores according to Table 1.1.

Surface diffusion

This mechanism primarily takes place when water molecules are mainly adsorbed by pore walls (which is the case if RH is low). On the one hand, when water molecules are forced to the solid walls, they have the trend to be adsorbed by walls; on the other hand, due to the strong difference of molecules concentration at different distances from the pore walls, water molecules have another trend to leave the solid walls and to diffuse to lower concentration region. The result is that water molecules move near pore walls. It is governed by leaps of water molecules between different adsorption sites.

In fact, during desorption, when there are less and less water molecules in pores, collisions between molecules become weaker and weaker, and Knudsen diffusion and surface diffusion are apt to be ordinary diffusion in capillary pores. All those phenomena will progressively speed up ordinary diffusion. Besides, ordinary diffusion is faster compared to other diffusion processes, so it represents the main part of mass diffusion. That is why, most researchers generally focus on ordinary diffusion in the literature. More discussions about Knudsen diffusion will be presented in Chapter 6.

1.3.2 Capillary transport

Capillary transport is the movement of liquid-water under the gradient of capillary pressure in porous media when there is no external hydraulic head. This is the result of interactions between liquid-water and pore walls. Capillary transport generally occurs when the liquid body is continuous. For high water content, the pores are almost filled with liquid-water (see Fig. 1.5a). When a driving force is available, capillary flow is established through the liquid body in the porous network. At the beginning of drying, the continuous liquid-water is driven by strong capillary forces with high liquid permeability. Thus, moisture transport is dominated by capillary transport. Along with drying time, liquid-water will progressively become discontinuous (see Fig. 1.5b). In this period, the capillary transport only remains preponderant in regions of the material where liquid-water is continuous, such as in segments AB and CD, whilst in the part BC the main transport is diffusion.

Capillary pressure is so powerful and can create severe damages more than any other transport

mechanisms. When the liquid phase is extracted by capillary pressure from the spaces between solids, the collapse will appear in the small pores due to no liquid phase supporting solid walls in cementitious materials (see Fig. 1.5b). By contrast, when the collapsed microstructure gains liquid-water, the volume of the system will expand and try to return to its normal state (see Fig. 1.5c).

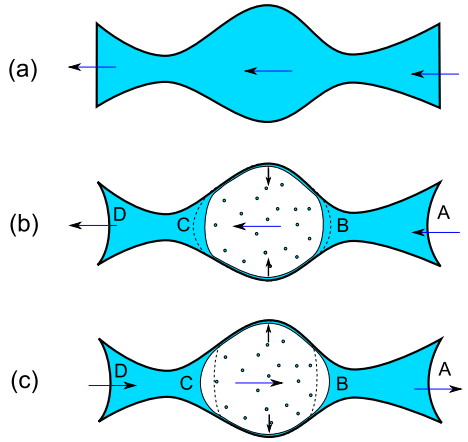

Figure 1.5: Illustration of capillary transport and evaporation-condensation is a single pore (adapted from [13]).

1.3.3 Evaporation-Condensation

Evaporation-Condensation occurs at the interface between liquid-water and gas. For instance, in Fig. 1.5, moisture evaporates from surface B and becomes vapour, so it can be transported by diffusion through the pore and condenses on surface C. This process is due to the non-equilibrium between vapour pressure (in segment BC) and capillary pressure (segments AB and CD) in the vicinity of the interfaces.

When there is no continuous liquid-water in the pore, a thin film of water may form on the pore walls above the adsorbed layers (see the middle pore in Figs. 1.5b and 1.5c). The thickness of this film is related to the van der Waals forces between water molecules and pore walls [67, 68]. This thin water film is linked with menisci, so it can move due to capillary pressure. This kind of transport is called "film flow" which is more obvious for rocks and porous media containing hydrophilic particles [69, 70].

In addition, in more porous materials, such as soils, rocks, cracked concretes, etc., hydraulic flow may be significant when the material is directly in contact with liquid-water. This transport is driven by capillary pressure or external applied liquid pressure. But this process only exits

in the largest pores and for specific boundary conditions; thus, it will not be considered in this study.

1.4 Continuum approach to model unsaturated moisture transport in porous media

Calculation of water transport in unsaturated systems was initially developed based on the saturated flow in porous media. In 1907, Buckingham [71] extended Darcy's law to the case of unsaturated flow. In 1931, Richards further improved Buckingham's idea and combined the unsaturated flux law with mass balance principles to derive a governing equation for unsaturated moisture transport which is known as Richards' equation [72]. Since then, a number of models were developed for modelling of moisture transport in porous media. The development of theoretical basis models started in the late 1950s in the research provided by Philip and de Vries [73]. Later on, in a series work performed by Bear [74, 75, 76, 34], the multiphase transport model for unsaturated porous media started to be used. Meanwhile, the principle of multiphase, including liquid-water, vapour and drying air, was also applied to studies on mechanics and physics of porous solids [77, 78]. In the field of civil engineering materials, several models, which described moisture taking into account vapour and liquid-water mobility, have been developed for the prediction of the service-life of concrete structures [79, 80, 81, 82]. In 2001, the multiphase model was further used to simulate drying of cementitious materials [42].

Nevertheless, the permeability of most materials of civil engineering range from very large values (10^{-10} m^2 for sands) to very low ones (10^{-21} m^2 for concretes). This feature explains that there exist as many ways of modelling as kinds of materials, since the models are generally adapted to specific microstructure and even to particular initial and boundary conditions (initial water content within the material, relative humidity and temperature prevailing in the surrounding environment, etc.). When engineers are trying to numerically predict moisture transport within building materials, the fundamental question which generally raises is which mechanisms govern the transport process: advection of liquid-water by capillarity, evaporation of liquid-water inside the material and/or water vapour diffusion, variations of total gas pressure, etc. To answer this question, models need to simulate all above mechanisms simultaneously.

In this section, a multiphase model which has been used in the work of Coussy [77, 78], and complemented by other researchers [42, 43, 44] will be recalled.

1.4.1 Mass balance equations

At the macroscopic level, most porous media can be viewed as homogeneous isotropic materials. The deformation of the porous solid is neglected. There are no ongoing chemical reactions. Because moisture transport in porous materials is occurring with a very low velocity, the momentum of each phase can be assumed in a quasi-equilibrium state. Hence, the transport process is only governed by mass conservation laws. By letting $\mathring{m}_{l\to v}$ represent the rate of liquid transforming into vapour, the continuity equations related respectively to phases of liquid (l), vapour (v) and dry air (a) are expressed in a 1D form as follows:

$$\frac{\partial[\rho_v\phi(1-S)]}{\partial t} = -\frac{\partial}{\partial x}(\rho_v v_v) + \mathring{m}_{l\to v} \tag{1.3}$$

$$\frac{\partial[\rho_l\phi S]}{\partial t} = -\frac{\partial}{\partial x}(\rho_l v_l) - \mathring{m}_{l\to v} \tag{1.4}$$

$$\frac{\partial[\rho_a\phi(1-S)]}{\partial t} = -\frac{\partial}{\partial x}(\rho_a v_a) \tag{1.5}$$

where ρ_v (ρ_a resp.) is the density of water vapour (dry air resp.). ϕ is the porosity through which the flows of liquid-water and water-vapour occur, and S is the liquid-water saturation which can include both capillary water (interstitial water) and bound water (physically-adsorbed water). ρ_l is the density of this mixture of these two types of water (capillary and adsorbed) which are encompassed in "liquid-water" as a generic designation. v_v (v_a resp.) represents the velocity of vapour (dry air resp.) within the porous material. v_l is the macroscopic velocity of liquid-water.

It should be remarked that in Eqs. (1.3)-(1.5), $\rho_v\phi(1-S)$, $\rho_a\phi(1-S)$, and $\rho_l\phi S$ correspond to apparent volumetric mass of vapour, dry air and liquid-water.

1.4.2 Transport laws

Vapour and dry air are transported both by advection of the gaseous mixture (according to Darcy's law) and by molecular diffusion (according to Fick's law). The velocity of the vapour-air mixture v_g is defined as a molar-averaged velocity $v_g = c_a v_a + c_v v_v$ where c_v or c_a represents the molar fractions related to vapour or dry air ($c_v + c_a = 1$). If the gaseous mixture is considered as ideal, the molar fractions express themselves according to the ratios of pressure ($c_v = P_v/P_g$ and $c_a = P_a/P_g$ where P_v and P_a are the partial pressure of vapour and dry air, respectively). In agreement with the second law of thermodynamics about entropy, the relationships governing the

transport of water vapour and dry air must satisfy the positiveness of the dissipation associated with the transport of both phases [77]:

$$-v_g \frac{\partial P_g}{\partial x} - (v_v - v_a)\frac{\partial c_v}{\partial x} \geq 0 \tag{1.6}$$

The first term accounts for the dissipation related to the advective transport of the mixture, while the second term represents the dissipation associated with diffusion. Using the kinetic theory of gases and the previous condition related to the second law of thermodynamics, the following relations governing the transport of vapour and dry air can be proposed in the case of unsaturated porous materials:

$$v_v = v_g - \phi(1-S)\alpha(S)\tau D_0 \frac{P_{atm}}{P_v}\frac{\partial}{\partial x}\left(\frac{P_v}{P_g}\right) \tag{1.7}$$

$$v_a = v_g - \phi(1-S)\alpha(S)\tau D_0 \frac{P_{atm}}{P_a}\frac{\partial}{\partial x}\left(\frac{P_a}{P_g}\right) \tag{1.8}$$

In Eqs. (1.7) and (1.8), D_0 is the diffusion coefficient of water vapour or dry air in the wet mixture. τ is the tortuosity coefficient which is affected by a relative tortuosity $\alpha(S)$ taking into account the fact that the material is not saturated (the quantity $\alpha(S)\tau$ represents the tortuosity of the sole gaseous phase in the porous medium). It should be noted that $\alpha(S)$ has to satisfy $\alpha(S=0)=1$ and $\alpha(S=1)=0$. The term $\phi(1-S)$ represents the available space for gas transport.

In this description of the movement of the gas mixture, the motors of diffusion are the gradients of the molar fractions of water vapour (c_v) and dry air (c_a) in the gaseous mixture. In addition, assuming that wet air is an ideal gas mixture (i.e., $P_g = P_v + P_a \;\Leftrightarrow\; 1 = c_a + c_v$), Eq. (1.8) can be simplified as:

$$v_a = v_g + \phi(1-S)\alpha(S)\tau D_0 \frac{P_{atm}}{P_a}\frac{\partial}{\partial x}\left(\frac{P_v}{P_g}\right) \tag{1.9}$$

The velocities v_g and v_l of the gaseous mixture and of the liquid-water phase are governed by the generalized Darcy law which is written for an unsaturated porous medium and which meet

the dissipation related to the advective transport of gas and liquid-water [83]:

$$v_g = -\frac{K_0}{\eta_g} k_{rg}(S) \frac{\partial P_g}{\partial x} \tag{1.10}$$

$$v_l = -\frac{K_0}{\eta_l} k_{rl}(S) \frac{\partial P_l}{\partial x} \tag{1.11}$$

where K_0 represents the intrinsic permeability. $k_{rg}(S)$ and $k_{rl}(S)$ are the relative permeabilities of the liquid and gaseous phases, respectively. η_l and η_g are the molecular viscosities of liquid and gas phases, respectively.

In this model, the gas intrinsic permeability is assumed equal to the liquid intrinsic permeability $K_g = K_l = K_0$. Actually, this assumption is reasonable because the "intrinsic" property is independent to the type of fluid and only related to the structure of pore network. However, many studies have already shown the necessity to make a difference between gas and liquid intrinsic permeabilities in order to satisfy experimental observations, especially pointing out that K_l is much smaller than K_g [11, 84, 85]. Coussy [78] considers that researchers are obliged to use a lower value of K_l than K_g in the framework of continuum modelling like the one presented here. Both cases $K_l = K_g$ and $K_l \ll K_g$ will be used to simulate moisture transport in cementitious materials in Chapter 2.

1.4.3 State equations

The local thermodynamic equilibrium between the liquid-water and vapour is assumed. This equilibrium is governed by Kelvin's law written in the following form:

$$-P_c + P_g - P_{atm} = \frac{\rho_l RT}{M_v} \ln\left(\frac{P_v}{P_{vs}}\right) \tag{1.12}$$

in which $P_c(S)$ appears as the macroscopic capillary pressure defined as the difference between macroscopic pressure of the gaseous phase and that of the liquid one ($P_c = P_g - P_l$). The relationship of P_c as a function of the saturation degree of liquid-water S is called the capillary pressure relationship. The relative humidity is defined as the fraction of vapour pressure to the saturated vapour pressure, RH $= P_v/P_{vs}$, where P_{vs} is the saturated vapour pressure. For most porous materials, the entry pressure P_{ent} exits at very high saturation $S \approx 0$ because in this range water in large pore can not be maintained by capillary pressure. In the case of weakly permeable materials such as cement-based materials, the entry pressure is very small.

Indeed, many studies have highlighted that for cementitious materials (concrete and mortars) the moisture content profiles, measured by gamma ray attenuation, X-ray projection [86] or Nuclear Magnetic Resonance imaging (NMR imaging) [87] show a negligible height of the fully saturated area near the surface in contact with liquid-water.

For cement-based materials, the capillary pressure curve is indirectly measured by means of sorption experiments performed for isothermal conditions (the so-called sorption isotherms [23], see Section 1.2). Capillary pressure is written in a dimensionless form:

$$P_c = \mathbb{M}\pi_c(S) \tag{1.13}$$

where $\mathbb{M}$ stands for a capillary modulus or for a reference pressure. $\pi_c(S)$ is a dimensionless function satisfying $\pi_c(0) = +\infty$ and $\pi_c(1) = 0$.

The partial pressure of water vapour P_v is much smaller compared to the total gaseous pressure P_g since P_v is bounded by the saturated vapour pressure P_{vs} at a given temperature. Thus, the assumption that the gaseous mixture behaves as an ideal gas is appropriate, yielding the following relationships between pressure of each phase and its density:

$$\rho_v = \frac{P_v M_v}{RT} \tag{1.14}$$

$$\rho_a = \frac{P_a M_a}{RT} \tag{1.15}$$

$$P_g = P_v + P_a \tag{1.16}$$

In Eqs. (1.14) and (1.15), M_v and M_a are the molar mass of vapour and dry air. R and T stands for the ideal gas constant and absolute temperature.

Concerning the liquid-water phase, the assumption of incompressibility is made because in the proposed modelling temperature is considered as constant.

1.4.4 Applications of the multiphase model for cementitious materials

In the literature, the above multiphase model has been applied to cementitious materials more than a decade ago in the research by Mainguy et al. [88, 42]. In that research, the liquid relative permeability k_{rl} was calculated by van Genuchten-Mualem model (VGMa, see Eq. 2.7 in Chapter 2) [89, 90]. The equation for k_{rg} was taken from the proposal of Parker et al. [91] and Kuckner et al. [92] (see Eq. 2.9). The tortuous effects on vapour diffusion was estimated by the equation

proposed by Millington [93] (see Eq. 2.37). The studied materials were imposed to constant external RH.

Simulation results showed a gas overpressure could be observed in the part near the material surface. Ignoring the transport of the gas-phase (including effects of gas pressure, vapour diffusion and advection of gas-phase, and evaporation between liquid and vapour), Mainguy et al. [88, 42] reported that the multiphase model turns to a single diffusion-like equation only with moisture transport in its liquid form. This simplification concerns the weakly permeable materials, such as cement-based materials:

$$\frac{\partial S}{\partial t} = \frac{\partial}{\partial x}\left[D_l(S)\frac{\partial S}{\partial x}\right] \tag{1.17}$$

where $D_l(S)$ represents the diffusivity of the liquid-phase.

Mainguy et al. concluded that Eq. (1.17) can provide a high accuracy prediction when it is used to determine K_0 by fitting drying kinetics (mass loss *vs.* time). They also recalled that most standard diffusion-like drying models [79, 80, 65] in the literature are developed based on the assumption of constant gas pressure. Actually, the multiphase model can be simplified as a standard diffusion equation according to two main assumptions:

- Gas pressure in the material is constant and always equal to the atmospheric pressure.
- The vapour transport is a pure diffusion process which means that advection of vapour is negligible.

These two assumptions lead the multiphase model to appear as:

$$\frac{\partial S}{\partial t} = \frac{\partial}{\partial x}\left[\left(D_l(S) + D_v(S)\right)\frac{\partial S}{\partial x}\right] \tag{1.18}$$

where $D_v(S)$ represents the diffusivity of vapour. In fact, Eq. (1.17) is a special case of Eq. (1.18) when vapour diffusion is negligible. Most models mentioned above [79, 80, 65] and in the next section [94, 95, 96, 16, 13] can be considered as a simplified form of the multiphase transport model.

However, Mainguy et al. [42] did not really state the relationship between K_0 and gas pressure variations (i.e., the definition of a weakly permeable porous medium), and the reasons they made two assumptions about gas pressure to obtain Eq. (1.18). In Chapter 2, a systemic study will present the whole scope of modelling moisture transport for cementitious materials according to the possibility to make a difference between liquid intrinsic permeability and gas intrinsic

permeability through a theoretical analysis and experimental verifications.

1.5 Modelling of moisture transport under varying ambient relative humidity

To study the internal moisture behaviour responding to external humidity changes, there are two processes that should be taken into account: how is moisture transport inside the materials? and how are moisture interactions between the material surface and the environment? The review of these two aspects will be presented in the following subsections.

In the literature, most of models were initially developed for drying, when the material is exposed to the surrounding with lower RH compared with RH in the material. However, one main characteristic of the natural environment is the arbitrary ambient humidity changes, which should include both drying and wetting. Wetting means a higher RH at the boundary than the one prevailing in the material. Drying and wetting appear alternatively in natural conditions. This is considered as the most unfavourable environmental situation for concrete structures exposed to high ions content surrounding, because drying and wetting cycles can accelerate the penetration of ions [97]. Therefore, to understand durability issues, it needs to model moisture behaviour under both drying and wetting processes. The terms "drying" and "wetting" used here are specified to moisture transport occurring in the hygroscopic range; namely, the present research only focuses on the research of the material exposed to the humid air, but not directly in contact with liquid-water.

In this section, the purpose is to review the model which can be used for periodic boundary conditions. To model drying and wetting cycles by using a continuum model, there are generally two ways which can be used: (1) A sorption isotherm is one of essential input data for the continuum model, so using the same sorption isotherm for different processes is a simplified approach to simulate drying and wetting cycles; (2) The more complicated method is to use distinct sorption isotherms for different processes, so that a hysteresis model has to be used to predict hysteresis loops. In the latter case, a moisture transport model needs to be coupled with a hysteresis model. Since there are many moisture transport models and different hysteresis models in the literature, this research cannot enumerate all combinations. Thus, the current section focuses on reviewing the model: (a) which has already been used in the field of cementitious materials, and (b) for hysteresis modelling, which has provided the combination of a moisture

transport model and a hysteresis model.

1.5.1 Cunningham's method - analytical solution

Cunningham [96] investigated diffusion which is driven by both the gradient of moisture concentration and temperature in a building material when it is subjected to periodic moisture and temperature boundary conditions. In other words, two-variable driving potentials with non-linear diffusion coefficients were used in this method. The diffusion equation for Cunningham's method is:

$$\frac{\partial S}{\partial t} = \frac{\partial}{\partial x}\left(D_S \frac{\partial S}{\partial x} + D_T \frac{\partial T}{\partial x}\right) \tag{1.19}$$

where D_S and D_T are moisture diffusivities under saturation gradient and under temperature gradient respectively. The part under saturation gradient is the same as Eq. (1.18), so D_S should contain both contributions of liquid-water and vapour.

To get an analytical solution to Eq. (1.19), three assumptions were made [96]:

(1) In practical, the time of response for temperature variations is very much shorter than for the moisture concentration, so that the Fourier number can assumed far bigger than 1.

$$Fo = \frac{\kappa}{\rho_v l^2 C_T} \gg 1 \tag{1.20}$$

where C_T is temperature energy capacity and l is the length of the material.

(2) Because of the rapid temperature diffusion, the second assumption is that the thermal conductivity κ is constant, meaning the gradient of temperature is not considered as a driving force.

(3) The terms $\frac{\partial D_S}{\partial S}$ and $\frac{\partial D_T}{\partial S}$ are assumed to be constant.

The initial condition corresponds to uniform moisture content and temperature. Boundary conditions are defined as sinusoidal moisture content and temperature fluctuations. Thus, analytical solutions can be obtained, inspired by the work from Carslaw and Jaeger [98].

Clearly, this model is only valid for specified initial and boundary conditions. Like most analytical solutions, the applicability is restricted.

1.5.2 EMPD model

The EMPD (Effective Moisture Penetration Depth) model was developed by Keresteciogl u et al. [99] and Cunningham [5], and later has been used in studies [100, 101, 102, 103, 104]. It is derived from considering cyclic variations of the external relative humidity. It also has been verified having good practical applications [105, 106] and has shown good agreement between predicted relative humidity and measured ones [103].

The EMPD model was developed based on the assumption that moisture transport takes place between the environmental air and a thin fictitious layer (also called the moisture buffering layer) of material with uniform moisture content. This moisture content is a function of RH and is characterised by the moisture penetration depth x_p (the thickness of the moisture buffering layer) which can be calculated based on the material properties. The governing equation in the EMPD model is expressed as [104]:

$$\rho_m x_p \frac{\mathrm{d}\theta}{\mathrm{d}t} = k_m(RH_p - RH^e) \tag{1.21}$$

where ρ_m is the dry density of the material, θ is water content, k_m is the moisture transport coefficient in the airside ($\mathrm{kg \cdot m^{-2} \cdot s^{-1}}$). Note that $\frac{\mathrm{d}\theta}{\mathrm{d}t} = \frac{\partial\theta}{\partial RH_p}\frac{\mathrm{d}RH_p}{\mathrm{d}t}$ where $\frac{\partial\theta}{\partial RH_p}$ is obtained based on sorption isotherms and RH_p is RH in the material at the point x_p.

The easiest way to solve this equation is to assume a series of x_p to calculate RH_p since x_p only exits on the left-hand side of Eq. (1.21). Besides, there are some variations using a little more complex equations [100, 101] which further separate the moisture buffering layer into a surface layer and a deep layer.

$$\rho_m x_p \frac{\partial\theta}{\partial RH_p}\frac{\mathrm{d}RH_p}{\mathrm{d}t} = \frac{(P_{v,p} - P_v^e)}{\frac{1}{k_m} + \frac{x_p}{2K_v(RH_p)}} + \frac{P_{v,r} - P_{v,p}}{\frac{x_p}{2K_v(RH_p)} + \frac{x_r - x_p}{2K_v(RH_r)}} \tag{1.22}$$

$$\rho_m x_r \frac{\partial\theta}{\partial RH_r}\frac{\mathrm{d}RH_r}{\mathrm{d}t} = \frac{P_{v,r} - P_{v,p}}{\frac{x_p}{2K_v(RH_p)} + \frac{x_r - x_p}{2K_v(RH_r)}} \tag{1.23}$$

where K_v is the vapour permeability, $P_{v,p}$ and P_v^e are the vapour pressures in the material (at depth x_p) and in the environment, respectively. The surface layer (subscript p) and the deep layer (subscript r) correspond to the first and the second term on the right side of Eq. (1.22). The surface layer is based on the short term RH fluctuations such as a day, and the deep layer is based on the longer term RH fluctuations which can be weeks to months. The prior parameters

in this model are x_p and x_r.

For a perfectly periodic boundary condition, based on the assumptions of constant K_v and knowing the sorption isotherm, the penetration depth is given as [96, 229]:

$$EMPD = \left(\frac{K_v P_{vs} t_p}{\rho_m \pi \frac{\mathrm{d}\theta}{\mathrm{d}RH}} \right)^{1/2} \tag{1.24}$$

where t_p is the cycle period. This equation can be also used to estimate both x_p and x_r in Eqs. (1.21), (1.22) and (1.23). Furthermore, these equations can be used to estimate the evolution of water content or RH in the moisture buffering layer.

Even though the EMPD model is a very handy method to estimate the moisture behaviour in influenced zones of the material, the drawbacks of this model are also clear. As it can be seen, this model highly relies on the moisture penetration depth, which has to be assumed or calculated by empirical equation (i.e., Eq. 1.24). That gives the results less accuracy. Another difficulty is that the EMPD model cannot be used for arbitrary boundary conditions since it is more suitable for perfectly cyclic boundary conditions.

1.5.3 Kirchhoff's flow potential

Kirchhoff's flow potential used for modelling of moisture transport in porous media was first introduced by Arfvidsson and Claesson [6, 7]. Fick's first law was chosen to describe the diffusion process. The potential can be relative humidity or water content. Let's take RH as an example, so that a new function ψ can be obtained by Kirchhoff transformation.

$$\psi(RH) = \psi_{ref} + \int_{RH_{ref}}^{RH} D_F(RH)\mathrm{d}RH \tag{1.25}$$

where $\psi_{ref} = \psi(RH_{ref})$. The reference values ψ_{ref} and RH_{ref} can be chosen arbitrarily for each material. For convenience, it is better to let $\psi_{ref} = 0$.

Thus, the diffusion equation can be rewritten as:

$$J_F = -\frac{\mathrm{d}\psi}{\mathrm{d}RH}\left(\frac{\partial RH}{\partial x}\right) = -\frac{\partial \psi}{\partial x} \tag{1.26}$$

Equation (1.26) indicates that moisture diffusion is driven by the gradient of ψ and $D_F(RH) \equiv 1$. This certainly is the simplest moisture diffusion potential for the case of one independent state

variable. Kirchhoff's potential $\psi(RH)$ has the same properties as $D_F(RH)$ and varies for different materials.

An important result is that the average value of Kirchhoff's potential in the material over a time period is equal to the average value of Kirchhoff's potential at the boundary. Another important feature of Kirchhoff's potential for numerical modelling, reported by Kalagasidis et al. in the study about moisture conductivity [107], is that it is very insensitive to the mesh refinement; thus, the numerical calculation converges much faster. In other words, it can give a stable numerical solution with a coarse or moderate mesh. But, using Kirchhoff's potential is extremely sensitive to the quality of the input data. It is not surprising because the integral form of $\psi(RH)$ is very sensitive to the shape of $D_F(RH)$ curve.

1.5.4 Method from Li et al.

Li et al. [94, 95] have performed a modelling of drying-imbibition cycles and their influence on the moisture influential depth. Li et al. [95] pointed out that the transport mechanisms are different during drying and imbibition: during drying, moisture transport to the surface is driven by a combined evaporation-diffusion-convection process, while an imbibition process is dominated by capillary absorption of liquid-water. If using water content as potential, considering 1D problem and without gas pressure variations, the mass balance equation according to Eq. (1.18) is given as:

$$\frac{\partial \theta}{\partial t} = \frac{\partial}{\partial x}\left(D(\theta)\frac{\partial \theta}{\partial x}\right) \tag{1.27}$$

The diffusivity $D(\theta)$ is different during the drying and imbibition processes. The diffusivity during drying is taken from [79].

$$D_d(\theta) = D_{d0}\left\{\alpha_0 + \frac{1-\alpha_0}{1+\left(\frac{1-\theta}{1-\theta_c}\right)^N}\right\} \tag{1.28}$$

where D_{d0} is the diffusivity at saturated condition, and α_0, θ_c and N are parameters to be determined by experiments. $D_d(\theta)$ should include both contributions of liquid-water and vapour.

The diffusivity during imbibition is taken from Hall [108].

$$D_w(\theta) = D_{w0}\exp(n\theta) \tag{1.29}$$

where D_{w0} is the diffusivity at fully-dried condition and n is a regression coefficient. $D_w(\theta)$ only includes the contribution of liquid-water.

Besides, in their later studies [109], the effective diffusivity, reported by Mainguy [42] on the basis of the works of Philip and de Vries [73], was also used for modelling of drying and wetting cycles. But, hysteretic effects were not considered. The main reason, according to [109], is that $D(\theta)$ for main desorption and main adsorption does not show significant hysteresis.

For cementitious materials, Baroghel-Bouny's experimental results have shown that no obvious hysteresis can be observed in apparent diffusivity $D_a(S)$ [11] for cementitious materials. In contrast, hysteresis in $D_a(RH)$ is much clearer. Hence, no hysteresis in $D_a(\theta)$ does not mean no hysteresis in $D_a(RH)$. In the literature, hysteresis has been proved important for modelling moisture transport in drying-wetting conditions [13, 14, 16]. Therefore, it seems not relevant to neglect hysteretic effects.

1.5.5 Hysteresis modelling methods

As discussed above, hysteresis is a common behaviour for moisture transport in porous media. Some models neglect hysteresis and use the main desorption isotherm to simulate moisture transport in both drying and wetting processes (e.g., [7]). More recently, modelling considering hysteresis has become a topic of interest.

For hysteresis modelling, both moisture transport and hysteresis models are needed. This subsection does not review these two kinds of models separately. Instead, it only focuses on models which have originally coupled moisture transport and hysteresis together. Chapter 3 will present a more detailed review of hysteresis models.

Method from Johannesson et al.

Johannesson et al. [14, 15] employed a two state-variable model to investigate moisture transport in building materials. The state-variable for liquid phase is the saturation S and for vapour phase it is the relative humidity RH. The mass balance equations are coupled to each phase through the mass exchange term which is related to either evaporation or to condensation.

The equation for liquid phase is written as:

$$\rho_l \frac{\partial \theta}{\partial t} = -\frac{\partial}{\partial x}\left(D_l \frac{\partial \theta}{\partial x}\right) - E_m(\theta^{eq} - \theta) \tag{1.30}$$

where $D_l = D_l(\theta)$ is the diffusivity of liquid-water, which is assumed to be an increasing function of S. The rate of mass exchange E_m is constant. The superscript "eq" represents the variable at equilibrium.

The governing equation for the vapour phase is:

$$(\phi - \theta)\frac{\partial \rho_v}{\partial t} - \rho_v \frac{\partial \theta}{\partial t} = -\frac{\partial}{\partial x}\left(D_v \frac{\partial \rho_v}{\partial x}\right) + E_m(\theta^{eq} - \theta) \tag{1.31}$$

where $D_v = D_v(\rho_v)$ is the diffusivity of water vapour, which is assumed to be an decreasing function of RH.

In this model, the use of term $E_m(\theta^{eq} - \theta)$ means that this model takes into account non-equilibrium or dynamic effects. Unlike the multiphase model, the assumption of local equilibrium is not applicable in this model.

A third degree polynomial function is used to express the both main desorption and adsorption curves, as well as scanning curves. This method was originally developed for wood materials.

$$\theta = b_1 RH + b_2 RH^2 + b_3 RH^3 \tag{1.32}$$

where b_1, b_2 and b_3 are parameters, needing to be determined by experimental data for the main sorption curves. For a scanning curve, it starts at the beginning point (RH_0, θ_0^{eq}) and is tangent to the main curve at the junction point $(RH_{junc}, \theta_{junc}^{eq})$. For a desorption scanning curve, there are several rules to calculate parameters.

At the beginning point:

$$\left.\frac{\mathrm{d}\theta^{eq}}{\mathrm{d}RH}\right|_{RH=RH_0} = k_d \frac{\mathrm{d}\theta_0^{eq}}{\mathrm{d}RH}(RH = RH_0) \quad 0 < k_d \leq 1 \tag{1.33}$$

$$\theta^{eq}(RH_0) = \theta_0^{eq}(RH_0) \tag{1.34}$$

At the junction point:

$$\left.\frac{\mathrm{d}\theta^{eq}}{\mathrm{d}RH}\right|_{RH=RH_{junc}} = \frac{\mathrm{d}\theta_d^{eq}}{\mathrm{d}RH}(RH = RH_{junc}) \tag{1.35}$$

$$\theta^{eq}(RH_{junc}) = \theta_d^{eq}(RH_{junc}) \tag{1.36}$$

where the subscript d represents the main desorption curve and k_d is a material constant that is used to determine the initial slope of the desorption scanning curve. It should be calibrated by experimental data. RH_0 and RH_{junc} are relative humidity at the starting point of the scanning curve and the junction point, respectively.

Equation (1.33) means that the slope of a scanning curve at the beginning point is the fraction of the slope of the previous scanning curve at the end point. Equation (1.35) shows that the slopes of the scanning curve and the main desorption curve are the same at the junction point. Equations (1.34) and (1.36) are used to make sure a continuous scanning curve. Totally, for each scanning curve, there are four unknowns (three in Eq. 1.32 and RH_{junc} (or θ^{eq}_{junc}) for the junction point) in four equations, so these equations can be mathematically solved. After the junction point, the scanning curve should be same with the main desorption curve. In the same manner, the rules for an adsorption scanning curve are given as:

$$\text{At the beginning point:} \quad \left.\frac{\mathrm{d}\theta^{eq}}{\mathrm{d}RH}\right|_{RH=RH_0} = k_a \frac{\mathrm{d}\theta^{eq}_0}{\mathrm{d}RH}(RH = RH_0) \quad 0 < k_a \leq 1 \tag{1.37}$$

$$\theta^{eq}(RH_0) = \theta^{eq}_0(RH_0) \tag{1.38}$$

$$\text{At the junction point:} \quad \left.\frac{\mathrm{d}\theta^{eq}}{\mathrm{d}RH}\right|_{RH=RH_{junc}} = \frac{\mathrm{d}\theta^{eq}_w}{\mathrm{d}RH}(RH = RH_{junc}) \tag{1.39}$$

$$\theta^{eq}(RH_{junc}) = \theta^{eq}_w(RH_{junc}) \tag{1.40}$$

where the subscript w represents the main adsorption curve and k_a is a material constant that is used to determine the initial slope of the adsorption scanning curve.

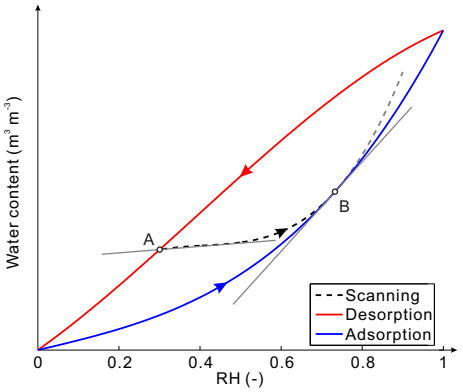

Figure 1.6: An example for the first wetting scanning curve calculated by the hysteresis model proposed in [60]. The scanning curve starts at point A and is tangent to the adsorption curve at the junction point B. The material constant $k_a = 0.2$.

An example for the first wetting scanning curve is shown in Fig. 1.6. This model is more suitable for the main sorption curves with low curvature and small hysteresis. If the main sorption curves have a high curvature, there may not have solutions to equations for the scanning curves. For example in Fig. 1.6, the calculated scanning curve may not be tangent to the adsorption curve and point B cannot be found. It indicates that this hysteresis model is generally suitable for more porous materials because these materials have small hysteresis and two main sorption curves are close to each other. But cementitious materials show bigger hysteresis, which can cause problems for the use of this model.

Method from Derluyn et al.

Derluyn et al. [16] assumed that moisture transport in concrete is induced by various RH and temperature conditions, so they coupled moisture and heat transport for porous building materials by adopting capillary pressure P_c and temperature T as potentials. Moisture transport is described as vapour transport using a vapour permeability K_v by considering constant gas pressure in the material.

$$C\frac{\partial P_c}{\partial t} = -\frac{\partial}{\partial x}\left(K_v(P_v)\frac{\partial P_v}{\partial x}\right) \tag{1.41}$$

where the moisture capacity $C = \dfrac{\partial \theta}{\partial P_c}$ and vapour pressure P_v can be calculated by using Kelvin's equation based on RH. The vapour permeability is formulated as a function of RH and it is also considered as the fraction of the vapour permeability in the air K_{v0}.

$$K_v = K_{v0}\left[\alpha_1 + \alpha_2 \exp(\alpha_3 RH)\right] \tag{1.42}$$

where α_1, α_2 and α_3 are three parameters. Derluyn et al. [16] argued that K_v includes transport in both liquid and gas phases. Equation (1.41) is one form of Eq. (1.18) by using the moisture capacity C on both sides of the equation.

To fit the main sorption isotherms, equations were introduced by Derluyn et al. [16] by summing a concave curve and a convex curve. Expressions to the main desorption and main adsorption isotherms are given as:

$$\theta_d = \theta^{max}\left\{\omega_l \frac{(1+a_d)RH_d}{1+a_d RH_d} + (1-\omega_l)\frac{1-\exp(b_d RH_d)}{1-\exp(b_d)}\right\} \tag{1.43}$$

$$\theta_w = \theta^{max}\left\{\omega_l \frac{(1+a_w)RH_w}{1+a_w RH_w} + (1-\omega_l)\frac{1-\exp(b_w RH_w)}{1-\exp(b_w)}\right\} \tag{1.44}$$

where a_d, b_d, a_w, b_w and ω_l are parameters which need to be determined by experimental data. Again, subscripts d and w represent the parameters for the main desorption and main adsorption processes, respectively.

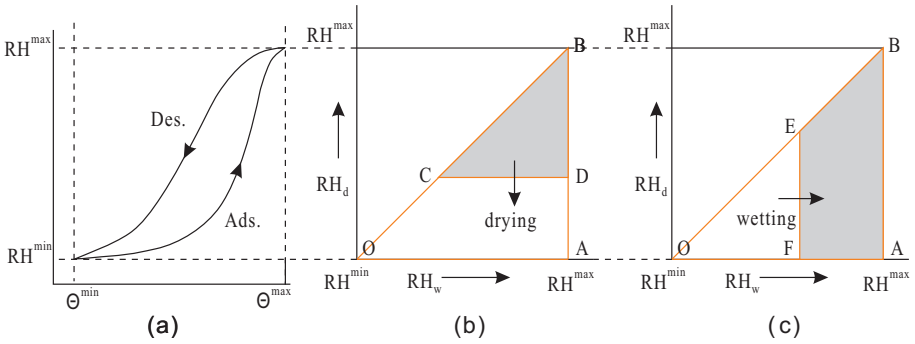

Figure 1.7: A triangular representation of PM domain for the main desorption and adsorption curves. The main drying process starts from point B (the maximum RH) and decreases gradually to point O (the minimum RH). The main adsorption process is the inverse process.

The scanning curves are predicted by an independent domain model, called PM model [50, 51], which was originally developed for studies on magnetism field and has been used for the research of moisture transport in wood [110]. The PM model assumes that a domain (pores in a porous material) consists of a number of sorption sites, which control the variation of water content according to the decrease or increase of RH. A triangular diagram was introduced to represent the PM domain (see Fig. 1.7 for the main sorption curves). The density distribution of these sites is represented by the function $\Phi(RH_w, RH_d)$ and the corresponding water content distribution is denoted by $\Theta(RH_w, RH_d)$. Therefore, water content at a given RH can be calculated by integrating two distribution functions along x-axis (wetting) and y-axis (drying) in a domain Ω.

$$\theta(RH_w, RH_d) = \iint_{\Omega} \Phi(RH_w, RH_d)\,\Theta(RH_w, RH_d)\;\mathrm{d}RH_w \mathrm{d}RH_d \tag{1.45}$$

The integral equation is not easy to use, so a function $H(RH_w, RH_d)$ is introduced instead. For a desorption scanning curve, a complex equation is given as:

$$\theta(RH_w, RH_d) = H_1(RH_w, RH_d) + H_2(RH_w, RH_d) \tag{1.46}$$

with

$$H_1(RH_w, RH_d) = \theta^{max}\omega_l \left(1 - \frac{(1+a_d)RH_d}{1+a_d RH_d}\right) \frac{(1+a_w+c_h RH_d)^{\frac{RH_w-RH_d}{1-RH_d}}}{1+(a_w+c_h RH_d)^{\frac{RH_w-RH_d}{1-RH_d}}} \tag{1.47}$$

$$H_2(RH_w, RH_d) = \theta^{max}(1-\omega_l) \left(1 - \frac{1-\exp(b_d RH_d)}{1-\exp(b_d)}\right) \frac{1-\exp\left((b_w+d_h RH_d)^{\frac{RH_w-RH_d}{1-RH_d}}\right)}{1-\exp(b_w+d_h RH_d)} \tag{1.48}$$

For an adsorption scanning curve, one needs to replace RH_d in $(1+a_d)RH_d$, $a_d RH_d$, $c_h RH_d$, $\exp(b_d RH_d)$ and $d_h RH_d$ by RH_w.

Totally, the H-function itself needs 7 parameters (a_d, b_d, a_w, b_w and ω_l for two main curves and c_h and d_h for scanning curves) which have to be experimentally determined.

DuCOM model

The DuCOM (*Du*rability *CO*ncrete *M*odel) computer codes, first released in 1999, is a thermo-hygro-physics coupled model which aims at integrating macroscopic material properties and durability performances. Furthermore, it also combines carbonation, chloride ion penetration, steel corrosion and calcium leaching [13].

Moisture transport model is developed on $10^{-10} - 10^{-6}$ m scale in DuCOM. The moisture mass balance includes both vapour and liquid-water. The conservation equation is expressed with moisture capacity, moisture transport conductivity and sink term on the referential volume.

$$\rho_l \left(\frac{\partial \phi_t S_t}{\partial P_c}\right) \frac{\partial P_c}{\partial t} = \nabla\left(J_l + J_v\right) - \rho_l S_t \frac{\partial \phi_t}{\partial t} + W_p \frac{\partial \beta}{\partial t} \tag{1.49}$$

where the total porosity ϕ_t is the sum of gel porosity ϕ_{gl}, interlayer porosity ϕ_{il} and capillary porosity ϕ_{cap}. The total saturation S_t is related to the adsorbed water saturation S_{ads}, the condensed water saturation S_{con} and the interlayer water saturation S_{il}. S_t is calculated by Eq. (1.64). J_l and J_v are the fluxes of liquid-water and vapour. The second term on the right-hand side is related to the pore structure development. The last term $W_p \frac{\partial \beta}{\partial t}$ is the sink term accounting for the moisture loss consumed by hydration.

Knudsen diffusion theory was applied for vapour transport. Under isothermal conditions, the vapour flux is described as [111]:

$$J_v = -\frac{\phi D_0}{\tau}\int_{r_c}^{\infty}\frac{\mathrm{d}V}{1+N_k}\nabla\rho_v \tag{1.50}$$

where V is the pore volume, τ is a parameter representing the tortuous effect of the pore network ($=(\pi/2)^2$). r_c is the threshold pore radius, and pores with radii below r_c are considered to be fully filled by liquid-water. N_k is the Knudsen number of the water molecule.

If assuming cylindrical pores, the flux of liquid-water is derived as [111]:

$$J_l = -\frac{\rho_l\phi^2}{50\eta_l}\left(\int_0^{r_c} r\mathrm{d}V\right)^2\nabla P_c \tag{1.51}$$

where η_l is the viscosity of liquid.

The moisture capacity (see the first term in Eq. 1.49) enumerates moisture content with regard to capillary pressure. Quasi-equilibrium is assumed at any time in micro-pores. So, capillary pressure can be obtained by Kelvin's equation.

To solve Eq. (1.49), the relation between S_t and RH (sorption isotherms) must be known. In DuCOM, the liquid-water is viewed in three states: adsorbed, condensed and interlayer. To calculate the water content in these different states, it needs to know the pore size distribution, which is simply represented by the Raleigh-Ritz distribution function.

$$V = 1-\exp(-rB), \qquad \mathrm{d}V = rB\exp(-rB)\mathrm{d}\ln r \tag{1.52}$$

where B is a distribution parameter, which in fact represents the peak of pore size distribution on a logarithmic scale.

In natural conditions, drying and wetting cycles have small influence on the adsorbed water, so DuCOM assumes that adsorption is the perfectly reversed drying. If regarding pores are cylinders, the contribution of adsorbed water to the total liquid-water is obtained as:

$$S_{ads} = \int_{r_c}^{\infty}\left[1-\left(\frac{r-t_a}{r}\right)^2\right]\mathrm{d}V \tag{1.53}$$

where t_a is the thickness of the adsorbed layer which is calculated by the BET theory [38] modified by Hillerborg [112].

DuCOM considers that hysteresis in sorption isotherms for cementitious materials is mainly due to the "ink-bottle effect". The amount of trapped water in "ink-bottles" and free water can be described by considering the pore size distribution (see Fig. 1.8). Trapped water means water

in the pore whose size is below the ink-bottle neck (threshold radius r_c).

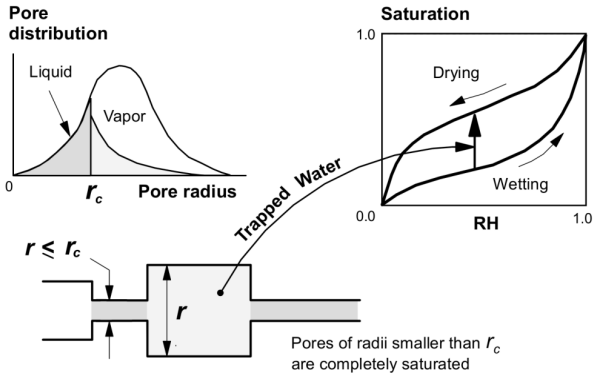

Figure 1.8: Water in pores trapped by ink-bottle necks (taken from [13]).

Under equilibrium conditions, the pores with radii smaller than r_c would be completely saturated. The main wetting curve starts from the totally dried state, so r_c also begins from the minimum pore size (see Fig. 1.9). The condensed water saturation is the integration of the pore size distribution function from the minimum pore size to r_c.

$$S_{con} = S_c = \int_0^{r_c} \frac{\mathrm{d}V}{\mathrm{d}r}\mathrm{d}r = 1 - \exp(-Br_c) \tag{1.54}$$

where S_c is the contribution of trapped water.

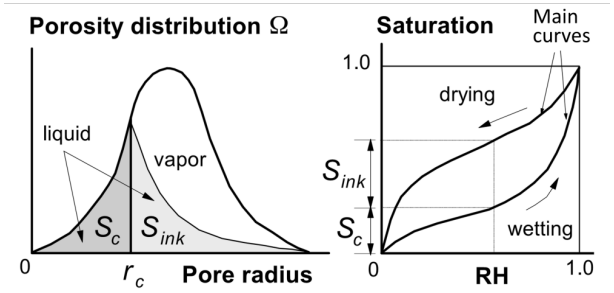

Figure 1.9: Main desorption and adsorption curves calculated based on the pore size distribution [13]. Hysteresis between two main sorption curves is also shown in this figure.

The main drying curve starts from the totally saturated state, so r_c also begins from the maximum pore size. The saturation S_{ink} due to the additional water present in trapped pores can be calculated by summing water in pores having a radius greater than r_c:

$$S_{ink} = \int_{r_c}^{\infty} \frac{V_{r_c}}{V_r}\mathrm{d}V = -S_c \ln S_c \tag{1.55}$$

where V_{r_c} is the volume of the pores with radii less than r_c. V_r is the volume of pores with radii less than r in the pore size distribution. Therefore, saturation for the main drying curve can be obtained according to Fig. 1.9.

$$S_{con} = S_c + S_{ink} = S_c\,[1 - \ln S_c] \tag{1.56}$$

Obviously, the two main sorption curves are not enough to describe varying environment conditions. The model has to be able to simulate scanning curves from wetting to drying and from drying to wetting. For a drying scanning curve, the ink-bottle effect according to Fig. 1.10a can be obtained as:

$$S_{ink} = \int_{r_c}^{r_{max}} \frac{V_{rc}}{V_r} \mathrm{d}V = S_c\,(\ln S_{r_{max}} - \ln S_c) \tag{1.57}$$

where r_{max} is the radius of the largest pore which has been reached during the previous wetting process. Thus, the saturation for the drying scanning curve is written as:

$$S_{con} = S_c + S_{ink} = S_c\,(\ln S_{r_{max}} - \ln S_c) \tag{1.58}$$

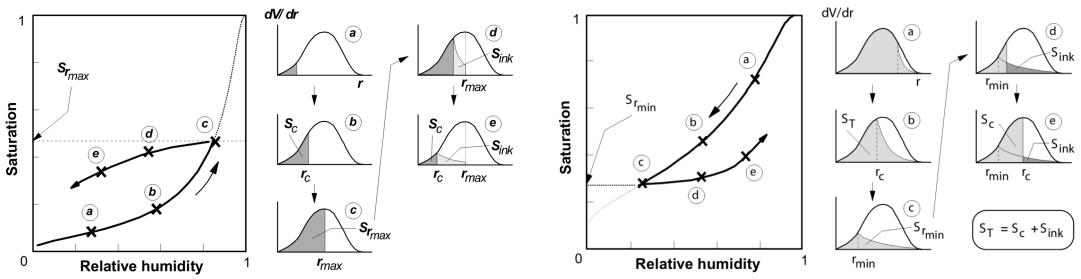

(a) Drying scanning curves.

(b) Wetting scanning curves.

Figure 1.10: Scanning curves calculated in the DuCOM [13].

In the same way, a wetting scanning curve can be obtained on the basis of Fig. 1.10b.

$$S_{con} = S_c + S_{ink} = S_c + \int_{r_c}^{\infty} \frac{V_{rc}}{V_r} \mathrm{d}V = S_c - S_{r_{min}} \ln S_c \tag{1.59}$$

where r_{min} is the radius of the smallest pore which has been reached during the previous drying process.

In DuCOM, subsequent hysteresis in the scanning curves is disregarded in order to getting more practical applicability; namely, no hysteresis after the first scanning curves will be consid-

ered. The inner loops are assumed to be reversible to make sure that closed form loops can be obtained.

However, hysteresis in condensed water can only explain hysteresis behaviour in the high RH range. For the low RH range, hysteresis is mainly affected by interlayer water. But the amount of interlayer water is very small and the behaviour has not been fully understood. DuCOM defines four empirical equations to correlate the interlayer saturation to relative humidity for the above mentioned four drying-wetting scenarios.

$$\text{For main wetting curve} \qquad S_{il} = RH \tag{1.60}$$

$$\text{For main drying curve} \qquad S_{il} = RH^{0.05} \tag{1.61}$$

$$\text{For the first drying scanning curve} \qquad S_{il} = 1 + (RH - 1)\left(\frac{S_{r_{min}}}{RH_{r_{min}}}\right) \tag{1.62}$$

$$\text{For the first wetting scanning curve} \qquad S_{il} = S_{r_{max}} RH^{0.05} \tag{1.63}$$

The total saturation can be calculated based on the contribution of each state of water.

$$S_t = \frac{(\phi_{gl} + \phi_{cp})(S_{ads} + S_{con}) + \phi_{il} S_{il}}{\phi_t} \tag{1.64}$$

where ϕ_{gl}, ϕ_{il}, ϕ_{cp} and ϕ_t are porosities of gel pores, interlayer, capillary and total pores, respectively.

In DuCOM, a complete set of equations have been proposed to calculate hysteresis, and further to simulate drying and wetting cycles. However, the pore size distribution function used in Eq. (1.52) is too simplistic to calculate the main sorption isotherms, and has not been verified by experimental data.

1.5.6 Interactions between materials and their surrounding

To study moisture transport, it needs to understand moisture interactions between the material and its surrounding. Normally, the boundary condition is used to represent those interactions. In the literature, there are two common boundary conditions. The Dirichlet type boundary condition (also called the first type boundary condition) fixes the value of RH (or P_v) on the exposed surface. For the case of RH chosen as the driving force for moisture transport, this boundary condition is formulated as:

$$RH^0 = RH^e \tag{1.65}$$

where RH^0 and RH^e represent the relative humidity at the material surface and in the environment, respectively.

The first type boundary condition can be found in earlier moisture transport research, such as in [6, 42]. However, RH in the natural environment varies a lot and fluctuates rapidly, which make the surface of the material is hardly in equilibrium with its surrounding. Therefore, the first type boundary condition, imposing RH, seems less applicable.

The other type of boundary condition, which has become more common in recent years [113, 16], is to impose a moisture flux at the boundary [113]. The total moisture flux J_{total} is given as:

$$J_{\text{total}}\Big|_{x=0} = E(P_v^0 - P_v^e) = EP_{vs}(RH^0 - RH^e) \tag{1.66}$$

The surface emissivity E ($\text{kg} \cdot \text{m}^{-2} \cdot \text{s}^{-1} \cdot \text{Pa}^{-1}$) depends on air velocity, porosity, surface roughness, etc., and it should be determined through experiments. In experiments carried out by Azenha et al. [114], emissivity values calibrated for two drying conditions (RH^e = 30 and 60%) are 3.93×10^{-8} and 2.19×10^{-8}. Uno [115] compared different drying conditions and finally concluded an equation for E, which is mainly related to the velocity of air v_e because the flowing air can significantly accelerate drying.

$$E = 2.188 \times 10^{-8} + 1.859 \times v_e \tag{1.67}$$

On the contrary to Azenha's experimental results [114], some researchers reported that E seems to be independent to the environmental RH [116]. A modification to Eq. (1.66) has been used in previous studies [24, 117].

$$J_{\text{total}}\Big|_{x=0} = \phi SEP_{vs}(RH^0 - RH^e) \tag{1.68}$$

Equation (1.68) includes both effects of material property (porosity ϕ) and the current saturation S. ϕS represents the accessibility of moisture in the porous material to the ambient environment. This boundary condition has been criticized in the case of the natural condition [118], in which the influence of wind and temperature makes the relationship between moisture ex-

change rate and saturation quite non-linear. Since in the current study no wind or temperature effects will been considered, Eq. (1.68) is still applicable.

From a numerical simulation point of view, the advantage of using the flux boundary condition compared to using the first type boundary condition is that it reduces the effect of a sharp relative humidity gradient at the beginning of drying, thus obtaining a faster convergence and a considerable reduction of oscillations in the solution.

Even though different boundary conditions have been considered in the modelling, they generally represent a simplification of complex interactions between the material and its surrounding. Further investigations, which include both mass transports in the material and in its surrounding, will be carried out in Chapter 6.

1.6 Critical review and conclusion

Compared to other models, the continuum model is the most rigorous one. It is expected to be more physical for modelling moisture transport and moisture storage within building materials. Thus, to model drying and wetting cycles, the continuum models should be the first choice. Only concerning continuum models, the above review summarises three different methods to simulate moisture transport under drying-wetting conditions:

(1) Using different transport coefficients for the drying and wetting processes [94, 95]. So, this kind model does not need sorption isotherm to address the equilibrium between liquid-water and vapour. All transport properties are only related to the water content.

(2) Non-hysteresis modelling which uses the same sorption isotherm for both drying and wetting. The main desorption curve is generally used in the literature [96, 6, 16]. There is a one-to-one relation between S and P_c.

(3) Hysteresis modelling, in which a hysteresis model is involved to calculate inner scanning curves (e.g., [13, 14, 15, 16]). This leads to a non-unique relation between S and P_c. This relation is highly dependent upon the sorption history.

The diffusion coefficients in the first method are highly dependent on the calibration of experimental data. Actually, for different cycles, transport coefficients are also different. Hence, for this method, it is definitely difficult to calibrate different coefficients by experimental data

for fluctuating and unstable drying and wetting cycles. Those limitations restrict the application of this method.

Non-hysteresis modelling is an easy way to achieve our purpose for modelling of drying and wetting cycle. Avoiding the calculation of scanning curves for each time step can speed up the numerical calculations. However, this method has shown low agreement with experimental data [117], and has been questioned by researchers when it is compared with hysteresis modelling. Johannesson et al. [14] reported that "the error (between non-hysteresis and hysteresis modelling) in determining the water content may be as high as 30-35% ". Derluyn et al. [16] concluded "durability risks may be underestimated when omitting moisture hysteresis". Both studies emphasised the necessity of considering hysteresis for the prediction of the moisture behaviour of cementitious materials.

All of these conclusions indicate that if the model is able to take into account hysteresis, more accurate results will be obtained. But, the conclusion has been only verified by limited supporting experimental data. It inspires us to carefully analyse hysteretic effects on moisture transport in cementitious materials through both experimental investigations and numerical modelling.

Chapter 2

Modelling of isothermal drying of unsaturated cementitious materials

Summary

In this chapter, the multiphase transport model described in Chapter 1 will be used to simulate isothermal drying of cementitious materials (mainly cement pastes). First of all, this model will be verified by means of experimental data selected from the literature. Asymptotic analysis concludes that cementitious materials can be viewed as weakly permeable materials in the case $K_g = K_l$ which is in agreement with the theoretical construction of the modelling. Simulation results show that the gas overpressure and underpressure can be observed in the material. Gas pressure variations are highly dependent on the initial saturation within the material. However, it is recognised that $K_l \ll K_g$ when comparing K_l provided by inverse analysis of drying kinetics and K_g directly measured by experiments. This provides the second case for numerical modelling which shows that gas pressure in the material is constant. By neglecting advection of the gas-phase, a simplified model, only including advection of liquid-water and vapour diffusion, can be obtained. In the last part of this chapter, the different moisture transport modes will be discussed according to the above two cases illustrating that quite different transport regimes can be achieved.

2.1 Introduction

The study on drying is of great importance for moisture transport within building materials. Porous building materials such as concretes and mortars are inevitably exposed to natural conditions. These conditions definitely have influence on their performances related to their mechanical properties, such as strength, shrinkage, creep, cracking, etc., as well as their durability since the chemical ingresses occurring in cementitious materials are strongly dependent on the moisture content. The importance of moisture transport in the field of civil engineering is thus particularly marked when the prediction of the service-life of concrete structures is required [79, 80, 81, 23].

Drying of cementitious materials has been widely studied by numerical modelling [79, 80, 42, 81]. By using the multiphase model described in Chapter 1 (see Section 1.4), Mainguy et al. [42] analysed two assumptions that gas pressure in the material is constant or non-constant and reported a simplified moisture transport model in the case of non-constant gas pressure (see Eq. 1.17). The current chapter will adopt this multiphase model to further discuss the impact of two assumptions about the concept of intrinsic permeability ($K_l = K_g$ or $K_l \ll K_g$) on gas pressure variations, and the regimes of moisture transport. Firstly, the case $K_l = K_g$ is use to simulate moisture transport during drying, and then the case $K_l \ll K_g$ will be discussed.

2.2 Modelling of drying porous media in the case of cementitious materials

The governing equations of the multiphase model have been given in Section 1.4 in Chapter 1 (see Eqs. 1.3-1.11). To perform numerical simulations, the initial and boundary conditions and equations for transport coefficients have to be defined.

2.2.1 Initial and boundary conditions and geometry of the problem

The flux boundary condition [119, 113] which has been introduced in Chapter 1 is used to account for an imperfect moisture transport between the environment and the surface of the material. If only focusing on the 1D transport problem for a given size material $x \in [0, l]$, the boundary

conditions are expressed as:

$$\text{for} \quad t > 0, \quad \text{at} \quad x = 0 \quad : \qquad J_{\text{total}} = \phi S E P_{vs}(RH^0 - RH^e); \quad P_g = P_{atm} \tag{2.1}$$

$$\text{for} \quad t > 0, \quad \text{at} \quad x = l \quad : \qquad J_{\text{total}} = 0 \tag{2.2}$$

State variables are considered to be uniformly distributed in the material at the initial.

$$\text{for} \quad x > 0, \quad \text{at} \quad t = 0 : \quad RH = RH_0; \quad P_g = P_{atm} \tag{2.3}$$

where $RH_0 = P_{v,0}/P_{vs}$ is the initial RH.

An idealized 1D drying experiment is considered. A sample of porous material is lying between $x = 0$ and $x = l$ (see Fig. 2.1). Initially, relative humidity RH_0 in the material is uniform. The initial liquid-water saturation S_0 is calculated from RH_0 according to the desorption isotherm. At time $t = 0$, the face $x = 0$ comes into contact with an ambient environment whose relative humidity RH^e is lower than RH_0.

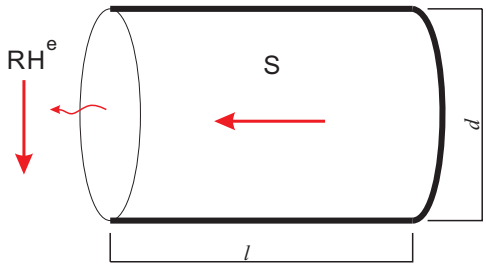

Figure 2.1: Schematic representation of the geometry of the problem. The surface in bold black lines is sealed by aluminium sheets and the ellipse in thin line on the left-hand side represents the surface that is exposed to the ambient environment.

2.2.2 Materials properties

The drying experimental data were collected from the literature [22, 42, 23, 24]. The properties of the selected materials are given in Table 2.1, including three cement pastes and one concrete, which were made from the same cement (CEM I 52.5, according to EN 197-1 European standard), but mixed with different water-to-cement ratios (w/c) or water-to-binder ratio (w/b). Paste3 and Concrete3 were cast in cylindrical moulds with a 16 cm-diameter [22, 42]. Smaller moulds were used for Paste4 and Paste5 with a 7 cm-diameter [24].

Before drying experiments, materials had been sealed more than 200 days for curing. After

Table 2.1: Properties of materials.

Materials	w/c (w/b)	Porosity	Initial RH (%)	Drying duration	Sources of data
Paste3	0.35	0.31	83	157 days	[23, 24]
Paste4	0.45	0.41	89	371 days	[23, 24]
Paste5	0.60	0.49	95	353 days	[23, 22, 42]
Concrete3	0.43	0.122	93	356 days	[23, 22, 42]

demoulded, materials were cut into around 10 cm-length cylinders, and then samples were sealed by self-adhesive aluminium foil sheets, but one face was open for moisture exchanges with ambient environment (see Fig. 2.1). All samples were stored in a sealed space (e.g., desiccators or dry keepers) for measurements at room temperature ($T = 23 \pm 0.1°C$). The external RH was fixed at $RH^e = 53.5\%$ by using a saturated salt solution (magnesium nitrate, $Mg(NO_3)_2$). Besides, Paste3 was also submitted to drying at $RH^e = 63.2\%$ (ammonium nitrate, NH_4NO_3). The total porosity was calculated based on the mass differences between the weight of saturated samples and the weight of fully dried samples (at 105 °C) [22, 23, 24].

One important property of the material is its capillary pressure curve. As mentioned in Section 1.2 in Chapter 1, capillary pressure curve addresses the equilibrium between liquid-water and vapour. For drying, the desorption curve is required for numerical simulations. At a given temperature, the desorption curve is experimentally determined by the saturated salt solution method [23]. However, measurements can only provide limited points for a capillary pressure curve, such as 11 points in Fig. 2.2. From a practical point of view, in the purpose of numerical modelling, an analytical equation is necessary to represent the capillary curve. The equation can be obtained by fitting the measured curve. Different fitting equations can be found in the literature. Some of them will be compared and analysed in Chapter 3 (see Section 3.4). Following the work carried out by Mainguy et al. [42], the current study tentatively chooses a simple and commonly-used equation, proposed by van Genuchten [90].

$$P_c(S) = a_V \left(S^{-m_V} - 1\right)^{1/n_V} \tag{2.4}$$

where a_V, m_V and n_V are parameters, which will be evaluated by experimental data. In practice, $m_V = 1 - 1/n_V$ is used to simplify Eq. (2.4); thus, only two parameters need to be determined. Fitting results by using this two-parameter equation for the selected materials are presented in Fig. 2.2. Values of these parameters for all the selected materials are presented in Table 2.2.

Table 2.2: Values of a_V and m_V for the selected materials fitted by Eq. (2.4).

Materials	Paste3	Paste4	Paste5	Concrete3
a_V ($\times 10^7$ Pa)	4.43	3.21	1.35	4.06
m_V	0.48	0.47	0.39	0.49

Figure 2.2 shows quite good fitting results, especially for the points in the moderate RH range. Some points in the very high RH range (e.g., RH = 97%) and at RH = 33% are not fitted very well.

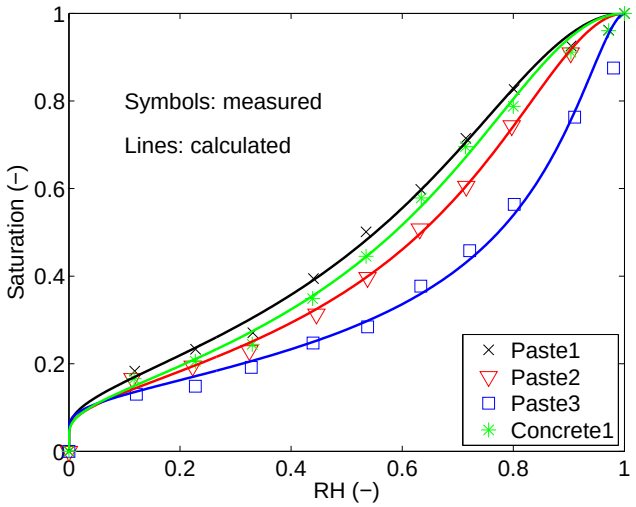

Figure 2.2: Fitted desorption curves for the selected materials by using Eq. (2.4).

2.2.3 Transport coefficients

Due to the lack of experimental data, tortuous and unsaturated effects on gas diffusion introduced in Eqs. (1.7) and (1.8) were calculated by the equation proposed by Millington [93].

$$\alpha(S)\tau = \phi^{x_D-1}(1-S)^{x_D+1} \tag{2.5}$$

The parameter x_D was fixed at 4/3 in Millington's study for soils. However, soils are more porous than cementitious materials and therefore the resistant effects should be more significant in the case of cementitious materials. Thiéry et al. [120] suggested $x_D = 2.74$ based on the fitting of experimental data for O_2 and CO_2 diffusion measurements conducted by Papadakis et al. [121]. The comparison of $\alpha(S)\tau$ calculated by these two proposals for the studied three materials are shown in Fig. 2.3. Thiéry's suggestion provides smaller resistance factor values as it has been

shown in studies [43, 44, 122, 123], which may be closer to the real condition of cementitious materials compared to the original x_D value.

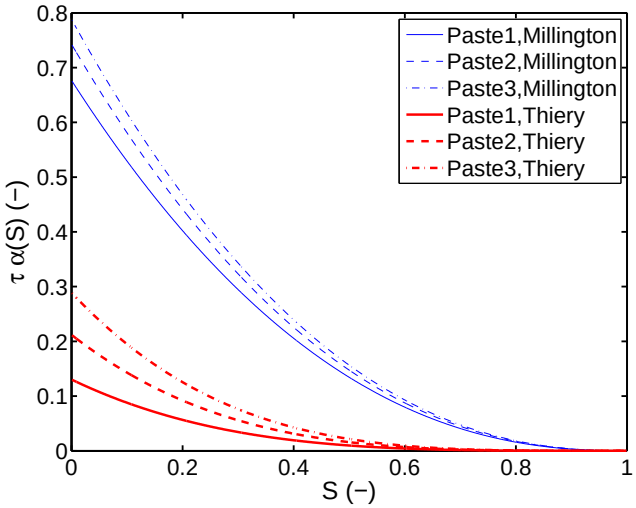

Figure 2.3: Predicted $\alpha(S)\tau$ for three materials calculated by Millington's [93] and Thiéry's [120] proposals.

For cementitious materials, measuring the permeability to liquid-water for different RH is very difficult due to the fact that advective liquid transport and vapour diffusion always occur together [11]. Hence, analytical equations are normally used to calculate k_{rl}. One most common method is to consider k_{rl} as a function of S ($k_{rl} = k_{rl}(S)$), which was first reported for two-phase flow by Geffen et al. [124] and Osaba et al. [125]. The equation for the gas relative permeability k_{rg} can be deduced based on the equation for k_{rl}.

Relative permeabilities - Method-1

Mualem proposed an equation for porous materials based on the known capillary curve [89].

$$k_{rl}(S) = S^{\ell}\left(\frac{\int_0^S \frac{\mathrm{d}S}{P_c}}{\int_0^1 \frac{\mathrm{d}S}{P_c}}\right)^{\gamma} \tag{2.6}$$

In Eq. (2.6), the term $\int_0^1 \mathrm{d}S/P_c$ is related to the total pore volume which is available for liquid-water transport, and the term $\int_0^S \mathrm{d}S/P_c$ stands for the actual pore volume which has been occupied by liquid-water. The term S^{ℓ} is a correction factor, which accounts for the influence of tortuous effects of pores on the liquid transport. Different suggestions of parameter ℓ have been

proposed by researchers [89, 91]. In Mualem's studies, ℓ varies between -1 and 3, and finally the value 0.5 was considered as the best choice. The parameter γ is generally taken as $\gamma = 1/\ell$. These values of ℓ and γ have been adopted for cementitious materials [126, 42].

If putting the capillary curve equation (Eq. 2.4) into Eq. (2.6), a simple and easy-to-use analytical equation is provided [90]:

$$k_{rl}(S) = S^{0.5}\left[1 - \left(1 - S^{1/m_V}\right)^{m_V}\right]^2 \tag{2.7}$$

where the parameter m_V is the same as one used in Eq. (2.4).

Equation (2.6) indicates that the pore volume which has been filled by liquid-water is used for liquid transport, so that it is easy to understand that the pore volume which has not been occupied by liquid-water is available for gas transport. Hence, the expression of the gas relative permeability can be deduced following the form of Eq. (2.6) [127]:

$$k_{rg}(S) = (1 - S)^{\ell}\left(\frac{\int_S^1 \frac{\mathrm{d}S}{P_c}}{\int_0^1 \frac{\mathrm{d}S}{P_c}}\right)^{\gamma} \tag{2.8}$$

In a similar manner, if plugging Eq. (2.4) into Eq. (2.8) and letting $\ell = 0.5$, an analytical equation [91, 92] appears as:

$$k_{rg}(S) = (1 - S)^{0.5}\left[1 - S^{1/m_V}\right]^{2m_V} \tag{2.9}$$

One can notice that Eqs. (2.7) and (2.9) are definitely easier to use in numerical modelling due to analytical forms. This version of Mualem's model [89] indicates that there is a relation between k_{rl} and k_{rg} if merging Eqs. (2.6) and (2.8).

$$\left(\frac{k_{rl}}{S^{\ell}}\right)^{1/\gamma} + \left(\frac{k_{rg}}{(1 - S)^{\ell}}\right)^{1/\gamma} = 1 \tag{2.10}$$

Therefore, if either k_{rl} or k_{rg} is known, the other one can be determined by using Eq. (2.10).

Relative permeabilities - Method-2

Based on the simplified independent domain theory [53], Mualem [128] developed a comprehensive model to calculate the relative permeability. The main feature of this model is that it has

taken into account hysteresis in the relation $k_{rl}(S)$. Thus, the equations to calculate k_{rl} corresponding to the main sorption (desorption and adsorption) and scanning curves are different. The principle of the independent domain theory will be described in Chapter 3 (see Section 3.2). The complete equations for this model will be given in Chapter 5 (see Section 5.6.5). Since there are two versions of Mualem's models for k_{rl}, let's denote Eq. (2.6) as Mualem's model-a [89] and the model mentioned in this paragraph as Mualem's model-b [128]. These two models are combined with van Genuchten's equation to calculate k_{rl}. Thus, the combination of "van Genuchten's equation + Mualem model-a" is further denoted by VGMa (see Eq. 2.7) and the combination of "van Genuchten's equation + Mualem model-b" is denoted by VGMb. Here, only equations to calculate k_{rl} for the main desorption process are introduced.

$$k_{rl}(S) = S^{0.5}\left[KL - (1 - KL)\,KH\right]^2 \tag{2.11}$$

where KL and KH are two normalized integral functions calculated based on capillary pressure. The expressions to these two functions are:

$$KL = \frac{\displaystyle\int_{P_c}^{+\infty} \frac{\mathrm{d}L(S)}{P_c}}{\displaystyle\int_{0}^{+\infty} \frac{\mathrm{d}L(S)}{P_c}} \qquad KH = \frac{\displaystyle\int_{P_c}^{+\infty} \frac{\mathrm{d}H(S)}{P_c}}{\displaystyle\int_{0}^{+\infty} \frac{\mathrm{d}H(S)}{P_c}} \tag{2.12}$$

where L and H are two cumulative pore water distribution functions. Their expressions are:

$$L(P_c) = S_w(P_c) \qquad H(P_c) = \frac{S_d(P_c) - S_w(P_c)}{1 - S_w(P_c)} \tag{2.13}$$

where $S_w(P_c)$ and $S_d(P_c)$ are the saturation of the main adsorption and desorption curves.

Since Eq. (2.11) cannot be solved analytically, it is difficult to apply the same theory as the one used in Mualem model-a (see Eq. (2.10) to directly infer k_{rg}. Here, an alternative method is chosen. Thiéry et al. [129] adopted the formula based on the theory of Mualem model-a [89] for k_{rg} but proposed different values for ℓ and γ. By the validation of experimental data taken from Villain et al. [130], Monlouis-Bonnaire et al. [131] and Thiéry [132], Thiéry et al. [129] concluded that $\ell = 7.15$ and $\gamma = -8.02$ should be the best choice for cementitious materials.

Figure 2.4 shows calculated $k_{rl}(RH)$ and $k_{rg}(RH)$ for Paste3 by using the above two methods. It is clear that Method-2 provides smaller k_{rl} and k_{rg} in the whole range of RH than Method-1. The relative permeability to gas-phase k_{rg} calculated by Method-2 has been verified by

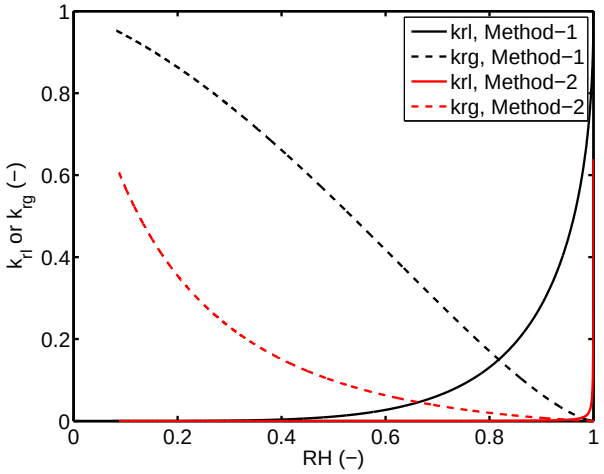

Figure 2.4: Comparison of k_{rl} and k_{rg} calculated by Method-1 and Method-2 for Paste3.

experimental data [120], while there are no measured data available in the literature to verify k_{rl}. Therefore, the next subsection will discuss effects of different choices to k_{rl} and k_{rg} on moisture transport in unsaturated porous materials.

For cementitious materials, directly measuring the intrinsic permeability to liquid-water K_0 is extremely difficult because the measurement requires very high pressure gradient, which may destroy the material. Since K_0 is the only undetermined parameter in the multiphase moisture transport model in the case $K_l = K_g = K_0$, a method called "inverse analysis" can be used to determine K_0 through fitting the measured mass loss curve obtained in a drying experiment. The inverse determination of K_0 has been used in [133, 42, 134]. The modelling results in the case of distinguishing K_l and K_g will be shown in Section 2.4.

2.2.4 Simulation results verified by experimental data of drying

Experimental data include mass loss curves and saturation profiles [22, 42, 24]. During experiments, samples were weighed to get mass loss curves and saturation profiles were measured by gamma-ray attenuation.

During the sealed-curing period, the cement hydration processes consumes water molecules and self-desiccation occurs in the material. This means that the material undergoes a decrease of its internal RH. After moulds had been removed, the internal RH, which should be the initial condition for numerical modelling, was measured for all the selected materials (see Table 2.1) [22]. Since the material has been assumed as a homogeneous porous medium, the internal RH is also considered to be distributed uniformly in the material.

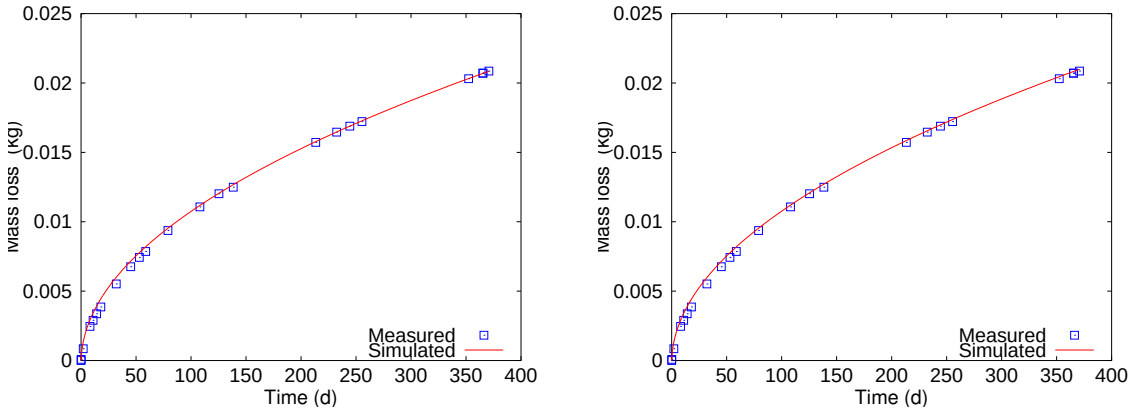

(a) Method-1 ($K_0 = 1.95 \times 10^{-21}\mathrm{m}^2$). (b) Method-2 ($K_0 = 3.5 \times 10^{-19}\mathrm{m}^2$).

Figure 2.5: Comparisons of simulated mass loss curves based on two different methods to calculate k_{rl} and k_{rg} for Paste4.

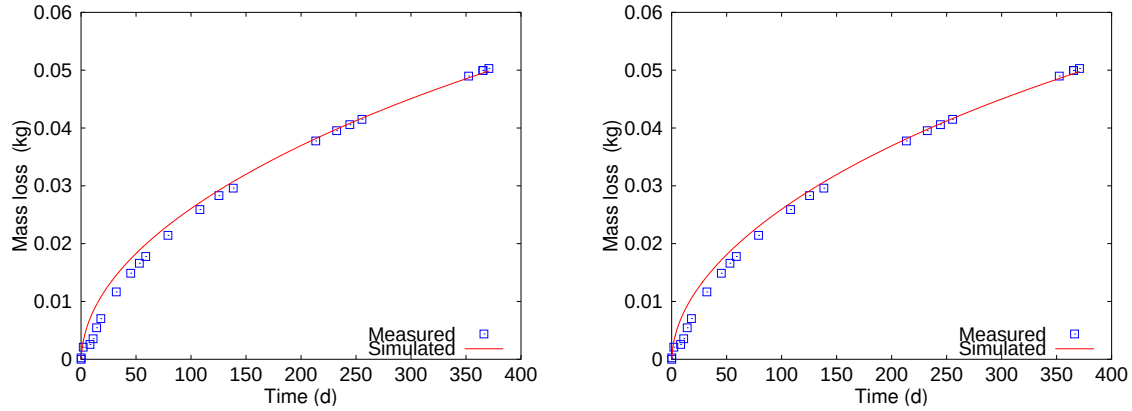

(a) Method-1 ($K_0 = 30 \times 10^{-21}\mathrm{m}^2$). (b) Method-2 ($K_0 = 160 \times 10^{-19}\mathrm{m}^2$).

Figure 2.6: Comparisons of calculated mass loss curves based on two methods to calculate k_{rl} and k_{rg} for Paste5.

Simulation results for materials Paste4, Paste5, Concrete3 and Paste3, are shown in Figs. 2.5-2.10. Numerical calculations are carried out in two cases corresponding to each method to determine k_{rl} and k_{rg} (see Method-1 and Method-2 described in Section 2.2.3).

Figures 2.5, 2.6 and 2.9 show that calculated mass loss curves can fit experimental curves very well. Simulated saturation profiles in Figs. 2.7, 2.8 and 2.10 show good agreements with measured profiles, either for using Method-1 or Method-2 to calculate k_{rl} and k_{rg}. Besides of the differences in fitted intrinsic permeabilities, there are no effects of two methods on the calculated mass loss curves and saturation profiles. Beyond the relevancy of the fitting results for mass loss curves, the good agreements between the simulated and measured saturation profiles represent a

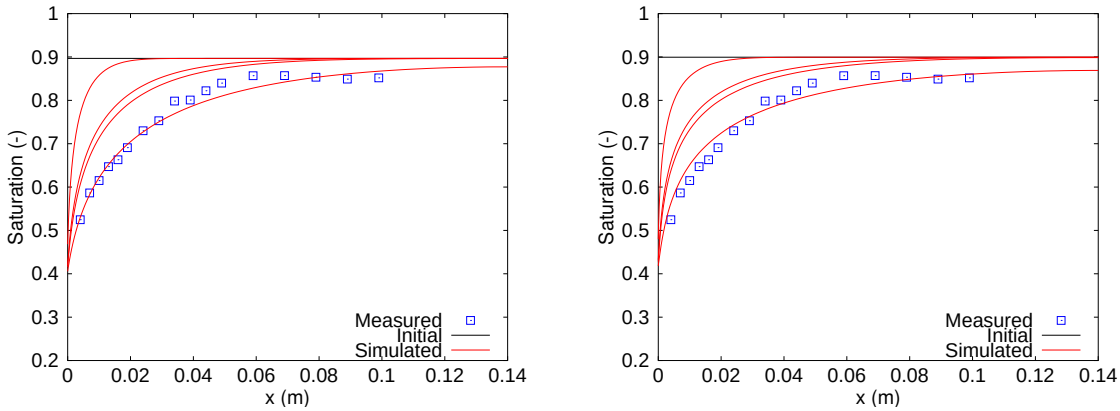

(a) Method-1 ($K_0 = 1.95 \times 10^{-21}\mathrm{m}^2$). (b) Method-2 ($K_0 = 3.5 \times 10^{-19}\mathrm{m}^2$).

Figure 2.7: Comparisons of simulated saturation profiles based on two different methods to calculate k_{rl} and k_{rg} for Paste4.

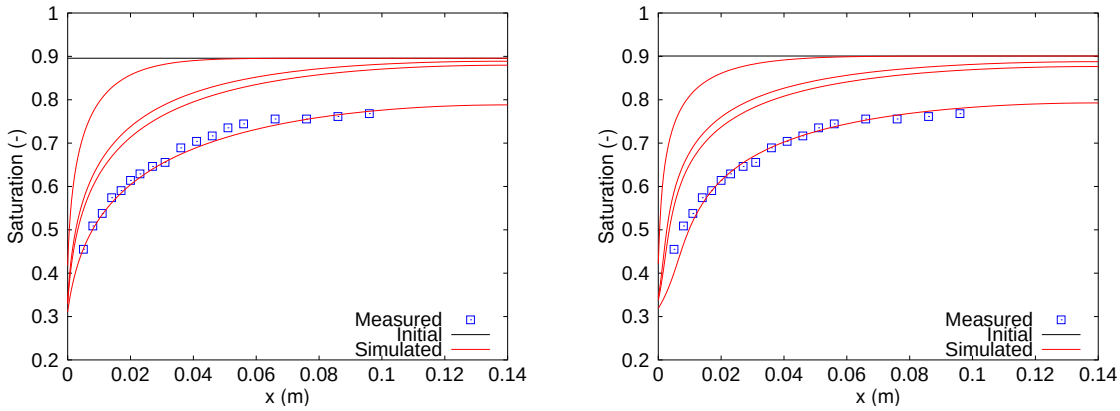

(a) Method-1 ($K_0 = 30 \times 10^{-21}\mathrm{m}^2$). (b) Method-2 ($K_0 = 160 \times 10^{-19}\mathrm{m}^2$).

Figure 2.8: Comparisons of simulated saturation profiles based on two different methods to calculate k_{rl} and k_{rg} for Paste5.

powerful verification of these approaches and show their reliability to model moisture transport through the samples.

Table 2.3: The intrinsic permeabilities fitted by inverse analysis for different materials.

	Methods	Paste3	Paste4	Paste5	Concrete3
K_0	Method-1 ($\times 10^{-21}\mathrm{m}^2$)	0.39 (0.25 [a])	1.95	30	1.8
	Method-2 ($\times 10^{-19}\mathrm{m}^2$)	1.7 (1.0 [a])	3.5	160	2.3
	Katz-Thompson ($\times 10^{-21}\mathrm{m}^2$)	37	71	231	-

Intrinsic permeabilities calibrated by experimental data are presented in Table 2.3 for different

[a] Obtained by drying at RH = 63.2%.

materials. Values for Paste3, Paste4 and Paste5 determined by Katz-Thompson model [135] (taken from the reference [24]) are also shown in this table. Obviously, K_0 determined based on Method-1 are larger than that calibrated by Method-2. The differences can be up to 500 times. The order of magnitude of the intrinsic permeabilities determined by Method-1 is around 10^{-21} m^2, which is close to results provided in [22], but smaller than results calculated by the Katz-Thompson model. Experiments, such as the beam-bending method [136, 137] and the dynamic pressurization method [138], show that the intrinsic permeability is around 10^{-20} m^2 for cement pastes with equivalent w/c. Thus, it is not easy to say which method to calculate k_{rl} and k_{rg} is better than the other one. Nevertheless, Method-1 seems to be easier to use since all equations are analytical.

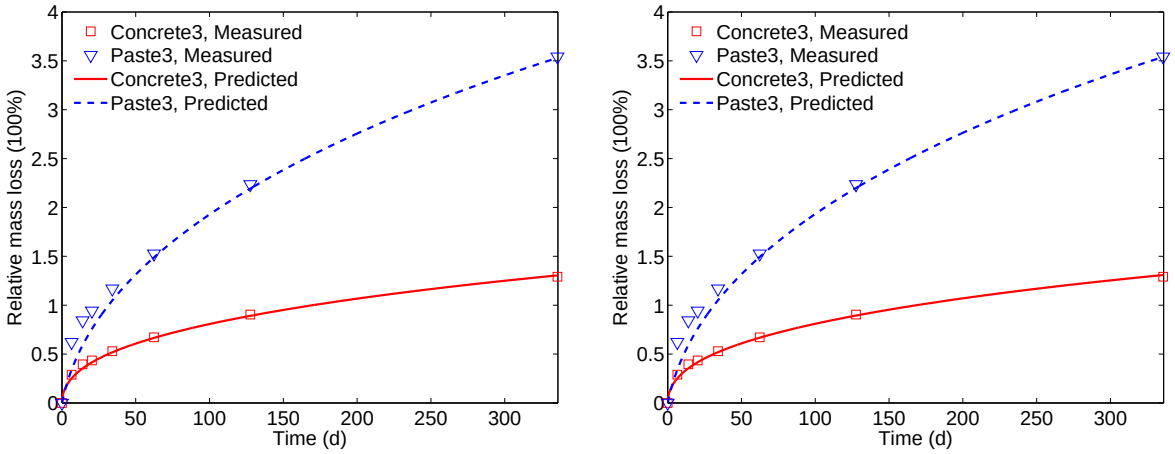

(a) Method-1. (b) Method-2.

Figure 2.9: Comparisons of simulated mass loss curves based on two different methods to calculate k_{rl} and k_{rg} for Concrete3 and Paste3.

2.3 Gas pressure variations during drying of unsaturated cementitious materials

When applying the multiphase model to simulate moisture transport in cementitious materials, it reveals the existing of gas overpressure (above the atmospheric pressure) in the material. This phenomena has been reported by Mainguy et al. [42], but these authors used Millington's proposal of x_D for the resistance factor (see Eq. 2.5) and chose Method-1 to calculate k_{rl} and k_{rg}. This section will utilize different equations to calculate the resistance factor, k_{rl} and k_{rg} and to analyse gas pressure variations during drying.

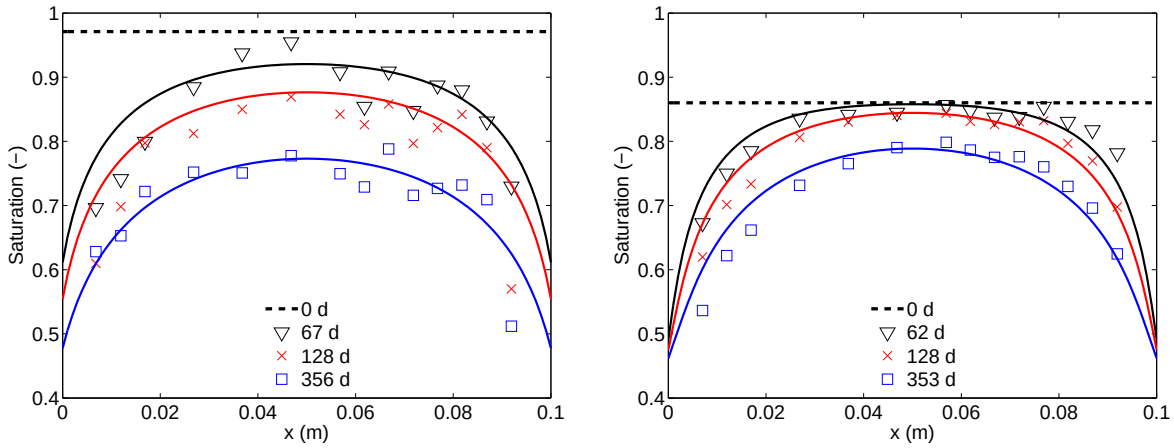

(a) Concrete3 ($K_0 = 1.8 \times 10^{-21}\mathrm{m}^2$). (b) Paste3 ($K_0 = 0.39 \times 10^{-21}\mathrm{m}^2$).

Figure 2.10: Calculated saturation profiles for Concrete3 and Paste3 (Method-1 to calculate k_{rl} and k_{rg}).

2.3.1 Mass balance equations of gas and moisture

By putting Eqs. (1.14)-(1.16) into the mass balance equations of gas-phase Eqs. (1.3) and (1.5), and merging them, it is possible to derive the following mass balance equation for the gas mixture:

$$\phi \frac{\partial}{\partial t}\left[P_g(1-S)\right] = -\frac{\partial}{\partial x}\left(P_g v_g\right) + \frac{RT}{M_v}\mathring{m}_{l\to v} \tag{2.14}$$

The left hand side of the above equation is divided into two parts leading to the following equation:

$$\phi(1-S)\frac{\partial P_g}{\partial t} = \phi P_g \frac{\partial S}{\partial t} - \frac{\partial}{\partial x}\left(P_g v_g\right) + \frac{RT}{M_v}\mathring{m}_{l\to v} \tag{2.15}$$

Equation (2.15) shows that there are three components which contribute to gas pressure variations: (a) The term involving the evaporation rate $\mathring{m}_{l\to v}$ causes an increase of gas pressure. The evaporated vapour is forced to diffuse toward the surrounding air because the maximum vapour pressure is far below vapour pressure in saturated condition (P_{vs}). According to Fick's law, a symmetric diffusion of dry air occurs simultaneously to diffusion of vapour, and may engender an increase of pressure by provoking a net arrival of fresh air. This phenomenon was studied in detail in [42]. (b) The term involving the derivative of S with respect to time is negative during drying, and thus it entails a decrease of pressure due to the release of liquid-water in the pores. (c) The divergence term stands for the advective Darcean flow of the gas-phase which can dissipate any variations of pressure. The existence of an overpressure or underpressure of gas during drying depends on the time scales at which the three above-mentioned mechanisms can

occur.

Substitution of Darcy's law (see Eq. 1.11) into the mass balance equation (see Eq. 1.4), the following expression of the evaporation rate $\mathring{m}_{l\to v}$ can be derived:

$$\mathring{m}_{l\to v} = -\rho_l \phi \frac{\partial S}{\partial t} + \frac{\rho_l}{\eta_l} K_0 \frac{\partial}{\partial x}\left[k_{rl}(S)\left(\frac{\partial P_g}{\partial x} - \mathbb{M}\frac{\mathrm{d}\pi_c}{\mathrm{d}S}\frac{\partial S}{\partial x}\right)\right] \tag{2.16}$$

Putting the previous expression of $\mathring{m}_{l\to v}$ into the mass balance equation of gas (see Eq. 2.14), the equation governing the advective transport of the vapour-dry air mixture is given as:

$$\begin{aligned}\frac{\partial}{\partial t}[P_g(1-S)] + \frac{\rho_l RT}{M_v}\frac{\partial S}{\partial t} &= \frac{1}{2\eta_g}\frac{K_0}{\phi}\frac{\partial}{\partial x}\left[k_{rg}(S)\frac{\partial P_g^2}{\partial x}\right] \\ &+ \frac{\rho_l RT}{M_v \eta_l}\frac{K_0}{\phi}\frac{\partial}{\partial x}\left[k_{rl}(S)\left(\frac{\partial P_g}{\partial x} - \mathbb{M}\frac{\mathrm{d}\pi_c}{\mathrm{d}S}\frac{\partial S}{\partial x}\right)\right]\end{aligned} \tag{2.17}$$

By putting the expression of $\mathring{m}_{l\to v}$ in Eq. (2.16) into Eq. (1.3) and by accounting for Eq. (1.7), it comes the equation governing the transport of moisture in both liquid and vapour form:

$$\begin{aligned}\frac{\partial}{\partial t}\left[(1-S)P_v\right] + \frac{\rho_l RT}{M_v}\frac{\partial S}{\partial t} &= -\frac{1}{\eta_g}\frac{K_0}{\phi}\frac{\partial}{\partial x}\left[P_v k_{rg}(S)\frac{\partial P_g}{\partial x}\right] \\ &+ D_0 P_{atm}\tau\frac{\partial}{\partial x}\left[(1-S)\alpha(S)\frac{\partial}{\partial x}\left(\frac{P_v}{P_g}\right)\right] \\ &+ \frac{\rho_l RT}{M_v \eta_l}\frac{K_0}{\phi}\frac{\partial}{\partial x}\left[k_{rl}(S)\left(\frac{\partial P_g}{\partial x} - \mathbb{M}\frac{\mathrm{d}\pi_c}{\mathrm{d}S}\frac{\partial S}{\partial x}\right)\right]\end{aligned} \tag{2.18}$$

Among the three thermodynamic variables S, P_v and P_g involved in Eqs. (2.17) and (2.18), only two are actually independent since the equilibrium between liquid-water and vapour must be ensured. This equilibrium state is governed by the Kelvin's law (see Eq. 1.12).

2.3.2 Asymptotic analysis

According to studies performed by Coussy and Thiery [78, 139], it is possible to identify three characteristic times on the basis of analysis of Eqs. (2.17) and (2.18):

$$\mathbf{t}_F = \frac{l^2}{D_0\tau} \qquad \mathbf{t}_D^g = \frac{\phi\eta_g l^2}{P_{atm}K_0} \qquad \mathbf{t}_D^l = \frac{\phi\eta_l l^2}{\mathbb{M}K_0} \tag{2.19}$$

The characteristic time $\mathbf{t}_F$ scales the rate at which diffusion of vapour and dry air occur, and $\mathbf{t}_D^g$ and $\mathbf{t}_D^l$ scale the rates at which the advective flows of gas and liquid-water take place,

respectively. Then, the following dimensionless quantities are introduced:

$$\mathbf{x} = \frac{x}{l} \quad \mathbf{P}_g = \frac{P_g}{P_{atm}} \quad \mathbf{P}_v = \frac{P_v}{P_{atm}} \tag{2.20}$$

To simplify the expressions, another parameter Λ is introduced:

$$\Lambda = \frac{1}{P_{atm}} \frac{\rho_l RT}{M_v} \tag{2.21}$$

This parameter represents the ratio of pressure that the water vapour would have if its density was the same value as the density of the liquid-water ρ_l to the atmospheric pressure P_{atm}. Adopting an absolute temperature of 293 K, the value of the parameter Λ is around 1350.

The time scale at which the coupled transports (liquid-water, vapour and dry air) successively occur depends on the relative range of the characteristic times $\mathbf{t}_D^l$, $\mathbf{t}_D^g$ and $\mathbf{t}_F$. The drying mechanism will be explored according to the intrinsic permeability K_0 of the material.

The value $\mathbb{M}$ stands for a reference capillary pressure related to the whole pore size distribution corresponding to the entry radii of the pores. By considering Laplace's equation with a zero wetting angle, a relationship between the capillary modulus $\mathbb{M}$ and a radius of pore representing the pore size distribution appears as $r \sim \sigma/\mathbb{M}$ where σ is the air-water interfacial energy (7.3×10^{-2} J $\cdot$ m^{-2}). Moreover, it is well recognized that the intrinsic permeability is proportional to the square of a characteristic length related to the porous volume where the flow takes place. By adopting the percolation theory [140], K_0 is demonstrated to be proportional to $r^2\phi\tau$. Thus, it follows:

$$\mathbb{M} \sim \sigma \sqrt{\frac{\phi\tau}{K_0}} \tag{2.22}$$

Adopting $T = 293$ K, $\eta_g = 1.8 \times 10^{-5}$ Pa $\cdot$ s, $\eta_l = 1.0 \times 10^{-3}$ Pa $\cdot$ s, $P_{atm} = 10^5$ Pa and $D_0 = 2.5 \times 10^{-5}$ m$^2 \cdot$ s^{-1}, the three following ratios can be assessed in the form:

$$\frac{\mathbf{t}_F}{\mathbf{t}_D^g} \sim 2.2 \times 10^{14} \frac{K_0}{\phi\tau} \tag{2.23}$$

$$\frac{\mathbf{t}_D^l}{\mathbf{t}_D^g} \sim 7.7 \times 10^{7} \sqrt{\frac{K_0}{\phi\tau}} \tag{2.24}$$

$$\frac{\mathbf{t}_F}{\mathbf{t}_D^l} \sim 2.9 \times 10^{6} \sqrt{\frac{K_0}{\phi\tau}} \tag{2.25}$$

A quite permeable porous material can be defined when the ratio $\mathbf{t}_F/\mathbf{t}_D^g \gg 1$ ($\Leftrightarrow$ $K_0/(\phi\tau) \gg$

4.5×10^{-15} m^2). Notice that this condition also implies the fact that the ratio $\mathbf{t}_D^l/\mathbf{t}_D^g$ (see Eq. 2.24) is far larger than 1 ($\Leftrightarrow\ K_0/(\phi\tau) \gg 1.7\times10^{-16}$ m^2). The situation of a quite permeable porous material corresponds to the fact that the advective transport of the gaseous phase occurs much faster than transports of both liquid-water by capillarity and water vapour by diffusion.

In contrast, because of a sufficiently low value of intrinsic permeability, i.e., $K_0/(\phi\tau) \ll 4.5\times10^{-15}$ m^2, vapour diffusion occurs much faster than the advective transport of gas ($\mathbf{t}_F/\mathbf{t}_D^g \ll 1$) and of liquid-water ($\mathbf{t}_F/\mathbf{t}_D^l \ll 1 \Leftrightarrow K_0/(\phi\tau) \ll 1.2\times10^{-13}$ m^2). However, the condition $K_0/(\phi\tau) \ll 4.5\times10^{-15}$ m^2 does not imply that the ratio $\mathbf{t}_D^l/\mathbf{t}_D^g$ is much lower than 1. Because of the much lower value of the liquid-water viscosity compared to that of the gaseous mixture, it could be expected that advective of liquid-water occurs slower than advection of gas-phase in the material. Indeed, as shown by Eq. (2.24), for the weakly permeable porous media, advection of liquid-water takes place either at the same rate as advection of the gaseous mixture or much faster. Actually, the huge difference of viscosity between the liquid-water and the gas is compensated by the huge value of capillary pressure driving the liquid flow. High values of capillary pressures are associated with a large value of capillary modulus $\mathbb{M}$ and low values of permeability.

On the whole, two cases are distinguished in this asymptotic analysis of drying:

- **Quite permeable porous materials**: $\mathbf{t}_F/\mathbf{t}_D^g \gg 1$; $K_0/(\phi\tau) \gg 4.5\times10^{-15}$ m^2 leading to $\mathbf{t}_D^l/\mathbf{t}_D^g \gg 1$;

- **Weakly permeable porous materials**: $\mathbf{t}_F/\mathbf{t}_D^g \ll 1$; $K_0/(\phi\tau) \ll 4.5\times10^{-15}$ m^2 leading to $\mathbf{t}_F/\mathbf{t}_D^l \ll 1$. Moreover, concerning the ratio $\mathbf{t}_D^l/\mathbf{t}_D^g$, no conclusion can be drawn for either $\mathbf{t}_D^l/\mathbf{t}_D^g \ll 1$ or $\mathbf{t}_D^l/\mathbf{t}_D^g \approx 1$.

2.3.3 Simulated gas pressure variations for cementitious materials

According to the definition of quite or weakly permeable material in the previous section (see Eq. 2.23), all the selected materials in this chapter are considered as weakly permeable materials by using K_0 values in Table 2.3 and considering τ in the order of magnitude of 0.01. Therefore, advection of the gas-phase is slower than diffusion of the gas-phase (vapour + dry air), $\mathbf{t}_D^g \gg \mathbf{t}_F$, which causes that gas pressure in the material cannot dissipate in a short time. Meanwhile, since advection of liquid-water is slower than the gas diffusion, $\mathbf{t}_D^l \gg \mathbf{t}_F$, the space for gas-phase does not increase too much. Hence, gas pressure variations are expected during drying of cementitious materials.

To demonstrate the above explanation, simulations of gas pressure during drying need to be carried out. Here, let's take Paste4 as an example. Two different initial conditions are considered: $S_0 = 0.9$ and 0.99. The external $RH^e = 53.5\%$ is used as the same as experiments (see Section 2.2.2). Simulation results of gas pressure profiles are shown in Fig. 2.11.

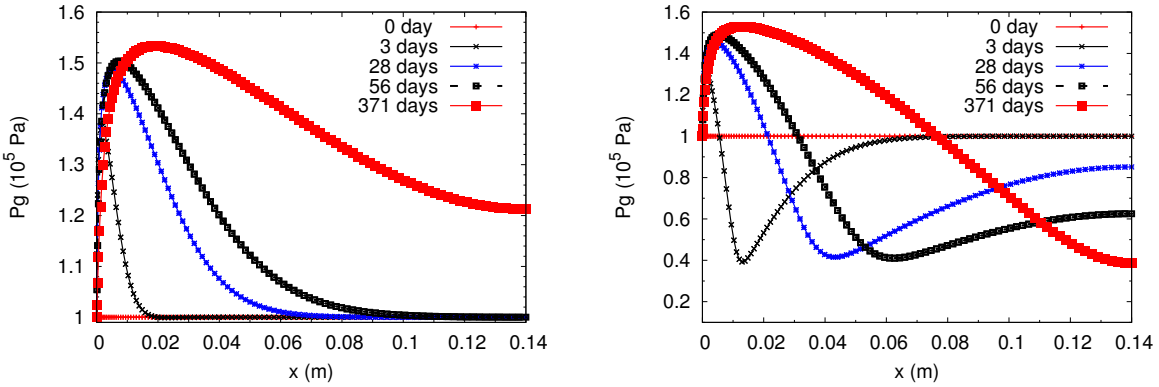

(a) Initial $S_0 = 0.9$.

(b) Initial $S_0 = 0.99$.

Figure 2.11: Profiles of gas pressure during drying of Paste4 with different values of initial saturation.

It is clear that a significant gas overpressure appears at the border layer of the specimen. The predicted gas pressure can reach up to 1.5 times higher than the initial value of gas pressure (atmospheric pressure). This is rather unusual because the gas conductivity of porous materials is generally so high that any change of gas pressure vanishes quasi-instantaneously. Nevertheless, numerical simulations [42] have already shown that the advective Darcean transport of gas (the second term on the right-hand side of Eq. (2.15)) is low for cementitious materials. Thus, the overpressure phenomena related to liquid-water evaporation are not easily dissipated so that the role of the third term on the right-hand side of Eq. (2.15) is predominant.

It is worth noting that when the initial condition $S_0 = 0.99$, an obvious gas underpressure (below the atmospheric pressure) behaviour is observed within the material, but not in the vicinity of the surface (see Fig. 2.11b). It gradually moves toward the inner part of the sample, while for a lower initial condition $S_0 = 0.90$, there is no observed gas underpressure. It shows that the previous asymptotic analysis remains questionable since it does not include the effects of S on the transport parameters and is not valid near the surface under the influence of the boundary condition. Thus, one may expect a role of the initial moisture state of the material, as well as the boundary condition. On one hand, drying of a material which is initially close to saturation shows significant movements of liquid-water due to the strong gradient of capillary

pressure. On the other hand, the diffusion coefficient of water vapour is lower because of the high water content according to Eq. (2.5) and therefore diffusion of water vapour is restricted and cannot move to inner of the sample concurrently. In this process, the desaturation of the porosity causing by liquid-water flow contributes to the decrease of gas pressure in the material (the first term on the right-hand side of Eq. (2.15)).

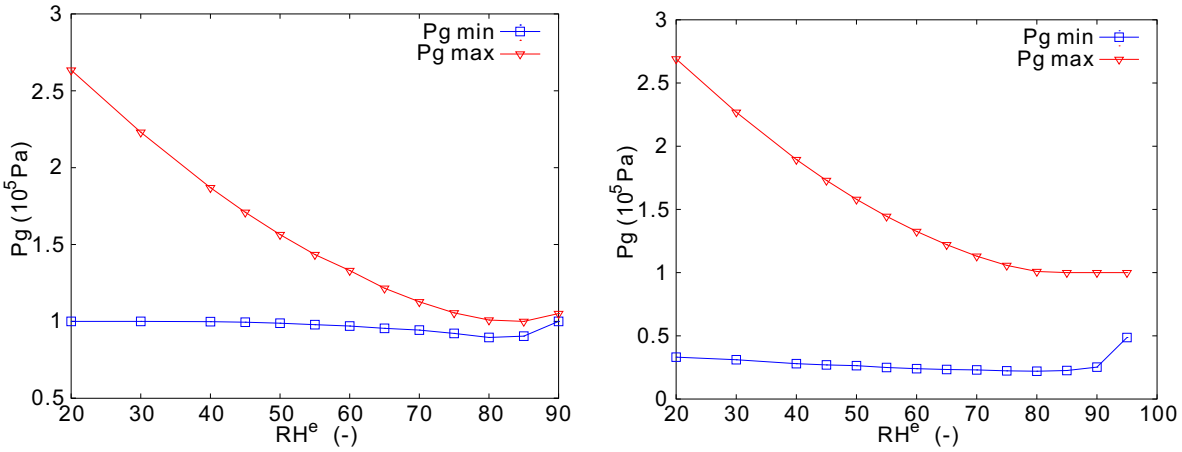

(a) Initial $S_0 = 0.9$. (b) Initial $S_0 = 0.99$.

Figure 2.12: The maximum and minimum gas pressure during drying of Paste4 under various external RH with two different values of initial saturation.

Besides, almost the same maximum values of overpressure for two these different initial saturations are found in Fig. 2.11. A series of simulations on various initial and external RH have shown that, for a given material (such as Paste4), the major factor determining the maximum overpressure during drying is the external RH prevailing in the atmosphere. For example, almost the same curves for maximum overpressure varying with external RH are given in Fig. 2.12 for the two different studied initial conditions. On the contrary, the curves for the minimum gas pressure in the same figure are also illustrating that they mainly depends on the initial saturation. If the initial saturation is very high (such as 0.99), underpressure behaviour appears easily according to results shown in Fig. 2.12.

2.4 Modelling of drying cementitious materials in the case $K_l \ll K_g$

The multiphase model, described in Section 1.4 in Chapter 1, forced $K_l = K_g = K_0$. However, the measured data by CEMBUREAU method (e.g., [141, 142]) and other techniques (e.g., [84, 85])

show that intrinsic permeabilities to gas-phase corresponding to values in Table 2.3 are too small. In other words, the measured data reveal that $K_l \ll K_g$ [84, 85]. Hamami et al. [84] measured the gas permeability for 24 compositions of cement pastes and mortars (w/c = 0.4 and 0.6) and results show the measured data are between 10^{-16} and 10^{-17} m^2. The same results can be found in the work by Loosveldt et al. for mortars [85]. More recently, Kameche et al. [142] reported $K_g \approx 2.5 \times 10^{-17}$ m^2 for concrete (w/c = 0.5). It should be acceptable to assume that K_g is around 1×10^{-17} m^2.

Table 2.4: The intrinsic permeabilities to liquid-water validated by experimental data for different materials.

	Methods	Paste3	Paste4	Paste5	Concrete3
K_l	VGMa model ($\times 10^{-21}$m^2)	0.36 (0.24[a])	1.7	25	1.8
	VGMb model ($\times 10^{-19}$m^2)	1.6 (1.0[a])	3.2	160	2.3

Actually, it is reasonable to observe $K_l \ll K_g$, because: 1) Liquid-water has higher viscous effects from pore walls and therefore its transport should be slower than gas-phase. 2) Ions in liquid-water are able to decrease the chemical activity of liquid-water and to slow down advection of liquid-water. 3) Generally, there are some impurities in pore network, such as unhydrated cement particles, which affect the velocity of liquid transport, but have small influence on gas transport. 4) Liquid phase has stronger electricity charges exchanges with pore walls than gas phase (see explanation in Section 1.2), so that perfect Darcy transport is not valid in micropores. Besides, the faster gas advection can also result from the slipping contact between gas and pore walls (also known as Klinkenberg's concept [143, 11]), while there is no slipping between liquid-water and pore walls.

Since the value of K_g has been fixed at around 1×10^{-17} m^2, K_l becomes the only unknown in the multiphase model. By using the same inverse analysis as Section 2.2.3, K_l can be obtained for the case $K_l \ll K_g$ for the studied materials (see Table 2.4). Compared to Table 2.3, only some values of K_l in Table 2.4 are a little smaller.

One example of simulation results for Paste5 is shown in Fig. 2.13. Results provide quite good agreements with measured data. It is clear that both cases $K_g = K_l$ and $K_l \ll K_g$ can be used to fit mass loss curves and predict saturation profiles.

[a]Obtained by drying at RH = 63.2%.

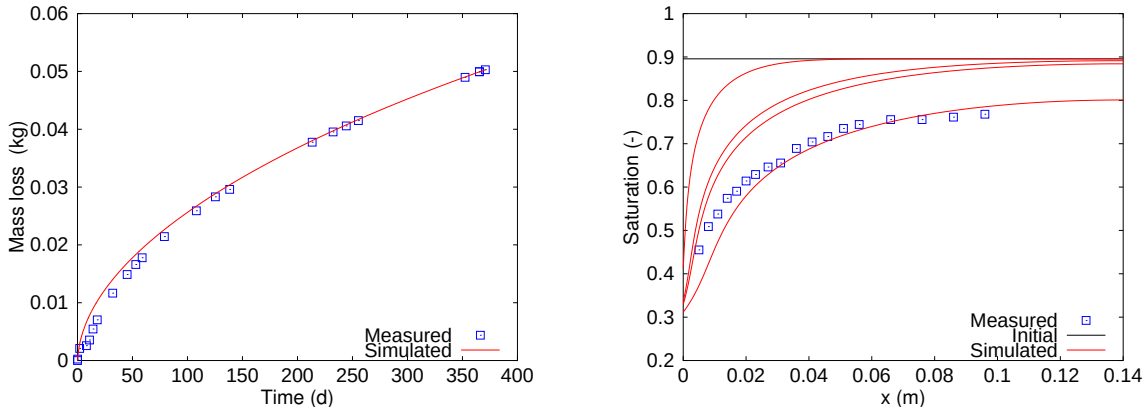

(a) Mass loss curve.

(b) Saturation profiles.

Figure 2.13: Calculated mass loss curve and saturation profiles in the case $K_l \ll K_g$ based on Method-1 to calculate k_{rl} and k_{rg} for Paste5.

2.4.1 Gas pressure variations

In the case $K_l \ll K_g$, three characteristic times in Eq. (2.19) can be rewritten as equations which should be involved by the effect of K_g.

$$\mathbf{t}_F = \frac{l^2}{D_0\tau} \qquad \mathbf{t}_D^g = \frac{\phi\eta_g l^2}{P_{atm}K_g} \qquad \mathbf{t}_D^l = \frac{\phi\eta_l l^2}{\mathbb{M}K_l} \tag{2.26}$$

Like in Eq. 2.22, the capillary modulus can be considered as a function of K_l.

$$\mathbb{M} \sim \sigma\sqrt{\frac{\phi\tau}{K_l}} \tag{2.27}$$

Following Eqs. (2.23), (2.24) and (2.25), the relationships between the three characteristic times can be rewritten as:

$$\frac{\mathbf{t}_F}{\mathbf{t}_D^g} \sim 2.2\times10^{14}\frac{K_g}{\phi\tau} \tag{2.28}$$

$$\frac{\mathbf{t}_D^l}{\mathbf{t}_D^g} \sim 7.7\times10^{7}\frac{K_g}{K_l}\sqrt{\frac{K_l}{\phi\tau}} \tag{2.29}$$

$$\frac{\mathbf{t}_F}{\mathbf{t}_D^l} \sim 2.9\times10^{6}\sqrt{\frac{K_l}{\phi\tau}} \tag{2.30}$$

Thus, the criterion to distinguish quite or weakly permeable porous materials is related to the ratio of K_g to $\phi\tau$:

- **Quite permeable porous materials**: $\mathbf{t}_F/\mathbf{t}_D^g \gg 1$ leading to $K_g/(\phi\tau) \gg 4.5 \times 10^{-15}$ m^2. Because $K_l \ll K_g$, there is $\mathbf{t}_D^l/\mathbf{t}_D^g \gg 1$;

- **Weakly permeable porous materials**: $\mathbf{t}_F/\mathbf{t}_D^g \ll 1$ leading to $K_g/(\phi\tau) \ll 4.5 \times 10^{-15}$ m^2. Because $K_l \ll K_g$, there is $\mathbf{t}_F/\mathbf{t}_D^l \ll 1$.

If putting the values of ϕ and K_g into Eqs. (2.28), (2.29) and (2.30), it yields $\mathbf{t}_F/\mathbf{t}_D^g > 1$ for all the selected materials. This means that for the case $K_l \ll K_g$ the selected materials can be considered as quite permeable materials according to the classification mentioned above. In this situation, advection of gas-phase is faster than diffusion of gas phase. According to Eq. (2.15), the advective flow of gas-phase is able to dissipate any variations of gas pressure, either related to evaporation-diffusion phenomena for movement of liquid-water by capillarity. Expectedly, gas pressure variations are not as significant as the case $K_l = K_g$.

One example for Paste3 is shown in Fig. 2.14. Only small gas pressure variations can be seen in the part near the surface of the material. After a certain period of drying, gas pressure in the material is almost equal to the atmospheric pressure. Figure 2.14 reveals that the main reason causing gas pressure variations is advection of gas-phase. The larger K_g is able to dissipate gas pressure quickly.

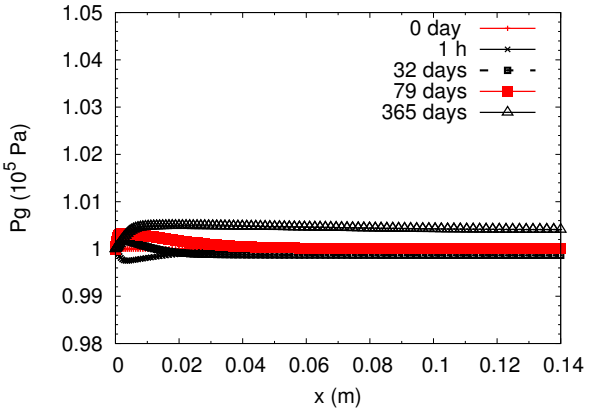

Figure 2.14: Profiles of gas pressure during drying of Paste4 with initial saturation $S_0 = 0.99$.

Above simulations and comparisons conclude that whether gas pressure variations in the material can be observed depends on the relationship between two intrinsic permeabilities: the case $K_l = K_g$ means non-constant gas pressure and the case $K_l \ll K_g$ corresponds to constant gas pressure.

2.4.2 Simplification of moisture transport models

A dimensionless time is introduced $\mathbf{t} = t/\mathbf{t}_D^l$. Thus, the time is scaled by the characteristic time of advection of liquid-water. The equation governing the transport of the gaseous mixture (see Eq. 2.17) can be rewritten in a dimensionless form:

$$\begin{aligned} \frac{\partial}{\partial \mathbf{t}}[\mathbf{P}_g(1-S)] + \Lambda \frac{\partial S}{\partial \mathbf{t}} &= \frac{\mathbf{t}_D^l}{2\mathbf{t}_D^g}\frac{\partial}{\partial \mathbf{x}}\left(k_{rg}(S)\frac{\partial \mathbf{P}_g^2}{\partial \mathbf{x}}\right) \\ &\quad + \Lambda \frac{\partial}{\partial \mathbf{x}}\left[k_{rl}(S)\left(\frac{P_{atm}}{\mathbb{M}}\frac{\partial \mathbf{P}_g}{\partial \mathbf{x}} - \frac{\mathrm{d}\pi_c}{\mathrm{d}S}\frac{\partial S}{\partial \mathbf{x}}\right)\right] \end{aligned} \tag{2.31}$$

In the case $K_l \ll K_g$, diffusion of vapour occurs much slower than advection of gas-phase. Keeping terms which have the same order of magnitude with regard to $\mathbf{t}_D^l/\mathbf{t}_D^g$, Eq. (2.31) for $\mathbf{t} \sim 1$ reduces to:

$$\frac{\partial}{\partial \mathbf{x}}\left(k_{rg}(S)\frac{\partial \mathbf{P}_g^2}{\partial \mathbf{x}}\right) = 0 \tag{2.32}$$

Owing to the symmetry condition in Eq. (2.1) and the boundary condition, the integration of Eq. (2.32) yields the simple equality $P_g \sim P_{atm}$. Taking benefit of this result, the first term on the right-hand side of Eq. (2.18) can be neglected. Noting that $\Lambda \gg 1$ results in $P_v \ll P_{atm} \ll \dfrac{\rho_l RT}{M_v}$, meaning that the moisture mass is mainly represented by liquid phase. Therefore, the mass balance equation of moisture (liquid and vapour, see Eq. (2.18) is written in the following simplified form:

$$\frac{\partial S}{\partial t} = \frac{\partial}{\partial x}\left[\left(D_l(S) + D_v(S)\right)\frac{\partial S}{\partial x}\right] \tag{2.33}$$

where

$$D_l(S) = -\frac{K_l}{\phi \eta_l} k_{rl}(S)\mathbb{M}\frac{\mathrm{d}\pi_c}{\mathrm{d}S} \tag{2.34}$$

$$D_v(S) = \frac{M_v}{\rho_l RT} D_0 \tau \alpha(S)(1-S)\frac{\mathrm{dP_v}}{\mathrm{d}S} \tag{2.35}$$

Actually, Eq. (2.33) is the same as the one that has been reported by Daïan [80] (see Eq. 1.18). The sum of D_v and D_l is the so-called apparent diffusivity D_a [11]. The ratio of D_v and D_l is

given based on Eqs. (2.34) and (2.35):

$$\frac{D_v}{D_l} = \left(\frac{M_v}{\rho_l RT}\right)^2 \eta_l D_0 P_{vs} RH(S) \frac{f(\phi, S)}{K_l k_{rl}(S)} \tag{2.36}$$

where $f(\phi, S)$ is the resistance factor of vapour diffusion.

$$f(\phi, S) = \phi\tau\alpha(S)(1 - S) \tag{2.37}$$

If adopting $T = 293$K, with $P_{vs} = 2333$ Pa, it gives that $\left(\frac{M_v}{\rho_l RT}\right)^2 \eta_l D_0 P_{vs} \approx 3 \times 10^{-21}$ m^2. Equation (2.36) is rewritten as:

$$\frac{D_v}{D_l} = \frac{3 \times 10^{-21}}{K_l} \frac{f(\phi, S)RH(S)}{k_{rl}(S)} \tag{2.38}$$

The ratio of D_v and D_l depends on the relationship between $\frac{3\times10^{-21}}{K_l}$ and $\frac{f(\phi,S)RH(S)}{k_{rl}(S)}$. The value 3×10^{-21} is in the same order of magnitude with K_l validated by using VGMa model [89, 90] to calculate the liquid relative permeability (see Table 2.3). If assuming $\frac{3\times10^{-21}}{K_l} \approx 1$ such as for Paste4, the ratio of D_v and D_l is largely dependent on the relationship between $f(\phi, S)RH(S)$ and $k_{rl}(S)$. Calculated curves for the relation between these two parameters are shown in Fig. 2.15 for Paste4 by using VGMa model to compute k_{rl}. Roughly speaking, point at $S \approx 0.42$ (RH ≈ 0.56) divides the mass transport into two parts. Below this point, the dominant transport is vapour diffusion (represented by $f(\phi, S)$RH), and above this point, it is liquid-transport transport (represented by $k_{rl}(S)$).

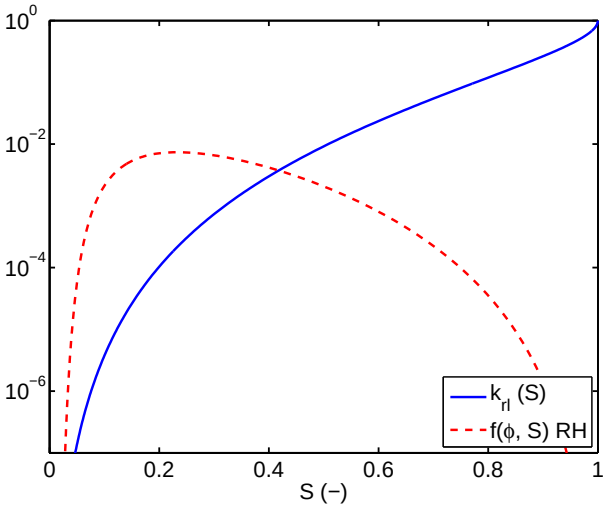

Figure 2.15: Relationships of $f(\phi, S)RH(S)$ *vs.* S and $k_{rl}(S)$ *vs.* S for Paste4.

For most natural conditions (such as in the range of RH $> 56\%$), the liquid-water movement is the main transport mode in unsaturated porous media like cementitious materials. Therefore, if ignoring the gas-phase transport, the moisture transport model is further simplified as a single diffusion equation only with liquid-water as it has been reported by Mainguy et al. [42] (see Eq. 1.17).

Table 2.5: The intrinsic permeabilities to liquid-water validated by experimental data for two versions of simplified models.

	Methods	Paste3	Paste4	Paste5	Concrete3
K_l ($\times 10^{-21}$m^2)	First simplified model (Eq. 1.17)	0.5 (0.33[a])	2.2	34	10
	Second simplified model (Eq. 2.33)	0.46 (0.3[a])	2.0	32	8

Equation (1.17) is another form of Richards equation able to describe moisture transport by the sole movement of liquid water. The liquid-water diffusivity D_l in Eq. (1.17) is a simplified version of Eq. (2.34). Thus, there are two versions of simplified models, Eq. (1.17) and Eq. (2.33). The intrinsic permeabilities inversely obtained by using drying kinetics for these two simplified models are provided in Table 2.5 for the case using Method-1 to calculate k_{rl} and k_{rg}. Compared to Table 2.4, those values are larger than that from the full multiphase model, which is because more mass transport is needed to balance neglected advection of the gas-phase in the first simplified model and the neglected vapour diffusion in the second simplified model.

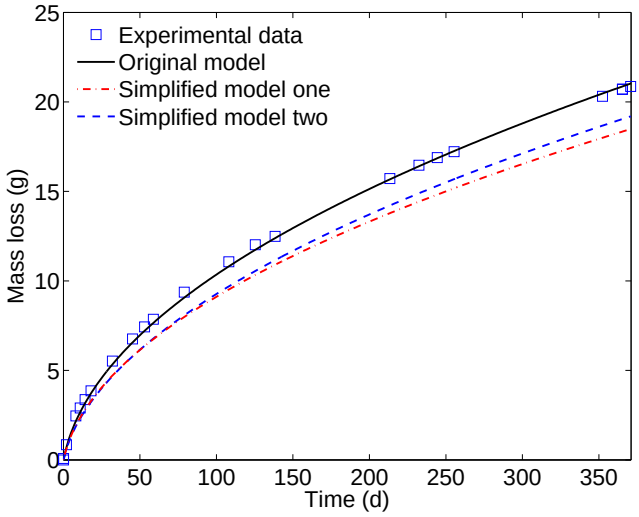

Figure 2.16: Mass loss curves calculated by three versions of models for Paste4, using the same $K_l = 1.7 \times 10^{-21}$ m^2 validated by the multiphase model (see Table 2.3). The external RH is 53.5%.

[a]Obtained by drying at RH = 63.2%.

Using the same K_l validated by the multiphase model (see Table 2.3), mass loss curves simulated by three versions of models for Paste4 are shown in Fig. 2.16. Actually, the differences between these three curves are not significant, which implies that if one only focuses on the mass transport, these three versions of models are applicable. But notice that the first simplified model is only suitable for the high RH range (e.g., RH> 56% for Paste4). For the low RH range, this version cannot provide a high enough apparent diffusivity as shown in experimental data [11] because the liquid permeability $K_l k_{rl}(S)$ is a monotonically increasing function with RH or S (see Eq. 2.34). Therefore, the second simplified model will be used in Chapter 5 for modelling of drying and wetting cycles.

2.5 Transport modes analysis

According to the above simulations and comparisons, drying of a porous material is mainly controlled by two transport modes: (1) Liquid-water is transported to the surface layer and then evaporates to the surrounding environment (see Fig. 2.17a); (2) Along with advection, liquid-water also evaporates within the material to water vapour, which diffuses through the porous network to the surrounding environment (see Fig. 2.17b).

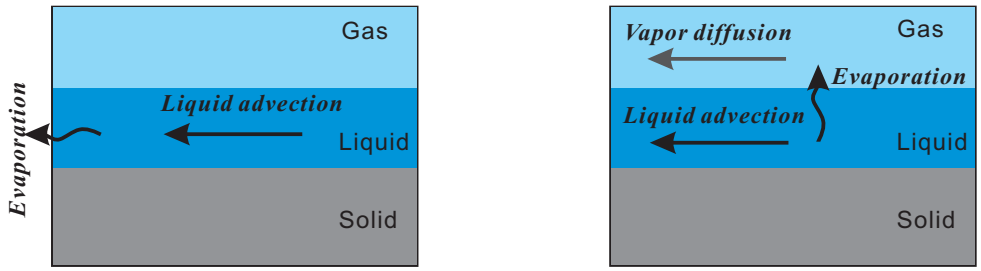

(a) Transport mode one. (b) Transport mode two.

Figure 2.17: Schematic representations of two moisture transport modes.

To identify the different moisture transport modes, one not only needs to quantify the contribution of each phase to the total mass transport within the material but also to know how much liquid-water or vapour can be transported to the surface layer.

This section will employ the multiphase model to investigate the different transport modes. Since the case using Method-1 to calculate k_{rl} and k_{rg} has been already studied in [42], only Method-2 is used here for the simulations (see Section 2.2.3).

2.5.1 Contribution of mass transport in the material

The contribution of liquid-water transport to the total mass transport in the material can be easily achieved by calculating the ratio of liquid flux J_l to the total flux $J_l + J_v + J_a$. By taking Paste4 as an example, the contribution of liquid-water transport is shown in Fig. 2.18 in cases $K_l = K_g$ and $K_l \ll K_g$.

In Fig. 2.18, the ratio remains near 1 for the inner part of the material, implying that the mass transport is mainly in its liquid form. But along with drying, the ratio near the boundary decreases; namely, contributions of vapour diffusion and advection of gas-phase increase with the decrease of S (see saturation profiles in Fig. 2.7). For the case $K_l \ll K_g$, the contribution of liquid-water transport drops more quickly compared to the case $K_l = K_g$ (see bold black curves at 371 days in Fig. 2.18). At the end of simulations, the contribution of liquid-water transport at the surface is around 0.5 in Fig. 2.18a, but it is only 0.2 in Fig. 2.18b. This may mean that the exchange rate from liquid to vapour ($\mathring{m}_{l\to v}$ in Eqs. (1.3) and (1.4)) is enhanced for the case $K_l \ll K_g$.

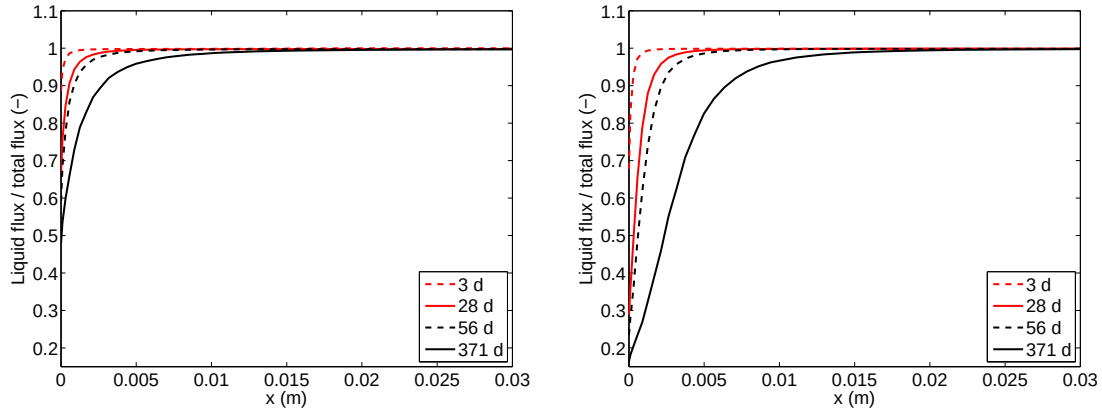

(a) The case $K_l = K_g$.

(b) The case $K_l < K_g$.

Figure 2.18: Ration of liquid-water flux to the total flux in the material during drying of Paste4 ($\mathrm{RH}_0 = 89\%$ and $\mathrm{RH}^e = 53.5\%$).

The simulation results show that the transport mode in the material is greatly related to the drying time and the current saturation. In the part with high saturation, advection of liquid-water is definitely predominant. However, at the boundary the contribution of liquid advection decreases with drying time due to strong interactions between liquid-water and gas phase. Hence, it should be more interesting to investigate the contribution of liquid advection by an integration at the boundary to identify the different transport modes.

2.5.2 Contribution of mass transport by an integration at the boundary

At the boundary, moisture is transported out the material through evaporation. In a same way with the calculation of mass loss curve, one can calculate the mass loss due to the movement of liquid-water (time integration of liquid flux J_l at the boundary) to the total mass loss (time integration of fluxes of liquid, vapour and dry air $J_l + J_v + J_a$) at the boundary during drying.

$$\frac{Q_l}{Q_t} = \frac{\int_0^t J_l \, \mathrm{d}t}{\int_0^t (J_l + J_v + J_a) \, \mathrm{d}t} \tag{2.39}$$

Simulation results for drying of Paste4 are shown in Fig. 2.19, which include both cases: $K_l = K_g$ and $K_l \ll K_g$. The initial and boundary conditions used here are the same as experiments (see Section 2.2.2 and Table 2.1).

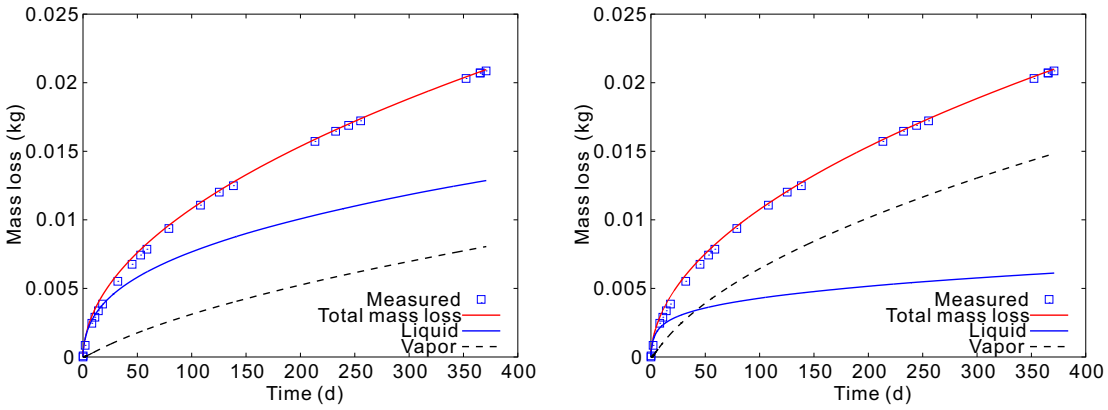

(a) The case $K_l = K_g$.

(b) The case $K_l \ll K_g$.

Figure 2.19: Simulation results of mass loss curves, including total, liquid-water and vapour, during drying of Paste4 ($\mathrm{RH}_0 = 89\%$ and $\mathrm{RH}^e = 53.5\%$).

Figures 2.19a and 2.19b clearly show that at the beginning of drying (only several days) the mass loss related to liquid-water movement plays the major role, while the contribution of water vapour increases gradually. This is because the liquid-water is released from the pore network during drying, and more space is available for the transport of water vapour. At the end of simulation, the contribution of liquid-water movement in Figs. 2.19a and 2.19b should correspond to the ratios of the bold black curves at the boundary in Figs. 2.18a and Fig. 2.18b.

The differences between two cases $K_l = K_g$ and $K_l \ll K_g$ are obvious in Fig. 2.19. In the former case, advection of liquid-water is always predominant in the total mass loss during

the drying period (transport mode (1)), while in the latter case the vapour transport increases rapidly and plays a dominant role in the long term of drying (transport mode (2)).

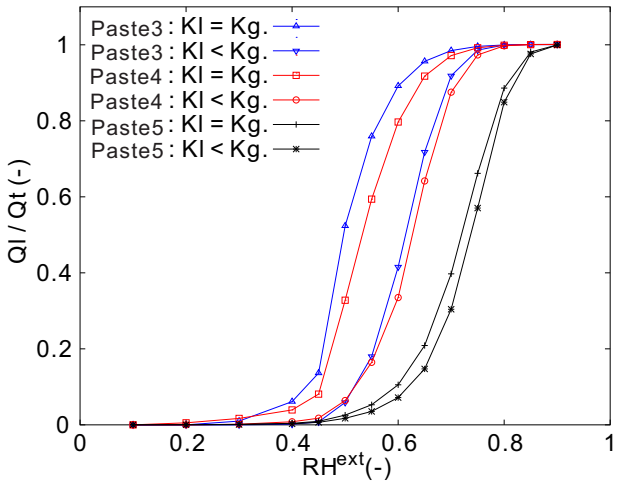

Figure 2.20: Comparison of the contribution of liquid-water transport to total mass loss during drying of Paste3, Paste4 and Paste5 for initial RH_0= 90% and varying external relative humidity.

Moreover, simulations for the contribution of liquid-water transport to the total mass transport are also carried out for cement pastes Paste3, Paste4 and Paste5 for an initial RH_0 = 90% and varying external RH values from 10% to 90% to investigate the influence of these variables. Numerical results are illustrated in Fig. 2.20. The duration of simulations used here is 371 days, the same as experiments (see Table 2.1). It is clear that the liquid-water contribution is dependent on both the external RH and types of materials. In this figure, the following points can be observed:

a) In the low external RH range, the water vapour transport is prominent to the total mass loss (transport mode (2), see Fig. 2.17b), while in the high external RH range, it is liquid-water transport (transport mode (1), see Fig. 2.17a). A larger difference between external and initial RH means a larger gradient of vapour pressure between the material and the surrounding environment, which can accelerate the movement of water vapour to the surface. The exchange rate of liquid-water to water vapour is also promoted due to the absence of vapour.

b) Paste5 always has the smallest contribution of liquid-water transport (the largest contribution of water vapour transport) in the whole range of external RH, then Paste4 and the last one is Paste3. It is expected to link this result with the microstructure (porosity) of the material. For the material with the largest porosity (such as Paste5), water vapour

can diffuse easier compared to the material with low porosity (such as Paste3 or Paste4). For a given external RH, Paste5 always has the lowest S at the boundary (see sorption curves in Fig. 2.2). It indicates that the volume of water vapour $\phi(1-S)$ for Paste5 is larger than Paste3 and Paste4. Hence, more water vapour can be transported to leave the material for Paste5 than for the other two cement pastes.

c) The third aspect from Fig. 2.20 is the differences between the two cases $K_l = K_g$ and $K_l \ll K_g$. The case $K_l = K_g$ provides a larger contribution of liquid-water transport compared to the case $K_l \ll K_g$ in the whole range of external RH. This can be also seen in Fig. 2.19. These differences are much clearer in the moderate range of external RH between 40% and 80%. One possible reason is that the gas overpressure (in the case $K_l = K_g$) in the border layer of the material can reduce the evaporation of liquid-water, which forces the mass transport mainly in its liquid form. By contrast, vapour transport should be a little more significant in the case $K_l \ll K_g$.

Through the above analysis, it can be concluded that transport modes (1) and (2) occur simultaneously in most situations. The fact that which transport mode is predominant is dependent on the boundary condition (external RH), material properties (e.g., porosity and PSD), the initial condition and the duration of drying.

2.6 Conclusion

In this chapter, a multiphase moisture transport model for isothermal conditions was recalled, which considers that the mass transport consists of advection of liquid-water, advection of gas-phase (vapour + dry air) and diffusion of gas-phase. Since the intrinsic permeabilities to liquid-water K_l and gas-phase K_g are only two undetermined parameters in this model, two relationships were introduced: $K_l = K_g = K_0$ and $K_l \ll K_g$. The first case naturally comes from the theoretical analysis. The second case is given based on the fact that measured value of K_g is much larger than the value of indirectly-determined K_l by inverse analysis of drying kinetics. For both cases, the simulation results for four cementitious materials (three cement pastes and one concrete) showed that they provided good agreements with measured mass loss curves. Verifications of modelling results were conducted through comparing simulated saturation profiles with measured ones. Comparisons revealed that the predicted profiles match the measured curves

quite well. Hence, this multiphase transport model has a high applicability in case of cementitious materials.

During experimental verifications, two methods to calculate relative permeabilities of liquid-water and gas-phase were also compared. Both methods can provide acceptable simulation results compared with experimental data. The only difference was found in the values of K_l validated by these two methods. Method-1 based on Mualem model-a [89] provided K_l values slightly lower than other indirect methods such as the Katz-Thompson model or the beam bending method, while values from Method-2 based on Mualem model-b [128] are higher. Method-1 seems easier to be implemented because equations in this method are analytical.

Quite permeable and weakly permeable porous materials were defined according to an asymptotic analysis. For cementitious materials, the case $K_l = K_g$ implies that materials are considered as weakly permeable, while materials are considered as quite permeable when $K_l \ll K_g$. Gas pressure variations, including overpressure and underpressure, were observed for weakly permeable materials. But for quite permeable materials, gas pressure in the material is always constant (equal to the atmospheric pressure), which is because gas pressure variations can dissipate very quick due to the significant gas-phase advection.

For the case $K_l \ll K_g$, a simplified model was obtained, including advection of liquid-water and vapour diffusion. Further simplification was achieved if ignoring vapour diffusion, so moisture transport is only in its liquid form. Even though the latter version was verified by experimental data, it is not recommended because advection of liquid-water is only predominant in the high water content range. In the low RH range, liquid-water is disconnected and vapour diffusion should be more significant.

Different transport modes were identified for moisture transport both at the boundary and in the material. At the beginning of drying, due to the high initial saturation, advection of liquid-water is more significant. Thus, during drying, liquid-water near the surface layer loses quickly and the vapour transport gradually becomes the main transport mode. In a word, the transport mode highly depends on saturation. In the high water content range, advection of liquid-water is predominant, while in the low water content range, the vapour transport plays a main role. But for most cases, two transport modes always occur simultaneously.

Chapter 3

Review of hysteresis models

Summary

Hysteresis of water vapour soption isotherms (WVSIs) has been widely recognized as one of main factors which can significantly affect moisture transport within building material in the natural environmental conditions. In experiments, only a limited number of WVSI loops can be measured. Nevertheless, in natural conditions, concrete structures undergo arbitrary drying and wetting cycles. Thus, using relevant models to predict these curves for cementitious materials is necessary for modelling of moisture transport.

A detailed review of hysteresis models, including for the fitting of main sorption isotherms and the prediction of scanning loops, has been carried out in the study [144], which has been published in Cement and Concrete Research journal. The main content of the current chapter has been included in this paper. Comparison results conclude a best set of equations to calculate hysteresis for cementitious materials. By the verification of experimental data, it shows that for the prediction of the first scanning isotherms, hysteresis models (either physical or empirical) do not have significant different. But a non-physical behaviour, called "pumping effect" produced by empirical models is problematic and needs more studies to fully understand its effect on moisture transport.

3.1 Introduction

For the modelling of moisture transport in cementitious materials, such as the continuum model proposed in [77], WVSIs, representing the relationship between relative humidity RH (or capillary

pressure P_c) and water content θ (or degree of saturation S), are used to describe the equilibrium between liquid-water and vapour. A group of typical WVSIs are illustrated in Fig. 3.1, which contains two main isotherms (adsorption AB and desorption BA) and several scanning curves (the first and secondary wetting scanning curves CB and EB, and the first scanning curve in drying DE).

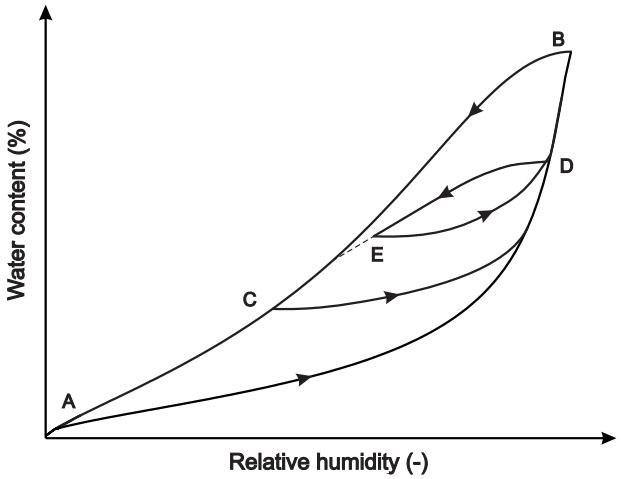

Figure 3.1: Schematic representation of WVSIs. The main desorption curve (BA), the main adsorption curve (AB), the first scanning curve in drying (DE), the first scanning curve in wetting (CB) and the second scanning curve in wetting (EB) are illustrated.

A main characteristic of WVSIs is their hysteretic behaviour, referring to the different water content at the same RH value (see the differences between two main curves in Fig. 3.1, as well as Fig. 1.2b in Chapter 1). For cementitious materials, the characteristics of the hysteretic behaviour might be different to soils or sands because cementitious materials contain a wider range of magnitude of pore sizes (from gel pores nm to capillary pores μm) [111]. Experiments showed that in the low RH range ($\leq 33\%$, according to [23]), hysteresis between the desorption and adsorption isotherms is much smaller than in the high RH range. This results from the nanostructure of C-S-H [29] which is not found in soils and sands.

Although different types of materials have different pore systems, it is of interest to test whether hysteresis models from soil science are also applicable to cementitious materials, as there are few studies on the hysteresis behaviour of such materials. Carlier et al. [145] evaluated several different closed-forms of analytical expressions used in soil science for the main desorption curve. The authors concluded that all models were able to correctly represent the desorption isotherms for mortars and concretes. Recently, Johannesson et al. [14] and Derluyn et al. [16] have used hysteresis models to investigate hysteretic effects on moisture behaviour in cementitious

materials. Hence, more work is needed to investigate methods which are able to predict sorption isotherms and their hysteresis for cementitious materials.

3.2 History of development of hysteresis models

The first documented description of the relation $P_c - \theta$ in porous media was provided by Haines [45]. Since then, the hysteretic behaviour of this relation was widely recognized and several models had been developed in the purpose of prediction of this behaviour. Those models can roughly be classified into two groups: conceptual and empirical models [146, 147].

The conceptual models are mainly developed based on the "independent" or "dependent" domain theories, which usually employ "distribution diagrams" to demonstrate the theory. They assume that a domain is made up of groups of pores in a porous medium. Poulovassilis was one of the first to adopt the independent domain model from magnetism science to the research of water transport in porous media [148]. This theory, including Preisach space and Néel's diagram, was developed and improved by Preisach [50], Néel [149], Everett [48, 49], *etc.* However, it was reported that those models showed discrepancies with experimental data [150, 151, 152]. Hence, researchers tried to modify and develop new models for porous materials. Based on the "similarity hypothesis" proposed by Philip [153], Mualem [52, 53] introduced the simplified independent domain models. The basic idea of Mualem's independent models is that no interactions between pores in the domain are considered. In other words, each pore is independent of its neighbours. So, the drying or wetting of the pore system is only determined by the pore geometry itself, in which the pore necks and pore bodies are used to characterise the pore geometry. Two normalized variables, $\bar{r}$ and $\bar{\rho}$ varying from 0 to 1, are used to represent the normalized radii of pore necks and pore bodies, respectively. When $\bar{r}$ (or $\bar{\rho}$) $= 1$, it corresponds to the minimum capillary pressure ${P_c}^{\min}$ and $\bar{r}$ (or $\bar{\rho}$) is 0 when $P_c = {P_c}^{\max}$. At a given capillary pressure, θ can be obtained by integrating the pore water distribution function $f(\bar{r}, \bar{\rho})$. In independent domain models, $f(\bar{r}, \bar{\rho})$ is formulated by the contribution of two independent pore water distribution functions $h(\bar{r})$ and $l(\bar{\rho})$, which describe the radii of pore necks and pore bodies, respectively.

$$\theta = \int\int f(\bar{r}, \bar{\rho}) \mathrm{d}\bar{r}\mathrm{d}\bar{\rho} = \int l(\bar{\rho})\mathrm{d}\bar{\rho} \int h(\bar{r})\mathrm{d}\bar{r} \tag{3.1}$$

A rectangle diagram was proposed by Mualem (see Fig. 3.2) [53] to depict how the independent domain model works. The horizontal axis represents the water distribution function $h(\bar{r})$

and the vertical axis represents the function $l(\bar{\rho})$. At equilibrium, capillary pressure throughout the pore network is constant [154], either for pore necks or in pore bodies. So, $h(\bar{r})$ and $l(\bar{\rho})$ always change at the same capillary pressure, which is illustrated as the diagonal line in Mualem's diagram (see Fig. 3.2). Hence, the diagram is able to describe the total water distribution ($f(\bar{r},\bar{\rho})$) through the product of $h(\bar{r})$ and $l(\bar{\rho})$. The water content at P_c during the wetting process is obtained by integrating the water distribution function from the smallest pore size (at ${P_c}^{\max}$) to current pore size (at P_c):

$$\theta_w(P_c) = \int_0^{\bar{\rho}(P_c)} l(\bar{\rho})\mathrm{d}\bar{\rho} \int_0^1 h(\bar{r})\mathrm{d}\bar{r} \tag{3.2}$$

To formulate water content clearly and to avoid using integral forms, two cumulative pore water distribution functions were introduced instead of the integral forms for each axis [52].

$$L(P_c) = \int_0^{\bar{\rho}(P_c)} l(\bar{\rho})\mathrm{d}\bar{\rho} \qquad H(P_c) = \int_0^{\bar{r}(P_c)} h(\bar{r})\mathrm{d}\bar{r} \tag{3.3}$$

According to Mualem's diagram, $L({P_c}^{\max}) = 0$, $L({P_c}^{\min}) = \theta^{\max}$ (maximum water content), and $H({P_c}^{\max}) = 0$, $H({P_c}^{\min}) = \theta^{\max}$. Hence, Eq. (3.2) can be rewritten as:

$$\theta_w(P_c) = \theta^{\max} L(P_c) \tag{3.4}$$

The expression of water content during the drying process is obtained in a similar manner by an integration of Mualem's diagram.

$$\begin{aligned} \theta_d(P_c) &= \int_0^{\bar{\rho}(P_c)} l(\bar{\rho})\mathrm{d}\bar{\rho} \int_0^1 h(\bar{r})\mathrm{d}\bar{r} + \int_{\bar{\rho}(P_c)}^1 l(\bar{\rho})\mathrm{d}\bar{\rho} \int_0^{\bar{r}(P_c)} h(\bar{r})\mathrm{d}\bar{r} \\ &= \theta_w(P_c) + [\theta^{\max} - \theta_w(P_c)]\, H(P_c) \end{aligned} \tag{3.5}$$

From Eq. (3.5), the expression of H is given as follows:

$$H(P_c) = \frac{\theta_d(P_c) - \theta_w(P_c)}{\theta^{\max} - \theta_w(P_c)} \tag{3.6}$$

If both main isotherms are known ($\theta_d(P_c)$ and $\theta_w(P_c)$), functions H and L can be determined easily by using Eqs. (3.4) and (3.6). Then, they are used to calculate scanning loops.

The assumption of "independent" domain means that the pore systems are fully-dried or

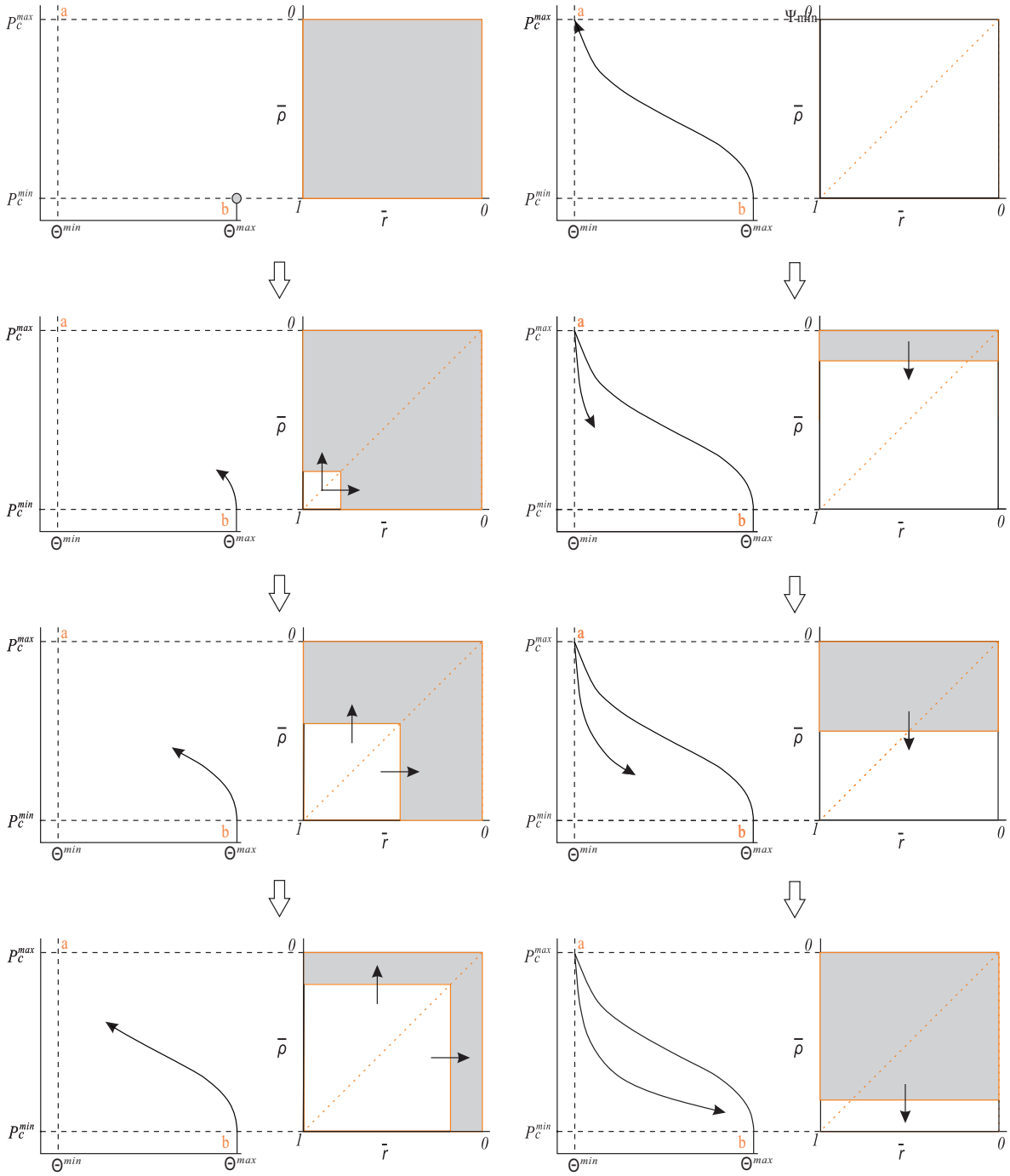

(a) The main desorption process

(b) The main adsorption process

Figure 3.2: Schematic representation of Mualem's diagram [53] for the main desorption and adsorption processes. The gray domain represents completely-filled pores and the blank domain stands for fully-dried pores.

fully-wet along with the changes of pressure. Following the research of Topp [151], Mualem and Dagan [54] adjusted the water distribution function (see Eq. 3.1) by adding two weighting

functions ($p_d \leq 1$ and $p_w \leq 1$).

$$\theta = \int \int p_d(\bar{r}, \bar{\rho}, \theta) p_w(\bar{r}, \bar{\rho}, \theta) f(\bar{r}, \bar{\rho}) \mathrm{d}\bar{r} \mathrm{d}\bar{\rho} \tag{3.7}$$

where p_d represents the volumetric ratio of the actually dried pores to pores supposed to be dried in the independent domain theory. Similarly, p_w is the ratio for the wetting process. Introducing these two weighting functions implies that interactions between pores and their neighbours are considered. This is the basic idea of the "dependent" domain models.

Through a comparison with experimental data, Mualem and Dagan [54] found that p_d played the major role during both drying and wetting processes, while the effect of p_w could be neglected ($p_w = 1$). Obviously, p_d is the key factor for Mualem's dependent models. Various methods attempting to determine p_d have been reported in the literature [155, 55, 156].

Empirical models, which have been applied to the modelling of moisture transport in building materials (e.g., [14]), are developed based on fitting the shapes of experimental WVSIs. Normally, an empirical was proposed without physical meanings. In the literature, there are a number of empirical models, such as linear models (e.g., [56]), slope models (e.g., [57]) and scaling-down models (e.g., [58]). Initially, they were developed for one type of porous medium (such as soils and sands) and not based on the physical representation of hysteresis. This thesis has chosen recently developed and easy-to-apply empirical models which can provide reasonable fitting results for experimental curves of cementitious materials. Such models usually have one or two parameters which need to be determined from experimental data. For example, Li [59] proposed an incremental relation to calculate hysteresis, with one parameter controlling the shape of the curve. In the methods introduced by Wei et al. [61] and Nyman et al. [60], parameters are used to initialise the slope of the scanning curves.

3.3 Adopted comparison strategy

A strategy of comparison of models for WVSIs and hysteresis to experimental data has to be introduced. Statistical analysis tools will be presented in the following sections.

3.3.1 Procedure of comparisons

According to the availability of experimental data, the normal procedure for the calculation of hysteresis is like as follows:

- If experimental data for both main adsorption and desorption branches are measured, a model is needed to fit them, and then another model can be used to predict scanning curves;
- If only one main branch is measured, the other one has to be determined by means of a model, and then scanning curves can be predicted by another model.

Based on above procedure, a multi-level approach to model hysteresis is proposed in Table 3.1. It depends on the amount of available experimental data. This approach may lead to different levels of prediction accuracy, which will be revealed through comparisons in next sections.

Table 3.1: Proposed multi-level approach to model hysteresis.

Levels	Available experimental data	Description
Level 1	Both main branches and one scanning curve for each drying and wetting process	One scanning curve is used to determine parameters.
Level 2	Both main branches	Predicting scanning loops without additional parameters
Level 3	One main branch	Determining the other main branch and then predicting scanning loops

Table 3.1 indicates that a complete set of hysteresis models consists of three parts: ① models to fit two main sorption isotherms; ② models to determine one main sorption isotherm on the basis of the other measured main branch; ③ models to predict scanning loops. In next sections, hysteresis models will be compared following these three stages.

3.3.2 Experimental data collection

In order to test the performance of hysteresis models, measured WVSIs were collected from the literature. The requirements for data collection are:

- The collected data contain at least both main desorption and main adsorption isotherms. It is better if some scanning curves have been measured.
- The number of measurement data for each isotherm must be larger than the number of undetermined parameters in models.

WVSIs can be measured by different methods. The saturated salt solution method is a common gravimetric one in which RH is controlled by the saturated salt solution in a small volume, such as in a desiccator. The mass of a specimen decreases (during desorption) or

increases (during adsorption) until equilibrium (mass stabilization) is reached. Other methods, such as dynamic vapour sorption (DVS) [157, 12], use a small specimen, usually less than 1 g, and a microbalance to monitor mass changes. The advantage of this kind of instrument is that the entire desorption and adsorption loop can be measured in one month or less, more rapidly than with the saturated salt solution method, for which a method can take many months and even years. However, a potential problem with small specimens is that they cannot contain aggregates. Measurements probably only quantify the sorption behaviour for the paste in concrete or mortar, rather than the global sorption behaviour of the material. For instance, the influence of paste-aggregate interfacial transition zone (ITZ) on the sorption is not investigated in this method. This may lead to different measurement results. The crushed materials can also increase the surface area, which let more water molecules can adsorb on the material surface. Another risk is that small specimens can be carbonated quickly during the preparation.

Table 3.2: Collected datasets of WVSIs measured by the saturated salt solution method [23].

No.	Name	Materials	Binders	w/c (w/b)
1	Concrete1	Concrete	CEM I-52.5 [a]	0.45
2	Concrete2	Concrete	CEM I-52.5+10%SF [b]	0.27 (0.24)
3	Concrete3	Concrete	CEM I-52.5	0.43
4	Paste1	Cement paste	CEM I-52.5 [a]	0.45
5	Paste2	Cement paste	CEM I-52.5+10%SF	0.20 (0.18)
6	Paste3	Cement paste	CEM I-52.5	0.35
7	Paste4	Cement paste	CEM I-52.5	0.45
8	Paste5	Cement paste	CEM I-52.5	0.60

The studied experimental data are gathered in Table 3.2 from [23] measured by the saturated salt solution method. These data can meet the above-mentioned comparison requirements very well. All materials are made from the same OPC cement (CEM I-52.5, according to EN 197-1 European standard). They include ordinary and high performance hardened cement pastes and concretes. Water-to-cement ratios range from 0.2 to 0.6. High performance materials are Concrete2 and Paste2, which contain 10% of silica fume to cement in weight. In order to reach chemical stability before the measurements, materials were sealed-cured for at least 6 months for concretes and 2 years for cement pastes. Then, cement pastes were crushed into small specimens with mass of about 8 g. Because the content of aggregates has a small influence on the measured sorption curves [23], concrete specimens were cut into thin slices, 2 or 3 mm

[a] The same cement is used for Concrete1 and Paste1, but it is from different supplier to other materials.
[b] Silica fume.

thickness with mass between 20 and 100 g. This size still can keep small sands and partial ITZ effects. Measurements started from desorption at RH = 100%, decreasing step-by-step to RH = 3%, which is considered as the dry reference state. Then, RH increased stepwise to 100% to obtain the adsorption isotherm. To reduce the variations of RH during the measurements as well as the carbonation risk, only a small hole on the top of the desiccator is open for weighing. Besides, the equilibrium state for each RH step was carefully defined as that the mass change is less than 0.001 g after one month. At least three specimens were measured individually to determine one point on the sorption curve for each material.

3.3.3 Comparison criteria

For the fitting of the main sorption isotherms, all parameters in the models are optimized to fit the experimental curves using a nonlinear least squared optimization procedure, which aims to minimize the sum of the squares of the errors.

Two kinds of statistical criteria have been used to evaluate the accuracy of the modelling results in the literature, the coefficient of determination (R^2) and a differential residual-based error metrics (see [146, 145]). R^2 is defined as the ratio between the dispersion predicted by the model and the total dispersion of the measured data [146].

The accuracy of fitting (or prediction) is related to the number of parameters used in a model. More parameters usually yields a higher R^2 value, but low robustness and low sensitivity to parameters. To take into account the effect of the number of parameters, this study employs an adjusted R^2 [145]:

$$R^2_{adj} = \frac{(n-1)R^2 - (m-1)}{n-m} \tag{3.8}$$

where m is the number of parameters, n is the number of measured data. Equation (3.8) implies that $R^2_{adj} < R^2$ when $m > 1$, $R^2_{adj} = R^2$ when $m = 1$ and $R^2_{adj} > R^2$ when $m = 0$. The latter case shows the advantage of using a model without undetermined parameter.
The other statistical criterion is known as the normalized mean error (NME):

$$\text{NME} = \frac{1}{n}\sum_{i=1}^{n}\frac{|S_i^{pr} - S_i^{ms}|}{S_i^{ms}} \tag{3.9}$$

where S_i^{ms} and S_i^{pr} are measured and fitted (or predicted) values, respectively. Notice that the absolute value is used in Eq. (3.9). It can avoid the cancellation of positive and negative

residuals. If the value of NME is close to 0, it indicates a better result.

3.4 Comparisons of main isotherms fitting models

Numerous models have been proposed to fit the main branches of WVSIs. Each of these equations is applicable to one or several groups of materials (e.g., sands and soils). Models were selected in this research primarily based on whether they can fit both desorption and adsorption isotherms for cementitious materials.

On the whole, two types of methods to fit WVSIs can achieve our purpose. They are uni-modal and multi-modal models. As the name suggests, uni-modal models assume that the material consists of one pore system. Thus, a simple single equation can satisfactorily fit experimental data. In the research of Carlier et al [145], the Kosugi model (K) [158] seems to be the better one for the fitting of the main desorption isotherm. Besides, the van Genuchten's model [90], including two-parameter (VG2) and three-parameter (VG3) versions, will be compared. The former version has been used in studies on concretes [42, 159]. Two more models, (Feng and Fredlund's model (FF) [160] and Fredlund and Xing's model (FX) [161]) performing well in soil science, will be validated for cementitious materials. Multi-modal models consider that there are two or even more pore systems in the material [162]. This consideration can improve the fitting accuracy. A brief description of each selected model will be presented below.

3.4.1 Feng and Fredlund's model (FF)

The FF model is an empirical relationship which was used to fit desorption and adsorption curves of a ceramic material [160]. A simple equation is used in this model.

$$S = \frac{a_F}{a_F + {P_c}^{b_F}} \tag{3.10}$$

Two parameters (a_F (Pa) and b_F) in Eq. (3.10) need to be determined. The research performed in [163] showed that this curve-fitting equation is most applicable for low swelling materials (e.g., clay loam).

3.4.2 Van Genuchten's model

The equation proposed by van Genuchten [90] has been given in Chapter 2 (see Eq. 2.4). Both three-parameter (VG3) and two-parameter (VG2) versions are compared in this chapter.

3.4.3 Fredlund and Xing's model (FX)

When Fredlund and Xing [161] studied the pore size distribution on the basis of the VG2 model, they found that this model was not suitable in the high capillary pressure region. The authors introduced a modified pore size distribution function. Integration of this function yielded a new equation:

$$S = \left[\ln\left[e + \left(\frac{P_c}{a_X}\right)^{n_X}\right]\right]^{-m_X} \tag{3.11}$$

where e is the Euler number (a mathematical constant).

3.4.4 Kosugi's model

Using a lognormal pore size distribution, Kosugi [158] deduced the following expression:

$$S = Q\left({\sigma_p}^{-1} \ln \frac{P_c}{P_{cm}}\right) \tag{3.12}$$

where P_{cm} (Pa) is capillary pressure related to the medium pore radius. σ_p is the standard deviation of log-transformed pore radii which is related to the width of the pore size distribution. If the pore size distribution is unknown, P_{cm} and σ have to be obtained by fitting experimental sorption isotherms. In Eq. (3.12), Q denotes the complementary normal distribution function, which is defined as:

$$Q(x) = (2\pi)^{-1/2} \int_x^\infty \exp\left(-\frac{x^2}{2}\right) \mathrm{d}x \tag{3.13}$$

3.4.5 Multi-modal model

The generalized form of multi-modal models is written as:

$$S = \sum_{i=1}^{N} w_i S_i(P_c) \tag{3.14}$$

where N is the number of pore systems and $w_i \in [0,1]$ ($\sum_i^N w_i = 1$) is a weighting factor characterizing the pore system i and w_i represents the water content contribution of the pore

system i to the total water content in the material. If $N = 2$, Eq. (3.14) becomes a bi-modal model. One well-known bi-modal model was proposed by Durner [162], adopting VG2 equation for each pore system.

3.4.6 Comparison results and discussion

All materials in the collected database have been fitted by above models. Two statistical criteria R^2_{adj} and NME for the fitting of the two main sorption isotherms are provided in Figs. 3.3 and 3.4. Results for two materials (Paste2 and Paste3, representing a high performance and an ordinary materials) are illustrated in Figs. 3.6 and 3.5. Overall, all models provide satisfactory fitting results (mean $R^2_{adj} > 0.98$). The bi-modal model [162] shows better fitting results than uni-modal models. For all models, the fitting of the adsorption isotherm is better than the fitting of the desorption isotherm.

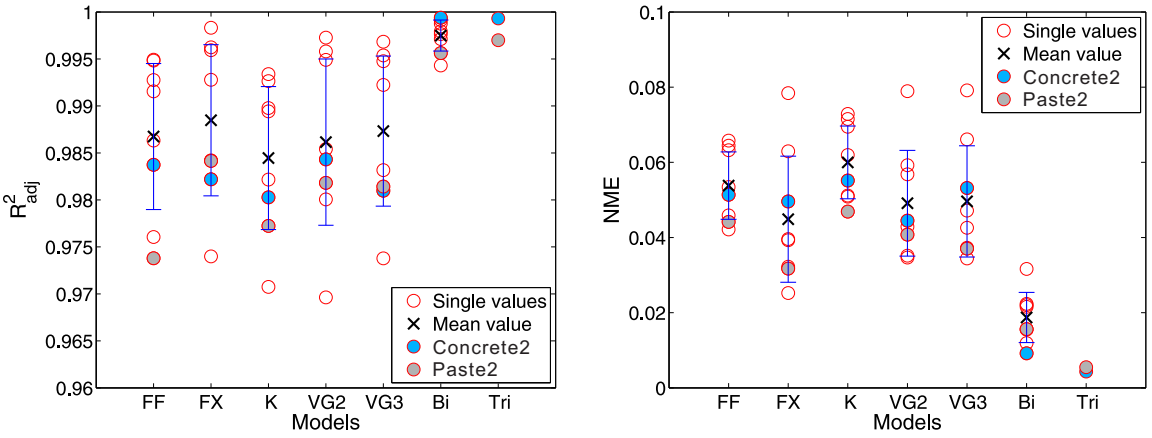

Figure 3.3: Comparison of R^2_{adj} and NME for desorption isotherms. Each circle (○) in the figure stands for one material (see Table 3.2). Concrete2 and Paste2 are highlighted. The error bars represent the standard deviation for each studied statistical criteria (R^2_{adj} and NME) and each model.

Concerning uni-modal models, they show a non-physical behaviour since the adsorption curves intersect the desorption curves at the low RH (around 0.05 in two examples, see the enlarged figures in Figs. 3.5 and 3.6 for Paste2 and Paste3, respectively). This phenomenon is not consistent with experimental data. But for the FX and VG3 models, this behaviour is not as significant as for the other two-parameter models (see the enlarged figures in Fig. 3.6). Both these models show better fitting results than other uni-modal models (see values of R^2_{adj} and NME in Figs. 3.3 and 3.4), either in desorption or in adsorption isotherms. This suggests that

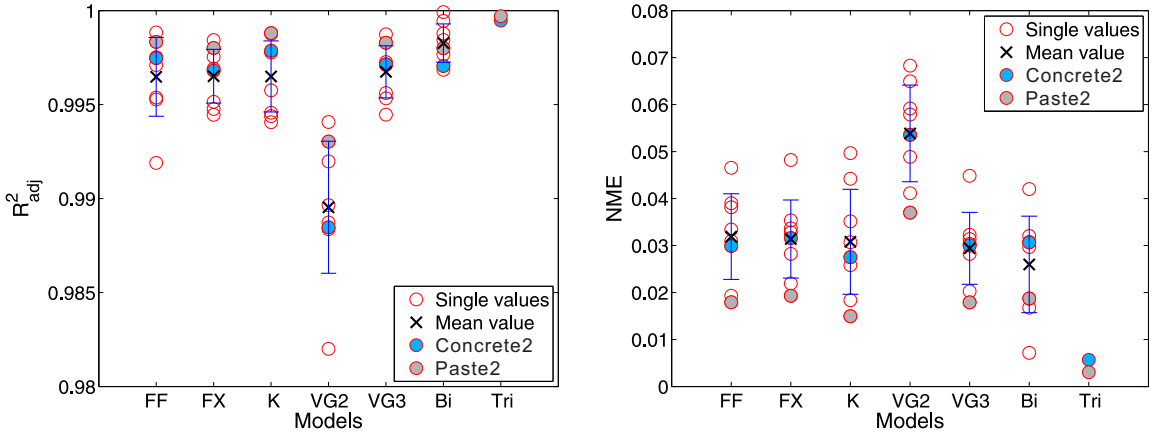

Figure 3.4: Comparison of R^2_{adj} and NME for the main adsorption isotherms. Each circle (○) in the figure stands for one material (see Table 3.2). Concrete2 and Paste2 are highlighted. The error bars represent the standard deviation for each studied statistical criteria (R^2_{adj} and NME) and each model.

these three-parameter models can be used for a variety of cementitious materials. Moreover, one can remark that the widely-used VG2 model [90] does not perform better than other models (see Figs. 3.3 and 3.4). Results also show that no selected model can simulate the sudden drop of the desorption isotherms from 44% to 33% RH (see Fig. 3.6). This drop may be because there is a threshold pore size (between RH = 44% to 33%) for capillary pores and gel pores. When measured water content changes from capillary pores to C-S-H pores as emphasised in reference [23], the drop on measured sorption curves can be seen.

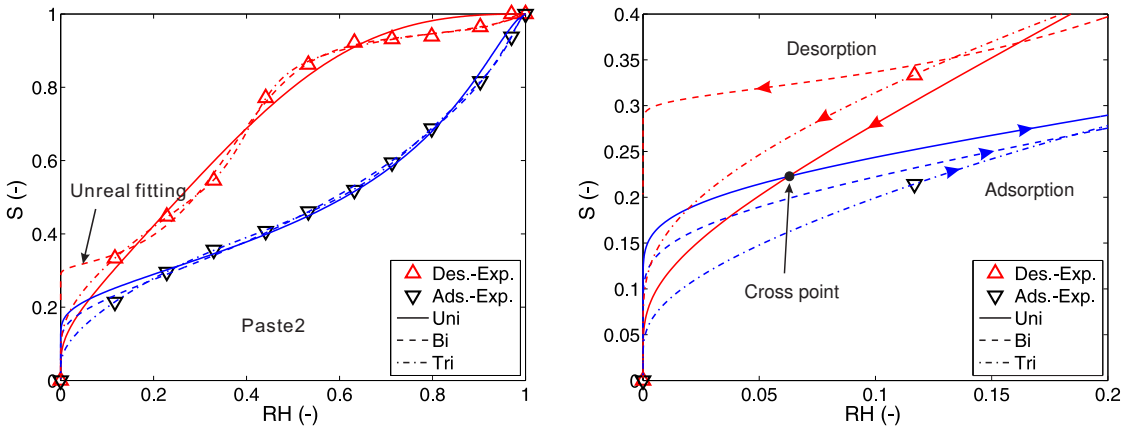

(a) Paste2 material.

(b) Enlarged figure for Paste2.

Figure 3.5: Fitting results for Paste2 material to compare results of uni-(VG2), bi- and tri-modal models. Fitting results for low RH values are shown in the enlarged figure.

Mean values of R^2_{adj} for the bi-modal model are higher than 0.99 for both desorption and

adsorption isotherms and values of NME are close to 0. For Paste3, the bi-modal model roughly shows the same shape as the ones described with other models (see Fig. 3.6a). For Paste2, this model performs much better in higher RH range, while the predicted desorption isotherm does not reach $S = 0$ at RH $= 0$. This is clearly an non-physical fitting result (see Fig. 3.5a). The result is likely caused by the very fine microstructure of the high performance cement pastes (e.g., Paste2) and concretes (e.g., Concrete2). Because those materials can hold much water in the low RH range, the measured points in the low RH range are higher compared to the ordinary materials, such as the point at RH $= 12\%$ in Fig. 3.5. This leads the non-physical fitting. Thus, it is worth fitting WVSIs by using higher modal models.

A comparison of uni-, bi- and tri-modal models is made in Fig. 3.5. The performance of the tri-modal model, nearly passing through all measured points, is obviously better than the uni- and the bi-modal models for both main isotherms in the low RH range. In terms of statistical analysis, using a tri-modal model improves the fitting results greatly (see highlighted values of R^2_{adj} and NME for Concrete2 and Paste2 in Figs. 3.3 and 3.4). In the high RH range, the tri-modal model yields a similar shape of curve as the bi-modal model.

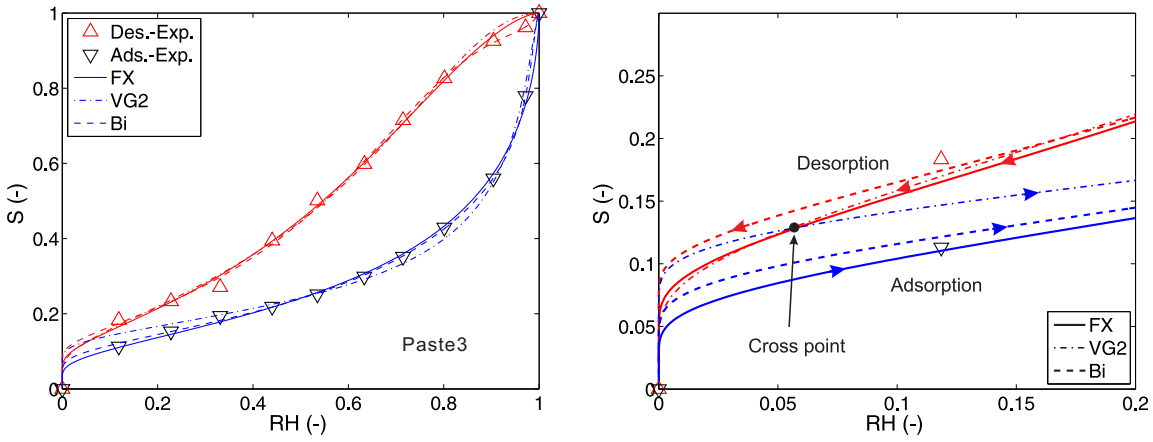

(a) Paste3 material.

(b) Enlarged figure for Paste3.

Figure 3.6: Main curves fitting results for Paste3 material. To make the display clearly, only three models, VG2, FX and bi-modal models, are chosen to represent uni- and multi-modal models. Fitting results for low RH values are shown in the enlarged figure.

However, the number of parameters in multi-modal models may be several times higher than in uni-modal models. This results in a more difficult fitting procedure and can even lead to instability. However, uni-modal models show acceptable fitting results for the selected database, except for high performance materials. The choice of WVSI model is thus highly dependent on

the complexity of the measured isotherm.

Above, some commonly-used WVSIs models have been compared to measured isotherms. In many cases, these models do not have a clear physical meaning. The models proposed by Fredlund and Xing [161], van Genuchten [90] and Brutsaert [164] originally come from Brooks and Corey's power type function [165], in which two parameters are involved: the air-entry pressure and a dimensionless parameter referring to the pore-size distribution [165]. When van Genuchten developed the closed form equation, the introduced parameter a_V was disconnected to the air-entry pressure [166]; the same is true for a_X in the FX model. So, a_V and a_X should be only seen as air-entry pressure related parameters. In the same way, n_V, m_V, n_X and m_X are parameters related to the pore size distribution. Kosugi's model [158] was developed for the soil and two parameters (P_{cm} and σ_p) have to be determined based on the measured pore size distribution. Due to the lack of experimental data of the pore size distribution for cementitious materials, the fitted P_{cm} and σ_p in this model cannot be verified whether they still retain the same physical meaning as when they were first introduced. The FF model is a pure empirical equation for the purpose of fitting experimental data, without any physical meaning being mentioned.

To conclude the above comparisons, this section recommends that uni-modal models, FX and VG3, can be used as a first tentative fitting. If one does not get satisfying fitting results, multi-modal models can be used. In next sections of current chapter, the FX model will be used to fit the main sorption isotherms because it shows a slightly better performance to fit desorption isotherms than the VG3 model (see Fig. 3.3).

3.5 Prediction of one main isotherm from the other main branch

Most hysteresis models require at least both main curves to predict scanning loops. Nonetheless, measuring both desorption and adsorption isotherms for cementitious materials is time consuming and quite costly. In practice, it is still under debate whether the initial fully dried state can change the microstructure during measurements of adsorption isotherms. Instead, the desorption isotherm is easier to determine from an initially saturated state, which is also closer to the condition after the concrete structure formworks are removed. From this point of view, only the models to predict the adsorption isotherm from the desorption isotherm are evaluated herein.

In the literature, some comparisons have been done for sands and soils. Pham et al. [146] compared and ranked fives selected models. Feng and Fredlund's model [160] (improved by

Pham et al. [163]) appeared to be the most accurate one, followed by Mualem Model IV [167]. Meanwhile, in Maqsoud's comparison [147], Parlange's model [168] (modified by Braddock et al. [169]) showed the best prediction for silty sand and fine sand.

According to the requirements of experimental data, comparisons will here be carried out in two groups: models only based on the measured main desorption branch and models needing additional data besides the main desorption branch.

3.5.1 Models only based on the measured main desorption branch

Mualem Model II-1 [170]

The Mualem Model II-1 [170] is the extension of Mualem Model II [53]. In a totally homogeneous porous medium, two pore water distribution functions h and l can be considered identical for pore necks and pore bodies. This leads to $h(\bar{\rho}) = l(\bar{\rho})$ (or $h(\bar{r}) = l(\bar{r})$, see Eq. 3.1). Hence, the same distribution function is applied to both pore necks and pore bodies. The water distribution function (see Eq. 3.1) can be rewritten as:

$$f(\bar{r}, \bar{\rho}) = h(\bar{r})h(\bar{\rho}) \tag{3.15}$$

The water content during the wetting process (see Eq. 3.4) is rewritten as:

$$\theta_w(P_c) = \theta^{\max} H(P_c) \tag{3.16}$$

This simplification does not affect the expression for water content during a drying process (see Eq. 3.5). Combining Eq. (3.16) with Eq. (3.6), an equation calculating $\theta_w(P_c)$ from $\theta_d(P_c)$ is derived as:

$$\theta_w(P_c) = \theta^{\max} - [(\theta^{\max})^2 - \theta^{\max}\theta_d(P_c)]^{1/2} \tag{3.17}$$

The equivalent equation as a function of S appears as:

$$S_w(P_c) = 1 - [1 - S_d(P_c)]^{1/2} \tag{3.18}$$

Parlange's model [168], modified by Braddock et al. [169]

Based on Parlange's hysteresis model [168], an expression of the adsorption isotherm can be obtained as:

$$\frac{\mathrm{d}S_w}{\mathrm{d}P_c} = \frac{S_w - S_d}{P_c} \tag{3.19}$$

Taking VG2 equation to describe the desorption isotherm and integrating Eq. (3.19), an analytical form of the adsorption isotherm was provided by Braddock et al. [169].

$$S_w = -\frac{P_c}{a_{dV}} + \left[1 + \left(\frac{P_c}{a_{dV}}\right)^{n_{dV}}\right]^{1/n_{dV}} \tag{3.20}$$

where a_{dV} and n_{dV} are fitting parameters for the desorption isotherm.

3.5.2 Models needing additional data besides the main desorption branch

Feng and Fredlund's model [160], improved by Pham et al. [163]

In Section 3.4, it showed that there are two coefficients in FF model [160] (see Eq. 3.10). This indicates that two points on the adsorption isotherm are enough to determine these two parameters and to calculate the entire adsorption isotherm. Based on this idea, Pham et al. [163] introduced a method to find the positions of two such points (denoted by A and B). The position of point A corresponds to a capillary pressure:

$$P_{c,w\mathrm{A}} = \left(\frac{a_d}{10}\right)^{1/b_d} \tag{3.21}$$

where a_d and b_d are parameters used in FF equation [160] for the desorption isotherm.

Point B on the adsorption isotherm is defined as the point having a capillary pressure which is symmetrical to capillary pressure of point A with respect to a horizontal line passing through point E on the adsorption isotherm (see Fig. 3.7):

$$|P_{c,w\mathrm{A}} - P_{c,w\mathrm{E}}| = |P_{c,w\mathrm{B}} - P_{c,w\mathrm{E}}| \tag{3.22}$$

In the above equation, the position of point E is unknown. Pham et al. [163] introduced a method to determine the position of point E. The authors defined two other points on the desorption isotherm to find point B. Point C is in the middle of the desorption isotherm at

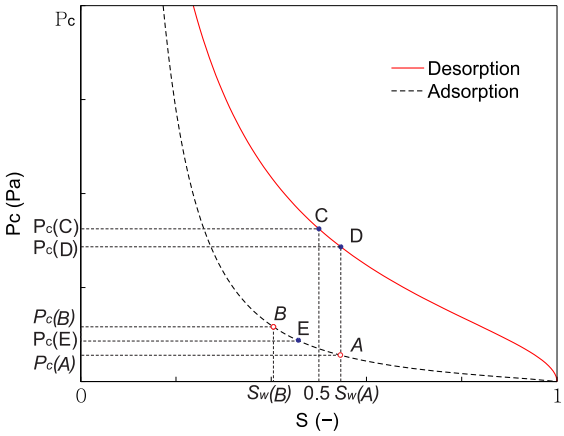

Figure 3.7: Schematic drawing of Feng and Fredlund's model [160] (improved by Pham et al. [163]) to predict the adsorption branch from the desorption branch. Three points A, D and C are used to calculate point B.

$S = 0.5$:

$$P_{c,d\mathrm{C}} = (a_d)^{1/b_d} \tag{3.23}$$

The other point D is on the desorption curve and has the same saturation value as point A:

$$P_{c,d\mathrm{D}} = \left(\frac{a_d}{S_{w\mathrm{A}}} - 1\right)^{1/b_d} \tag{3.24}$$

Points A, C, D and E should satisfy the relation:

$$|P_{c,w\mathrm{A}} - P_{c,w\mathrm{E}}| = |P_{c,d\mathrm{D}} - P_{c,d\mathrm{C}}| \tag{3.25}$$

Capillary pressure of point B on the adsorption curve is obtained by solving Eqs. (3.22)-(3.25).

$$P_{c,w\mathrm{B}} = P_{c,w\mathrm{A}} - 2\left[\left(\frac{a_d}{S_{w\mathrm{A}}} - a_d\right)^{1/b_d} - {a_d}^{1/b_d}\right] \tag{3.26}$$

Finally, the two parameters (a_w and b_w) used in Feng and Fredlund's model [160] are calculated on the basis of capillary pressure at points A and B.

$$a_w = \frac{S_{w\mathrm{A}} {P_{c,w\mathrm{A}}}^{b_w}}{1 - S_{w\mathrm{A}}} \tag{3.27}$$

$$b_w = \frac{\log\left[\dfrac{1-S_{w\mathrm{B}}}{S_{w\mathrm{B}}}\dfrac{S_{w\mathrm{A}}}{1-S_{w\mathrm{A}}}\right]}{\log\left[\dfrac{P_{c,w\mathrm{B}}}{P_{c,w\mathrm{A}}}\right]} \tag{3.28}$$

Mualem Model IV [167]

The Mualem Model IV [167] is an improved version of Mualem Model II [53, 170]. In addition to the main desorption branch, a wetting scanning cure is needed to predict the main adsorption branch. The prediction is divided into two parts: from the highest capillary pressure to the starting point of the wetting scanning curve, and for capillary pressure lower than the starting point of the wetting scanning curve. The first part is predicted using the same method as Mualem Model II-1 [170]. The second part is calculated by using both the main desorption branch and the wetting scanning curve. Thus, for the main adsorption branch, the saturation can be expressed as follows:

$$S_w\left(P_c\right) = \begin{cases} 1-\left[1-S_d(P_c)\right]^{1/2} & \text{for } P_{c,1} \leqslant P_c \leqslant P_c^{\max} \\ 1-\dfrac{1-S_{1,w}(P_c)}{\left[1-S_d(P_{c,1})\right]^{1/2}} & \text{for } P_c^{\min} \leqslant P_c < P_{c,1} \end{cases} \tag{3.29}$$

where $P_{c,1}$ is capillary pressure at the starting point of the additional wetting scanning curve. The subscript $(1, w)$ represents the first wetting scanning curve.

The accuracy of this model is sensitive to the position of the starting point of the wetting scanning curve. If the scanning curve starts at a high RH, the model tends to be the same as Mualem Model II-1 [170]. If the scanning curve starts at a low RH, it will only use the wetting scanning curve to predict the adsorption isotherm. According to the position of the starting point in available experimental data, comparisons were performed in three levels: low RH ($\mathrm{RH}_1 = 12\%$), medium RH ($\mathrm{RH}_1 = 33\%$) and high RH ($\mathrm{RH}_1 = 53\%$). Not all materials in the database can reach this requirement. Only five materials (Concrete1, Concrete2, Concrete3, Paste2 and Paste3) are used for validation and comparisons.

3.5.3 Comparison results and discussion

The prediction results for Paste2 are shown in Figs. 3.8. For the models only using the main desorption curve (Mualem Model II-1 [170] and Parlange's model [168] modified by Braddock et al. [169]), the standard deviation of the statistical criteria R^2_{adj} and NME are very large (see Fig. 3.9). Furthermore, R^2_{adj} values are low and NME values are high. Figure 3.8 also displays that the prediction of these two models do not show good agreements with measured curves. As

a result, one can conclude that only using one main curve is not sufficient to predict the other main curve in the case of cementitious materials.

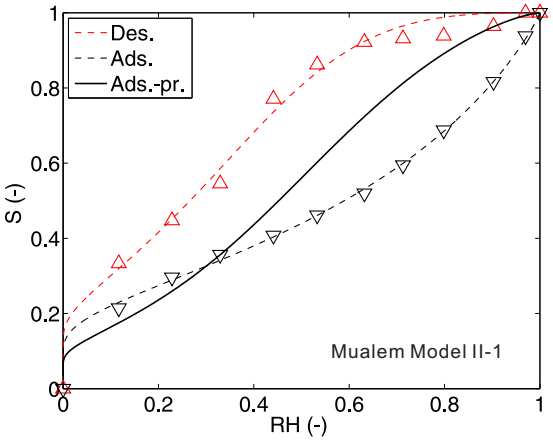

(a) Mualem Model II-1 [170].

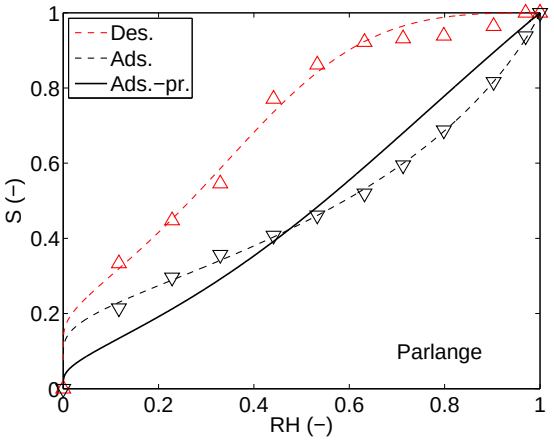

(b) Parlange's model [168] (modified by Braddock et al. [169]).

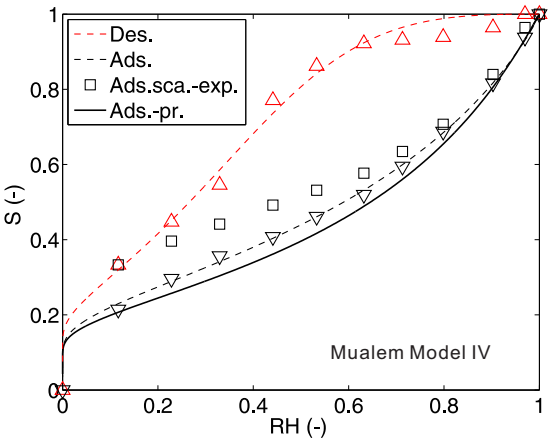

(c) Mualem Model IV [167], $RH_1 = 12\%$.

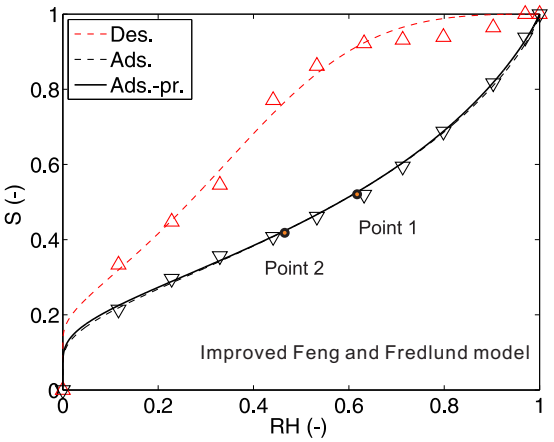

(d) Feng and Fredlund's model [160] (improved by Pham et al. [163]).

Figure 3.8: Prediction results of the main adsorption curves for Paste2 material. Two points in the Feng and Fredlund's model [160] (improved by Pham et al. [163]) are at RH = 67% and RH = 46%.

With regard to models needing additional data, Fig. 3.9 clearly shows that the improved Feng and Fredlund's model [160] yields the best prediction with the highest R^2_{adj} and the lowest NME. This is due to the fact that adding two additional measured points significantly improves the prediction accuracy. In spite of needing one wetting scanning curve, by contrast, Mualem Model IV [167] does not provide good performance regardless of the level of RH.

The requirement of additional experimental data limits the application of the improved Feng and Fredlund's model [160]. In fact, the positions of points A and B depend on the shape of the

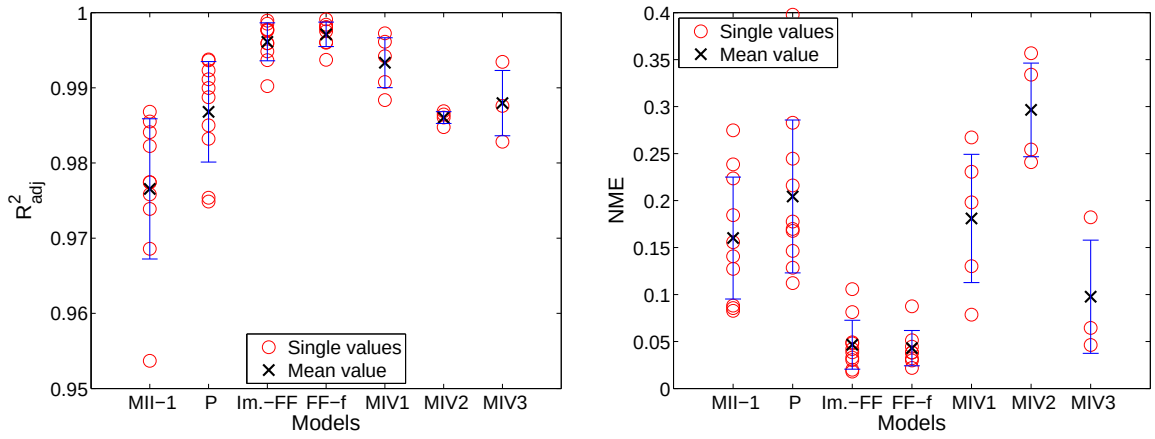

Figure 3.9: Comparison of the predicted main adsorption branch based on the measured main desorption branch. Results are from models: Mualem Model II-1 (MII-1) [170], Parlange's model (P) [168] (modified by Braddock et al. [169]), Feng and Fredlund model's (FF) [160] (improved by Pham et al. [163]), fixed points version of Feng and Fredlund's model (FF-f) and Mualem Model IV [167] of the wetting scanning curve starting at $RH_1 = 12\%$ (MIV1), $RH_1 = 33\%$ (MIV2) and $RH_1 = 53\%$ (MIV3).

desorption isotherm; thus, they vary according to the studied materials. If these two points are fixed independently of the material, it will be more interesting from a practical point of view to determine the adsorption isotherm. The mean RH values for these two points are calculated according to the prediction results, which are around 67% and 86%. They almost correspond to the RH values (63.2% and 90.4%) used in the measurements of the sorption isotherms in [23]. Thus, these two points can be fixed at 63.2% and 90.4%. The main adsorption isotherms can be determined by using Eq. (3.10). The predicted results are compared with other methods in Fig. 3.9. It is clear that the fixed points method has an equivalent accuracy as Feng and Fredlund's model [160] (improved by Pham et al. [163]). This implies that if one wants to know the entire adsorption isotherm, it is enough to determine two adsorption points at RH = 63.2% and 90.4%.

The above comparisons reveal that it may be not appropriate to predict one main isotherm by using the other main isotherm only (e.g., Mualem Model II-1 [170] and Parlange's model [168] modified by Braddock et al. [169]). Two additional measured points on the adsorption isotherm can provide a better prediction (improved Feng and Fredlund model [160]) than using one wetting scanning curve (Mualem Model IV [167]).

3.6 Prediction of scanning isotherms

Comparisons of different hysteresis models can be found in the literature [57, 171, 172, 146, 173] for a large variety of porous media, not including cementitious materials. By statistical analysis, Viaene et al. [171] concluded that models based on domain theories give the best predictions. A similar conclusion has been drawn in the comparisons performed by Pham et al. [146]. However, besides the domain models, several recently developed empirical models were also selected for comparisons due to their simplicity of application.

3.6.1 Mualem Model II

In Mualem Model II [53], a series of equations to calculate scanning curves have been proposed based on Mualem's diagram (see Fig. 3.2). They use two basic functions H (see Eq. 3.3) and L (see Eq. 3.6), which are determined by two main sorption isotherms (desorption and adsorption). In practice, expressions to H and L are also written as the function of S (see Eq. 2.13). The first scanning curve in drying (scanning curve of order $N = 1$), starting on the adsorption isotherm at the point ($S_w(P_{c,1})$, $P_{c,1}$), is formulated according to Mualem's diagram:

$$S_{1,d}(P_c) = S_w(P_{c,1}) - [L(P_{c,1}) - L(P_c)]\,[1 - H(P_c)] \tag{3.30}$$

The first scanning curve in wetting (order $N = 1$), starting on the desorption isotherm at the point ($S_d(P_{c,1})$, $P_{c,1}$), is calculated by:

$$S_{1,w}(P_c) = S_d(P_{c,1}) + [L(P_c) - L(P_{c,1})]\,H(P_{c,1}) \tag{3.31}$$

It can be noted that the expression for the first drying scanning is different to the first wetting scanning curve. The expression for the wetting scanning curve of order N (odd number and > 1) is deduced according to Mualem's diagram:

$$S_{N,w}(P_c) = S(P_{c,N}) + [L(P_c) - L(P_{c,N})]\,[1 - H(P_{c,N})] \quad \text{for } L(P_c) \leq L(P_{c,N-1}) \tag{3.32}$$

where $S(P_{c,N})$ is the saturation at the starting point of the current scanning curve, which must be the end point of the previous scanning curve. If $L(P_c) \geq L(P_{c,N-1})$, Mualem's diagram indicates that $L(P_{c,N-3})$ will be used instead of $L(P_{c,N-1})$ until the scanning curve reduces to the main

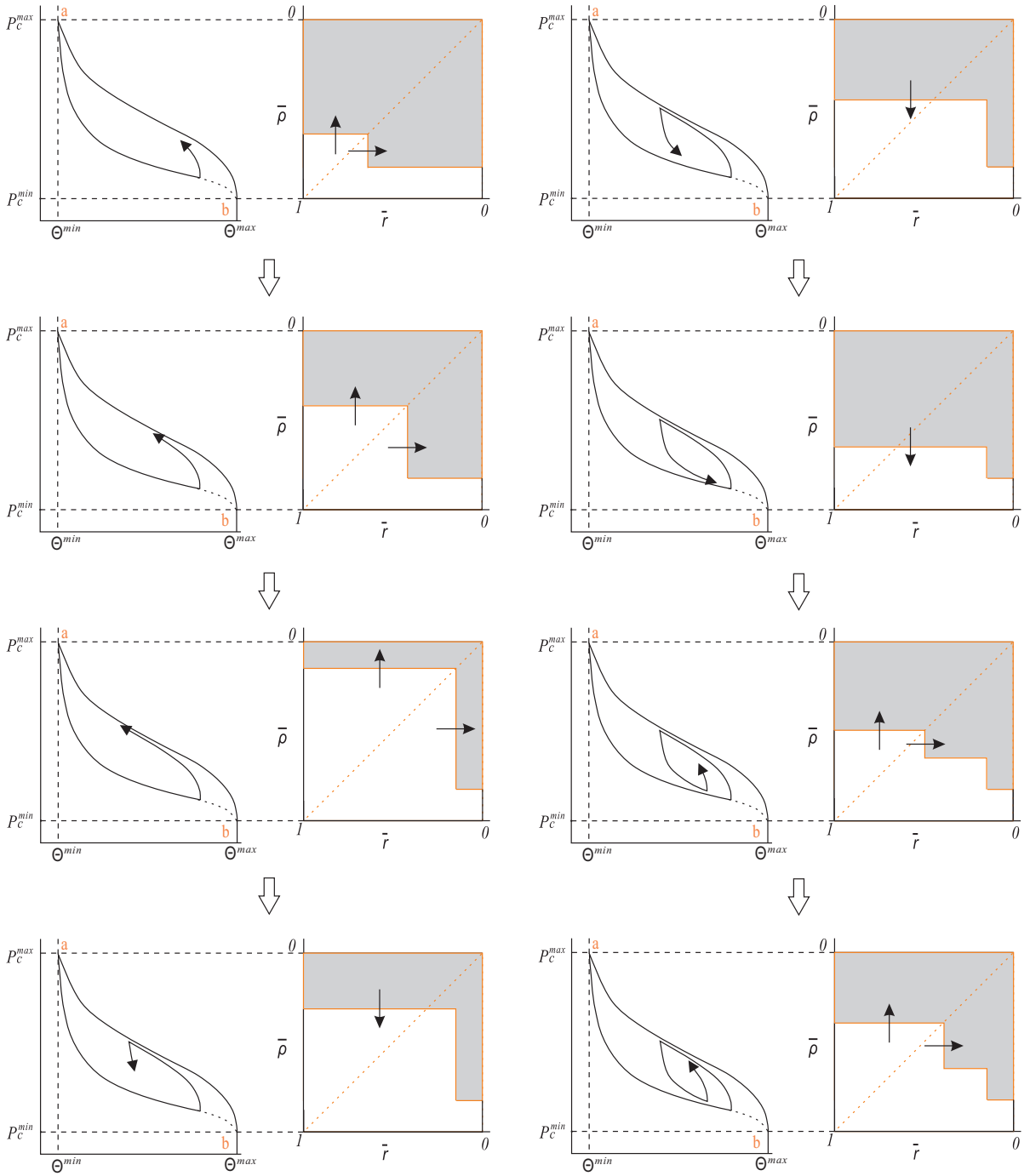

Figure 3.10: The scanning loops simulated by Mualem's diagram. The first drying, second wetting and third drying scanning curves are shown in this figure.

isotherms (order $N = 0$). For example in Fig. 3.11, if the third scanning curve in wetting CB continues to decrease after point B, it must do so on curve BD, which is the extension line of the first scanning curve in wetting AB. This ensures that all scanning loops are closed and enclosed in the main loop.

In the same manner, the expression for the drying scanning curve of order N (even number) is written as:

$$S_{N,d}(P_c) = S(P_{c,N}) - [L(P_{c,N}) - L(P_c)]\,[1 - H(P_c)] \quad \text{for } L(P_c) \geq L(P_{c,N-1}) \tag{3.33}$$

If $L(P_c) \leq L(P_{c,N-1})$, $L(P_{c,N-3})$ will be used instead of $L(P_{c,N-1})$ for calculation.

Equations (3.31-3.33) comprise a set of formulas to calculate arbitrary scanning loops.

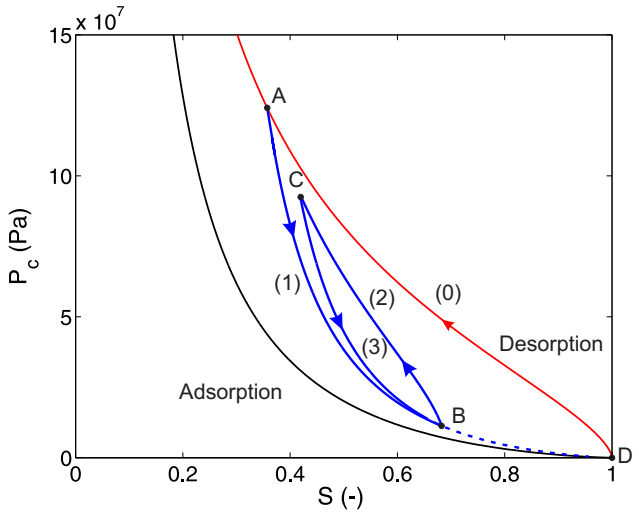

Figure 3.11: An example of scanning loops calculated by Eqs. (3.31)-(3.33).

3.6.2 Mualem dependent model

Based on the assumption of "dependent" of the neighbouring pores in Mualem Model III [54], Mualem and Miller [155] and Mualem [55] have provided different weighting functions p_d to improve the prediction of the scanning curves (see Mualem's diagram for dependent model in Fig. 3.12). The improved version in [55] seems to provide a better agreement with experimental data for soils [55, 156, 173]. This version (hereafter called "Mualem dependent model"), as the same as Mualem Model II [53], only needs both main sorption isotherms. The formula of p_d is given by [55]:

$$p_d(S) = \frac{1 - S}{[1 - S_w(P_c^+)]^2} \tag{3.34}$$

where P_c^+ is capillary pressure corresponding to $S_d(P_c^+) = S$ (the current saturation, see Fig. 3.13).

The function for the first scanning curve in drying (order $N = 1$), starting on the adsorption

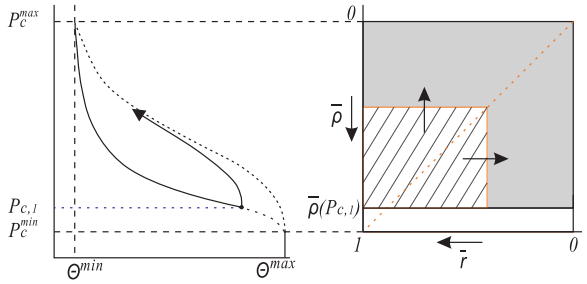

(a) The drying scanning process

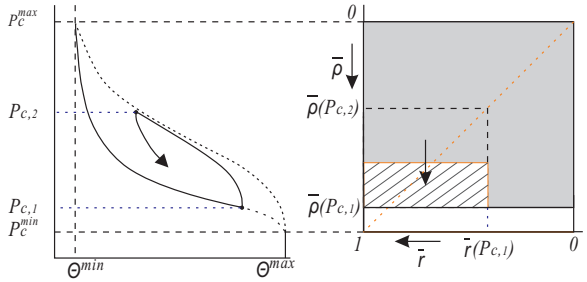

(b) The wetting scanning process

Figure 3.12: Schematic representation of Mualem's diagram [54] for scanning processes described with the dependent domain model. The gray domain represents completely-filled pores and the blank region is fully-dried pores. Shaded part is the partially-dried pores controlled by the weighting function p_d.

isotherm, is deduced as:

$$S_{1,d}(P_c) = S_w(P_{c,1}) - p_d(S)\left[1 - S_w(P_c)\right]\left[S_w(P_{c,1}) - S_w(P_c)\right] \tag{3.35}$$

The first scanning curve in wetting (order $N = 1$), starting on the main desorption isotherm, can be calculated by:

$$S_{1,w}(P_c) = S_d(P_{c,1}) + p_d(S_1)\left[1 - S_w(P_{c,1})\right]\left[S_w(P_c) - S_w(P_{c,1})\right] \tag{3.36}$$

where $p_d(S_1)$ is p_d at the starting point $(S_d(P_{c,1}), P_{c,1})$. Functions for scanning loops can be easily derived based on Mualem's diagram [54, 155, 55]. For the wetting scanning curves of order N (odd number and > 1), the expression is written as:

$$S_{N,w}(P_c) = S(P_{c,N}) + p_d(S_N)\left[1 - S_w(P_{c,N})\right]\left[S_w(P_c) - S_w(P_{c,N})\right], S_w(P_c) \leq S_w(P_{c,N-1}) \tag{3.37}$$

For the drying scanning curves of order N (even number), the expression is:

$$S_{N,d}(P_c) = S(P_{c,N}) - p_d(S)\left[1 - S_w(P_c)\right]\left[S_w(P_{c,N}) - S_w(P_c)\right], S_w(P_c) \geq S_w(P_{c,N-1}) \quad (3.38)$$

One can see that wetting scanning curves are provided by explicit formulas, while equations for drying scanning curves are implicit forms with respect to the current capillary pressure P_c. Therefore, a drying scanning curve must be calculated by an iterative method. Substitution of Eq. (3.34) into Eq. (3.36) yields the same equation for the first scanning curve in wetting as the one used by Mualem Model II. It means that these two models will share the same first wetting scanning curve.

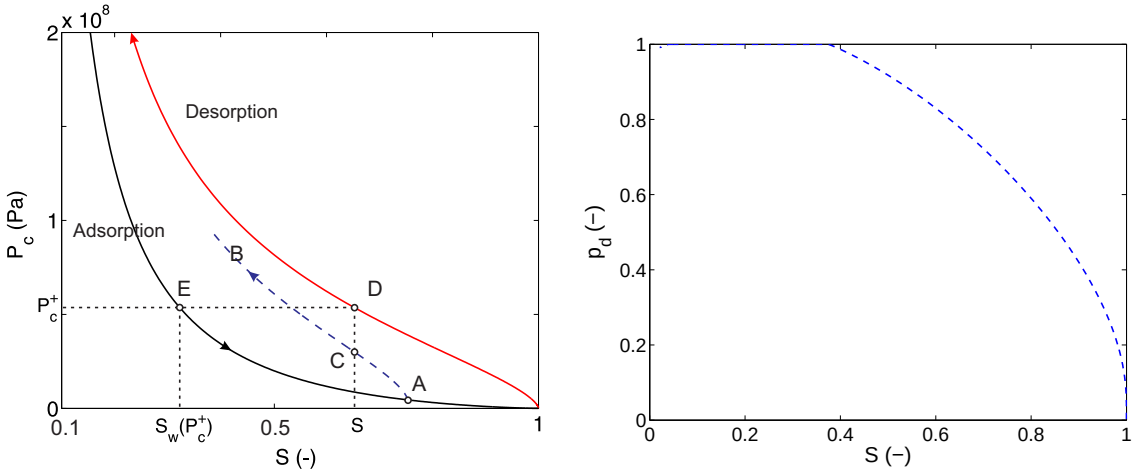

(a) Schematic representation of calculation procedure

(b) An example of calculated p_d.

Figure 3.13: The calculation of p_d during a drying process in Mualem dependent model [55].

3.6.3 Incremental models

Elastoplastic models have been used in porous media field to describe the relation between P_c and S [59, 61]. Usually, a simple incremental relation is used. It is generally assumed that the differential of P_c on the scanning curve is related to the differential of P_c or S on the main isotherm. Two typical models are described below.

(1) Li's model [59]

In this method, the scanning curve is obtained by integrating the incremental relation $\mathrm{d}P_c - \mathrm{d}S$. A proposition for the incremental form of $P_c(S)$ is given in [59] as follows:

$$\mathrm{d}\ \ln[P_c(S)] = \left[\frac{\ln[\bar{P}_c(S)] - \ln(P_{c,1})}{\ln[P_c(S)] - \ln(P_{c,1})}\right]^{\beta} \mathrm{d}\ \ln[\bar{P}_c(S)] \tag{3.39}$$

where β is a material parameter. $\bar{P}_c(S) = P_{c,d}(S)$ is capillary pressure on the main desorption branch for the drying process and $\bar{P}_c(S) = P_{c,w}(S)$ is on the main adsorption branch for the wetting process (see Fig. 3.14). By integrating Eq. (3.39), one can obtain the expressions for a drying scanning curve:

$$\ln[P_c(S)] = \ln(P_{c,1}) + \left(|\ln[P_{c,d}(S)] - \ln(P_{c,1})|^{\beta_d+1} - |\ln(P_{c,d1}) - \ln(P_{c,1})|^{\beta_d+1}\right)^{1/(\beta_d+1)} \tag{3.40}$$

and for a wetting scanning curve:

$$\ln[P_c(S)] = \ln(P_{c,1}) - \left(|\ln(P_{c,1}) - \ln[P_{c,w}(S)]|^{\beta_w+1} - |\ln(P_{c,1}) - \ln(P_{c,w1})|^{\beta_w+1}\right)^{1/(\beta_w+1)} \tag{3.41}$$

One can notice that in this method the scanning curve always starts with an infinite slope (i.e., $|\mathrm{d}P_c/\mathrm{d}S| \to \infty$).

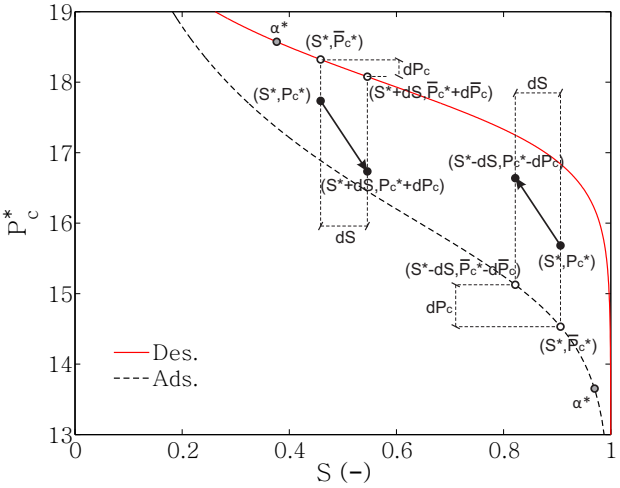

Figure 3.14: Schematic representation of the calculation of scanning curves by Li's model [59].

(2) Wei's model [61]

Based on reference [174], Wei et al. [61] suggested a new and simpler incremental relation, expressed as:

$$\mathrm{d}P_c = -K_p \mathrm{d}S \tag{3.42}$$

where $-K_p$ is the slope of the scanning curve.

According to Wei's theory, when P_c changes, the water content in the material is assumed to be additively decomposed into two parts, a reversible part and an irreversible part. The irreversible part of water content is dependent on capillary pressure, while the reversible part is independent. Accordingly, the slope of each scanning curve can be divided into two parts, one is an irreversible part affected by the main isotherm (e.g., the first term on the right side of Eq. (3.43)), and the other is based on the effect of both reversible and irreversible water content (e.g., the second term on the right side of Eq. 3.43). At current P_c, the slope of the drying scanning curve can be calculated by:

$$K_p = -\frac{\mathrm{d}P_{c,d}(S)}{\mathrm{d}S} + \frac{c_d|P_c - P_{c,d}(S)|}{P_{c,d}(S) - P_{c,w}(S) - |P_c - P_{c,d}(S)|} \tag{3.43}$$

For a wetting scanning curve, it is:

$$K_p = -\frac{\mathrm{d}P_{c,w}(S)}{\mathrm{d}S} + \frac{c_w|P_c - P_{c,w}(S)|}{P_{c,d}(S) - P_{c,w}(S) - |P_c - P_{c,w}(S)|} \tag{3.44}$$

where c_d and c_w are the internal state variables for drying and wetting processes, respectively. In Eqs. (3.43) and (3.44), the slope of the main sorption isotherm ($-\frac{\mathrm{d}P_{c,d}(S)}{\mathrm{d}S}$) and the distance between two main isotherms ($P_{c,d}(S) - P_{c,w}(S)$) represent irreversible effects. The part of $|P_c - P_{c,d}(S)|$, depending on the current capillary pressure, represents the reversible effect. The coefficients of c_d (or c_w) is used to control the reversible effect and it is a function of the water content. To simplify the application of this model, Wei et al. [61] assumed constant values of c_d and c_w. Clearly, the reversible effect can be observed at the beginning of the scanning curve due to the large initial slope, like it has been illustrated by Wei et al. [61] and in the model of Hogarth et al. [175, 176] for soils.

When Eqs. (3.43) and (3.44) are applied to simulate scanning curves for cementitious materials, the model predicts that the scanning curve crosses the main sorption isotherm because of the significant reversible effect. However, experimental data of the scanning curves [23, 12] do not show such a reversible effect. Hence, a modification to Eqs. (3.43) and (3.44) is proposed in this thesis to reduce the reversible effect and new relations are yielded for a drying scanning

curve:

$$K_p = -\frac{\mathrm{d}P_{c,d}(S)}{\mathrm{d}S} + \frac{c_d|P_c - P_{c,d}(S)|}{P_{c,d}(S) - P_{c,w}(S)} \tag{3.45}$$

and for a wetting scanning curve.

$$K_p = -\frac{\mathrm{d}P_{c,w}(S)}{\mathrm{d}S} + \frac{c_w|P_c - P_{c,w}(S)|}{P_{c,d}(S) - P_{c,w}(S)} \tag{3.46}$$

One can notice that K_p depends on the current position of the scanning curve. An iterative method is needed to compute the current capillary pressure.

3.6.4 Improved Rubin's empirical hysteresis model

The basic idea for the calculation of the scanning curve is to determine the distance between the scanning curve and the main isotherm which the scanning curve approaches. Here, considering the saturation as an independent variable, this thesis takes the prediction of the drying scanning curve as an example of how to develop an empirical hysteresis model.

As above models show, the distance between the drying scanning curve and the main desorption curve should be a function of the current saturation (S_d) and the starting point of the scanning curve, which is simply formulated as:

$$P_{c,d} - P_c = F(S_d, P_{c,1}, S_1) \tag{3.47}$$

Various F functions can be found in the literature. For instance, Rubin [177], as well as Feng and Fredlund [160], proposed expressions for the first drying scanning curve, considering F as proportional to the distance between the two main isotherms. Nevertheless, these two models did not take into account the position of the starting point in their expressions. Thus, these expressions were only valid for the first scanning curve in drying and not able to simulate scanning loops. Here, a new function F is introduced by adapting the original form of [177]. The exponential relation is used to control how fast the scanning curve approaches the main isotherm. Finally, the following expression is given for the drying scanning curve:

$$P_c(S) = P_{c,d}(S) - [P_{c,d}(S) - P_c(S_1)] \exp\left[\gamma_d\,(S - S_1)\right] \tag{3.48}$$

The negative value of $\gamma_d(S - S_1)$ limits the exponential expression from 1 (at the starting point) to near 0 (almost on the main isotherm). Similarly, the expression for the wetting scanning curve is derived as:

$$P_c(S) = P_{c,w}(S) + [P_c(S_1) - P_{c,w}(S)] \exp[\gamma_w (S_1 - S)] \tag{3.49}$$

The constant γ_d and γ_w are used to determine the shape of the scanning curve and needs to be assessed from experimental data.

3.6.5 Comparison results and analysis

Overall, five materials, (Concrete1, Concrete2, Concrete3, Paste2 and Paste3, see Table 3.2), have been studied. One example of a comparison between experimental data and predictions (Paste3) performed by above models are provided in Fig. 3.15 (other comparison results are included in the document "supplementary materials"). The results obtained by Mualem Model II [53] and Mualem dependent model [55] are illustrated in the same figure. For each empirical model, one parameter should be valid for all measured wetting scanning curves as well as the other one should be valid for all measured drying scanning curves. Thus, during fitting, these unknown parameters (β_d and β_w in Eqs. 3.40 and 3.41, c_d and c_w in Eqs. 3.45 and 3.46 and γ_d and γ_w in Eqs. 3.48 and 3.49), are optimized to be suitable for all measured wetting (or drying) scanning curves for each material.

Empirical models reveal that the predicted wetting scanning curves increase slowly at the beginning where the curves are almost parallel to the horizontal axis (see Fig. 3.15), so that these curves can approach the main adsorption branch in a shorter range of RH. This has been observed by Åhs [12] in experimental results on hardened cementitious materials. As a consequence, the first wetting scanning curves probably reach the main curve before RH = 100%, as illustrated by modified Wei's model and improved Rubin's model (see Fig. 3.15). The wetting scanning curves predicted by Mualem's models [53, 55] increase more smoothly and reach the main wetting curve at RH close to 100%. It results in a poorer agreement with measured data than empirical models.

Experimental data for the first drying scanning curves are only available for Paste2 and Paste3 materials in our database [23]. Predictions from Mualem Model II [53] show that curves decrease with a lower slope and turn towards the desorption isotherm more gently than curves predicted by empirical models. Therefore, empirical models yield predictions with a lower accuracy compared

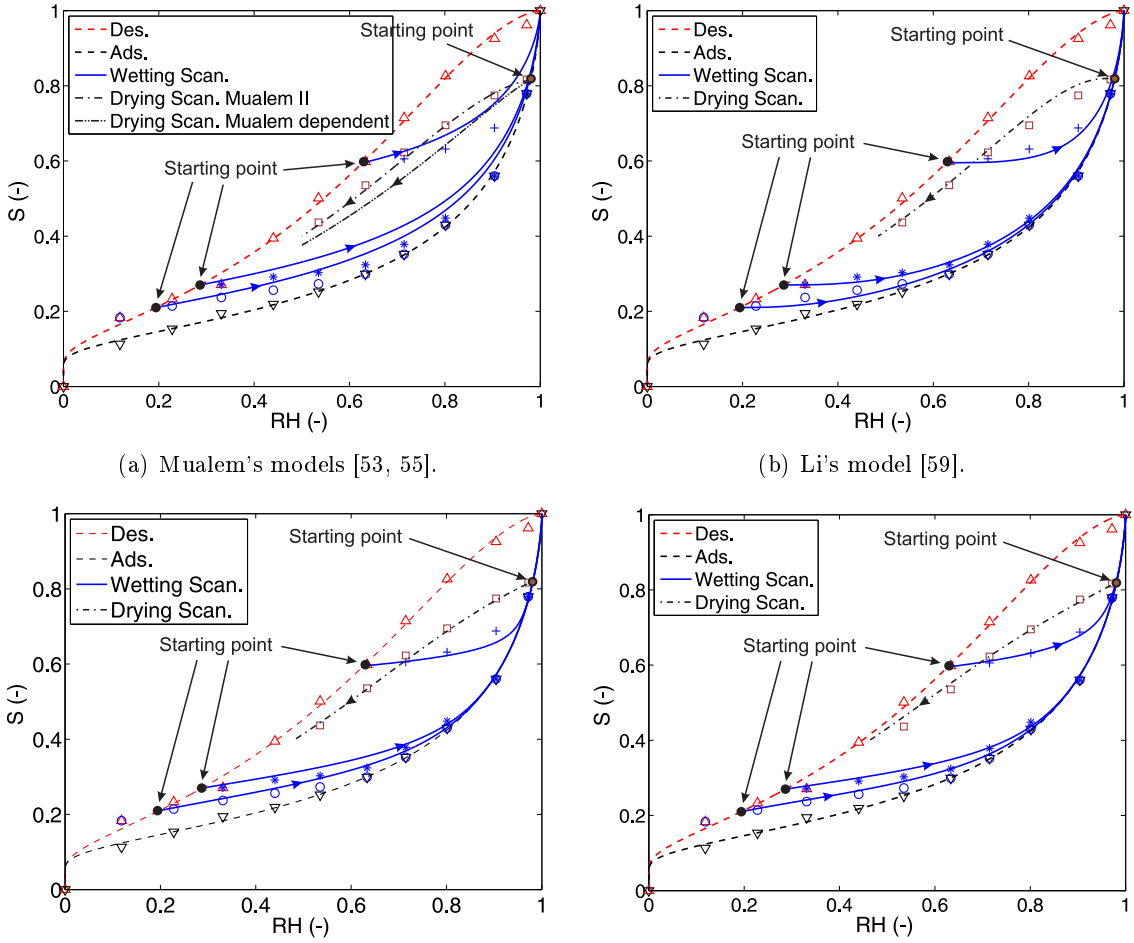

(a) Mualem's models [53, 55].

(b) Li's model [59].

(c) Modified Wei's model (proposed).

(d) Improved Rubin's model (proposed).

Figure 3.15: Predicted wetting scanning curves (solid lines) and drying scanning curves (dashed-dotted lines) for Paste3 compared with experimental data (symbols) from [23].

to Mualem Model II. With respect to Mualem dependent model [55], it does not provide a good prediction for the drying scanning curves (see Fig. 3.15a).

The two criteria R^2_{adj} and NME for the prediction of the first wetting scanning curves are shown in Fig. 3.16. They illustrate that empirical models can give higher R^2_{adj} and lower NME values than the Mualem Model II. This is definitely due to that the two additional parameters in empirical models can be adjusted to fit experimental data, while Mualem's models essentially depend on the shape of the two main sorption isotherms. In contrast, in the prediction of the first drying scanning curves for Paste3, Mualem Model II reveals a better prediction than the empirical models.

Figure 3.16 also shows that all empirical models have almost equal accuracy for the estimation of the first scanning curves, either wetting or drying. None of the selected hysteresis models is

considerably better than the others. This conclusion is similar to that reported by Jaynes [57] when he compared hysteresis models for soils. Hence, it needs the comparison of higher order scanning curves.

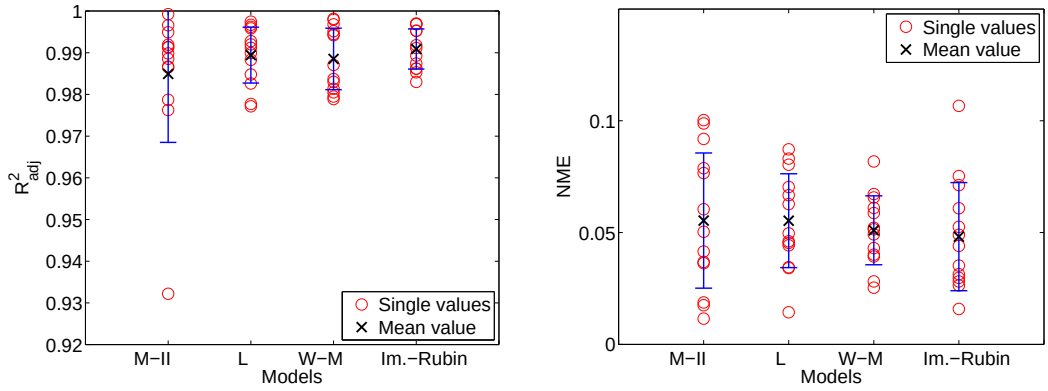

Figure 3.16: Comparison results for wetting scanning isotherm predicted by Mualem Model II (M-II) [53], Li's model (L) [59], modified Wei's model (W-M) [61] and improved Rubin's model (Im.-Rubin) [177].

Predictions of scanning loops

Scanning loops have been measured for Paste2 and Paste3 [23]. Here three measured loops, one for Paste2 and two for Paste3, have been chosen to verify the applicabilities of the selected hysteresis models. One of the prediction result is shown in Fig. 3.17 (other comparison results are included in the document "supplementary materials").

Because of the poor prediction of the first wetting scanning curves, Mualem dependent model [55] do not show better prediction results than Mualem Model II [53]. Among empirical models, Li's model [59] appears to be the best one to predict the shape of the measured scanning loops. Besides, the improved Rubin's model [177] shows a better prediction of secondary drying scanning curves than the modified Wei's model [61] (see Fig. 3.17).

Analysis of the pumping effect

One hysteretic behaviour, called the "pumping effect", should be noticed for empirical models. It refers to the non-closure of scanning loops when the secondary and higher order scanning curves are calculated. Researchers consider that pumping effect is an artifact of the algorithm and does not correspond to an actual material property [176, 178]. Thus, this behaviour is also called the "pumping errors" (PEs), which is defined and illustrated in Fig. 3.18. Point A is the starting

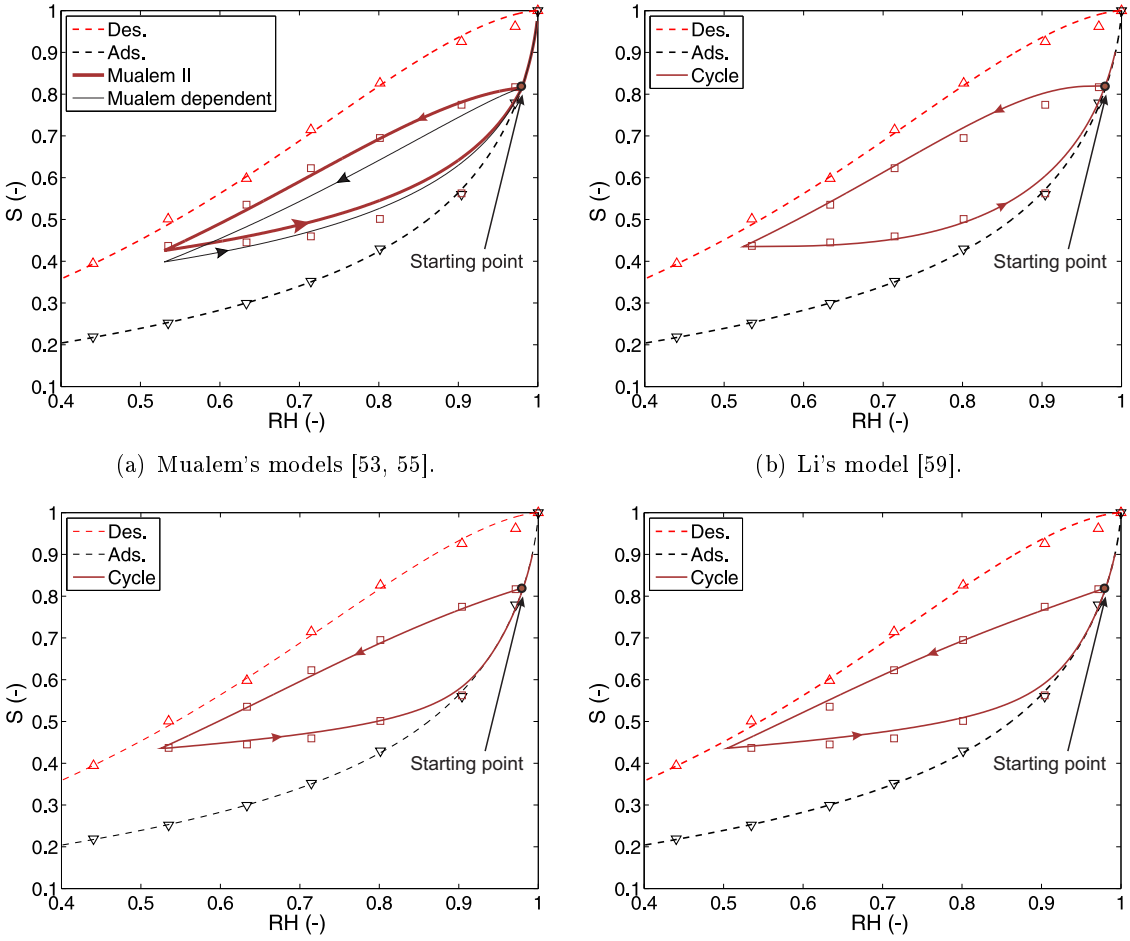

(a) Mualem's models [53, 55].

(b) Li's model [59].

(c) Modified Wei's model (proposed).

(d) Improved Rubin's model (proposed).

Figure 3.17: Predicted scanning loop (solid lines) for Paste3 compared with experimental data (symbols) from [23]. Simulated RH cycle: 97% → 53% → 99%.

point of the scanning loop. Point B is on the secondary scanning curve in drying at the same RH as point A. The difference of S between A and B is defined as the "drying pumping error" (DPE). Similarly, a "wetting pumping error" (WPE), originating from wetting scanning curves (difference between point C and point D in Fig. 3.18), is also observed for empirical models. Figure 3.18 implies amplitudes of DPE and WPE can be quantified.

The evolution of PEs is not only dependent upon the initial state but also upon the magnitude of RH oscillations. Thus, to assess the evolution of DPE and WPE, two initial states of RH cycles are tested: an initial drying state and an initial wetting state. Paste3 material is taken as an example because many measured scanning curves are available for this material, including the first and secondary drying curves and the first wetting scanning curves. Two RH oscillations have been chosen for each initial state. The first one has been provided by experiments, with

RH changing between 63% and 97% (see Figs 3.19a and 3.19c). The second one reduces the RH difference to 20%, such as for an RH oscillating between 63% and 83% (see Figs 3.19b and 3.19d).

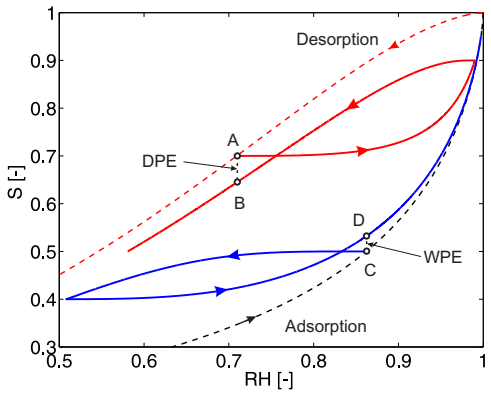

Figure 3.18: Definitions of DPE and WPE.

The simulated scanning loops are shown in Fig. 3.19. Results of PEs *vs.* the number of cycles are plotted in Fig. 3.20. Pumping errors are clearly more significant for small RH oscillations than for large RH oscillations. The first loop produces the largest PE, and then it reaches a constant value after about 2 cycles for large RH oscillations and about 5 cycles for small RH oscillations. Li's [59] and improved Rubin's models [177] provide similar PEs (less than 0.1) for large RH oscillations, while improved Rubin's model yields larger PEs (around 0.3) than Li's model (around 0.2) for small RH oscillations. It is also clear that WPEs are larger than DPEs in both empirical models for the same kind of RH oscillations.

For large RH oscillations, PEs of empirical models are acceptable. Nevertheless, for small RH oscillations, if the model fails to eliminate PEs, the cumulative errors associated with oscillations of hysteresis loops are probably significant and lead to unrealistically simulated results. Some works have been done to avoid PEs when a hysteresis model was developed. By assuming that scanning curves have the same shape as the main branches, Parker and Lenhard [91] and Huang et al. [176] enforced closure of scanning loops to eliminate pumping errors. The problem of these methods is that they need to rescale and reformulate each scanning curve if the direction changes, and this may be inefficient for modelling of frequent drying and wetting cycles.

3.6.6 Discussion

Compared with empirical models, Mualem's models (Model II [53] and dependent model [55]) have the advantage to avoid PEs, even though their predictions are not as good as empirical

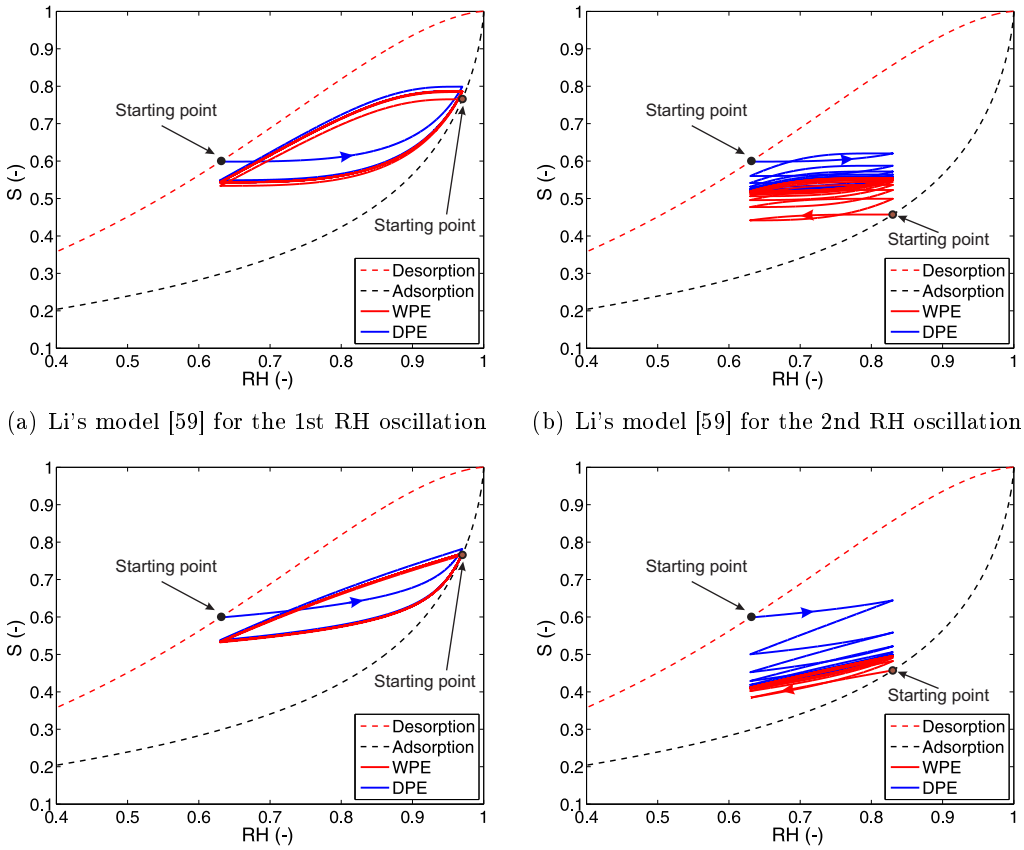

(a) Li's model [59] for the 1st RH oscillation

(b) Li's model [59] for the 2nd RH oscillation

(c) Improved Rubin's model for the 1st RH oscillation

(d) Improved Rubin's model for the 2nd RH oscillation

Figure 3.19: Simulated hysteresis loops by Li's model [59] and improved Rubin's model (taking Paste3 as an example).

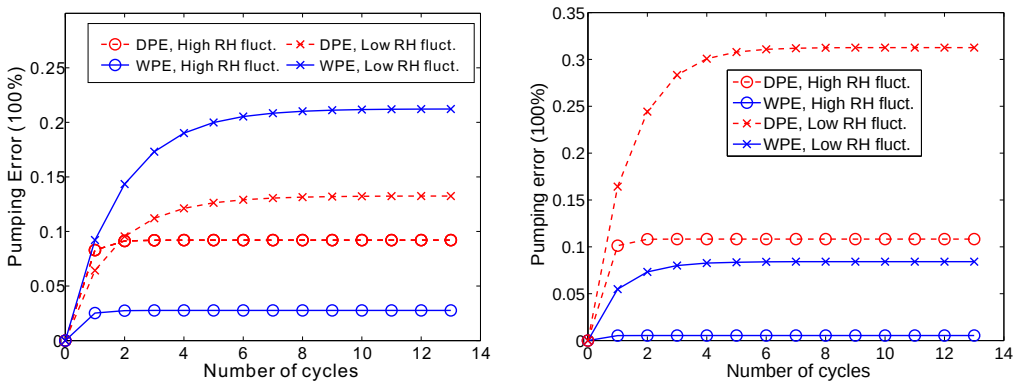

(a) Li's model [59]. (b) Improved Rubin's model.

Figure 3.20: The evolution of PEs calculated based on two RH fluctuations.

models. They may be more applicable for smaller RH oscillations comparing with empirical models. Another advantage of Mualem's models is that they need only the two main sorption isotherms to predict scanning loops, unlike empirical models that require at least two scanning curves to determine parameters.

Notably, from a practical point of view, equations of Mualem Model II [53], Li's model [59] and improved Rubin's model are expressed in explicit forms which are easier to implement in a numerical modelling of moisture transport. In particular, the improved Rubin's model uses very simple equations and provides an acceptable prediction. The modified Wei's model [61] and Mualem dependent model [55] correspond to implicit formulas which significantly increase the difficulty of application. A drawback for Li's model [59] is that the scanning curve always starts in a horizontal line, which leads to the moisture capacity $C = \frac{\partial S}{\partial P_c} = 0$ for the beginning point. It will definitely numerical problem when this model is implemented into a moisture transport model.

To conclude the above analysis about hysteresis models, this thesis recommends Mualem Model II [53] and improved Rubin's models to be used for moisture transport modelling within cementitious materials exposed to cyclic boundary conditions. The empirical one (improved Rubin's models) is more suitable for large RH oscillations, in which pumping effect can be reduced.

3.7 Models for the proposed multi-level approach to simulate hysteresis

Based on experimental verifications, models for the fitting of main isotherms, the prediction of one main curve from the other one and the simulation of scanning loops have been evaluated. However, from a practical point of view, it needs to organise those models in the framework of a multi-level approach capable of providing different possibilities to predict hysteresis according to the available data and the level of sophistication which is required. Different combinations of those models for this multi-level approach are provided in Table 3.3.

Table 3.3: Proposed models for the multi-level approach to model hysteresis.

Levels	Experimental data	Models combination
Level 1	Both main isotherms and one scanning isotherm	FX (VG3) + L (W-M1)
Level 2	Both main isotherms	FX (VG3) + M-II
Level 3	One main isotherm	FX (VG3) + M-II-1 + M-II
Level 4	No isotherm data	No models available

Comparisons in previous sections show that Level 1 and Level 2 provide very reliable predictions. Because there is no model which is able to infer one main isotherm from another main curve, the prediction accuracy of Level 3 needs to be improved. Level 1 and Level 2 indicate that at least both measured main desorption and adsorption isotherms are required to calculate scanning loops.

3.8 A method to fit both main curves by using the fewest measured data

Since measuring sorption isotherms is quite time-consuming when using the saturated salt solution method. The DVS measurement can significantly save time, but no every researcher is able to afford the expensive apparatus. Thus, it could be interesting to find a way requiring the fewest measured data to predict both main desorption and main adsorption curves. The similar idea can be found in the literature, such as in [179], while only the main desorption was considered. Another main advantage of the proposed method in current study is that it is developed based on data measured by the saturated salt solution method, and will be applied for DVS data (see

Chapter 4).

Section 3.5 showed that improved Feng and Fredlund's model [160, 163] needs two measured points on the main adsorption curve and the entire main desorption curve to predict the main adsorption curve. These two points are not random and have been fixed at RH = 63.2% and 90.4% in the current study. However, comparisons in Section 3.4 revealed that the FF model [160], which is used in improved Feng and Fredlund's model, is not the best model to fit the main sorption curves. This may result in improved Feng and Fredlund's model less accurate. As Section 3.4 suggested, FX or VG3 models [161, 90] can provide better fitting than FF. Hence, it would be necessary to use FX or VG3 instead of FF to improve the prediction accuracy.

The above discussion inspires us to think about a more interesting question: can the number of experimental data for the fitting of the main sorption curves be reduced? In particular from a practical point of view, it is worth finding a method which needs the fewest experimental data to predict both main desorption and adsorption isotherms. In the literature, there is a lack of research trying to estimate how many experimental data are required for the fitting of the main sorption isotherms.

This attempt indicates that two steps need to be done: determine the number of points needed to predict each main curve and find the most relevant positions of those points.

3.8.1 A proposed new statistical criterion

Statistical criteria R^2, R^2_{adj} and NME were introduced in Section 3.3. In this section, only three-parameter models are chosen so there is no need of R^2_{adj}. R^2 will be used for the comparison purpose. In fact, NME yields the same results with another criterion, so-called the mean multiplicative error (MME). The only difference between these two criteria is that the value of NME is in the range of $[0, +\infty]$, but MME is in the range of $[1, +\infty]$. If plotting MME and R^2 in a same figure, it will allow a synthetic representation of the relevancy of the model in a unique figure. Thus, comparison will be easier and clearer. The equation of MME is expressed as [180]:

$$\text{MME} = \exp\left[\frac{\sum_{i=1}^{n} |\ln(S_i^{pr}/S_i^{ms})|}{n}\right] \tag{3.50}$$

Notice that the above equation uses the absolute value which is able to avoid the cancellation of positive and negative residuals. If the value of MME is close to 1, it indicates a good prediction.

The above description implies that for a high accuracy fitting, both values of R^2 and MME

should be close to 1 (R^2 from a low value and MME from a high value). In a figure including both MME and R^2, one only needs to compare the distance between R^2 and MME to assess models. If these two values are close, it implies a good fitting result.

3.8.2 Determination of the number of points for the fitting

Adopting a three-parameter model to fit both main sorption curves means totally six undetermined parameters (three for each main curve). In fact, an alternative approach can reduce the number of undetermined parameters. The parameter a_X in Eq. (3.11) (or a_V in Eq. 2.4) is an air-entry pressure-related parameter. For cementitious materials, the air-entry pressure is very low and is negligible. Thus, the "first simplification" for the fitting is proposed: $a_{X,w}$ (or $a_{V,w}$) for wetting is assumed to be equal to $a_{X,d}$ (or $a_{V,d}$) for drying.

$$a_{X,w} = a_{X,d}\,; \quad a_{V,w} = a_{V,d} \tag{3.51}$$

To use the first simplification, the main desorption curve should be fitted firstly by using all measured data, and then $a_{X,d}$ (or $a_{V,d}$) is used to determine two other undetermined parameters for the main adsorption curve by fitting measured data. Thus, to check the fitting accuracy, one only needs to compare the main adsorption curves fitted by using the first simplification and by using the original method (with three undetermined parameters). Comparisons of fitted curves for Paste2, Paste3, Concrete2 and Concrete3 are presented in Fig. 3.22 by using the FX equation. Good agreement between the first simplification and the original method is observed in this figure.

According to the first simplification, the number of undetermined parameters for the fitting of both main sorption curves is reduced to five: three for the main desorption and two for the main adsorption isotherms. This may indicate that much less data are able to fit two main sorption curves. Therefore, the "second simplification" is proposed here: five points are enough to predict both main sorption isotherms (three points on the main desorption curve and two points on the main adsorption curve). Mathematically, this simplification is no problem, but it needs to carefully examine the accuracy of the fitting. The priority for the second simplification is to determine the positions for these five points.

3.8.3 Determination of the relevant positions of those five points

A simple way is used to determine the positions of those points. Firstly, a model (FX or VG3) is used to fit all the collected materials based on the first simplification, and then the mean residual (MR) at each measured point can be calculated.

$$\mathrm{MR} = \frac{1}{M}\sum_{i=1}^{M}|S_i^{pr} - S_i^{ms}| \tag{3.52}$$

where M is the number of materials. In this study, eight materials from the literature [23] are used so $M = 8$ (see Table 3.2).

The MR results for FX and VG3 models at each measured point are presented in Fig. 3.21. Points with the minimum values of MR are chosen as the more relevant positions to determine the desorption or adsorption isotherm.

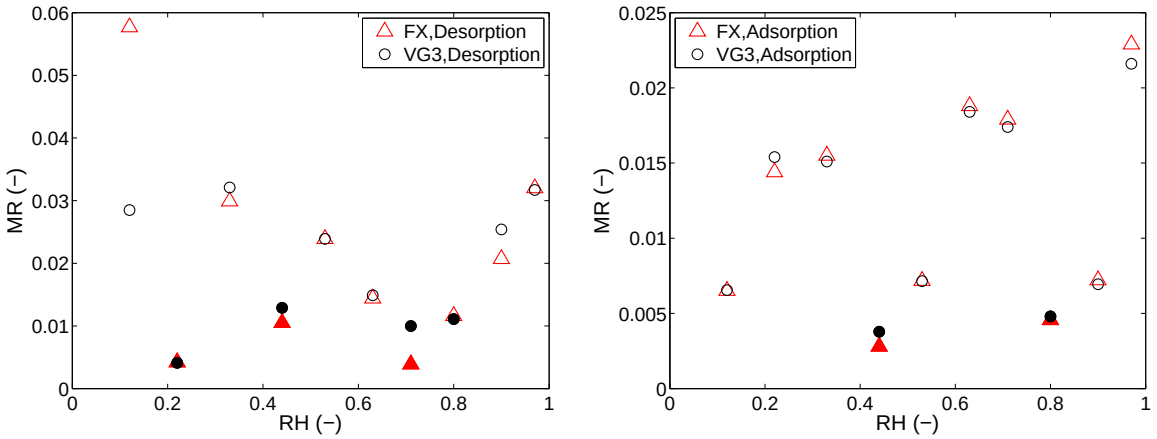

(a) Desorption. (b) Adsorption.

Figure 3.21: The mean residual for all materials at each measured point.

Relevant three points for the main desorption curve

MR results from FX model show that three most relevant points for the desorption isotherm are at RH = 22%, 44% and 71%, which correspond to the low, medium and high RH range. However, three points for VG3 are at RH = 22%, 71% and 80%, which gives two points in the high RH range. Actually, the MR value at RH = 44% is no significant different to RH = 80%. Hence, three points on the desorption isotherm are determined at RH = 22%, 44% and 71% for the purpose of getting the same positions for two models.

Relevant two points for the main adsorption curve

Results for the most relevant two points are at RH = 44 and 80% for the adsorption isotherm. FX and VG3 models reveal a high consistency for these two points.

3.8.4 Fitting results and comparisons

In the previous study on Feng and Fredlund's model [160] (see Section 3.5.2), two points on the main adsorption curve were fixed at RH = 63% and 90%. In this section, this method is also compared with the newly proposed method.

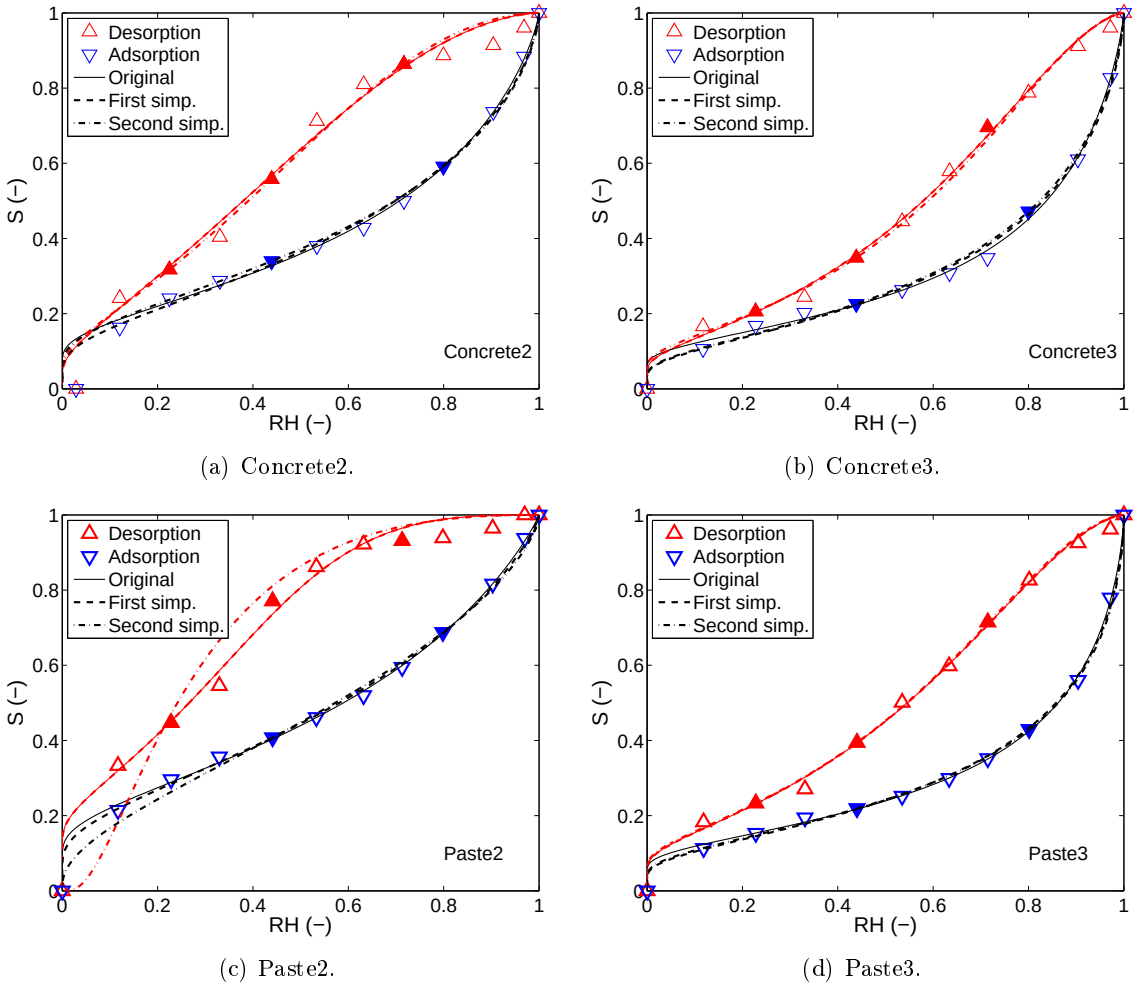

(a) Concrete2. (b) Concrete3.

(c) Paste2. (d) Paste3.

Figure 3.22: Comparison of results calculated by three versions of FX model. Points chosen to solve equations are highlighted (solid symbols).

The fitted main sorption curves for several selected examples (Concrete2, Concrete3, Paste2 and Paste3) are shown in Fig. 3.22. The suggested five points are highlighted in this figure. Only

results for FX model are presented here because VG3 provides the similar fitting results. Values of the new criterion for all the compared methods are given in Figs. 3.23 (FX) and 3.24 (VG3).

Firstly, let's focus on the results calculated by the first simplification. Bearing in mind that this simplification only affects the fitting of the main adsorption curve. Figure 3.22 shows that adsorption curves fitted by using the first simplification are nearly identical to curves fitted by the original method. Figures 3.23 (FX) and 3.24 (VG3) also show that this simplification can provide the similar accuracy to the original method.

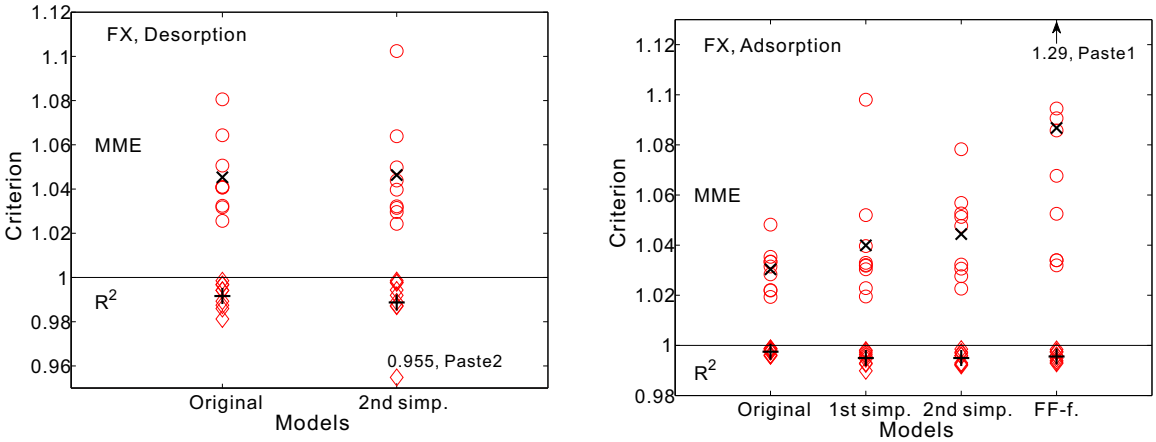

(a) Desorption. (b) Adsorption.

Figure 3.23: Comparison of calculated R^2 and MME for FX model. Each diamond ($\diamond$) or circle ($\circ$) for R^2 or MME stands for one material. "+" is the mean value of R^2 and "$\times$" is the mean value of MME.

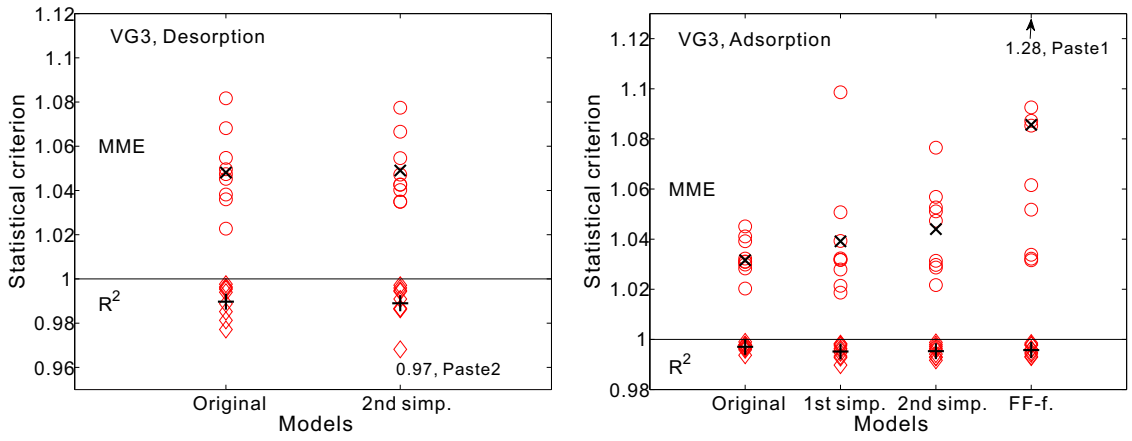

(a) Desorption. (b) Adsorption.

Figure 3.24: Comparison of calculated R^2 and MME for VG3 model. The other explanations of legend are the same as Fig. 3.23.

Then, let's check the applicability of the second simplification. For most materials, this simplification works quite well for both main desorption and adsorption curves. However, for Paste2, it shows clear disagreement with the original model for the fitting of the main desorption curve. It is mainly due to the shape of measured desorption isotherm. For Paste2, the desorption curve remains at high water content in the range of RH $>$ 63%. But when RH $<$ 63%, the curve drops more rapidly than other materials.

Values of the new criterion in Figs. 3.23 and 3.24 clearly show that the second simplification has the equivalent accuracy as the original method for both FX and VG3 equations when they are used to fit the main desorption curve. Only Paste2 shows the poor performance for the second simplification (see the highlighted diamonds in Figs. 3.23 and 3.24). For the fitting of the main adsorption curves, the distance between mean MME and mean R^2 increases from the original method to the second simplification. Nonetheless, the mean value of MME for the second simplification remains around the same order as that in the prediction of desorption isotherm. Thus, the slight difference between the original method and the second simplification is acceptable.

Lastly, let's focus on the prediction accuracy of improved Feng and Fredlund's model [160, 163] whose MME and R^2 are presented in Figs. 3.23b and 3.24b. Obviously, this model provides a high mean value of MME, meaning that it performs poorer than the two simplifications which were proposed in this section. It is concluded that two points which were previously suggested for Feng and Fredlund's model [160] cannot be used for FX or VG3.

3.8.5 Discussion on the proposed approach

A method to fit the main desorption and adsorption curves by using five points has been proposed. There are some details which need to be discussed.

Comments on the necessary number of points

Results from the second assumption reveal that this assumption is valid for most materials, except Paste2. This may imply that more points are needed for this kind of material. Paste2 has more C-S-H pores which mainly control the shape of sorption isotherm in the low RH range. Thus, one more measured data is added in this range for the main desorption curve. Here, the point with lowest RH in the measured data is chosen (at RH = 12%). Therefore, two points (RH = 12% and 22%) in the low RH range are used for the fitting. Results fitted by FX and VG3

models are shown in Fig. 3.25.

Notice that after adding one point for the main desorption curve, it will affect the value of $a_{X,d}$ (or $a_{V,d}$). This may have an indirect influence on the fitting of the main adsorption curve. But it still needs two points for the main adsorption curve. Obviously, Fig. 3.25 show that one more point can significantly improve the prediction accuracy. The calculated curves (either for main desorption or main adsorption) show extremely high agreements with the original method. Hence, it requires four points to predict the main desorption curve for Paste2.

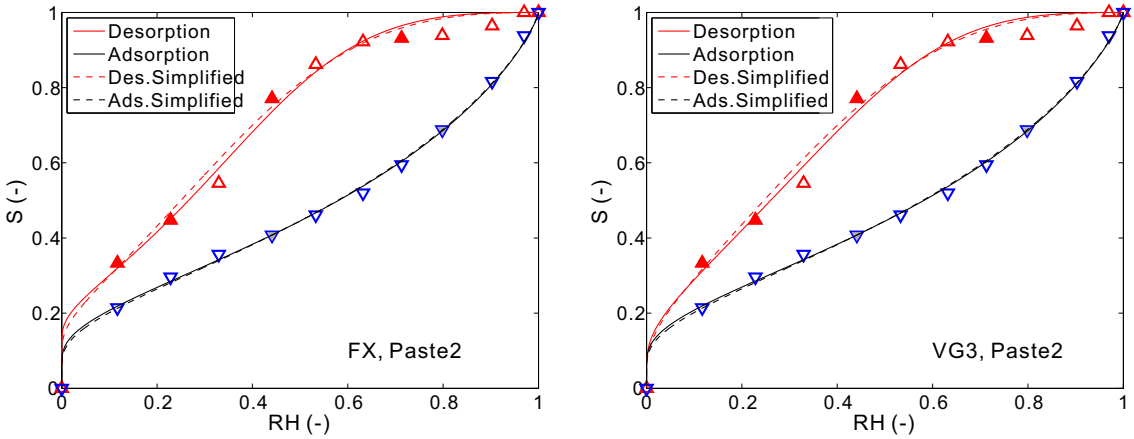

(a) The FX model. (b) The VG3 model.

Figure 3.25: Results calculated by FX and VG3 models for Paste2 in the case of adding one more point.

Comments on the relevant positions of points

Three points on the main desorption curve can be considered as three parts: low RH range (represented by RH = 22%), medium RH range (represented by RH = 44%) and high RH range (represented by RH = 71%). In the low RH range, moisture transport is dominated by C-S-H pores, while in the high RH range it is controlled by capillary pores. The medium range shows a mixed influence from both C-S-H and capillary pores. Those positions may vary according to different methods to measure WVSIs (the saturated salt solution, DVS, etc.). However, these three parts of a desorption isotherm should be always remained.

The point at RH = 44%, which is a special point that has been emphasised in the literature [23], is used for the fitting of both main desorption and main adsorption curves. It was reported that almost all the studied materials have the same shape of adsorption isotherms when RH<44% [23]. It can roughly be considered as the threshold value which is able to separate C-S-H

and capillary porosities.

3.9 Conclusion and recommendations

Detailed comparisons of hysteresis models for cementitious materials were performed in the current chapter. Two quantitative criteria, R^2_{adj} and MME, were used to quantitatively evaluate comparisons. A new way to fit the main desorption and main adsorption curves by using the fewest experimental data was proposed. A number of conclusions about hysteresis models are drawn from this study.

1) Although the cementitious materials have quite different pore structure compared to soils, sands and rocks, most models from these fields can be used to fit the main curves and to predict hysteresis loops for cementitious materials.

2) Among the selected five main isotherm fitting equations, the three-parameter fitting models provided better results than the two-parameter models. The equation proposed by Fredlund and Xing [161] provided the best fitting results. It is able to fit the shape of WVSIs very well and to capture the physical relationship between the desorption and adsorption isotherms.

3) There is no relevant model which is able to infer one main isotherm based on the other main isotherm. By using more experimental data, one wetting scanning isotherm for Mualem [167] and two uncertain points on the adsorption isotherm for improved Fend and Fredlund's model by Pham et al. [163], they show a high accuracy prediction. But these requirements restrict the use of these two models.

4) Concerning hysteresis models, empirical ones have a slight better prediction for the first scanning isotherms than the domain theory models. For multi-loops hysteresis simulations, empirical models also showed the simplicity of use. However, the non-physical behaviour, "pumping effect", is a controversial issue for empirical hysteresis models.

5) The domain theory models is able to avoid the pumping effect autogenously due to the assumption used in the diagram such as Neel diagram [149] and Mualem diagram [53]. This is one of main advantages to use conceptual models. In this chapter, the recommended models are Mualem Model II [53] and improved Rubin's model [177, 144] for further use.

6) To predict both desorption and adsorption isotherms, for ordinary materials, suggested five points (three for the main desorption isotherm and two for the main adsorption isotherm) can provide the same fitting accuracy as using the original model. For some high performance materials (e.g., Paste2), the use of one more point at low RH is able to greatly improve the fitting accuracy.

7) The positions of those points were verified by collected experimental data. Finally, those points are given at RH = 22%, 44% and 71% for the main desorption curve and at RH = 44% and 80% for the main adsorption curve. One more point for the main desorption curve for Paste2 is chosen at RH = 12%.

In this chapter, although a complete set of hysteresis models was concluded, it still needs more experimental data to refine these conclusions. Because only experimental data measured by the saturation salt solution were chosen in the current chapter, one main task for the next chapter is to carry out measurements of sorption curves by using DVS method.

Chapter 4

Experimental investigations

Summary

As stated in the previous chapters, the objective of this work is to study the internal moisture behaviour responding to external RH changes, not only by numerical modelling but also by experimental investigations. A simplified model for moisture transport during drying has been introduced in Chapter 2. In Chapter 5, this model will be used to simulate moisture transport under drying and wetting cycles. Experimental data will be needed to feed the model, to calibrate undetermined parameters and to verify the modelling results. This chapter will provide these experimental data. They are complementary to the data taken from the literature or data which have been measured at IFSTTAR in the previous studies [21, 22, 23, 11, 24].

Two main experiments, drying-wetting cycles measurements and sorption isotherms measurements, will be introduced. Sorption isotherms measured by DVS and pressure plate are the input data for modelling. DVS and pressure plate measurements were conducted at Lund University which is one research partner in the TRANSCEND project. Measured mass loss curves during drying will be used to determine the liquid intrinsic permeability by inverse analysis which has been adopted in Chapter 2. Mass loss curves in latter processes (wetting and re-drying) and saturation profiles measured by gamma-ray attenuation technique will be used to verify the different modelling methods in Chapter 5.

4.1 Materials preparation

In previous studies led by Baroghel-Bouny [22, 23, 11] and Nguyen [24], many experiments for various mixtures of cementitious materials have been done. In this study, cements and mixture designs are different from experiments mentioned above. Three water-to-cement (or binder) ratios (w/c or w/b) were used for all binders. Materials and their porosities are presented in Table 4.1.

Table 4.1: Materials and mix designs used in the present study.

Binders	Name	w/c (w/b)	Porosity ($\times$ 100%)[a]
CEM I-32.5 R	PCEMI04	0.4	0.377
	PCEMI05	0.5	0.457
	PCEMI06	0.6	0.511
CEM III/B-42.5 N	PCEMIII04	0.4	0.216
	PCEMIII05	0.5	0.456
	PCEMIII06	0.6	0.510
CEM I-32.5 R + 10% silica fume	PSF04	0.4	0.344
	PSF05	0.5	0.407
	PSF06	0.6	0.498

The classification of these binders is according to EN 197-1 European standard. Cements were supplied by HeidelbergCement®. There are 9 different mix designs (3 w/c $\times$ 3 binders). The procedure of preparing paste materials followed European standard EN 196-1. The pastes were cast in cylindrical plastic bottles with 7 cm-diameter and 14 cm-height. After the casting, these bottles were kept at room temperature for curing (23 °C).

The hardened samples were submitted to gamma-ray attenuation test to check the homogeneity inside the sample after one-day curing. Results for two examples (CEM I with w/c = 0.6 and CEM III with w/c = 0.5) are presented in Fig. 4.1. The density of the material is quite uniform throughout samples, implying no severe aggregation occurred.

4.2 Drying-wetting experiments

During drying-wetting experiments, materials were subjected to cyclic RH at the boundary. In order to quantitatively measure mass loss and saturation profiles, the geometry of samples has to be properly defined. After more than four months of sealed curing, the cylindrical bottles were demoulded and cut into samples of 10 cm-length (7 cm-diameter).

[a]Measured by weighing.

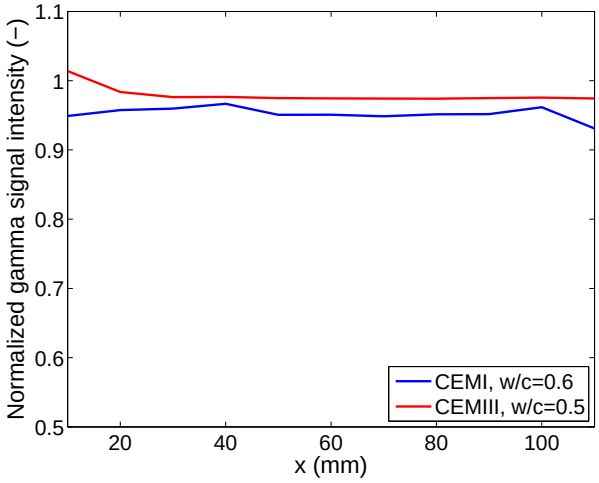

Figure 4.1: The gamma-ray signal intensity at different positions inside materials after 1-day curing.

4.2.1 Experimental procedure

The drying-wetting experiments started with the saturated state because it is the easiest way to be sure that the materials have uniform water content. The saturation method corresponds to the vacuum saturation. The procedure to conduct the vacuum saturation has already been used in the literature [24, 122, 181, 123]. After the vacuum saturation, all sides of the sample were tightly sealed by at least double layers of adhesive aluminium sheet, except one face which is exposed to the ambient environment (see Fig. 2.1 in Chapter 2).

Experiments were conducted under room temperature (23 °C). The RH cycle used during experiments is presented in Table 4.2. All samples were stored in dry keepers with a certain saturated salt solution which provided a stable and constant RH environment.

Table 4.2: RH cycles used during drying-wetting experiments.

Materials	RH cycles (%)
All Pastes	Saturation→33.0 →80.0→53.5

The weight of samples was regularly measured. Meanwhile, the gamma-ray attenuation measurements were conducted to provide data for calculation of porosity and saturation profiles. It was carried out monthly or when RH was switched to next step. The description of gamma-ray attenuation technique can be found in references [130, 182]. This technique has been widely-used in studies on cementitious materials, especially at IFSTTAR (e.g., [132, 24, 122, 181, 123]).

The last step of the experiment was to dry the sample at 105°C to get the dried mass in

order to determine porosity and liquid-water saturation.

4.2.2 Porosity profiles

Due to the absorption of gamma-ray photons by the material, the intensity of gamma rays suffers a loss of intensity while passing through the material. The amount of lost radiation depends on the type of the radiation source, the density of the material and the traversed thickness. The relationship between the intensity of incident and transmitted photons is given by Beer-Lamber's law [183],

$$I = I_0 \exp(-\mu \rho_m d) \tag{4.1}$$

where I_0 is the incident photon intensity (the number of photons measured in the air). I is the transmitted photon intensity (the amount of photons that passes through the material with thickness d (m)). ρ_m ($\mathrm{kg \cdot m^{-3}}$) is the material density and μ ($\mathrm{m^2 \cdot s^{-1}}$) is the mass absorption coefficient of the material (also called attenuation coefficient). If parameters μ, d, I and I_0 are known, the material density ρ_m at the measured point can be calculated.

Table 4.3: The mass adsorption coefficient for studied CEM I pastes.

Composition	μ_i	w/c = 0.4		w/c = 0.5		w/c = 0.6	
		w_i	$w_i\mu_i$	w_i	$w_i\mu_i$	w_i	$w_i\mu_i$
CEM I	0.0774	0.7143	0.0553	0.6667	0.0516	0.6250	0.0484
Water	0.0857	0.2857	0.0245	0.3333	0.0286	0.3750	0.0321
$\sum w_i\mu_i$			0.0798		0.0802		0.0805

The mass absorption coefficient is calculated based on the chemical composition of the material. Because calculation results show that cement pastes made by three binders (CEM I, CEM III and CEMI+SF) have very close μ values [132, 122]; only calculated coefficients for CEM I pastes are presented in Table 4.3 (w_i is the weight ratio of each composition).

If applying Eq. (4.1) to the saturated state and the dried state, it gives the equation to calculate porosity at each depth of the sample [132]:

$$\phi = \frac{\rho_{sat} - \rho_{105}}{\rho_l} = \frac{1}{\rho_l \mu_l d} \ln\left(\frac{I_0^{sat} I^{105}}{I^{sat} I_0^{105}}\right) \tag{4.2}$$

where superscripts *sat* and 105 represent measured data at the saturated state and the dried state, respectively.

The porosity profiles measured by gamma-ray attenuation for nine mixtures are shown in

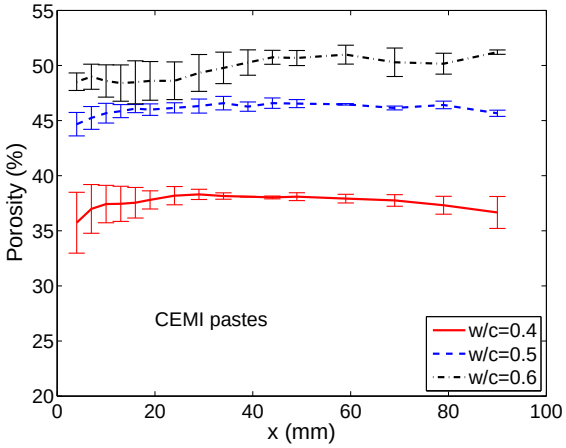

(a) CEM I pastes

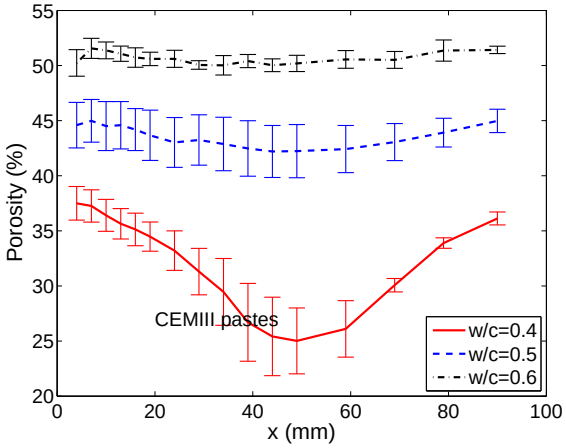

(b) CEM III pastes

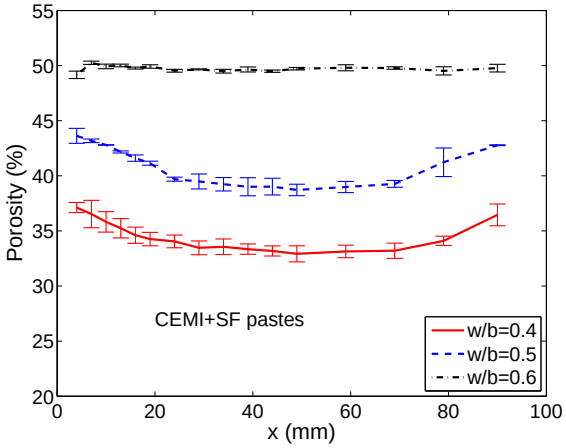

(c) CEM I+SF pastes

Figure 4.2: Profiles of porosity measured by gamma-ray attenuation for cement pastes. Error bars are added.

Fig. 4.2. Each curve in this figure corresponds to the average of at least two samples. Most porosity profiles are flat, showing homogeneous density distribution in the material. However,

for PCEMIII04, PCEMIII05, PSF04 and PSF05, there are some discrepancies between the middle and the surface of the material. This phenomenon is more significant for PCEMIII04, whose discrepancy reaches 15%. The main reason is that materials were not completely saturated during the vacuum saturation at the beginning of experiments. Because materials of CEM III and CEM I+SF with lower w/c (w/b) have fine pore structures, the duration of vacuum saturation was not long enough to let all C-S-H pores filled with water. Therefore, the initial state of experiments is not uniformly-saturated as it was expected. It leads to low accuracy of experimental data for PCEMIII04, PCEMIII05, PSF04 and PSF05.

Another thing for all curves is that error bars at the surface are much larger than them inside materials. This is clearer for CEM I pastes (all three w/c). The possible reason is that the latent hydration process was still going on inside materials, but hydration for the part near the surface has been already stopped due to less water in this part when the material was subjected to low RH for drying.

The global porosity for the sample is approximately calculated through the known porosity at each depth by gamma-ray attenuation.

$$\phi_\gamma = \frac{1}{l} \sum \phi_i \Delta x_i \tag{4.3}$$

where l is the length of the sample and Δx_i is the length associated with the ith measured depth.

Besides, when the sample was vacuum saturated, the global porosity is also determined by the weight of the sample in the air, in the water and after dried at 105 °C.

Table 4.4: The comparison of global porosity (%) measured by weighing and gamma-ray for cement pastes.

Materials	Methods	w/c = 0.4	w/c = 0.5	w/c = 0.6
CEM I	ϕ_{weigh}	37.7 ± 0.6	45.7 ± 0.2	51.1 ± 0.0
	ϕ_γ	37.6 ± 0.1	46.1 ± 0.4	49.8 ± 0.9
CEM III	ϕ_{weigh}	31.6 ± 1.5	45.6 ± 2.2	51.0 ± 1.0
	ϕ_γ	31.6 ± 1.4	43.5 ± 1.9	50.7 ± 0.7
CEM I+SF	ϕ_{weigh}	34.4 ± 0.3	40.7 ± 0.0	49.8 ± 0.1
	ϕ_γ	34.3 ± 0.2	40.5 ± 0.1	49.7 ± 0.2

Comparisons of global porosities measured by these two methods are given in Table 4.4. It shows a high agreement between porosities measured by these two methods. The biggest difference which is found for paste CEM III with w/c = 0.5 is only around 2.2%.

4.2.3 Profiles of saturation

Saturation during experiments at each point is calculated based on measured densities at saturated and dried states. As mentioned above, variations of measured gamma-ray intensities at different time are caused by the different moisture content in the material. Thus, S is calculated based on measured gamma-ray intensities at saturated and dried states at each depth of the sample.

$$S = \ln\left(\frac{I_0 I^{105}}{I_0^{105} I}\right) / \ln\left(\frac{I_0^{sat} I^{105}}{I^{sat} I_0^{105}}\right) \tag{4.4}$$

Two examples of measured saturation profiles for PSF05 and PSF06 during drying, wetting and re-drying are shown in Fig. 4.3. Because the duration for each process is not long enough, the influence of varying RH at the boundary on water content has not reached the inside part of the material. Saturation in PSF05 beyong $x = 40$ mm shows no changes during experiments. For PSF06, there is only a small decrease. Both Figs. 4.3a and 4.3b show that some measured data are slightly higher than 1. This is due to the problem that materials were not fully saturated when the experiments started. For PSF05, this mistake is much clearer than PSF06.

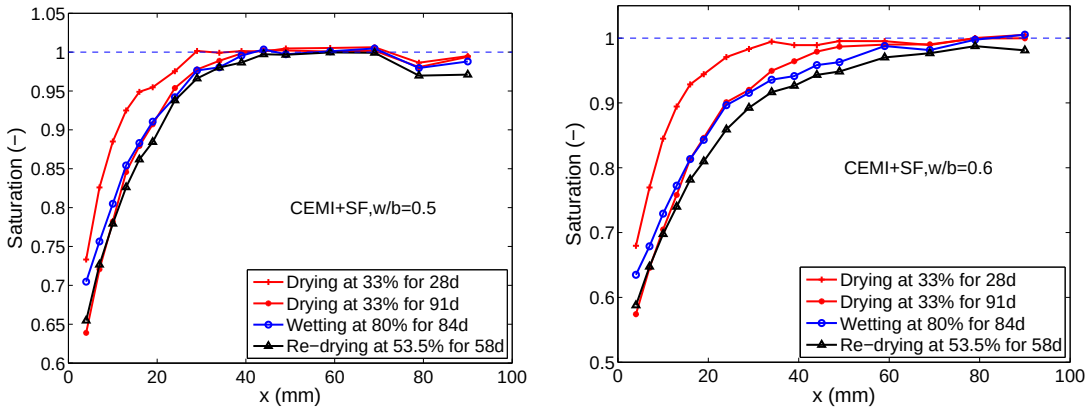

(a) PSF05 (CEM I+SF, w/b = 0.5)

(b) PSF06 (CEM I+SF, w/b = 0.6)

Figure 4.3: Examples of saturation profiles measured by gamma-ray attenuation.

4.2.4 Data consistency analysis

Actually, the total mass loss at the different times can be calculated based on the saturation profiles measured by the gamma-ray attenuation method.

$$m_{loss} = \sum m_{loss,i} = \sum (S_{0,i} - S_i) \Delta x_i \phi_i A \rho_l \tag{4.5}$$

where $S_{0,i}$ and S_i represent the initial saturation and measured saturation at each depth, respectively. ϕ_i is the porosity of the ith depth. A is the area of the cross section.

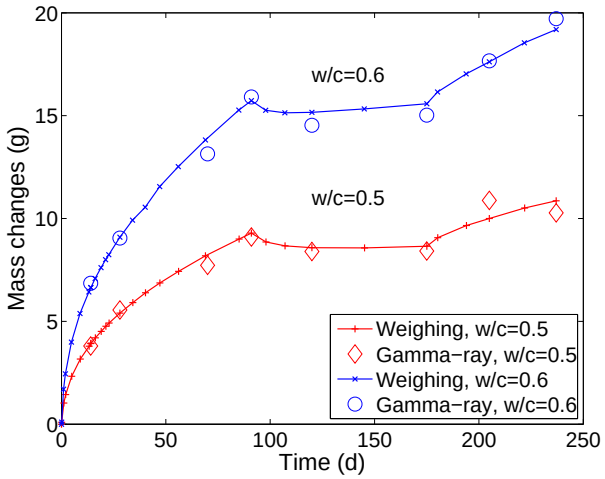

Figure 4.4: Comparisons of mass loss curves measured by gamma-ray attenuation and by global weighing for CEMI + SF pastes.

As mentioned before, the mass loss curve has been measured by weighing and therefore data consistency between the global weighing and the integration of gamma-ray attenuation data can be obtained. In other words, two mass loss curves measured by two methods should match. Good agreements between these curves for PSF05 and PSF06 are shown in Fig. 4.4. It proves the applicability of using these two methods to measure mass changes of cementitious materials.

4.2.5 Results of drying and wetting experiments

Two sets of experimental results, including mass loss curves and saturation profiles, have been shown in Figs. 4.4 and 4.3 for PSF05 and PSF06. Even if RH fluctuates at the boundary from drying to wetting, and then to re-drying, saturation profiles inside the material constantly decrease. The main reason is that RH at the boundary is smaller compared to RH in the inner part; therefore, moisture is always moving to the surface part. However, because the boundary RH (80%) during the second step is higher than that during the first (33%) step, moisture is able to transport from the surrounding to the surface region of the material. Owing to effects of these two opposite transports, mass loss curves are quite flat during the period at $\mathrm{RH}^e = 80\%$. Another reason is that it needs time to show effects of RH changes at the boundary on internal moisture transport due to the very slow moisture transport in the material. Longer experiments would be able to show more obvious differences between different measured saturation profiles.

4.3 Sorption isotherms measurements

As mentioned in Chapter 3 (see Section 3.3.2), both saturated salt solution method and DVS are able to measure WVSIs. Compared to the saturated salt solution method, DVS uses tiny specimens, usually less than 1 g, so that it takes much shorter time to obtain a sorption curve. Besides, this research only uses cement pastes and therefore no effect of aggregates needs to be considered. Hence, the choice of a DVS instrument to measure WVSIs should be acceptable. However, DVS is only valid in the hygroscopic range, up to around RH = 95%. For higher RH, such as above 97%, water content was determined by another method called "pressure plate".

4.3.1 DVS method

DVS is a relatively new technique for water vapour sorption analysis in the field of cementitious materials. Three main aims that a DVS apparatus needs to achieve are: constant temperature, stable RH and accurate mass weighing [184, 185, 186, 187, 8, 188, 189, 190]. The equipment is placed in an incubator, permitting the temperature to be kept constant. The required RH is created by mixing two gas flows with known RH: one is a completely dry nitrogen gas and the other with 100% RH. Each flow is controlled by thermal conductivity mass flow controllers. The relative humidity of the mixed gas flow could be varied between 0 and 98%. Nitrogen gas can also prevent the further carbonation during measurements.

The other main component of a DVS system is the micobalance, which continuously weighs the mass of the sample as a function of time. The microbalance is protected against high relative humidity by a continuous flow of dried nitrogen gas.

Procedure of DVS measurements

Before measurements, the large sample was vacuum saturated, and then crushed into small pieces. Usually, 30-70 mg materials (pieces mixed with powders) were randomly chosen and put in the sample pan. All measurements were performed at 23 ± 0.1 °C.

A full cycle of measurements starts with desorption at RH = 95% and continues stepwise to a low RH = 30%. After equilibrium, the inverted process was performed, until RH = 95%, and then the direction would be changed again until the completely dried gas flow (RH = 0%, see Fig. 4.5). As mentioned above, a maximum RH approximately 98% can be used. However, RH = 95% was chosen since the time needed to reach equilibrium at a higher RH is estimated

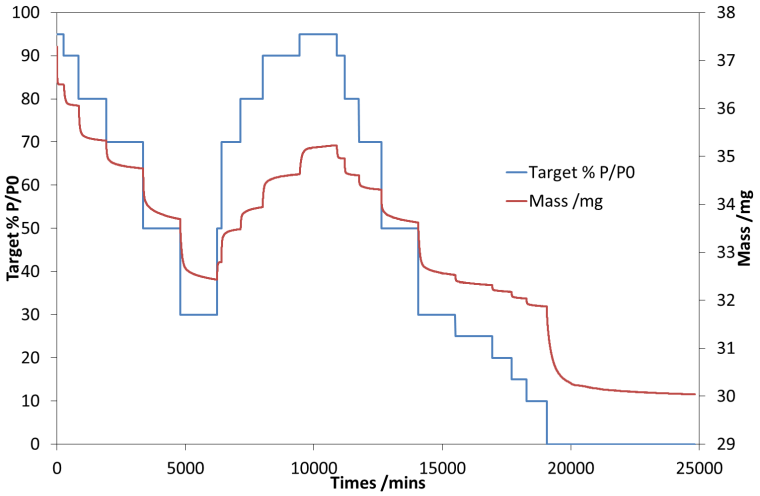

Figure 4.5: An example of controlled RH used in measurements (blue line) and measured mass changes (red line) at different RH.

extremely long. Because the lower RH can induce the more serious drying shrinkage [3]. Hence, in our measurements, RH only decreases to 30% in the first desorption process to avoid the further damage of the microstructure.

The equilibrium is defined in two ways, either by setting a fixed duration for each RH step or by using the relative mass change difference in time. The relative mass difference in time ($\mathrm{d}m/\mathrm{d}t$) is the rate of the change in mass over a certain period. Preliminary testing revealed that the balance was insufficiently stable to allow use of the relative mass difference in time as an equilibrium criterion [190]. The swing of the sample because of the gas flow made the measurement difficult to reach an equilibrium state. Therefore, a relative mass difference criteria ($\mathrm{d}m/\mathrm{d}t = 0.0001$ %/min) coupled with a fixed maximum duration (2000 minutes) was used for each RH step.

Extrapolation of the mass loss curve

Sometimes, the mass loss curve for an RH step may not reach equilibrium. This could make the measured total relative mass change less than the realistic one. The curve extrapolation is needed to improve the measured results. Drying of the porous media, an exponential decay function is usually used to describe the mass loss as a function of time [12]:

$$\frac{m(t) - m_0}{m_f - m_0} = 1 - \exp(-pt) \tag{4.6}$$

where $m(t)$ is the measured mass of the sample, m_0 and m_f are the initial mass and the final mass, respectively. p is a parameter. m_f and p are needed to be fitted by the measured curve. The final mass m_f used to improve the measured results.

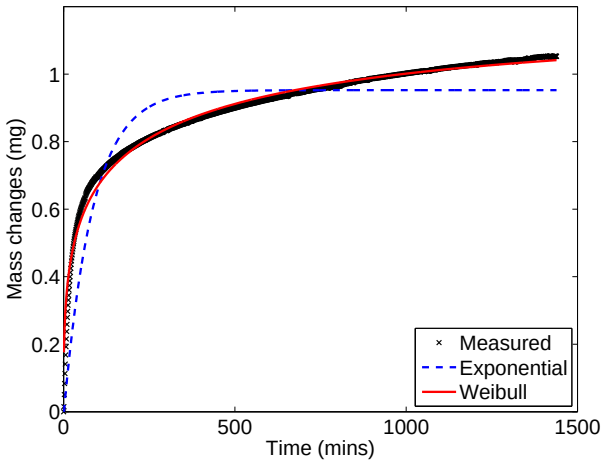

Figure 4.6: An example showing different extrapolation methods.

However, the curve extrapolated by the exponential function seems not match the measured curve very well as it is shown in Fig. 4.6.

Weibull [191] has proposed a cumulative distribution function which has been used to predict the mass loss of drying food [192, 193, 194]. The advantage of this method is that it is able to provide very good fitting results for drying of irregular shapes of materials like crushed cement pastes. This distribution function is written as:

$$\frac{m(t) - m_0}{m_f - m_0} = 1 - \exp\left[-\left(t/a_W\right)^{b_W}\right] \tag{4.7}$$

where parameters a_W and b_W, and the final mass m_f are adjusted to obtain good fitting with the measured curve. One result in Fig. 4.6 shows that Eq. (4.7) can provide very good fitting with measured mass loss curve.

Figure 4.7 shows one example of extrapolated mass loss curves and comparison between original and predicted desorption curves using Eq. (4.7). Since the equilibrium state was almost reached during each measurement process, the extrapolation does not show significant improvement to the desorption curve, especially in high and low RH ranges. However, in RH = 30-50% range, the extrapolation improves the results. Baroghel-Bouny [23] has reported that this feature is related to the transitional range between capillary porosity and C-S-H porosity. Sorption

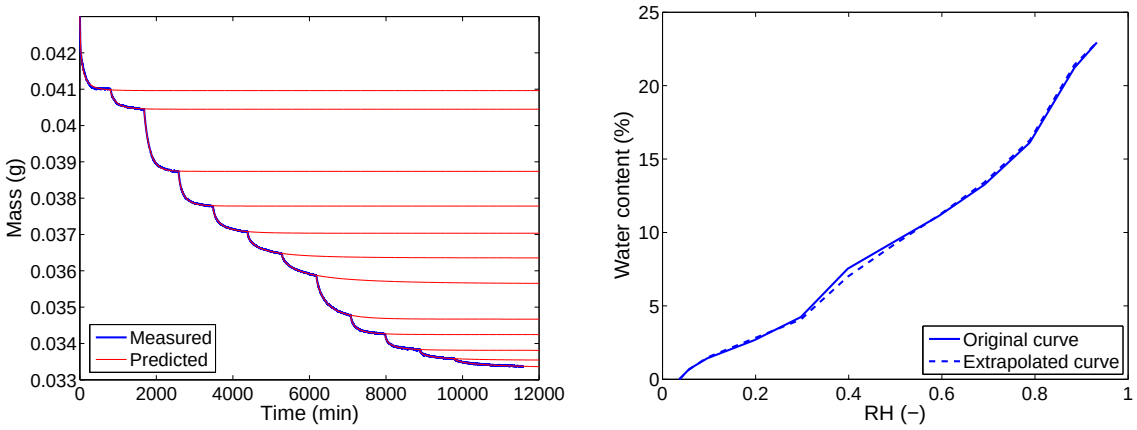

(a) Extrapolated curves. (b) Desorption curves.

Figure 4.7: One example of the comparison of original and extrapolated desorption curves measured by DVS.

equilibrium is not easy to be reached due to unstable moisture transport. This may indicate that in this RH range more strict equilibrium criteria should be used during a DVS measurement.

4.3.2 Sorption isotherms in high RH - pressure plate measurements

The sorption isotherm above the hygroscopic range is not only related to the sorption of water vapour, but also the suction of liquid-water. This part of curve shows the relationship between moisture content and pore water pressure. The simplest way to determine the curve in this part is to expose the material to a negative pressure $-\triangle P$, which is equal to the macroscopic capillary pressure P_c within the material at equilibrium. Therefore, liquid-water in the material can move under external pressure. This method has been widely used for more porous materials such as soils. By using Kelvin's equation, the relationship between this pressure and relative humidity can be established.

$$\mathrm{RH} = \exp\left(-\frac{M_v}{RT\rho_l} \triangle P\right) \tag{4.8}$$

Pores in cementitious materials are smaller than pores in soils, so the external pressure for cementitious materials is higher. The traditional measurement methods, which are only for smaller pressure, cannot be used for cementitious materials. This makes researchers to develop a new apparatus, called "pressure plate" (see Fig. 4.8) [190].

The detailed description of the theory and the measurement procedure of pressure plate have been reported in [190]. Here, only several important points are mentioned. Specimens for cement

pastes are prepared as very thin slices, between 3-4 mm, and the surface size is about 3 mm × 3 mm. Before the tests, all specimens were vacuum saturated.

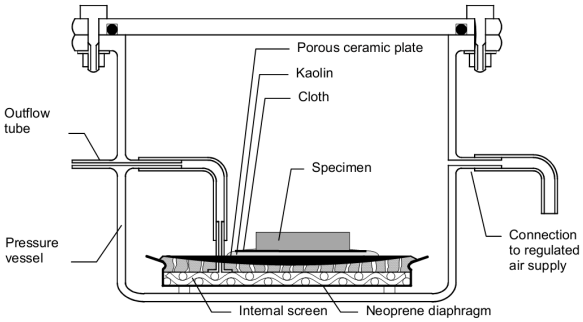

(a) Schematic sketch of the pressure plate extractors for pressure 1 MPa [185].

(b) Deployed specimens in the pressure plate extractor for pressure 3 MPa.

Figure 4.8: Pressure plate extractors used in measurements at Lund University. The circled specimen was blown away from the center due to the suddenly increased gas pressure.

For the tests, two different pressures were used: 1 MPa and 3 MPa, corresponding to RH = 99.26 and 97.81%, respectively. Tests for two pressures were run in two separate pressure plates. The schematic design of the pressure plate is depicted in Fig. 4.8a. For the low pressure test (1 MPa), to ensure hydraulic contact between the ceramic plate and the specimen, a thin layer of kaolin clay was applied to the ceramic plate. The thickness of kaolin clay is around 2 mm. Above the kaolin, a nylon cloth was put to prevent the specimen from being contaminated by direct contact with clay. For the high pressure tests (3 MPa), a cellulose membrane with considerably smaller pores was used instead of the ceramic plate to avoid that the high pressure may break the ceramic plate. A thin disc-shaped metal grid was located under and kaolin clay the cellulose membrane to allow water flow through the cellulose membrane. On the bottom, a Plexiglas plate was placed to provide a smoother and flat bed for specimens.

After the metal lid was sealed, the gas was let in to provide a certain pressure. Nitrogen was used instead of air to prevent further carbonation. At the beginning, the gas had to be provided very gently to avoid the displacement of specimens. Figure 4.8b shows that the suddenly increased gas pressure can induce high speed gas flow to blow the specimens away. After the pressure was applied, the water for the system flowed out through the outflow tube. The extracted water was continuously measured by a pipette. The equilibrium is defined when the water level in the pipette was constant for 48 hours. At this point, it is considered that the pressure in the plate is equal to the macroscopic capillary pressure within the specimens.

The measurement for each pressure lasted around 8 weeks. The mass of specimens was measured after the pressure plate opened. Those specimens were then dried at 105°C in an oven to get dried mass. Thus, water content of specimens for measurements at each pressure was determined.

4.3.3 Sorption isotherm measurements results

An example of the measured results for CEM I materials with three different w/c is illustrated in Fig. 4.9. From this figure, several behaviours can be observed:

(1) When RH decreases from 95% to 50%, desorption curves for the three studied materials are nearly parallel. This phenomenon is also found for desorption curves between RH = 30% and 5%, and for adsorption curves from RH = 30% to 95% which indicates that the drying behaviour (the process of releasing water) and the wetting behaviour (the process of adsorbing water) of these three materials are quite similar. This can only be explained by the fact that these three CEM I materials have some common features in microstructure properties, such as pore network connectivity which lets these materials release or adsorb the same amount of amount of water molecules in the same RH interval.

(2) For all these three materials, there is a large drop when RH changes from 40% to 30% (from 50% for w/c = 0.5 and 0.6 due to no measured data at 40%). Actually, the same trend is also found in experimental data measured by saturated salt solution method [23] between RH = 44% and 33%. This may be due to the fact that above this RH range, the capillary water presents in the material, but below this RH range there is no capillary water (even discontinuous capillary water) and water is mainly located in gel and interlayer pores.

(3) Points measured by pressure plate at RH = 99.26% are greatly higher than points measured by DVS at RH = 95%. It is acceptable because RH = 99.26% is above the hygroscopic range (capillary water range) and most large pores are filled up by liquid-water. However, there are some obvious problems for points at RH = 97.81%. For CEM I with w/c = 0.5, this point is very high, but for CEM I with w/c = 0.4 this point is slightly low compared to the point at RH = 95%. This may be due to some unpredicted measurement mistakes. Hence, the point measured at RH = 97.81% will not be used for modelling.

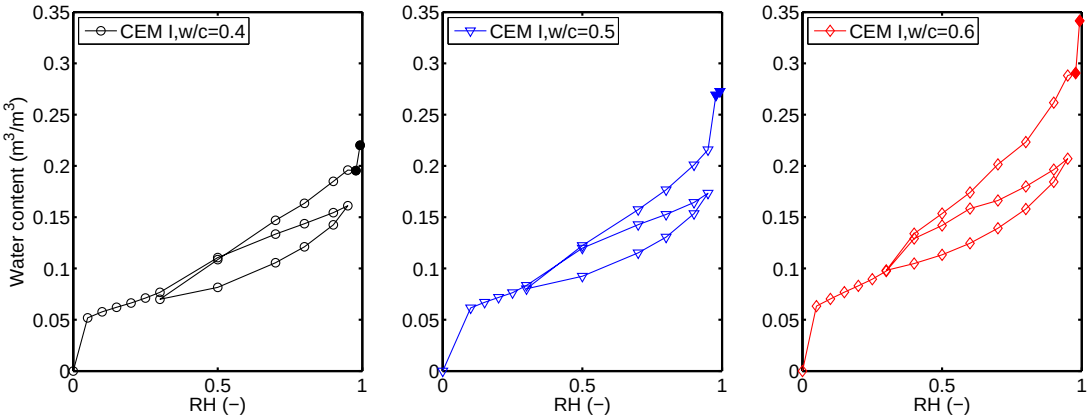

(a) PCEMI04 (CEM I, w/c = 0.4). (b) PCEMI05 (CEM I, w/c = 0.5). (c) PCEMI06 (CEM I, w/c = 0.6).

Figure 4.9: WVSIs measured by DVS and pressure plate for CEM I materials. Two points measured by pressure plate have been highlighted (solid symbols).

4.4 Determination of the main adsorption curve

The above measurements show that no entire main sorption curve has been measured, either for desorption or adsorption. For the desorption process, two separated curves were measured in two steps, from RH = 99.26% to 30% and from RH = 30% to 0%. In this study, these two parts are presumed to merge into one main desorption curve because scanning loops are always closed for cementitious materials. However, there are no measured data corresponding to the main adsorption curve. As a matter of fact, the adsorption curve measured between RH = 30% and 95% can be considered as the first wetting scanning curve which starts at RH = 30%. Therefore, the main adsorption curve can be approximately estimated by using the method proposed in Chapter 3 (see Sections 3.5 and 3.8).

Indeed, when discussing the use of the fewest data to predict the main adsorption isotherm (see Section 3.8), the conclusion was given that two points for the main adsorption curve in the high RH range and the middle RH (or low) range are enough to predict the entire curve. In the high RH range, the last point of the first wetting scanning curve measured at RH = 95% is supposed to be on the main adsorption curve. For the other point, the extended Mualem Model II (named Mualem Model II-1 in Chapter 3, see Section 3.5) is employed to estimate this point based on the point on the main desorption curve for the same RH. Even though this method has been criticised when it was used to predict the entire main adsorption curve, results in Chapter 3 presented that for points at RH = 44%, 33% and 22% this method showed smaller errors. Thus,

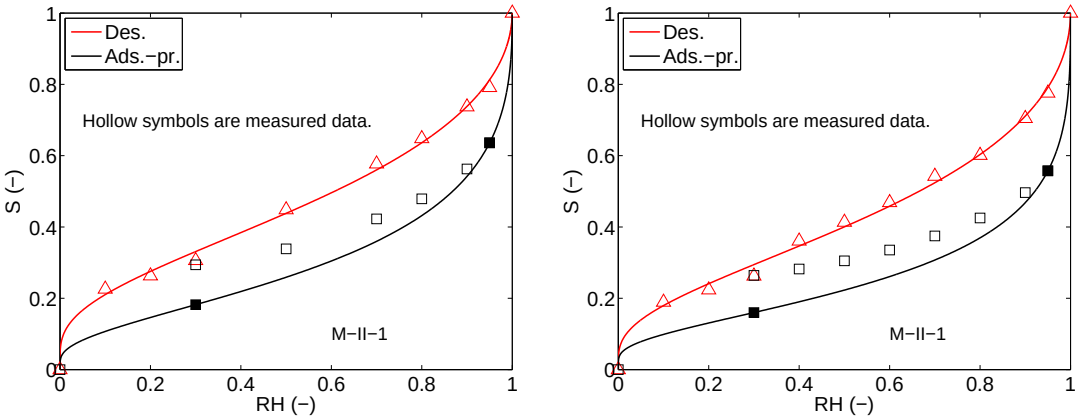

(a) PCEMI05 (CEM I, w/c = 0.5).

(b) PCEMI06 (CEM I, w/c = 0.6).

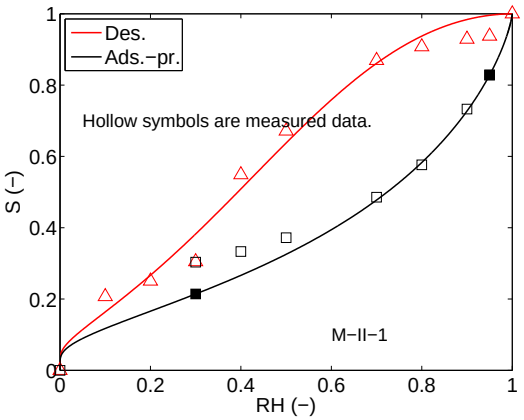

(c) PCEMIII05 (CEM III, w/c = 0.5).

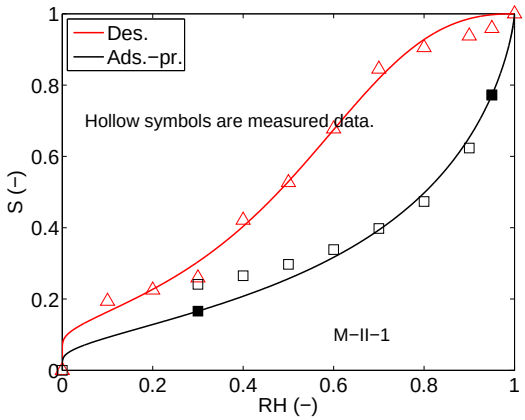

(d) PCEMIII06 (CEM III, w/c = 0.6).

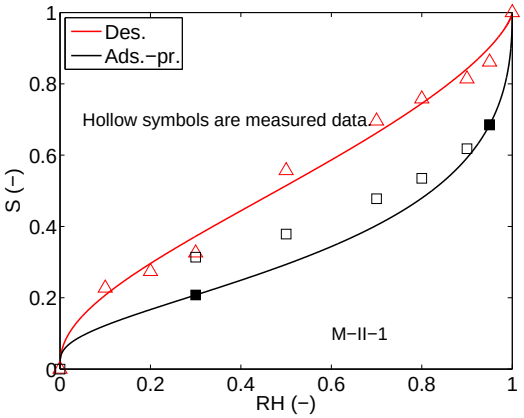

(e) PSF05 (CEM I+SF, w/b = 0.5).

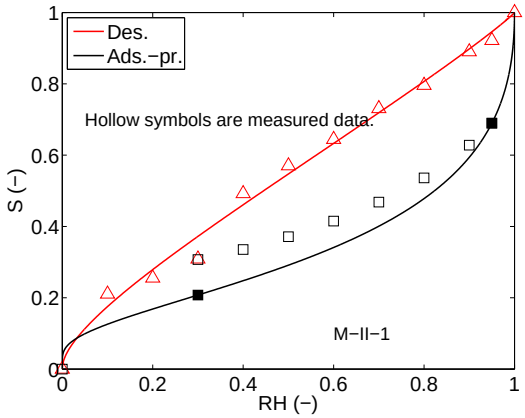

(f) PSF06 (CEM I+SF, w/b = 0.6).

Figure 4.10: Predicted main adsorption curves. Solid squares represent the points used to calculate the main adsorption curve.

the point at RH = 30% on the main desorption curve is chosen to estimate the point on the main adsorption curve for the same RH.

Prediction results for materials with w/c (w/b) = 0.5 and 0.6 are presented in Fig. 4.10. Overall, the predicted sorption isotherms have the similar trend to ones measured by the satu-

rated salt solution method in the literature (e.g., [23]). In the low RH range, hysteresis between two main sorption curves is smaller than hysteresis in the high RH range. This figure also clearly shows that CEM I materials have smaller hysteresis than CEM III and CEM I+SF materials. This is because the pore connectivity in CEM I materials is higher than that in CEM III and CEM I+SF materials.

If comparing sorption isotherms measured in this research with results obtained by the saturated salt solution method in [23] (see Fig. 3.6a for Paste3 in Chapter 3), one is able to find an obvious difference between these two measurement methods. DVS results show much smaller hysteresis between the two main sorption curves than results in [23].

This difference is certainly related to the different principle and procedure of these two measurement methods. DVS method is known as a dynamic approach which adopts flowing vapour to dry or wet the specimen. Flowing vapour can accelerate the drying or wetting rates. The real equilibrium between external RH and internal RH is not reached to some extent due to the disturbance of velocity of flowing vapour. Another important reason is the size of specimens. Tiny specimens were used for DVS measurements. In particular, these tiny pieces increase the total surface area of the material, so more water molecules can be adsorbed on the surface during wetting and released during drying. Besides, crushed materials contain less capillary pores so that "ink-bottle effect" is not so significant when DVS method is used.

4.5 Conclusion

In this chapter, the description of two experiments (drying-wetting experiments and WVSIs measurements) was presented. Based on the analysis of some results, the following conclusions are given.

1) Porosity profiles measured by gamma-ray attenuation method showed that most of the cement paste materials can be regarded as homogeneous porous media.

2) Comparisons of mass loss curves calculated based on data from gamma-ray attenuation and measured by weighing showed that gamma-ray attenuation technique provided very reliable results. Furthermore, the total porosities measured by gamma-ray attenuation also showed good agreements with these measured by weighing.

3) Weibull's equation is a good way to extrapolate the mass loss curve measured by DVS

when this curve has not reached equilibrium for an RH step.

4) The proposed method to estimate the main adsorption curve when it is not measured by DVS has provided satisfactory results. It should be further verified by more experimental data.

5) Compared to sorption isotherms measured by the saturated salt solution method, hysteresis between the two main sorption curves measured by DVS is smaller.

There are two problems for drying and wetting measurements. One problem is that samples were not fully saturated during vacuum saturation. This leads to experimental data for PCEMIII04, PCEMIII05, PSF04 and PSF05 less accurate. The other problem is that the duration for drying, wetting and re-drying was short. Hence, the measured saturation profiles are not distinctly different from one to another.

All experimental data obtained in this chapter will be used in the next chapter for validation of the proposed method to simulate moisture transport under varying boundary conditions. They will enrich the data previously obtained at IFSTTAR [21, 22, 23, 11, 24] and already used in Chapters 2 and 3. The use of the sorption isotherms measured by DVS instead of the saturated salt solution method and verification with more elaborated drying and wetting cycles will be clearly able to test the applicability of the proposed method.

Chapter 5

Modelling of moisture transport under drying-wetting cycles

Summary

In this chapter, a method coupling a moisture transport model with hysteresis models is proposed. Theoretically, this approach is applicable for most types of hysteresis models. Two hysteresis models, including a conceptual model and an empirical one, have been implemented and compared. Experimental data from the literature and measured in this thesis (see Chapter 4) are used to verify modelling results. Verifications show that the conceptual model yields better results than the empirical one. The main reason is that the empirical model provides a non-physical hysteretic behaviour, so-called "pumping effect". Meanwhile, comparisons of non-hysteresis and hysteresis modellings are carried out for different cycle durations, RH amplitudes, initial states, etc. All comparisons and investigations enhance the necessity of considering hysteresis to model moisture transport under cyclic drying and wetting conditions. The moisture penetration depth is also compared in cases of modelling with and without hysteretic effects. It has real valuable meaning for engineering.

Most simulation results in this chapter have been included in the paper that has been submitted to Cement and Concrete Research journal [195].

5.1 Introduction

In Chapter 1, a multiphase moisture transport model has been presented (see Section 1.4). In Chapter 3, commonly-used hysteresis models have been compared and verified by experimental data (see Section 3.6). It has concluded that Mualem Model II [53] and improved Rubin's model [177, 144] could be further integrated with moisture transport model. The current chapter is devoted to finding an appropriate modelling method to simulate moisture transport under varying ambient humidity loads. Hysteresis and non-hysteresis modelling methods will be implemented. Comparison of different modelling methods will be verified by experimental data, including mass loss curves and saturation profiles, from both literature and Chapter 4.

One important factor to evaluate the durability of concrete structures under varying RH at the boundary is called "moisture penetration depth" x_p which has major importance for engineers. This factor is used to quantify how deep moisture is able to penetrate into the material under cyclic RH at the boundary. It indicates as well the depth that ions can reach into the material with moisture variations. This is particularly important for the description of ions penetration under drying and wetting cycles. Earlier studies concluded that x_p is dependent on the material properties (porosity, diffusivity, etc.), the cycle duration and the external RH amplitude, except the initial condition [6]. Nevertheless, this conclusion was based on the non-hysteresis modelling. Results in the case of the hysteresis modelling have not been investigated yet. As a result, the current chapter will study effects of hysteresis on the moisture penetration depth.

5.2 Moisture transport models

In Chapter 2, a simplified moisture transport model has been introduced (see Eq. 2.33 in Section 2.4.2) based on the assumptions of constant gas pressure ($P_g = P_{atm}$) and negligible gas advection. Here, the mass balance equation is written as:

$$\frac{\partial S}{\partial t} = \frac{\partial}{\partial x}\left[D_a(S)\frac{\partial S}{\partial x}\right] \tag{5.1}$$

in which, the apparent diffusivity $D_a(S)$ has contributions from liquid-water and water vapour ($D_a(S) = D_l(S) + D_v(S)$, see Eq. 2.33).

As described in Chapter 1, Eq. (5.1) is one form of Richards' equation, which is known as the S-based form. If selecting other state variables, Richards' equation can be expressed in different

forms. A pressure-based form is obtained when the time derivative of S ($\partial S/\partial t$) on the left side of Eq. (5.1) is rewritten as follows: $C\partial P_c/\partial t$, where the moisture capacity C is defined as the slope of the sorption isotherm, that is $\mathrm{d}S/\mathrm{d}P_c$.

$$C\frac{\partial P_c}{\partial t} = \frac{\partial}{\partial x}\left[D_a(S)C\frac{\partial P_c}{\partial x}\right] = \frac{\partial}{\partial x}\left[K_a(P_c)\frac{\partial P_c}{\partial x}\right] \tag{5.2}$$

where $K_a(P_c) = D_a(S)C$ is the apparent permeability. In Eq. (5.2), P_c is used as the pressure potential. Actually, there is no difference to use P_c or P_l as the potential since $P_g = P_{atm}$.

A mixed form rises when both S and the pressure variables appear simultaneously in the governing equation.

$$\frac{\partial S}{\partial t} = \frac{\partial}{\partial x}\left[K_a(P_c)\frac{\partial P_c}{\partial x}\right] \tag{5.3}$$

These three forms of Richards' equations (Eqs. 5.1, 5.2 and 5.3) can be transformed from one to another based on the moisture capacity C. However, there are some differences in the numerical approaches to solve them. Milly [196] presented two mass-conservative schemes for computing nodal values of the moisture capacity in the pressure-based form to force global mass balance. In the study by Hills et al. [197], the S-based form of Richards' equation can show fast and accurate convergence for moisture infiltration. Kirkland et al. [198] expanded the work of Hills et al. by combining the S-based and pressure-based models to yield a transformation method applicable to unsaturated and saturated systems. Celia et al. [199] suggested that numerical solutions based on the standard pressure-based form of Richards' equation often present poor results, characterized by relatively large mass balance errors and incorrect predictions of the pressure distributions in the saturation profile. They solved the mixed form of Richards' equation that can reach mass-conserving properties for both finite difference and finite element spatial approximations. Additional transformations of Richards' equation, with the common goal of decreasing its non-linearity and increasing the efficiency of the numerical solution, were reviewed by Williams et al. [200]. Testing Dirichlet and Neumann boundary conditions for these three forms or equations, de Vasconcellos and Amorim [201] confirmed the conclusion by Celia et al. [199].

Hence, from the point of view of the numerical solution, S-based and mixed forms are better choices. The S-form allows for very efficient numerical convergence, even for infiltration into initially dry porous materials such as soils. However, moisture in porous materials does not necessarily flow under the gradient of S because the driving force for moisture movement is

not only the gradient of S, but also the pressure gradient. Another interesting thing between using S-based form and mixed form is quite special for modelling of moisture transport with hysteretic effects because these two forms can present different evolutions of scanning loops. This phenomenon will be discussed later in the current chapter (see Section 5.6.4).

In this research, the mixed form is adopted to simulate moisture transport. The potential in this form is capillary pressure (see Eq. 5.3).

5.3 Modelling methods

The main difference between non-hysteresis and hysteresis modelling is the use of sorption isotherms. Thus, methods to implement these two modelling methods are also different.

5.3.1 Modelling without hysteretic effects

Modelling of moisture transport without hysteretic effects is easily achieved by using the same sorption isotherm for both drying and wetting. Generally, the main desorption curve is used [6, 7, 16]. This method has been proved that simulation results do not agree with experimental data for the wetting process [117]. A new expression for sorption curves is proposed here on the basis of the measured main desorption and main adsorption curves involving a weighting factor $\omega = [0, 1]$.

$$S = \omega S_d + (1 - \omega) S_w \tag{5.4}$$

In Eq. (5.4), if $\omega = 1$, it corresponds to the main desorption curve; if $\omega = 0$, the main adsorption curve is used, and if $\omega = 0.5$ the sorption curve is the average curve. The parameter ω increases the flexibility of the use of this non-hysteresis modelling method.

5.3.2 Modelling with hysteretic effects

In order to incorporate a hysteresis model to simulate drying and wetting cycles, two issues need to be solved: how to check whether the node is going to change the state, and how to keep the node on the current state? Inspired by the work of Gillham et al. [202], two hysteresis indexes U and V are introduced to deal with each above issue. These two indexes have to be assigned to each node during the numerical calculations.

The index U is used to mark the current state. The initial values of U for all nodes are zero. If the initial step of a node is drying (the case of initial drying), U will keep on 0 until the state changes. If the initial step is wetting (initial wetting), U must change to 1. For the first node (the node on the surface of the material), the initial step can be determined by the sign of the RH difference between the boundary condition and the initial condition. The negative sign means initial drying, and the positive sign means initial wetting. For inner points, the initial step will be given during the numerical calculations. In the calculation, U will be added by 1 after the state changes once. So, the even numbers of U represent the drying process and the odd numbers stand for the wetting process.

The hysteresis index V is set as 0 at the beginning of the calculation. This index is used to notify the programme if one node has to change its state in next time step through checking whether the current state is consistent with the sign of the saturation difference between the current step and the previous step $\Delta S(i)$. If $\Delta S(i)$ is smaller than a criterion (such as $\xi = 10^{-10}$), but the current state is wetting (U is an odd number), this means that the node will turn to drying, and V is set as -1. If $\Delta S(i)$ is larger than a criterion ($\xi = 10^{-10}$), but the current state is drying (U is an even number), this implies that the node is going to change to wetting, and V is assigned to 1. If there is no state changes in the next time step, V has to become 0.

The combinations of these two indexes V and U are able to represent all states of one node during arbitrary drying and wetting cycles. After a number of cycles, index U can tell how many drying or wetting processes to which one given node has been subjected, and the Nth drying or wetting scanning curves on which the current node is. This is very useful for hysteresis modelling due to the strong sorption history-dependence.

Figure 5.1 demonstrates the use of these two indexes for one node. In natural conditions, the reinforced concrete covers are nearly saturated and exposed to a low RH environment which induces drying after the formwork removal. In this process, the $P_c - S$ relation is considered on the main desorption curve (see point A in Fig. 5.1) and it will stay on this curve until the next state changes. In this process, both V and U are zero and the programme checks if the state of this node is going to change by comparing the consistency between ΔS and U in each time step. Point B is where RH increases. At this point, ΔS is positive, but U is an even number, so the node will turn to wetting and the programme must assign 1 to V. After the state changes, V has to become 0. The scanning curve BC is used instead of the main desorption curve for this node. At the same time, U increases to 1 to note that the node is on the first wetting scanning

curve. In a similar way, when the state change occurs at point C, V becomes -1 to show that this node will be on drying in the next time step, and U increases to 2 to record the second drying scanning curve. In this way, the program can continue the calculation.

In this implementation method, reverse states (starting points of scanning curves) for each node have to be recorded, either for conceptual or empirical models. The programme can distinguish which state the node is on and continue the calculation through the combinations of these two indexes. For most hysteresis models, it is obviously easy to obtain reverse points for all nodes, so this method has a high applicability.

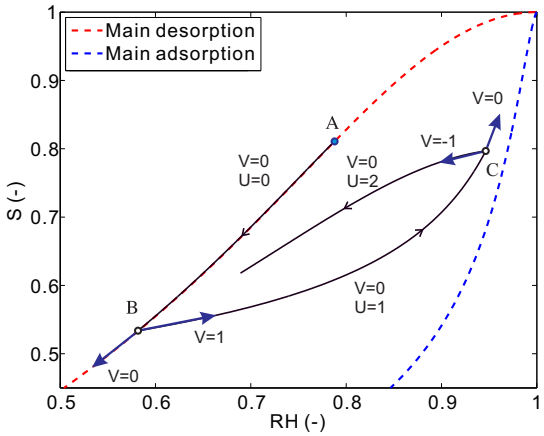

Figure 5.1: Implementation of the hysteresis modelling.

Overall, three modelling methods, including the hysteresis modelling (Mualem Model II and improved Rubin's model, see Section 3.6) and the non-hysteresis modelling, are able to simulate drying and wetting cycles. They will be compared in the following sections.

5.3.3 Numerical method

To solve the non-linear equations, a numerical algorithm has to be used. The spatial discretization is performed by the finite difference method, since only 1D problem is considered in this thesis. An implicit approximation (backward Euler method) in time step is employed to ensure the stability of the scheme. In each time step, the Picard iterative scheme is used to reach the numerical convergence criteria [199]. The time step is adaptive according to the convergence rate to solve the partial differential equation efficiently.

5.4 Verification with experimental data

5.4.1 Experimental data collection

Two main sources of drying and wetting experimental data will be used to verify the above proposed modelling methods. The first source of experimental data were collected from the literature [23, 24]. These materials are named Paste3, Paste4 and Paste5 (see Table 2.1). The drying experiments have been described in Section 2.2.2. After drying, all samples were exposed to $RH^e = 97\%$ (potassium sulfate, K_2SO_4) for wetting (see Fig. 5.2).

The water vapour sorption isotherms, including two main sorption curves and drying/wetting scanning curves, were measured by the saturated salt solution method as described in Chapter 3 (see Section 3.3.2). Saturation profiles were measured by the gamma-ray attenuation method [182, 24].

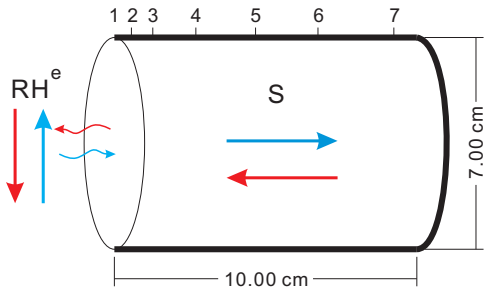

Figure 5.2: Schematic representation of a sample during the drying and wetting measurements. The bold black lines represent the sealed sides of the sample, and the ellipse in the thin line on the right-hand side represents the surface that is exposed to ambient environment. The numbers indicate the positions of nodes that are chosen to show the calculated k_{rl} and $f(\phi, S)$ in Fig. 5.8.

Figure 5.3 displays the comparison of measured and predicted sorption isotherms for Paste3. Main curves are fitted by the two-parameter version of van Genuchten's equation (see Eq. 2.4) and scanning curves are predicted by Mualem Model II [53] (solid scanning curves) and improved Rubin's model [177, 144] (dashed scanning curves). The two parameters used in improved Rubin's model are optimized to fit all measured scanning curves. They are $\gamma_d = 5.8$ and $\gamma_w = 24.8$ (see Eqs. 3.48 and 3.49). Due to the lack of measured scanning curves for Paste4 and Paste5, these parameters are considered as the same as for Paste3. Figure 5.3 shows that both hysteresis models yield similar results for the prediction of the first scanning curves, either for drying or wetting.

The current research has also conducted sorption isotherms measurements and drying-wetting

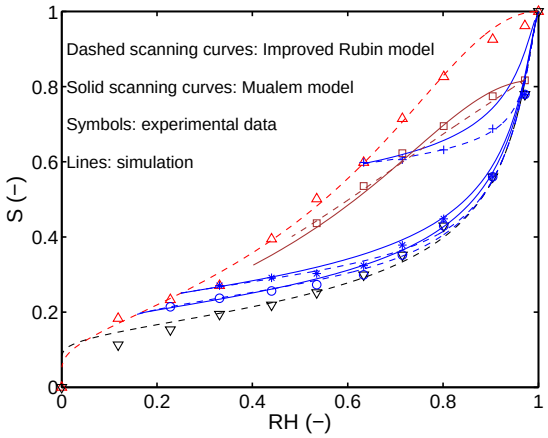

Figure 5.3: Simulated sorption isotherms *vs.* experimental data for Paste3. Measured data are taken from the reference [23].

experiments (see Sections 4.2 and 4.3 in Chapter 4). Those data provide the second source of experimental data for verifications.

5.4.2 Determination of transport coefficients

The resistance factor involved in D_v (see Eq. 2.35) is calculated by the formula proposed by Millington [93] and x_D suggested by Thiéry et al. [120] (see Eq. 2.37 in Chapter 2).

Another important transport coefficient is the relative permeability k_{rl}. The critical question about k_{rl} is whether hysteresis exists in relation $k_{rl}(S)$. The independent domain theory described by Poulovassilis [203] implies that k_{rl} in wetting should be larger than k_{rl} in drying for the same water content. This theory was supported by Mualem [128], in which a sophisticated hysteretic model for the prediction of k_{rl} was proposed. However, experimental data for glass-beam (a very porous material) have shown that there is no hysteresis in $k_{rl}(S)$ [150]. This conclusion was further proved in the cases of sands and soils [151, 152]. A multiscale network model for liquid-water and vapour transport in porous media also showed that obvious hysteresis in $k_{rl}(RH)$ but no hysteresis in $k_{rl}(S)$ [204].

This chapter will consider both cases, non-hysteresis and hysteresis in $k_{rl}(S)$. Because it is much simpler to implement, the first case will be applied firstly, and the second case will be discussed later (see Section 5.6.5). For the first case, it assumes that k_{rl} is a unique function of S. Following the choice in Chapter 2, the well-known VGMa model is used to calculate $k_{rl}(S)$ (see Eq. 2.7 in Section 2.2.3). Notice that the parameter m_V in Eq. (2.7) should be dependent on the sorption isotherm, while because there is no such parameter for a scanning curve, m_V

from the main desorption curve is used for all scanning cases.

The intrinsic permeability K_l in Eq. (2.34) was inversely determined by fitting drying kinetics measured during a drying experiment [133, 42, 134]. Results of K_l for the three studied materials from the literature have been reported in Table 2.4. The same values of K_l are also used for modelling the wetting process. In other words, besides the boundary conditions, the only difference between modelling of drying and wetting is the use of different sorption isotherms.

The flux boundary condition (see Eq. 1.68) is used for all simulations of drying and wetting cycles. The constant value of emissivity ($E = 2.188 \times 10^{-8}$ kg $\cdot$ m$^{-2} \cdot$ s$^{-1} \cdot$ Pa^{-1}) is used for all drying and wetting conditions since E seems to be independent to the environmental RH [116].

5.4.3 Verification with experimental data from the literature

Simulation results of the mass loss curves (mass loss *vs.* time) for Paste3 are shown in Fig. 5.4. Simulations performed by the non-hysteresis modelling are presented in two cases, $\omega = 0.5$ and 1, which correspond to the average sorption curve and the main desorption curve, respectively. Mass loss curves measured during the drying process are used to determine K_l. Thus, to evaluate the different modelling methods, it is necessary to compare simulation results during wetting. Mualem Model II provides the best agreement with measured mass loss curves for the wetting process, either with a boundary conditions of RH^e = 53.5% or 63.2% for drying. Meanwhile, improved Rubin's model overestimates the total moisture mass obtained during wetting. Both cases of non-hysteresis modellings ($\omega = 0.5$ or 1) unexpectedly provide very similar results which clearly underestimate the mass variation and cause that curves drop sharply during wetting.

Table 2.4 shows that two fitted K_l values by using data from drying experiments at RH^e = 53.5% and 63.2% are very close. These two K_l values are used to simulate moisture transport for the experimental condition at RH^e = 63.2Ṫwo calculated mass loss curves are shown in Fig. 5.5. The difference between these two curves is not significant (see Fig. 5.5). Therefore, in the next sections K_l determined by means of drying experiments at RH^e = 53.5% will be used for the modelling of the wetting process.

In the same way, simulated and measured mass loss curves for Paste4 and Paste5 are compared in Fig. 5.6. Saturation profiles at the end of drying and the end of wetting for these two materials are shown in Fig. 5.7. Even though predicted mass loss curves show a slight difference with the measured curves during the wetting processes (mainly for Paste5), Mualem Model II is still the best one which can provide a high agreement with experimental data. Again, results computed

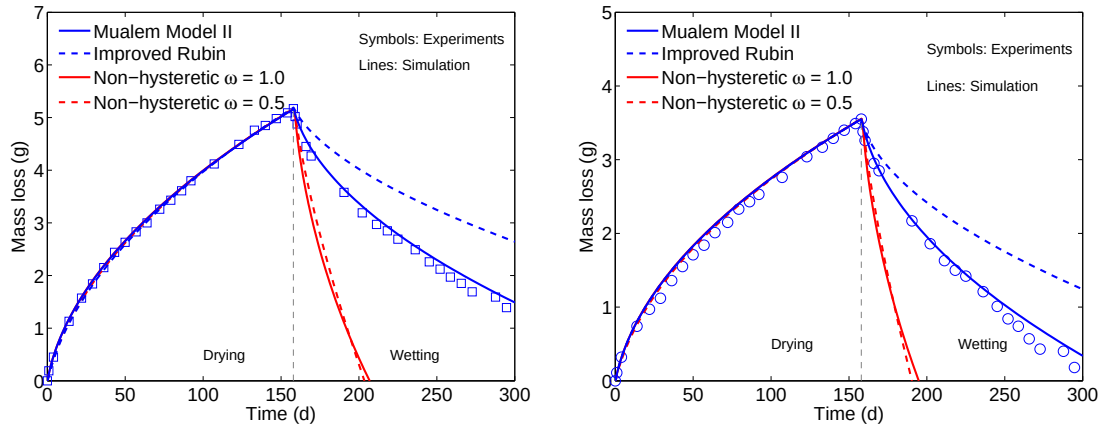

(a) Drying at $RH^e = 53.5\%$. (b) Drying at $RH^e = 63.2\%$.

Figure 5.4: Comparisons of mass loss curves simulated by non-hysteresis and hysteresis modellings for Paste3. Drying at $RH^e = 53.5\%$ or 63.2% and wetting at $RH^e = 97\%$.

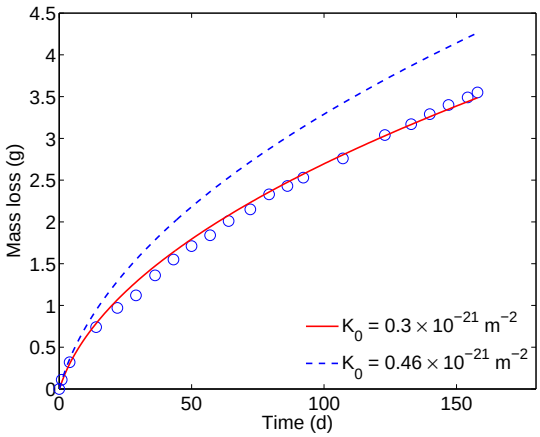

Figure 5.5: Comparisons of mass loss curves during drying $RH^e = 63.2\%$ simulated by using two fitted K_l values for Paste3.

by improved Rubin's model and the non-hysteresis modelling are not as good as Mualem Model II.

Because both cases of non-hysteresis modelling show similar results, the case of using the main desorption curve ($\omega = 1$) will be adopted to represent the non-hysteresis modelling in the following sections.

In terms of saturation profiles, Fig. 5.7 shows that these three modelling methods (Mualem Model II, improved Rubin's model and non-hysteresis) provide very different results at the end of wetting. Curves simulated by the non-hysteresis modelling are far above the measured ones (see the dashed-dotted curves in Fig. 5.7), which leads to around 20-30% differences on the surface of the material compared to the measured profiles. The case of using improved Rubin's model

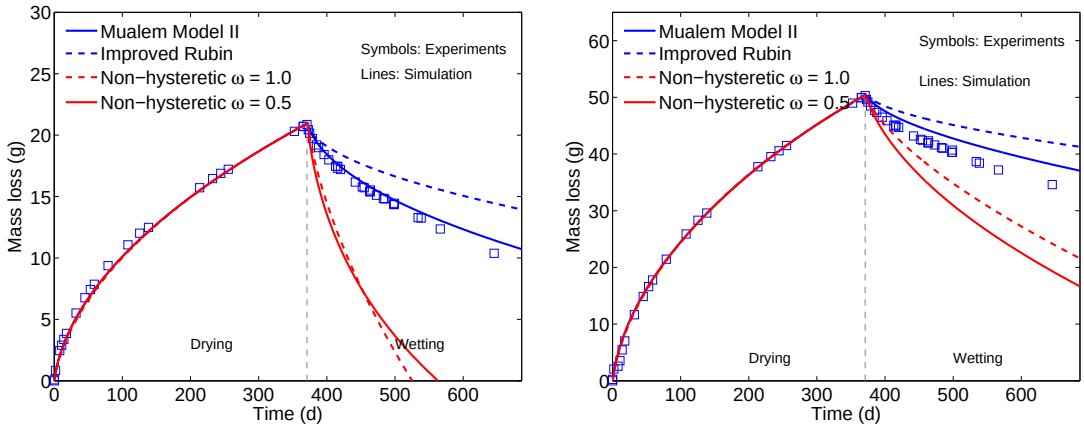

(a) Paste4. (b) Paste5.

Figure 5.6: Comparisons of simulated mass loss curves with experimental results for Paste4 and Paste5. Drying at $RH^e = 53.5\%$ and wetting at $RH^e = 97\%$.

shows that predicted saturation profiles are below the measured curves (see the dashed curves in Fig. 5.7). Mualem Model II obviously performs better than the others. One important reason is that S provided by Mualem Model II at the boundary is much closer to the measured results than the values provided by the other modelling methods (see the boundary points in Fig. 5.7). Other reasons will be analysed in Sections 5.5 and 5.5.2.

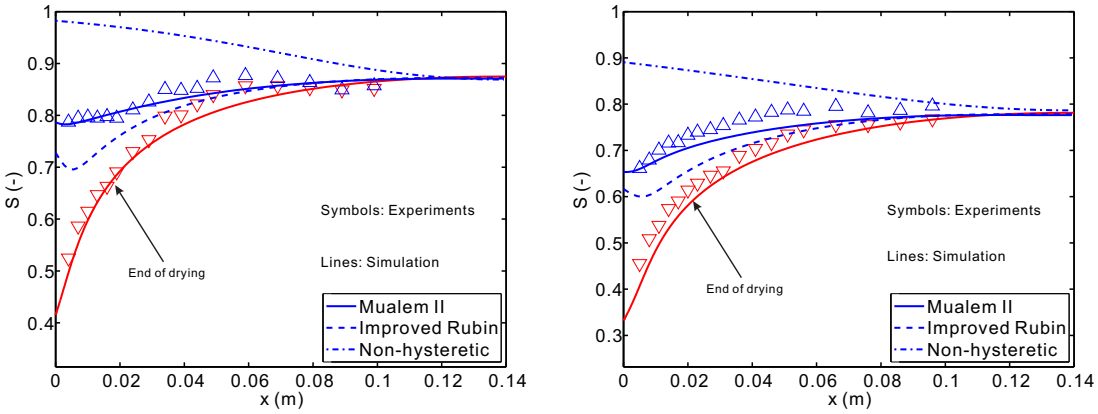

(a) Paste4. (b) Paste5.

Figure 5.7: Saturation profiles simulated by non-hysteresis ($\omega = 1.0$) and hysteresis modellings are compared with experimental data for Paste4 and Paste5, drying at $RH^e = 53.5\%$ and wetting at $RH^e = 97\%$. Red lines and inverted triangle symbols correspond to simulated and measured profiles at the end of drying, respectively. Blue lines and triangle symbols correspond to simulated and measured profiles at the end of wetting, respectively.

Based on verifications with the four sets of experimental data (two for Paste3, one for Paste4 and one for Paste5), it can be concluded that Mualem Model II is clearly more appropriate than

improved Rubin's model and the non-hysteresis method to simulate drying and wetting cycles. As mentioned in Section 5.2, there are two key transport coefficients for modelling of moisture transport, which are the relative permeability k_{rl} for the description of the advective transport of liquid-water and the resistance factor $f(\phi, S)$ for vapour diffusion. Both transport coefficients are expressed as functions of S which means that there is no hysteresis between these two coefficients and S. However, because of hysteresis in RH -S, hysteresis between these two coefficients (k_{rl} and $f(\phi, S)$) and RH can be observed. One example for Paste3 (drying at $RH^e = 53.5\%$) is shown in Fig. 5.8. The relative permeability k_{rl} monotonously increases with RH, but $f(\phi, S)$ monotonously decreases with RH. For nodes near the surface of the material (e.g., point 1 in Fig. 5.8), during the wetting process k_{rl} increases rapidly and $f(\phi, S)$ decreases sharply, while for inner nodes (e.g., points 6 and 7 in Fig. 5.8), they do not change significantly due to small RH fluctuations.

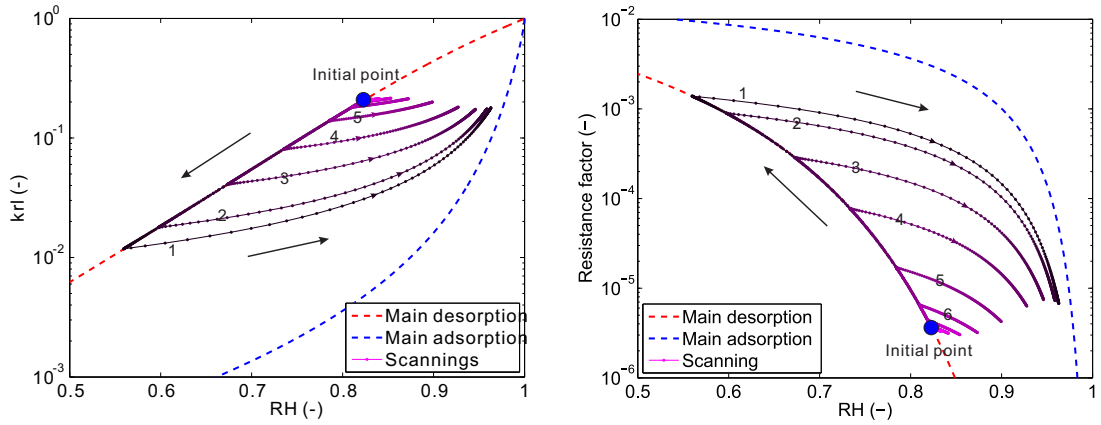

(a) Evolution of k_{rl}.

(b) Evolution of $f(\phi, S)$.

Figure 5.8: Evolutions of k_{rl} and $f(\phi, S)$ at different depths simulated by VGMa [90, 89] for Paste3 (drying at $RH^e = 53.5\%$). The numbers of curves corresponds to the node positions which have been marked in Fig. 5.2.

5.4.4 Verification with experimental data from the current study

As described in Section 4.2.3, because of the problem of vacuum saturation, experimental data for some materials are not accurate. Hence, only three examples (PCEMI06, PCEMIII06 and PSF06) are chosen to show simulation results and to compare with measured data (mass loss curves and saturation profiles).

Results simulated in the cases of hysteresis and non-hysteresis ($\omega = 1$) modellings are pre-

sented in Figs. 5.9, 5.10 and 5.11. These figures show that the fitting of mass loss curves during drying is less accurate. The main reason is that the initial saturation is not uniform because of the problem of vacuum saturaion as it has pointed out in Chapter 4 (see Section 4.2.3).

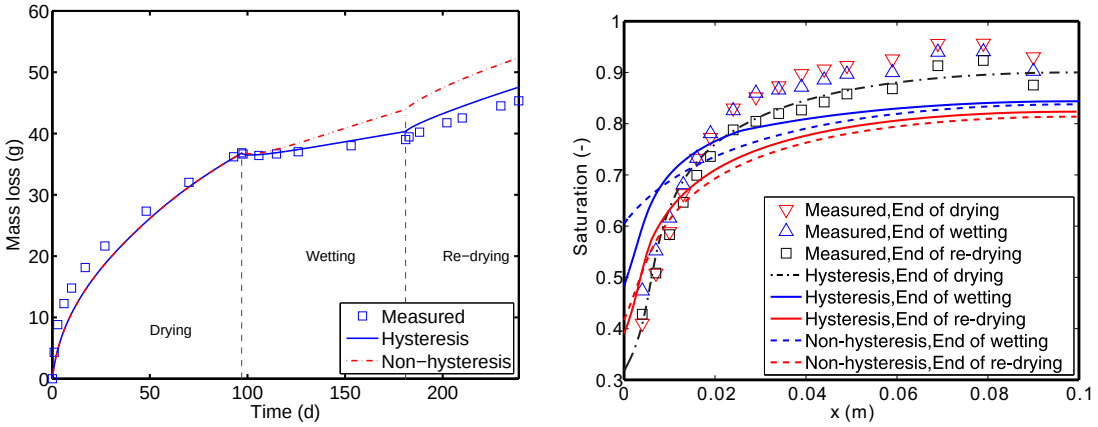

(a) Mass loss curves. (b) Saturation profiles.

Figure 5.9: Comparisons of simulation results with measured data for PCEMI6.

All figures clearly show that the hysteresis modelling certainly provides better simulation results than the non-hysteresis modelling. In Figs. 5.10a and 5.11a, during wetting, mass loss curves predicted by the non-hysteresis modelling drop sharply (reasons will be explained in Section 5.5), while in Fig. 5.9a this curve has a little bit increase. In fact, this behaviour is only observed in short term. For a long term simulation, the mass loss curve computed by the non-hysteresis modelling will increase slowly and goes underneath the curve calculated by the hysteresis modelling.

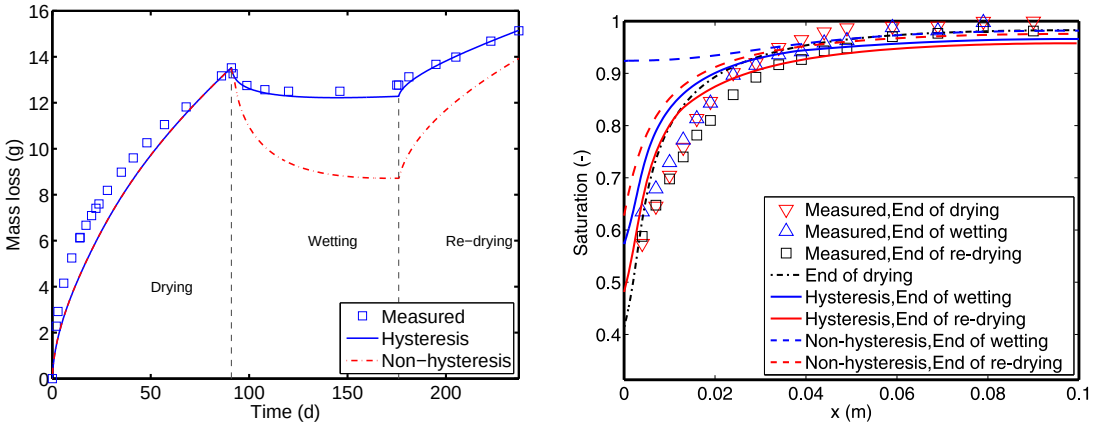

(a) Mass loss curves. (b) Saturation profiles.

Figure 5.10: Comparisons of simulation results with measured data for PCEMIII06.

In general, measured saturation profiles at the ends of drying, wetting and re-drying are very close because the duration for each process is not long enough. Three saturation profiles predicted by the hysteresis modelling show the same trends as measured curves. The drying process continuously occurs inside materials during experiments, because saturation inside is higher than that in the part near the surface. However, at the end of wetting, saturation profiles calculated by the non-hysteresis modelling are far above the measured curves. The same conclusion as experimental verifications by using data from the literature can be drawn here: a hysteresis modelling can provide better simulation results than the non-hysteresis modelling. However, it should also be noted that the differences between the non-hysteresis and hysteresis modellings at the end of wetting (both in mass loss curves and saturation profiles) are larger than the differences at the end of drying.

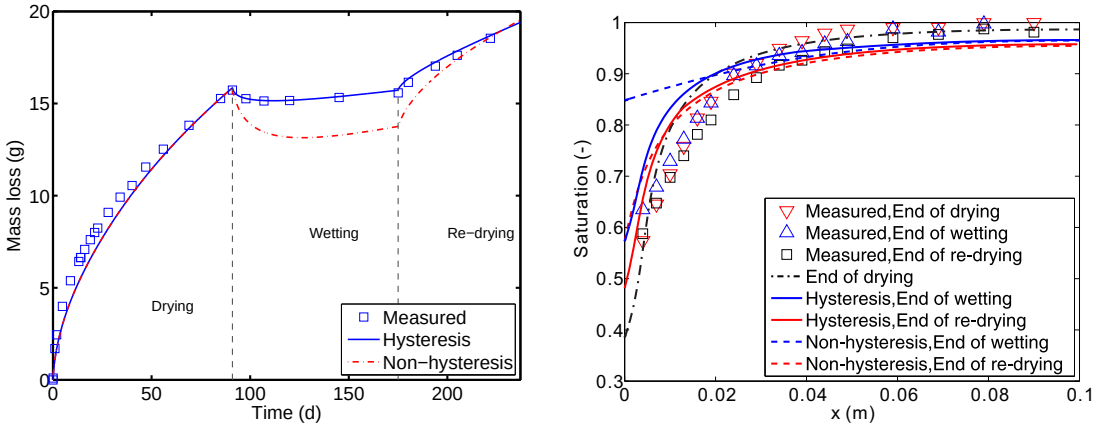

(a) Mass loss curves. (b) Saturation profiles.

Figure 5.11: Comparisons of simulation results with measured data for PCEMIII06.

Liquid intrinsic permeabilities in Table 5.1 are inversely determined by using mass loss curves during the first drying process. CEM I materials show much larger K_l than the materials blended with slag and silica fume (CEM III and CEM I+SF) which are known as able to improve the microstructure of cementitious materials (lower connectivity, lower tortuousity values, finer PSD, etc.). If comparing K_l for PCEMI06 with K_l for Paste5 in Table 2.4 (both materials have the same w/c), values in Table 5.1 are around twice larger. This may be due to the different types of cements. The cement used in TRANSCEND project is a low grade cement (CEM I-32.5 R, see Table 4.1), while the reference [23] used CEM I-52.5 (see Table 3.2).

Table 5.1: Validated liquid intrinsic permeabilities ($\times 10^{-21}$m^2) for different materials.

	PCEMI05	PCEMI06	PCEMIII05	PCEMIII06	PSF05	PSF06
K_l	28	73	0.14	0.25	0.65	0.95

5.5 Investigation of reasons of differences between three modelling methods

The above verifications show the differences between hysteresis and non-hysteresis modellings, and the differences between two hysteresis models (Mualem Model II and improved Rubin's model). In the following subsections, reasons of these differences will be analysed.

5.5.1 Differences between hysteresis and non-hysteresis modellings

Comparisons show that the non-hysteresis modelling ($\omega = 1$) yields higher S at the surface of the material during wetting than the hysteresis modelling. A figure has been drawn to explain the reason of this difference (see Fig. 5.12). Because the non-hysteresis modelling uses the same sorption curve, when drying is switched to wetting, S at the boundary will increase to the point corresponding to RH^e on the main desorption isotherm, as shown in Fig. 5.12. However, for the hysteresis modelling, the wetting boundary condition is much lower than the point on the main desorption curve for the same RH. This boundary condition is close to the main adsorption curve (see Fig. 5.12). It also agrees with the measured saturation at the boundary as explained in Section 5.4 and in Fig. 5.7. The saturation difference between these two cases of wetting boundary conditions is the primary cause that leads to saturation profiles simulated by the hysteresis modelling always lower than the ones predicted by the non-hysteresis modelling.

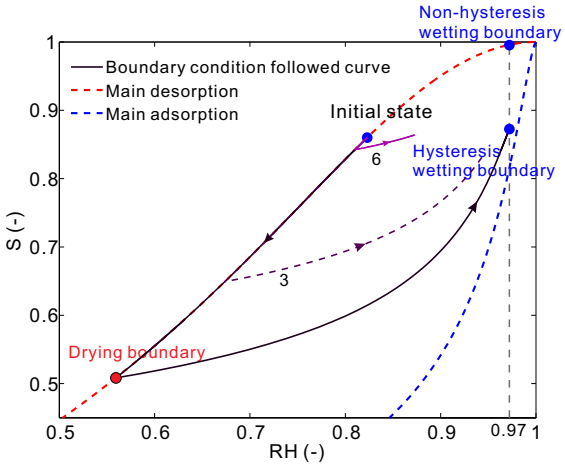

Figure 5.12: The differences of boundary conditions used in non-hysteresis and hysteresis modellings. Points 3 and 6 correspond to the nodes which have been shown in Fig. 5.2.

Besides, Fig. 5.12 also provides evolutions of sorption isotherms for two inner nodes (points 3 and 6 in Fig. 5.12). In the hysteresis modelling, these two nodes are always at lower S than the

non-hysteresis modelling for the same RH. This directly causes a lower k_{rl} for these two points (see curves 3 and 6 in Fig. 5.8a). The mass transport in a porous medium like cement-based material is mainly governed by liquid-water movement [42, 117]. Thus, the mass transport with the hysteresis modelling is slower than the mass transport in the non-hysteresis modelling. As a consequence, the mass variations predicted by the hysteresis modelling during wetting is smaller than that computed by the non-hysteresis modelling (see Figs. 5.4 and 5.6). This also results in a slower increase of saturation profiles during the wetting process if hysteretic effects are considered (see Fig. 5.7).

5.5.2 Differences between two hysteresis models

Comparisons also show significant differences between the case of using the conceptual model (Mualem Model II) and using the empirical model (improved Rubin's model). That is mainly due to the pumping effect, which can cause pumping errors (denoted PEs, see Section 3.6). It is recognised as the main difference between conceptual and empirical hysteresis models [144]. In this section, the PEs are further investigated through their influence on moisture transport. Simulations are performed on Paste3 by using the initial $RH_0 = 75\%$, drying at $RH^e = 53\%$ and wetting at $RH^e = 97\%$. Firstly, the material is submitted to drying, and then changed to wetting. Each process has the same duration, 15 days (30 days for a cycle). Three cycles are simulated.

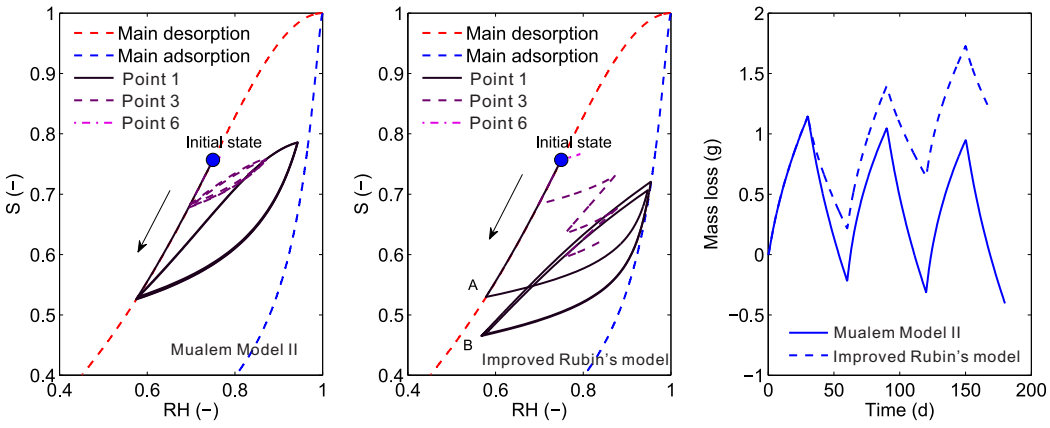

(a) (b) (c)

Figure 5.13: Simulation results performed with Mualem Model II [53] and improved Rubin's model [177, 144] to investigate the PEs. The subfigures (a) and (b) show sorption isotherms (scanning loops) simulated by both hysteresis models. The subfigure (c) presents mass loss curves.

In Fig. 5.13, improved Rubin's model clearly presents significant PEs for both surface point (e.g., point 1) and inner point (e.g., point 3). For point 1, during the first cycle it appears the largest PEs, which can be quantified by S difference between point B and point A (see Fig. 5.13b). If there is no PE, point B should return to point A on the main desorption curve after the first cycle. The later cycles seem to have very small relative errors for point 1. However, for point 3, the PEs constantly grow with the number of cycles, which causes that S becomes lower and lower. The different evolutions of PEs between point 1 and point 3 are because the surface point has larger RH fluctuations than the inner point. As it has been explained in [144], small RH fluctuations yield larger PEs than large RH fluctuations. Consequently, improved Rubin's model leads to a global increase of mass loss curve according to the number of cycles due to the lower saturation for each node (see Fig. 5.13c). The comparison results demonstrate that if the empirical model fails to eliminate the PEs, the cumulative errors associated with fluctuations of hysteresis loops become significant and cause non-physically simulated results.

5.6 Discussions about effects of different modelling conditions

Compared to the hysteresis modelling, the non-hysteresis modelling is much easier to implement and is able to save computing time. From an engineer's point of view, the non-hysteresis modelling is a handy method. That is why it is worth carefully analysing the applicability of these two different methods under various situations. Mualem Model II [53] will be used as a benchmark for comparisons because it has been confirmed to be the more relevant one in comparisons with experimental data in the laboratory (see Section 5.4).

Meanwhile, effects of other factors on modelling of moisture transport, such as the different forms of Richards' equations, different RH loads curves at the boundary and hysteresis in k_{rl} will be discussed. The last part has a focus on the analysis of the moisture penetration depth.

5.6.1 Effect of the drying and wetting cycle duration

This subsection focuses on discussion about the influence of the drying and wetting cycle duration. In real conditions, RH varies daily, monthly and seasonally, so for modelling purposes, these variations will be tested as different cycle durations: 1 day, 30 days and 90 days. The initial and drying/wetting boundary conditions used here are the same as the ones used for the analysis of the PEs (see Section 5.5.2). The reason using these initial and boundary conditions is that

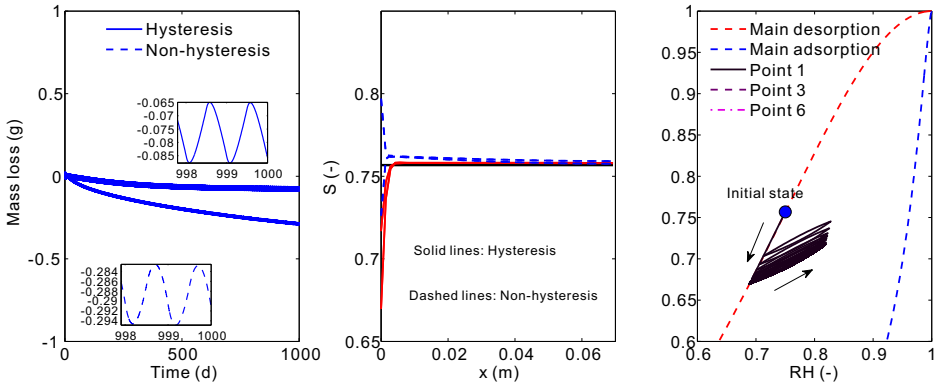

(a) The cycle duration is 1 day.

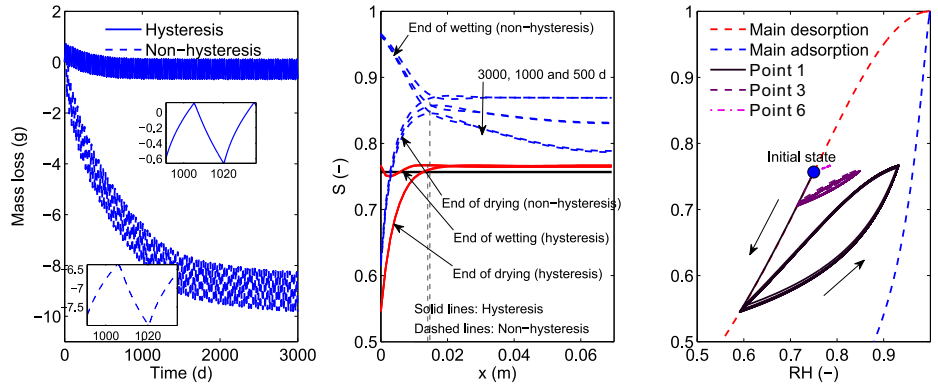

(b) The cycle duration is 30 days.

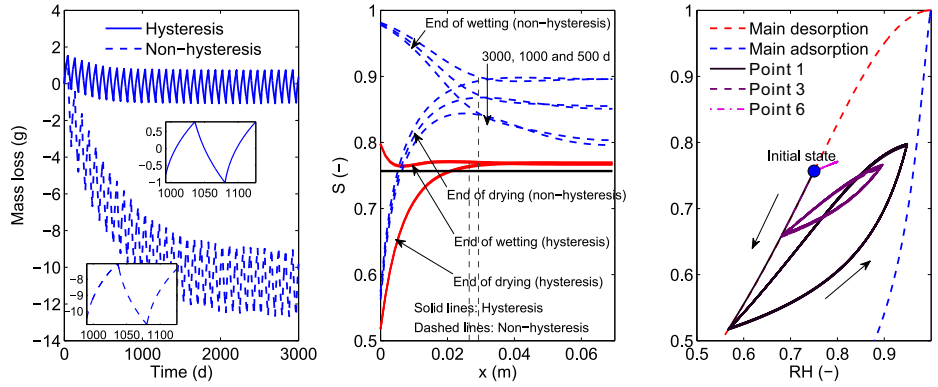

(c) The cycle duration is 90 days.

Figure 5.14: Simulation results of different cycle durations in the cases of non-hysteresis and hysteresis modelling by taking Paste3 as an example. The subfigures on the left-hand side show the mass loss curves. Partially enlarged figures are also provided. The central subfigures show saturation profiles at the end of drying and at the end of wetting after 500, 1000 and 3000 days. The solid-black lines indicate the initial condition. The gray dashed lines show the moisture penetration depth, calculated by the method provided in Section 5.6.6. The subfigures on the right-hand side show simulated sorption isotherms (scanning loops) at different depths. The positions of points 1, 3 and 6 in the material have been marked in Fig. 5.2.

mass variations simulated by the hysteresis method can quickly achieve stabilization (see mass loss curves in Fig. 5.14). Therefore, it is easier to compare the differences of mass loss curves between two modelling methods. Simulation results of saturation profiles and scanning loops are also shown in Fig. 5.14.

Obviously, the time to reach mass equilibrium is different between both modellings and depends on many factors (durations of the drying/wetting cycles, boundary conditions, initial RH, etc.). For the tested case in the current section, the mass loss curve provided by the hysteresis modelling reaches equilibrium quickly, while for the case of non-hysteresis modelling, this process takes longer time. After 3000 days of simulation, only approximate equilibrium is observed for 30- and 90-day cycle durations.

For the 1-day cycle duration, the differences of mass loss curves calculated by these two methods are very small, as well as saturation profiles, which always fluctuate around the initial state and only the part in the vicinity of the surface is really affected. But for cycle durations of 30 and 90 days, the differences between both modelling methods are more obvious. Mass loss curves calculated by the non-hysteresis method reach very low values. These differences are also illustrated with the simulated saturation profiles. The hysteresis modelling shows similar shapes of saturation profiles for 30- and 90-day durations. For the non-hysteresis modelling, the saturation profile progressively rises during the simulation. It is due to more moisture moving into the material so that the mass of the material increases gradually (see the left-hand side subfigures in Figs. 5.14b and 5.14c).

The main reason of this difference refers to the different levels of saturation at the boundary as explained in Section 5.5. The saturation for the wetting boundary conditions is remarkably inconsistent between hysteresis and non-hysteresis modellings. For the non-hysteresis modelling, saturations at the boundary are 0.87 and 0.90 for 30- and 90-day cycle durations, respectively, while for the hysteresis modelling saturation at the boundary is between 0.77 and 0.80. These different boundary conditions are also clearly presented in sorption isotherms (see the scanning loops for point 1 in the right-hand side subfigures of Fig. 5.14).

5.6.2 Effect of the boundary RH amplitude

The RH amplitude is another factor which significantly affects moisture transport under drying and wetting cycles. In the previous discussion about the cycle duration, an RH amplitude of 44% (53% - 97%) was used. Another RH amplitude is introduced here between 64% and 86%,

which is the half of the RH amplitude used in the previous discussion. The initial RH is still 75% and a moderate cycle duration of 30 days is chosen.

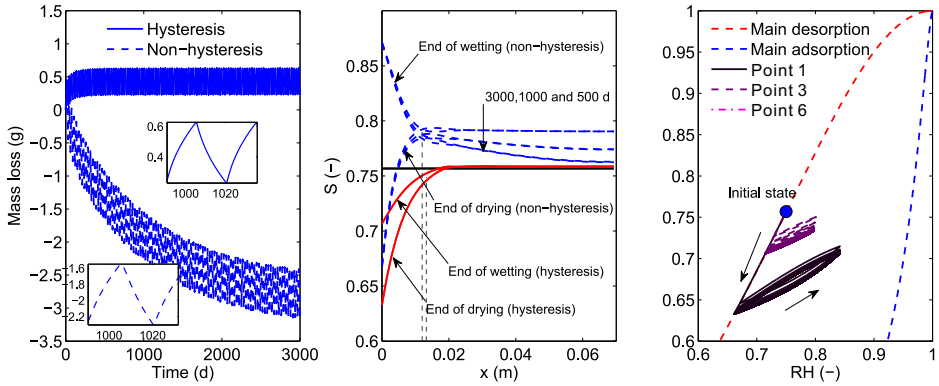

Figure 5.15: Simulation results in the case of using a RH amplitude = 22% (between 64% and 86%) by taking Paste3 as an example. The explanations of the legend are the same as in Fig. 5.14.

Simulated results for the proposed new RH amplitude are provided in Fig. 5.15. Compared to Fig 5.14b, the difference in the mass loss curves simulated by the hysteresis modelling between two RH amplitudes is shown at the beginning of simulations. The mass loss curve slightly drops in Fig 5.14b, whereas the curve rises a little in Fig. 5.15. The big differences are seen in the non-hysteresis modelling. A smaller RH amplitude provides a smaller mass loss. Again, the saturation difference between the drying and wetting boundary conditions is more obvious for the non-hysteresis modelling than for the hysteresis modelling, as it has already been emphasized in the comparisons between simulations and experimental results (see Fig. 5.7).

5.6.3 Effect of the initial step

To perform a numerical modelling for materials after self-desiccation, the initial position of the relationship RH-S needs to be determined. In sealed-cured conditions, the process of self-desiccation consumes free water in the material. Even though the hydration process is involved in self-desiccation, the initial position is considered to be located on the main desorption curve. This position should correspond to the stabilized state from the point of view of hydration. Experimental data shows that the internal RH varies a lot depending on the duration of the sealed-curing period. For example, in measurements carried out by Baroghel-Bouny et al. [22] for a large variety of cementitious materials, the internal RH is between 69% and 94% after a 1-year sealed curing period. Thus, based on these data and concerning the necessity to fix the same initial RH for all the studied materials for the comparison purpose, the choice of a middle

RH (e.g., RH_0 = 75%) on the main desorption curve as the initial condition for modelling seems a most relevant choice.

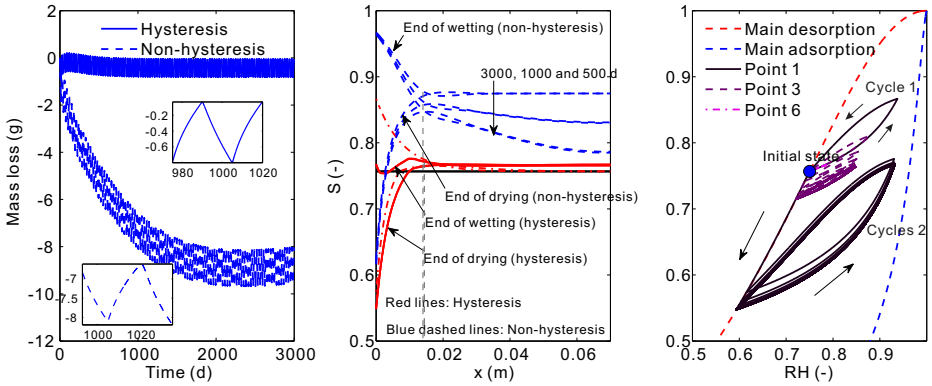

Figure 5.16: Simulation results in the case of initial wetting by taking Paste3 as an example. In the central subfigure, the red dash-dotted lines represent the saturation profiles at the end of drying and at the end of wetting of the first cycle. The explanations of the legend are the same as in Fig. 5.14.

The next question has to be answered before performing the simulation is whether the first step is drying or wetting. In experiments (see Section 5.4), materials were firstly exposed to a low RH, while in natural conditions, the external RH can be either higher or lower than the initial RH. So, both initial drying and wetting should be considered to represent the real conditions. Simulations in the case of initial drying have been done in the above sections (see Sections 5.5.2, 5.6.1 and 5.6.2). This subsection proposes to carry out the simulation in the case of initial wetting. For the purpose of comparison, the initial conditions is RH_0 = 75%, a 30-day cycle duration and RH amplitude = 44% (53%-97%, the same conditions used in Section 5.6.1 in the case of initial drying).

Simulation results are presented in Fig. 5.16, which should be compared with Fig. 5.14b for the case of initial drying. Firstly, the two mass loss curves in Fig. 5.16 are very similar to Fig. 5.14b. The total mass losses at the end of the simulation for the non-hysteresis modelling are very close in these two figures. Secondly, saturation profiles at the end of drying and wetting after 500, 1000 and 3000 days are quite similar in Figs. 5.14b and 5.16 for both modelling methods. In fact, the difference between initial drying and initial wetting is more significant in the first cycle for the hysteresis modelling. Results simulated with initial wetting show that saturation at the boundary in the first cycle is much higher than the following cycles (see the red dash-dotted line and the red solid lines at the end of wetting in the central subfigure of Fig. 5.16). Accordingly, the scanning loop of the first cycle is far above scanning loops of the following cycles (see Cycle

1 and Cycles 2 in the right-hand side subfigure of Fig. 5.16).

5.6.4 Effect of different forms of Richards' equations on hysteresis modelling

As it has been mentioned in Section 5.3, S-based and mixed forms of Richards' equations are two more relevant forms from the numerical point of view. These two forms use different state variables: S and P_c. Let's consider an experimental condition, in which the sample is firstly submitted to drying and then to wetting (see Fig. 5.17). For each process, if the simulation can reach an equilibrium state, the state variable should be uniform throughout the material. However, for most cases, the duration of drying is limited. This means that nodes are separately located on the main desorption curve as one example shown in Fig. 5.17a.

When the material is switched to wetting, each node will follow different scanning curves. If using S-based form, all scanning curves will go to the horizontal line at $S = S^e$ (line AB in the figure), while in the case of mixed form, final points for all scanning curves will be on the vertical line at RH = RH^e (line AC in the figure). It is clear that all scanning curves must pass the line AB if they have to reach the line AC. S^e is smaller than any point on the line AC so that the final mass loss in case of using the S-based form equation is definitely smaller than that of using the mixed form equation. As a result, in Fig. 5.17b, the red dashed curve (from S-based form) decreases more slowly than the blue curve (from mixed form). The area ABC in Fig. 5.17a is related to the gap between these curves in Fig. 5.17b. Hence, the mass loss curve simulated by the S-based form of Richards' equation does not match the measured curve well. This is one reason that the mixed form equation is chosen for our simulations in this chapter.

In real conditions, the water transport in porous materials is mainly due to the gradient of capillary pressure. So, there is no wonder why the mass loss curve predicted by the mixed form equation provides better results. Obviously, for the non-hysteresis modelling, there is no this kind of problem about the choice of different forms of Richards' equations. This also indicates that, if one wants to take into account hysteretic effects in modelling of moisture transport, choosing which state variable is an important consideration.

5.6.5 Effect of hysteresis in $k_{rl}(S)$

Generally, no hysteresis in $k_{rl}(S)$ is considered (see Section 5.4.2). Although this is accepted by most moisture transport models for soils, it is still of fundamental interest to study how the simulation results will be affected if hysteresis in $k_{rl}(S)$ is taken into account.

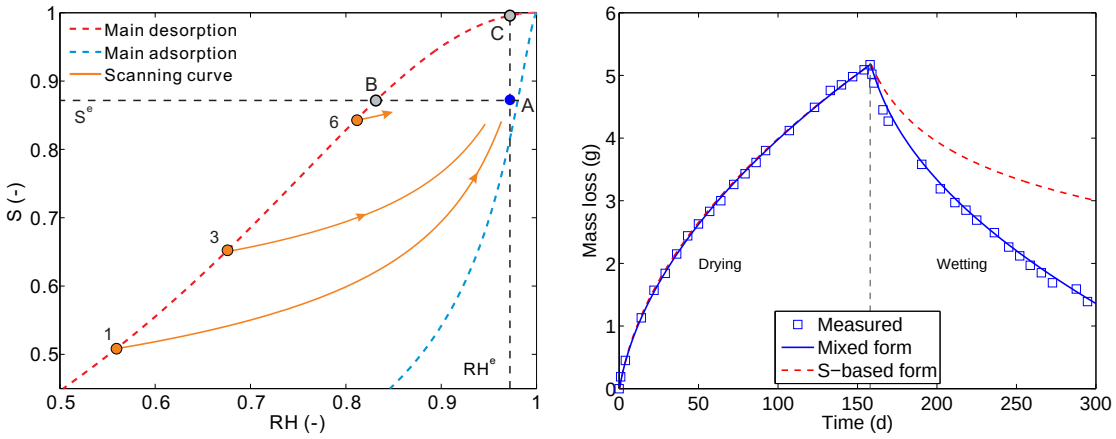

(a) The differences in sorption curves.

(b) Mass loss curves.

Figure 5.17: The differences of two forms of Richards equations (taking Paste3 as an example). The line numbers 1, 3 and 6 correspond nodes in Fig 5.2.

Among the number of models for $k_{rl}(S)$, according to our knowledge, Mualem's model-b [128] which was developed in later 1976 is the one that can consider hysteresis in $k_{rl}(S)$. Two basic equations KL and KH (see Eq. 2.12) are used to calculate k_{rl} during the main drying, the main wetting and scanning processes. Equations for the main desorption process have been given in Section 2.2.3 (see Eqs. 2.11-2.13). According to the principle of independent domain theory, k_{rl} for the main adsorption process is expressed as [128]:

$$k_{rl,w}(S) = S^{0.5} KL^{1/2} \tag{5.5}$$

Notice that if putting KL equation in Eq. (2.13) into Eq. (5.5) one can have the same equation to calculate k_{rl} for the main adsorption process as that in Mualem model-b (see Eq. 2.9). It is easy to deduce the equation for the first drying scanning process (1,d) according to Mualem's diagram (see Fig. 3.10).

$$k_{rl,1,d}(S) = S^{0.5} \left[KL - (KL_1 - KL)\, KH\right]^2 \tag{5.6}$$

For the first wetting scanning process (1,w), it is:

$$k_{rl,1,w}(S) = S^{0.5} \left[KL - (1 - KL)\, KH_1\right]^2 \tag{5.7}$$

where KL_1 and KH_1 are KL and KH calculated at the inverse points of the scanning curves.

In a similar way to calculate sorption isotherms by Mualem Model II [53], equations for the Nth drying and wetting scanning processes can be written as:

$$k_{rl,N,d}(S) = S^{0.5}\left[KL + (KL_{N,0} - KL)\,KH + \left(\frac{k_{rl,N-1,w}(S_{N,0})}{S_{N,0}}\right)^{0.5}\right]^2 \tag{5.8}$$

$$k_{rl,N,w}(S) = S^{0.5}\left[KL - (KL - KL_{N,0})\,KH_{N,0} + \left(\frac{k_{rl,N-1,d}(S_{N,0})}{S_{N,0}}\right)^{0.5}\right]^2 \tag{5.9}$$

where the subscript (N,0) represents the value at the starting point of the Nth scanning curve. Thus, $k_{rl,N-1,w}(S_{N,0})$ (or $k_{rl,N-1,d}(S_{N,0})$) corresponds k_{rl} at the end point of the previous scanning process (order $N-1$).

In the above equations, the current saturation S has to be known to further calculate the relative permeability. Thus, for a scanning process, the scanning curve must be computed firstly. Theoretically, any hysteresis model can be used to predict the scanning loops. But, only conceptual models such as dependent or independent models based on the domain theory always provide closed form of $k_{rl}(S)$ in the scanning loops. If RH-S scanning loops are not closed (e.g., results predicted by empirical models with PEs), it will generate errors at the end of each process and these errors will increase with the number of loops due to the pumping effect (see the explanation in Section 5.5.2). Hence, Mualem Model II [53] (see Section 3.6.1), which was also developed based on the independent domain theory, is used here.

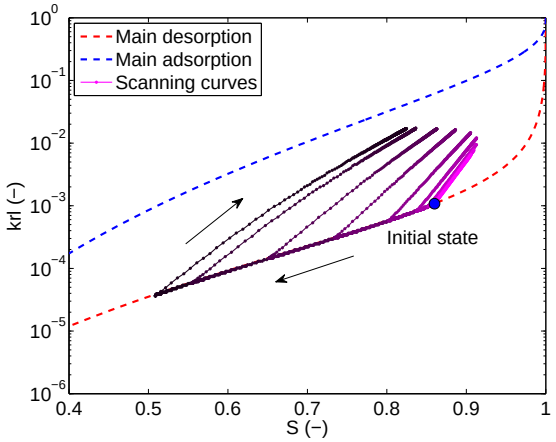

Figure 5.18: Evolutions of $k_{rl}(S)$ calculated by VGMb [90, 128] at different depths for Paste3 (for the case of drying at $RH^e = 53.5\%$ and wetting at $RH^e = 97\%$).

By taking experimental data for Paste3 as an example, simulation results are presented in Figs. 5.18 and 5.19. Compared to Fig. 5.8, Fig. 5.18 shows that VGMb (VG2 + Mualem model-

b) [90, 128] provide smaller k_{rl} values than VGMa model [90, 89], either for the main desorption process or the scanning processes. So, when using VGMb model to inversely determine K_l, the K_l value is much larger (several orders of magnitude) than that from VGMa model (see Table 2.4). However, the differences of k_{rl} values between Fig. 5.18 and Fig. 5.8a are much smaller than the difference in K_l. Moreover, when it is switched to wetting, the $k_{rl}(S)$ scanning curves increase and these k_{rl} values are larger than these for the main desorption process. Totally, the case of using VGMb model has larger liquid permeability $K_l k_{rl}$ in wetting than using VGMa model. As a result, the mass loss curve drops sharply when hysteresis in $k_{rl}(S)$ is taken into account. The prediction in this case cannot match the measured mass loss curve well as shown in Fig. 5.19.

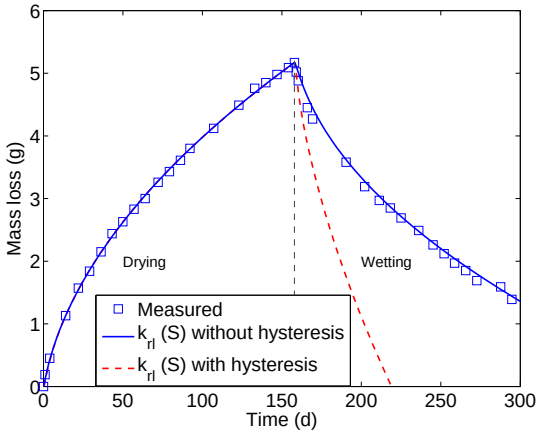

Figure 5.19: Comparisons of mass loss curves calculated in the cases of with or without hysteresis in relation S-k_{rl} for Paste3 (for the case of drying at 53.5%).

5.6.6 Analysis of the moisture penetration depth

As mentioned in the introduction, the penetration depth x_p is an important factor to evaluate the durability of the concrete structures since x_p is related to the depth that ions can penetrate into the material. Beyond x_p, it can be considered that the concentration of ions has no effects by the external ions concentration variations.

To determine this depth, two restrictions have been proposed by Arfvidsson [6].

(1) In a simulation after a number of drying and wetting cycles, there must be a part of the material with a constant saturation that cannot be disturbed by RH variations at the boundary. Let's name this saturation as the undisturbed saturation S_{und} (see Fig. 5.20).

(2) When the undisturbed saturation is reached, this means that the saturation profile at the

end of drying (and wetting) is the same for the following cycles. This also implies that the mass loss curve reach a mass equilibrium state for each cycle. The moisture penetration depth x_p is defined as the depth where the saturation difference (ΔS) between the end of drying and the end of wetting is equal to 1% (see Fig. 5.20).

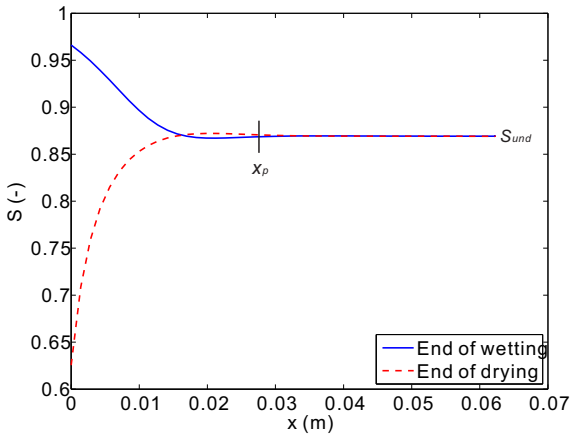

Figure 5.20: Definitions of the undisturbed saturation S_{und} and the moisture penetration depth x_p after a number of cycles.

To investigate x_p, the boundary condition, including the cycle duration and the RH amplitude, and the initial condition have to be determined. In this study, the cycle duration varies between 1 day and 90 days. The RH amplitude is between 44% (RH^{max} = 97%, RH^{min} = 53%) and 14% (RH^{max} = 82%, RH^{min} = 68%). The initial condition should be determined carefully. Arfvidsson [6] reported that S_{und} is not related to the initial condition, but the initial condition can affect the number of cycles when S_{und} is reached. In the simulations, it has been confirmed that this assumption is only valid in the case of non-hysteresis modelling as it will be presented below. Thus, for all simulations, the initial condition is fixed at RH_0 = 75% as the previous calculations (see Sections 5.6.1 and 5.6.2). This value is the mean value of the maximum RH and the minimum RH at the boundary. An initial drying step is chosen here.

Simulation results show that the trends of x_p for non-hysteresis and hysteresis modellings are quite similar (see Fig. 5.21). The moisture penetration depth x_p increases with the cycle duration and the RH amplitude. For the small cycle durations, such as 1, 5 and 10 days, even for 20 and 30 days, the differences in term of x_p calculated by both modelling methods are very small (less than 1 mm difference), regardless the RH amplitude. Notice that one example of using the 30-day cycle duration has been shown in Fig. 5.14b, which presents the similar x_p for hysteresis and non-hysteresis modellings (see the positions of the gray dashed lines in the

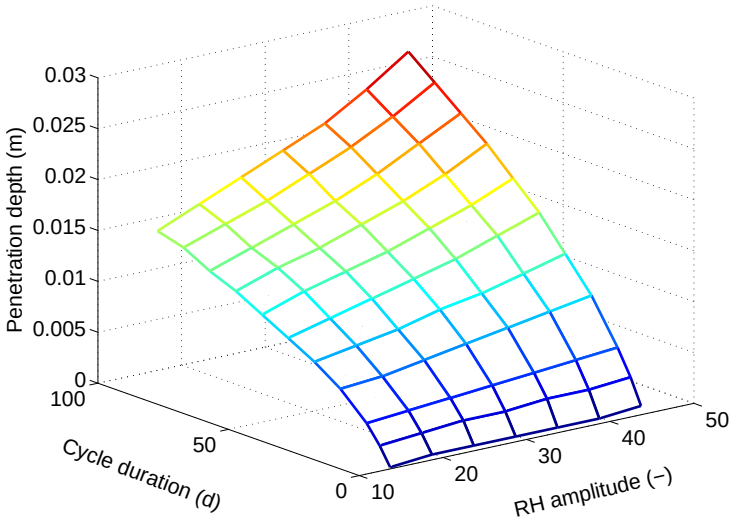

(a) Non-hysteresis modelling.

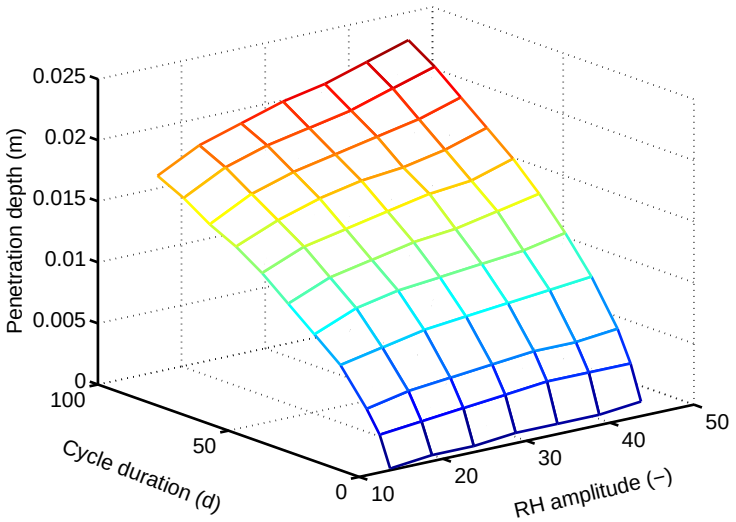

(b) Hysteresis modelling.

Figure 5.21: Moisture penetration depth in relation with the cycle duration and the RH amplitude for the cases of non-hysteresis and hysteresis modelling by taking Paste3 as an example.

central subfigures). That may be because the varying boundary conditions only affect moisture transport in the part near the surface of the material.

Nevertheless, the differences of x_p increase with the cycle duration and the RH amplitude (compare positions of gray dashed lines in Fig. 5.14b for a 30-day cycle duration and in Fig. 5.14c for a 90-day cycle duration). For the simulations with a 90-day cycle duration and 44% RH amplitude, Fig. 5.21 shows that difference in x_p between both modellings rises to 4 mm (24 mm for the hysteresis modelling and 28 mm for the non-hysteresis modelling). Overall, x_p increases more sharply with the cycle duration and the RH amplitude for the non-hysteresis modelling than

for the hysteresis modelling. This implies that the non-hysteresis modelling may overestimate x_p for large cycle durations and large RH amplitudes. This conclusion can help for the design of durability models used to predict service life in the case of cyclic boundary conditions.

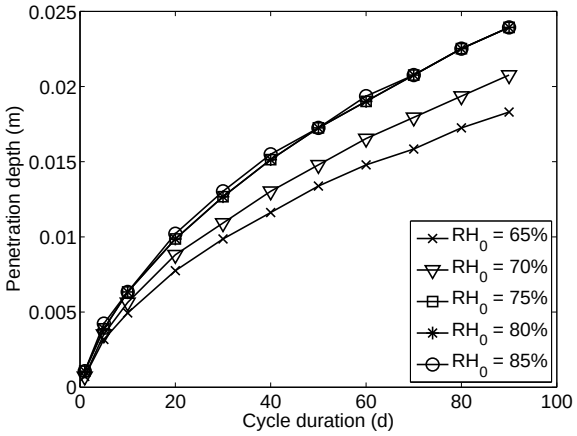

Figure 5.22: Comparisons of x_p for different initial conditions and cycle durations calculated by using Mualem Model II [53]. The RH amplitude is 44%.

To analyse the influence of the initial condition on x_p for the hysteresis modelling, simulations are performed for five different initial conditions, and results are provided in Fig. 5.22. For the high RH_0 values (= 85% and 80%), the predicted penetration depth is almost the same with the one obtained with the initial condition RH_0 = 75% (used previously for all simulations), while for lower RH_0 values (= 65% and 70%), x_p is lower, regardless the cycle duration. Figure 5.22 reveals that the proposed method (considering hysteresis) to predict x_p in valid for the case initial $RH_0 >$ 75%. If $RH_0 \leqslant$ 75%, this method may underestimate x_p.

In practice, the initial condition should be accessed according to the composition of the material and the curing duration. For most cases (maybe except high performance materials), the internal RH after self-desiccation seems to be higher than 75% [22]. Therefore, there is no need to consider the effect of the initial condition on the calculated x_p.

5.7 Conclusion

In this chapter, hysteresis models have been coupled with a moisture transport model to simulate drying and wetting cycles. Simulations in the case without hysteresis have also been performed. Based on experimental verifications and comparisons for different simulation conditions, the following conclusions can be drawn.

1) The proposed method to implement hysteresis models into moisture transport models has a high applicability. The method was used for both conceptual and empirical models. Two hysteresis indexes U and V have been introduced. The hysteresis index V was used to indicate if the node will change its state. The hysteresis index U recorded the drying and wetting history of each node and was very useful for hysteresis modelling because of its strong sorption history-dependence.

2) Comparisons with measured mass loss curves and saturation profiles for cement pastes showed that modelling with hysteresis explicitly provides better results than non-hysteresis modelling. It is principally because hysteresis models is able to provide more relevant RH-S relation, especially at the boundary.

3) Among hysteresis models, results simulated by using Mualem Model II (conceptual model) matched experimental data much better than improved Rubin's model (empirical model). This is largely because improved Rubin's model provided non-physical scanning loops, characterised by the "pumping errors" which is generally observed for empirical models. Thus, Mualem Model II could be the one recommended for modelling of moisture transport under varying boundary conditions.

4) Comparisons with different cycle durations revealed that smaller cycle durations cause smaller differences between non-hysteresis and hysteresis modellings. The differences increase with the cycle duration. At the same time, it also was shown that long term simulations cause larger errors than short term simulations. The errors simulated by the non-hysteresis modelling increase with the RH amplitude; therefore, for the situation with small cycle duration and small RH amplitude, the non-hysteresis modelling is still applicable.

5) For long term simulations, different initial steps (initial drying or initial wetting) did no show significant differences in mass loss curves and saturation profiles. The differences only occurred for the first cycle in the case of the hysteresis modelling.

6) Comparison of two (S-based and mixed) forms of Richards' equation revealed that the mixed form is a better choice, not only because it can provide good simulation results, but also because moisture transport is mainly due to the gradient of capillary pressure in the real condition. Although S-based form Richards' equation has higher speed of convergence

for the numerical simulation, it limits the evolution of sorption isotherms, leading simulated results away from the measured data.

7) Verifying by the limited experimental data showed that it is not necessary to consider hysteresis in $k_{rl}(S)$. Further investigations are needed to check this conclusion.

8) The moisture penetration depth x_p, which may also indicate the penetration depth of ions such as chlorides, has been carefully analysed. For the non-hysteresis modelling, this study confirmed that x_p is related to the cycle duration and the RH amplitude, apart from the initial condition, as this has already been pointed out in the reference [6]. But for hysteresis modelling, the initial condition has clear influence on x_p if RH_0 is below 75%. Hence, the use of the hysteresis modelling to estimate x_p should be more relevant for the case $\mathrm{RH}_0 \geqslant 75\%$.

9) Comparisons of x_p indicated that the non-hysteresis modelling overestimated x_p in the case of long cycle durations and large RH amplitudes.

According to comparisons provided in the current chapter, the cumulative errors associated with simulation time can become significant and unavoidable if the simulation cannot take hysteretic effects into account. The above conclusions are only based on the case of one ordinary cement paste (Paste3, see Table 3.2 in Chapter 3). In the next step research, more cementitious materials (e.g., mortars and concretes) will be used to verify the proposed modelling method and to refine the above conclusions.

Chapter 6

Investigation of the reliability of K_l determination

Summary

In the simplified model used in Chapter 5, the key transport coefficient is the liquid intrinsic permeability K_l which is rarely verified by experimental data. In Chapters 2 and 5, K_l was determined by inverse analysis through fitting drying kinetics. This chapter focuses on comparisons of different methods to determine K_l based on experimental data. These methods include fitting measured apparent diffusivity values and inverse analysis with different boundary conditions.

First of all, let's have a global overview of methods which are compared in this study (see Fig. 6.1). Totally, there are nine methods belonging to three main types. The Katz-Thompson model [20] is generally considered to estimate and compare K_l in case of cementitious materials in references [22, 42]. Values of K_l estimated by this model for the selected materials will be further compared with the other methods based on inverse analysis of drying kinetics and apparent diffusivity measurements in this chapter.

The first part of the current chapter will indirectly determine K_l by fitting the apparent diffusivity D_a data measured by Baroghel-Bouny [11]. In the fitting, the resistance factor $f(\phi, S)$ to vapour diffusion is also assessed. Four different models are used to calculate the liquid-water relative permeability k_{rl}. Results show that K_l values determined by this method are much lower than that provided by inverse analysis in Chapter 2.

Actually, the boundary conditions (the first type and the flux boundary conditions) used in

Chapters 2 and 5 may not be able to describe moisture transport for an experiment condition which uses the saturated salt solution to control a constant RH in a desiccator. Therefore, the second part of this chapter provides an analysis for the impact of the experiment condition on the result of determination of K_l by inverse analysis. The air part in a desiccator is described as the mass boundary region. A model is needed to simulate moisture diffusion in this region, and then this model will be coupled with the moisture transport model used in Chapter 5. The relationship between the thickness of this region and K_l will be discussed. Simulations and comparisons conclude that K_l values provided by the proposed method and by using the flux boundary condition do not have significant difference.

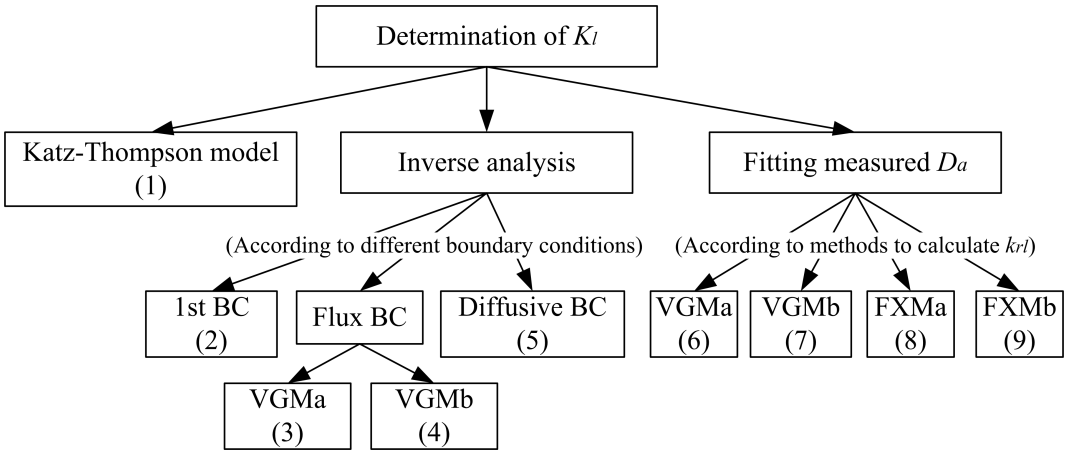

Figure 6.1: Methods to determine K_l which are compared in this research.

6.1 Determination of K_l by fitting measured apparent diffusivity values

As the conclusion in Chapter 2 indicates, if assuming that gas pressure remains constantly equal to the atmospheric pressure [42, 11] and neglecting advection of vapour transport, two transport mechanisms for moisture transport in cementitious materials are: advection of liquid-water and vapour diffusion. If S-based form of Richards' equation is used to express moisture transport process, the apparent diffusivity D_a should have two components: D_l for liquid-water and D_v for vapour. Following equations presented in the literature [11], expressions of D_l and D_v (see Eqs. 2.34 and 2.35) are given as:

$$D_l(S) = -k_{rl}\frac{K_l}{\phi\eta_l}\frac{\mathrm{d}P_c}{\mathrm{d}S} \tag{6.1}$$

$$D_v(S) = -\left(\frac{M}{\rho_l RT}\right)^2 D_{v0}\phi^{x_D}(1-S)^{x_D+2}\frac{P_{vs}RH}{\phi}\frac{\mathrm{d}P_c}{\mathrm{d}S} \tag{6.2}$$

where $\phi(1-S)$ is the available space for vapour transport and x_D is a parameter related to material properties. Terms $\mathrm{d}P_c/\mathrm{d}S$, k_{rl} and P_v depend on saturation S.

In Eq. (6.1), the liquid permeability $K_l k_{rl}(S)$ is one of crucial factors for liquid transport. Generally, $k_{rl}(S)$ is considered as a function of S and calculated based on sorption isotherms (see Section 2.2.3). To perform a moisture transport modelling, the liquid intrinsic permeability has to be determined. It can be measured by experiments or estimated by theoretical models. The conventional methods to measure K_l were carried out on fully saturated materials. Therefore, if vapour diffusion is negligible during the measurements, the flux of liquid-water is expressed by Darcy's law solely.

In these kinds of measurements, the sample must be sealed so that liquid-water is only injected from one face by applying extra pressure and leak from the opposite face, where the rate of outflow must be measured after the flow is stable [205, 206]. However, the disadvantages of the conventional methods are obvious. First, the extra pressure has to be very high. For modern cementitious materials with low water-to-cement ratios and fine pore structures, such as high performance concretes, moisture transport is much slower than the traditional ordinary cementitious materials. For such weakly permeable porous media, the order of MPa pressure may be used. This incredibly increases the risk of physical damage of the pore structure. Second, under the high pressure, the leakage is unpredictable. Third, the essentially saturated state is a strict requirement, especially for the low water-to-cement ratio material, it is very difficult to reach. More recently, an improved device using a controlled oedometer seems to be able to avoid the leakage problem, but it still needs a high extra pressure [207].

Owing to these reasons, the indirect method becomes prior to the direct methods. The beam bending method is one of rapid and indirect methods [208, 209, 210], which was originally developed for soft gels and later was applied to cementitious materials. It exerts a certain strain to a long and slender sample to obtain a relaxation curve, which is considered including both hydrodynamic and viscoelatic effects. By fitting this relaxation curve, K_l can be determined. This method has very clear requirements for the geometry of the sample. It is less applicable for

concretes due to needing very big samples to avoid the influences of aggregates. A method so-called thermopermeametry was also introduced to cementitious materials research from gels [211, 212, 213]. It could be used to supplement the shortcomings of the beam bending method. If assuming that the thermal expansion of liquid is always much greater than that from the solid phase, this method can estimate K_l by measuring the amount of liquid-water which flows out of the material due to the thermal expansion. The main problem is that this method is more sensitive to saturation condition. If there are some air voids or trapped air because of non-fully saturated materials, it will have significant influence on measured results. Comparatively, the dynamic pressurization method is much easier to control, which keeps the sample in a sealed vessel and gradually increases or decreases pressure [214, 138]. If repeating the pressure cycles, the residual air in the material can be dissipated. The latest literature revealed that the NMR technique is able to provide very good data for determination of liquid permeability [215].

Because of so many difficulties in experiments, using theoretical equations based on pore size distribution, pore geometry and connectivity to predict K_l become more vital for cementitious materials. Based on pore size distribution measured by mercury intrusion porosimetry, Katz-Thompson model [20] has been proven more suitable for estimating the permeability of sedimentary rocks. This method was also used for cementitious materials [22, 42]. However, it is only valid for materials with large pores, in which the surface effects can be neglected compared to the pore size. In Chapters 2 and 5, K_l was inversely determined by fitting drying kinetics based on numerical simulation results. Actually, this kind of method needs to solve one or more partial differential equations and require a plenty of experimental data. These requirements limit its application. Besides, this method is sensitive to the length of the drying period and the predicted K_l may vary according to the external RH during drying.

In Eq. (6.2), for the description of vapour diffusion, x_D is a very important factor. Millington [93] suggested $x_D = 4/3$ for variably saturated porous materials such as soils and this value has been used in cementitious materials research [42, 216]. However, soils are more porous materials ans their microstructures as less complex. For cementitious materials, x_D value may be larger than 4/3 to present the stronger tortuous effects. Calibrating with O_2 and CO_2 diffusion coefficient measurements for partially saturated mortars (performed by Papadakis et al. [121]), Thiéry et al. [120] proposed $x_D = 2.74$. However, diffusion of water molecules is different to O_2 or CO_2. A recent literature [215] adopted the moisture transport model from [42, 43, 44] to fit water content profiles measured by NMR at the steady state moisture flow conditions. In this

kind of fitting, both K_l and x_D can be adjusted and determined.

The current section will use another method to simultaneously determine K_l and x_D based on fitting the experimental data of apparent diffusivity. The determined K_l values by this method will be further compared with K_l values which have been provided in Chapter 2 (see Table 2.5) by inverse analysis.

6.1.1 Basic method

Theoretically, if knowing at least two values of D_a, K_l and x_D can be determined by fitting values of D_a based on Eqs. (6.1) and (6.2). But it must be sure that D_l and D_v cannot govern D_a in the same range of S. Otherwise, the fitting results will be unreliable. The relationship between D_l and D_v in the different ranges of RH has been discussed in Chapter 2 (see Fig. 2.15 in Section 2.4.2). Figure 2.15 showed that in the high RH range liquid transport coefficient is prominent whereas vapour diffusion coefficient plays the key role in the low S range. There is only very narrow S range where both D_l and D_v control moisture transport. This conclusion ensures that effects of K_l and x_D can be easily separated and more stable results will be achieved by fitting experimental D_a data.

But before the fitting of D_a is conducted, the relevant equation for sorption isotherms and k_{rl} have to be determined. In Chapters 2 and 5, two models to calculate k_{rl} for both main desorption and adsorption processes have been reviewed and applied: Mualem model-a [89] (see Eq. 2.6) and Mualem model-b [128] (see Eqs. 2.11 and 5.5). Because VG2 equation [90] (see Eq. 2.4, two-parameter version) was used to calculate the main sorption isotherms, there were two combinations for k_{rl}: VGMa (van Genuchten's equation + Mualem model-a) and VGMb (van Genuchten's equation + Mualem model-b).

In fact, any main isotherm fitting equation evaluated in Chapter 3 can be combined with Mualem model-a or Mulaem model-b to calculate k_{rl}. However, in our knowledge, only VGMa model appears as an analytical expression, which is much easier to implement into numerical modelling compared to the original integral function of k_{rl}. The problem is that in our comparisons (see Section 3.4) VG2 equation is not as good as other three-parameter main curve fitting equations. Hence, it is worth trying to introduce a three-parameter equation. Based on the comparison results in Chapter 3, FX equation is proposed to merge with Mualem's model-a [89] and Mualem's model-b [128]. These two combinations are denoted by FXMa and FXMb models.

Besides, different main curve fitting equations provide different shapes of sorption isotherms;

thus the validated K_l values will be also dependent on main curve fitting equations. However, the above discussions also revealed that if using other main curve fitting equations (beside of VG) k_{rl} values can be affected. In the study by Poyet [217], it has shown that using different main curve fitting equations to evaluate K_l is not a fully relevant to the effective permeability $K_l k_{rl}$. Hence, this study does not consider the influence of different main curve fitting equations on K_l.

Overall, four versions of k_{rl} models are used: VGMa, VGMb, FXMa and FXMb. Note that Mualem model-b uses different equations for the main desorption and adsorption processes so VGMb and FXMb need both main desorption and main adsorption isotherms. Besides, VGMb and FXMb present hysteresis in $k_{rl}(S)$. Therefore, through fitting the measured apparent diffusivity it will be possible to indirectly verify these k_{rl} models.

6.1.2 Experimental data and fitting results

Experimental data for D_a

For measurements of moisture diffusivity, Nilsson has compared different methods [218], including the cup tests, steady-state, non-steady-state measurements, etc. All methods seem time-consuming. Hence, it is better to use experimental data which are available in the literature. Baroghel-Bouny [23] provided measured D_a data for a variety of cementitious materials. These data were indirectly obtained during sorption isotherms measurements by using a theoretical method, in which moisture transport in the material between two small RH steps was described by Fick's diffusion with a constant D_a. Therefore, at each measured point for sorption isotherms, the value of D_a can be determined by fitting the mass loss curve. Actually, this is the inverse analysis method that we used in Chapters 2 and 5. But the difference is that Baroghel-Bouny [23] used small RH interval around 10%, while in Chapters 2 and 5 the RH intervals are much larger such 95% to 53.5% for Paste5 (see Table 2.1). The small RH interval allows to obtain accurate results, which showed good agreements with the cup test results [11]. Totally, experimental D_a data are available in the main desorption process for: Paste2, Paste3, Paste4 and Paste5, and in the main adsorption process for: Paste2 and Paste3. According to the method described above, all available measured curves of $D_a(RH)$ are fitted.

The desorption process

Examples of fitted $D_a(RH)$ and $D_a(S)$ curves in the desorption process for Paste5, Paste2 and Paste3 are presented in Figs. 6.2, 6.3 and 6.4. The shapes of fitted curves by all models (VGMa, VGMb, FXMa and FXMb) are very similar. However, VGMb shows the curve slightly lower compared to other models in the high saturation range in Fig. 6.2. In the range close to $S = 0$, all fitted curves drop sharply, which are mainly due to RH$\rightarrow 0$ in Eq. (6.2). The same trend is also shown by the experimental data in [215].

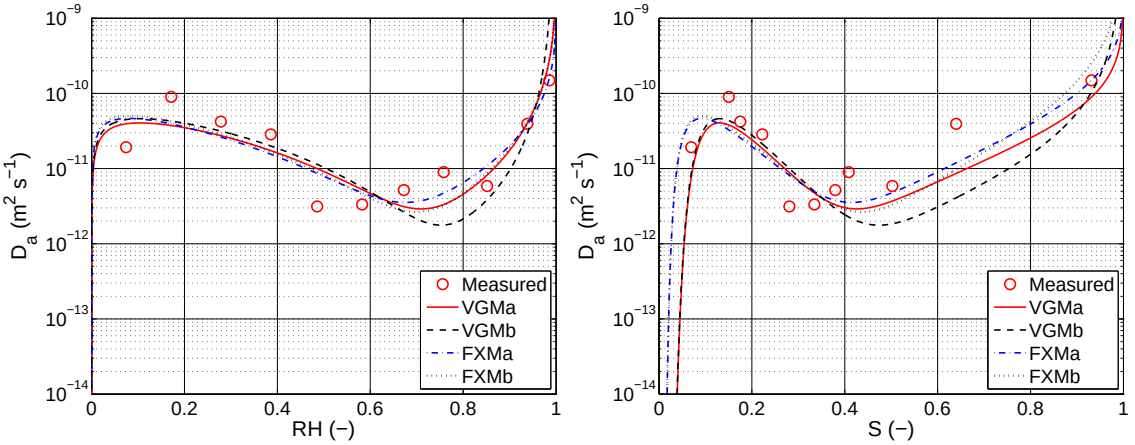

(a) RH-D_a (b) S-D_a

Figure 6.2: Fitted D_a curves by four models for Paste5 in the desorption process.

The calculated values of K_l for the four studied materials in the desorption process are provided in Table 6.1. Some K_l values estimated by the Katz-Thompson model (taken from [24]) and by inverse analysis using the flux boundary condition (taken from Table 2.5) are added in this table for comparison. Values validated by the current proposed method are much smaller. The difference is mainly due to the low accurate fitting. But Figs. 6.2, 6.3 and 6.4 show that several points are far away from the fitting curves. The fitting precision needs to be improved by using more relevant equation for D_a. It may be also due to the problem of experimental data. Figs. 6.3 and 6.4 show that some measured data at around RH = 40% are very low. As it has been shown in the literature [23], this range of RH corresponds to the threshold pore size separating C-S-H and capillary porosities (see Section 3.8.5). Therefore, unstable moisture transport in this RH range easily causes low accurate measurement results.

Table 6.1 shows that FXMb model unexpectedly provides a smaller K_l for Paste4 than Paste3. It may mean that FXMb is a less stable model.

Table 6.1: Fitted $K_l(\times 10^{-21}$ m$^2)$ for the desorption and adsorption processes.

Materials	Desorption						Adsorption	
	Katz-Thompson	Flux BC [a]	VGMa	VGMb	FXMa	FXMb	VGMa (VGMb)	FXMa (FXMb)
Paste2	$<10^{-3}$ [a]	-	0.026	0.219	0.022	0.039	0.02	3.01
Paste3	37 [c]	0.46(0.3 [d])	0.171	23.60	0.272	5.650	4.66	3390
Paste4	71 [c]	2.0	0.296	28.40	0.362	1.000	-	-
Paste5	231 [c]	320	3.010	751.0	290.0	46300	-	-

For a given material, the x_D values in Table 6.2 provided by different models are very close so that the D_a curves computed by different models are quite similar in the low RH range. The x_D value for Paste2 is close to the value proposed by Millington ($x_D = 4/3$) and the value for Paste3 is close to the value proposed by Thiéry et al. ($x_D = 2.74$). However, the values for Paste4 and Paste5 are much larger.

Hysteresis in $D_a(RH)$ and $D_a(S)$

Measured D_a data for Paste2 and Paste3 include both adsorption and desorption processes and therefore it is able to compare hysteresis between desorption and adsorption as it has been discussed in the literature [11]. Calculation results based on the four studied models for Paste2 and Paste3 are shown in Figs. 6.3 and 6.4, respectively. Because Mualem model-b [128] provides the same equation for the main adsorption process as Mualem model-a [89] (see Section 5.6.5), in Figs. 6.3 and 6.4 curves for "VGMa.Ads." and "FXMa.Ads." are the same as curves for "VGMb.Ads." and "FXMb.Ads.", respectively. The fitted K_l and x_D values for the adsorption process are presented in Tables 6.1 and 6.3, respectively.

Several observations can be seen in Figs. 6.3 and 6.4:

- Hysteresis in $D_a(S)$ curves is negligible, either for the measured data or the fitted curves. This is in agreement with the conclusion about hysteresis in $k_{rl}(S)$ which has been confirmed for soils and other porous materials [150, 151, 152].
- Experimental data for Paste2 show very clear hysteresis in $D_a(RH)$ curves between adsorption and desorption. All fitted curves by four models captured this trend. Hysteresis in $D_a(RH)$ for Paste3 is not as clear as for Paste2 and the fitted curves also

[a] Taken from research results by Baroghel-Bouny [11].
[b] Taken from Table 2.5.
[c] Taken from research results by Nguyen [24].
[d] Obtained by drying at RH^e = 63.2%.

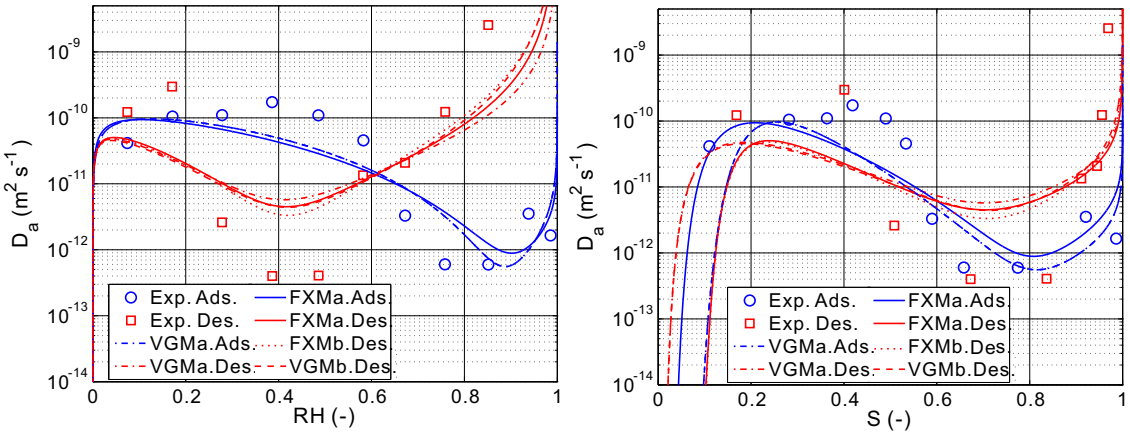

(a) RH-D_a (b) S-D_a

Figure 6.3: Fitted D_a curves for Paste2 during both desorption and adsorption processes.

show smaller hysteresis as well.

• Hysteresis in $D_a(RH)$ show that for each material there is a threshold RH value which divides hysteresis into two parts: below this threshold value, $D_a(RH)$ in adsorption is larger; above this threshold value, $D_a(RH)$ in desorption is larger. Besides of reasons of the differences in fitted K_l and x_D (see Tables 6.1 and 6.3), this trend is mainly due to the different shapes of the main desorption and adsorption isotherms.

• The fitting results for adsorption are much better than those for desorption. The main reason is that the measured desorption data are more fluctuating than the measured adsorption data.

• Although Mualem model-a provides hysteresis in both relations $k_{rl}(S)$ and $k_{rl}(RH)$, VGMb and FXMb do not present significantly different results to other models. Thus, hysteresis in $k_{rl}(S)$ or $k_{rl}(RH)$ cannot be used to explain hysteresis in $D_a(S)$ or $D_a(RH)$. In other words, hysteresis in $D_a(RH)$ observed with measured data (see Fig. 6.3a) may be not caused by hysteresis in $k_{rl}(S)$ or $k_{rl}(RH)$. It may be due to hysteresis in $RH(S)$ or $\mathrm{d}P_c/\mathrm{d}S$ (see Eqs. 6.1 and 6.1).

The above discussions reveal that x_D is clearly larger than the theoretical one. Besides, the fitting for desorption is not very good especially in the low RH range. In the next subsection, an improved method taking into account the Knudsen effect will be used to describe vapour diffusion.

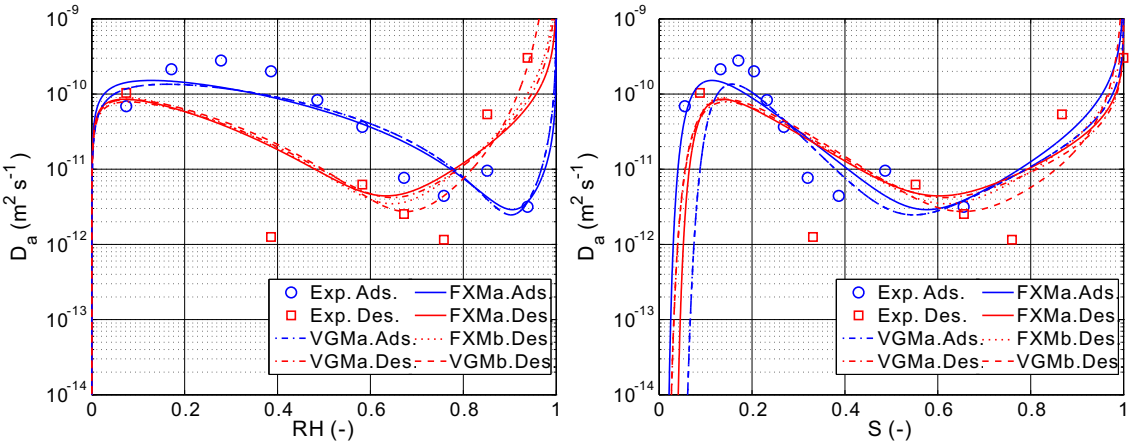

(a) RH-D_a (b) S-D_a

Figure 6.4: Fitted D_a curves for Paste3 during both desorption and adsorption processes.

6.1.3 Improved method

Obviously, Eq. (6.2) only takes into account ordinary diffusion. As it has been discussed in Chapter 1, ordinary diffusion predominantly occurs in pores between 50 nm and 10 μm (the typical range of large capillary pores) which corresponds to the range of RH $>$ 98% according to Kelvin's law (see Eq. 4.8). However, in most conditions, vapour diffusion occurs in the small range of pores whose size is definitely below 50 nm. In the pore size range 2-50 nm, Knudsen diffusion plays a main role (e.g., [219]). Hence, to describe vapour diffusion in this pore size range, Knudsen effect has to be taken into account. This effect is able to reduce the diffusion process due to the collisions between molecules and pore walls [80].

Assuming all pores are independent parallel cylinders, Knudsen diffusion coefficient for a single pore is formulated as [220, 80, 21]:

$$D_{K,\text{single}} = D_{v0}\frac{1}{1+\dfrac{\lambda}{2r_K}} \tag{6.3}$$

where r_K is the Kelvin pore radius (see Fig. 6.5) which is the effective radius for Knudsen diffusion. At a room temperature (around 293 K) and atmospheric pressure (1 atm), the mean free path λ of water molecules is about 8×10^{-8} m.

Knudsen diffusion only takes place in pores unfilled by liquid-water. Therefore, the macroscopic diffusivity in all parallel pores is obtained by integrating $D_{K,\text{single}}$ over unfilled pores (pore size $> r_p$) as:

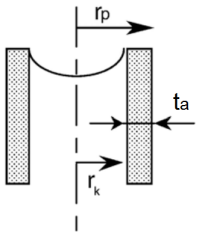

Figure 6.5: Definition of pore radii.

$$D_K = D_{v0} \int_{r_K}^{\infty} \frac{\dfrac{\mathrm{d}V}{V_v \mathrm{d}r_p}}{1 + \dfrac{\lambda}{2\left[r_p - t_a(RH)\right]}} \mathrm{d}r_K \tag{6.4}$$

where $\dfrac{\mathrm{d}V}{V_v \mathrm{d}r_p}$ is inferred from the pore size distribution (PSD), which is usually calculated based on measured sorption isotherms. V_v is the pore volume for vapour diffusion. The pore radius is given as $r_p = r_K + t_a$ where t_a is the thickness of the adsorbed layer. Hagymassy et al. [221] firstly published the water vapour t_a curve (t_a *vs.* RH) for non-porous adsorbent based on water vapour adsorption experiments. A generalized expression for the curve is:

$$t_a(\mathrm{RH}) = \frac{a_H}{\left[c_H - \log(RH)\right]^{b_H}} \tag{6.5}$$

where a_H, b_H and c_H are related to the properties of the material. Baroghel-Bouny [23] used Hagymassy's method to calculate the t_a curve for cementitious materials and found that there is a master curve which is suitable for all the studied materials (see Fig. 6.6). Fig. 6.6 shows that the master t_a curve is almost the same as that for Paste2 and Paste3, especially for RH< 63.2%. For PSD, a calculation approach called BJH method is adopted, which was proposed by Barrett, Joyne and Halenda [222]. This method assumes that both capillary and adsorbed water coexist in pores which are treated as cylinders. Radii of capillary pores are governed by Kelvin's law, corresponding to r_K in Fig. 6.5. The thickness of adsorbed layers varies with different RH and can be described by t_a curve. If the experimental sorption isotherms span from RH = 0 to 100%, the BJH method can theoretically calculate the pore size distribution in both mesopore (2 to 50 nm) and in micropore ranges (pore openings < 2 nm). The minimum RH used in sorption isotherms measurements is 11% [23] which corresponds to the minimum pore size around $r_p \approx 0.5$ nm.

According to the BJH method and measured sorption data [23], the calculated pore size

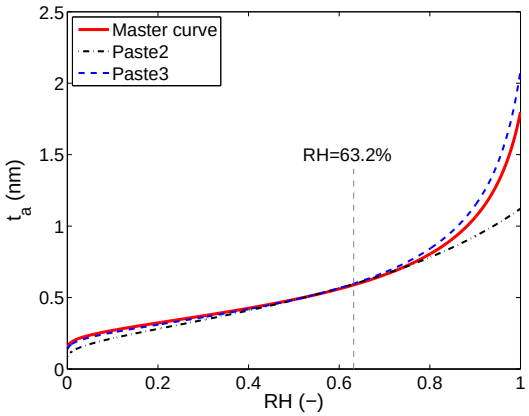

Figure 6.6: The t_a curves.

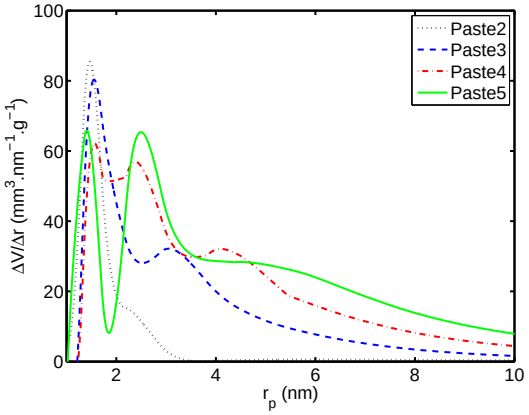

Figure 6.7: The pore size distribution calculated by BJH method.

distributions for the studied materials are displayed in Fig. 6.7. It shows that there are two or three peaks depending on the type of the material. The first peak is observed for all the materials corresponding to around $r_p = 1.7$ nm which is supposed to represent the microstrcture of the denser C-S-H. The second peak is quite different according to the studied materials and even the third peak can be observed for some materials such as Paste5. The second and third peaks may represent the microstructure of outer C-S-H. These differences in pore size distribution are able to significantly affect the moisture transport behaviour, in particular for the vapour diffusion.

The calculated curves with the Knudsen effect for the studied materials are presented in Fig. 6.8. As mentioned above, the Knudsen effect is only calculated for pores larger than 0.5 nm. For pore size below 0.5 nm, the Knudsen effect is considered as the same as that for $r_p = 0.5$ nm. Figure 6.8 shows that D_K/D_{v0} remains nearly constant when RH is below a certain value depending on the material. In the range above this RH value, D_K/D_{v0} increases quickly with

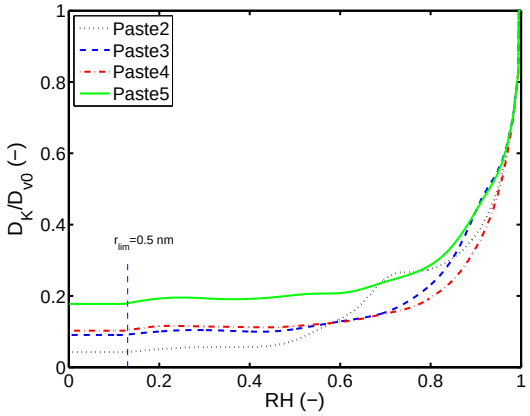

Figure 6.8: The calculated Knudsen effect for different materials.

RH. For Paste3, Paste4 and Paste5, this RH value is between 70% and 80%, but for Paste2 it is around 50%. This may indicate that the studied high performance material (Paste2) has quite different microstructure to other materials. However, vapour diffusion is only predominant in the low RH range and therefore the differences of D_K/D_{v0} values in the high RH range will have a very small influence on the fitting results for x_D.

Fitting results for K_l and x_D

The fitted x_D values for the case of taking into account the Knudsen effect are compared with the case of without the Knudsen effect in Tables 6.2 and 6.3 for desorption and adsorption, respectively. Because the Knudsen effect has no influence on liquid-water transport, the fitted K_l values for the basic and the improved methods are very similar. Thus, K_l values for the improved method are not shown here. But for the vapour diffusion, values of x_D are much smaller if the Knudsen effect is considered (see Tables 6.2 and 6.3).

Table 6.2: The fitted x_D for the desorption process.

Materials	Millington [93]	Thiéry et al. [120]	Without Knudsen effect				With Knudsen effect			
			VGMa	VGMb	FXMa	FXMb	VGMa	VGMb	FXMa	FXMb
Paste2	4/3	2.74	1.54	1.56	1.59	1.61	0.34	0.36	0.37	0.40
Paste3			2.23	2.17	2.25	2.21	0.90	0.89	0.92	0.91
Paste4			4.26	4.10	4.34	4.24	2.39	2.22	2.47	2.38
Paste5			4.47	4.32	4.42	4.33	2.83	2.67	2.77	2.68

An important observation in Table 6.2 which should be pointed out is that if considering the Knudsen effect x_D values for the four studied materials appear in two groups: Paste2 and Paste3 have very close x_D values which are below 1 ($0.3 < x_D < 0.92$), and x_D values for Paste4

and Paste5 are not so different ($2.22 < x_D < 2.83$). The phenomenon may indicate that Paste2 and Paste3 have some similarities in gel microstructures, as well Paste5 and Paste4 in capillary microstructures. This is rather reasonable because in the high performance material (Paste2) and the material with low w/c (Paste3), gel pores are predominant as Fig. 6.7 shows that these materials have a similar PSD.

Table 6.3: The fitted x_D for the adsorption process.

Materials	Without Knudsen effect		With Knudsen effect	
	VGMa (VGMb)	FXMa (FXMb)	VGMa (VGMb)	FXMa (FXMb)
Paste2	1.70	1.66	0.97	0.93
Paste3	2.54	2.38	1.79	1.63

Threshold values of RH for vapour and liquid transport

Figures 6.2, 6.3 and 6.4 show that for each D_a curve there is a threshold RH value which divides the curve into two parts. One part is related to D_l in the high RH range and the other part is from D_v in the low RH range. The same trend is also shown in Fig. 2.15. The threshold RH values are presented in Table 6.4 for all the materials in the case of using VGMa model and considering Knudsen effect.

Table 6.4: The calculated RH threshold values for using VGMa model with Knudsen effect.

	Paste2	Paste3	Paste4	Paste5
Desorption	0.41	0.66	0.67	0.74
Adsorption	0.87	0.92	-	-

Two trends can be seen in this table: the threshold values increase with w/c and values in adsorption are larger than that in desorption. A higher threshold value means that vapour diffusion is more significant. This is the same as the conclusion provided in Chapter 2 (see Section 2.5) when discussing the different transport modes. In adsorption, adsorbed layers are formed at low RH and more water molecules are condensed with the increase of RH. If there are more capillary pores in the material, the continuous liquid-water is not easy to establish in the low RH range so that the main transport mode remains vapour transport. The differences of threshold values between desorption and adsorption can be explained by the same reasons as hysteresis behaviour such as the "ink-bottle effect" (see Section 1.2).

6.1.4 Partial conclusion

This section has compared two ways to fit K_l and x_D based on the measured apparent diffusivity. One method considers vapour transport in cementitious materials as ordinary diffusion and the other method views it as Knudsen diffusion. Four models to calculate k_{rl} have also been compared. Through these comparisons of the different methods, it can be concluded:

1) Among the compared k_{rl} models, Mualem model-b [128] provides much higher values of K_l than the other methods (Katz-Thompson model, inverse analysis using the first boundary condition, fitting D_a using Mualem model-a). Moreover, this model is not very easy to use. By contrast, Mualem model-a [128] is an easy-to-use model, which could be the first choice for numerical purposes. Besides, hysteresis in $D_a(RH)$ is caused by hysteresis in sorption isotherms $RH(S)$ or moisture capacity $\mathrm{d}S/\mathrm{d}P_c$, but is not related to hysteresis in $k_{rl}(S)$ or $k_{rl}(RH)$.

2) K_l values determined by fitting measured D_a data are much lower values provided by inverse analysis. The main reason could be the low accuracy fitting.

3) If comparing cementitious materials with soils or sands, the resistance effects to water vapour diffusion should be more significant. Hence, when the Knudsen effect is taken into account, it provides more relevant x_D values which appear to separate the studied materials in two groups (high performance and ordinary materials). One group with low x_D values represents effects of gel microstructure and the other group with high x_D values shows effects of capillary microstructure.

In the previous chapter, only VGMa and VGMb model were implemented to simulate moisture transport in cementitious materials. The newly introduced FXMa, FXMb in this chapter have not been implemented in a moisture transport model yet. Further work is needed to implement these models to simulate moisture transport and to check the applicability of them.

Notice that k_{rl} can be indirectly verified if using the relationship between k_{rl} and k_{rg} provided by the theory of Mualem model-a [89] (see Eq. 2.10). Obviously, k_{rg} is much easier to be determined by experiments in case of cementitious materials. Such work has been done by Monlouis-Bonnaire et al. [131] and Thiéry et al. [129]. Based on the theory of Mualem model-a, they suggested that $\ell = 5.5$ and 7.15, respectively. These two proposals need to be verified in the future study.

6.2 Effect of boundary conditions on the determination of K_l by inverse analysis in laboratory condition

Coupling moisture transport between the porous material and its surrounding is a process of significant scientific and applied interest. It involves several mechanisms that affect the macroscopic behaviour. These include phase change between liquid and vapour, mass transport by diffusion and convection, etc. However, most moisture transport models for cementitious materials in the literature only focus on the mass transport taking place within the material. Moisture transport over the material surface is generally represented by a simplified boundary condition, either by the first type or by the flux boundary conditions (see Eqs. 1.65 and 1.68 in Section 1.5.6). These conditions only consider one-way effects and do not really take into account mutual interactions between the material and its surrounding.

In the early developed 1D-HAM (Heat-Air-Moisture) PC-program [223, 224], it considered that a fictitious surface film can be used to account for the material surface resistance. This film is simulated as a material layer without additional air flow resistance. This method is quite similar to the flux boundary condition. In building energy models, such as EnergyPlus [105], TRNSYS [106], HAM and simplified models (e.g., EMPD), they assume that state variables are uniform in the air, so that only one node is considered in the region of surrounding to couple moisture [105, 106]. Laurindo and Prat [225, 226] considered the presence of a mass boundary region (MBR) over the external surface of the porous media to estimate the drying rates. Thus, the coupled system of materials and their surrounding can be viewed as three parts: a) the porous material, b) the MBR and c) the part beyond the MBR in the environment (see Fig. 6.9). In the material, moisture transport can be simulated by models mentioned in Chapters 1 and 2. Actually, for most models in the literature, they do not distinguish the mass boundary region and part (c) [227, 228, 229, 230], and call them together as an atmospheric boundary layer (e.g., [231]). However, modelling results by Laurindo and Prat [225, 226] concluded that the thickness of the MBR x_e has a great effect on drying rate. Yiotis et al. [232] further pointed out that the drying rate is inversely proportional to x_e. These conclusions let us take a new look at the conditions used during our experiments which have been used to fit K_l in Chapters 2 and 5. In experimental conditions, samples were placed in desiccators with constant RH which is controlled by the saturated salt solution. Generally, the distance between the surface of the sample and the surface of the saturated salt solution is 5 cm - 15 cm. In this region, only water

vapour diffusion occurs. If vapour diffusion in this region has an influence on moisture transport in the material, K_l determined by inverse analysis in Chapters 2 and 5 can be also affected.

On the whole, the purpose of this section is to check whether there is an influence on K_l determined by inverse analysis if taking into account vapour diffusion in the mass boundary region. Let's call this condition as "diffusive boundary condition" since only vapour diffusion is considered. A simple 1D model will be introduced to simulate vapour diffusion in this region. Moisture transport in both material and the MBR are simultaneously solved. Some discussions about x_e and its effects on mass loss and K_l are presented in the last part of this section.

6.2.1 Modelling of water vapour diffusion in the MBR

The air in the MBR is viewed as an incompressible ideal gas. Uno [115] analysed several traditional equations for the drying evaporation from the surface of wetted concretes, and he finally concluded that the drying rate is related to the velocity of ambient air and how fast diffusion occurring at a given temperature. Since there is no air velocity in our experiments, the mass balance equation for vapour transport in the MBR only contains vapour diffusion with a constant diffusivity.

$$\frac{\partial \rho_v}{\partial t} = D_{v0} \frac{\partial^2 \rho_v}{\partial x^2} \tag{6.6}$$

At the surface, the continuity of vapour movement is expressed as:

$$(\rho_v)^- = (\rho_v)^+ \tag{6.7}$$

where "$-$" and "$+$" represent the MBR and the material sides as shown in Fig. 6.9.

Moisture transport in the material is simulated by the simplified mode used in Chapter 5 (see Section 5.2). The continuity of moisture flux at the surface is given by:

$$\left(D_{v0} \frac{\partial \rho_v}{\partial x} \right)^- = \left(D_a(\rho_v) \frac{\mathrm{d}S}{\mathrm{d}P_c} P_{vs} \frac{\rho_l}{\rho_v} \frac{\partial \rho_v}{\partial x} \right)^+ \tag{6.8}$$

The left boundary condition of the MBR is fixed by a constant vapour density and the right boundary condition is controlled by the flux with respect to the material. The transport equation in the MBR is solved simultaneously with moisture transport within the material for each iteration. The same numerical method as in Chapter 5 (see Section 5.3) is used here.

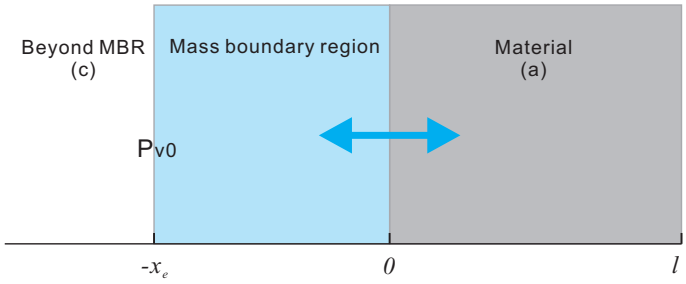

Figure 6.9: Schematic representation of the system in case of our experimental conditions. P_{v0} shows where vapour pressure is controlled by the saturated salt solution. x_e and l represent the thickness of the MBR and the sample. The moisture exchanges occur at the position $x = 0$.

6.2.2 Modelling validation

The validation will check if the newly developed method coupling internal and external moisture transport can provide simulation results that agree with experimental data. The agreement should be found in both mass loss curves and saturation profiles. Here, Paste4 is taken as an example (the case of drying at $RH^e = 53.5\%$) and experimental data have been displayed in Figs. 5.6 and 5.7. The description of experiments has been given in Chapters 2 and 5. In this coupled model, there are two unknowns: x_e and K_l. The value for K_l is set as 2.0×10^{-21} which was calibrated by inverse analysis using the flux boundary condition (see Table 2.4 in Chapter 2). Thus, the value for x_e can be changed to fit measured mass loss curve during drying. Eventually, $x_e = 3$ cm is found to be able to provide relevant simulation results. The same values of x_e and K_l are also used for modelling of wetting.

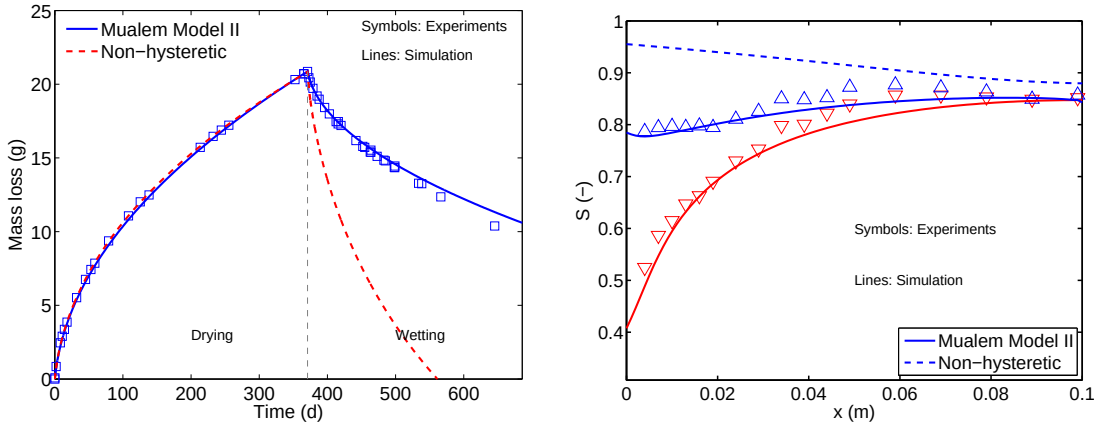

(a) Mass loss curves.

(b) Saturation profiles.

Figure 6.10: Comparisons of simulated mass loss curves and saturation profiles with measured ones for Paste4.

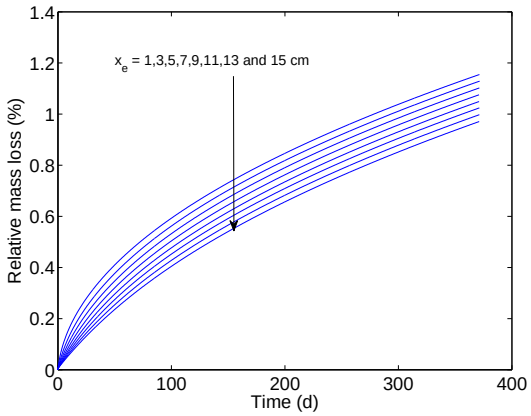

Figure 6.11: The effects of x_e on the mass loss. Taking Paste4 as an example.

Simulation results for both hysteresis (Mualem Model II) and non-hysteresis ($\omega = 1$, see Eq. 5.4) modellings are shown in Fig. 6.10. For the hysteresis modelling, good agreements between simulation results and experimental data can be found for both mass loss curves and saturation profiles. For the non-hysteresis modelling, it overestimates the mass changes during wetting. Actually, these results are very similar to results calculated by using the flux boundary condition as shown in Figs. 5.6 and 5.7.

6.2.3 Discussion about effect of the MBR on the fitting of K_l by inverse analysis

Effect of x_e on simulated drying kinetics

The above comparison may indicate that the main factor which can affect the simulation results is K_l, rather than x_e. To prove this assumption, the mass loss curves simulated by using the same K_l value but different x_e values are shown in Fig. 6.11. After drying around one year, the difference of the relative mass loss between $x_e = 1$ cm and 15 cm is only very small. This shows that x_e is less sensitive than K_l in the numerical modelling.

Relation between K_l and x_e

The value of x_e is adjusted between 0 and 15 cm to calibrate K_l based on the experimental mass loss curve during a drying experiment at controlled RH. The relation between x_e and K_l for the three studied materials are shown in Fig. 6.12. Points at $x_e = 0$ corresponds to the first type boundary condition (see Eq. 1.65).

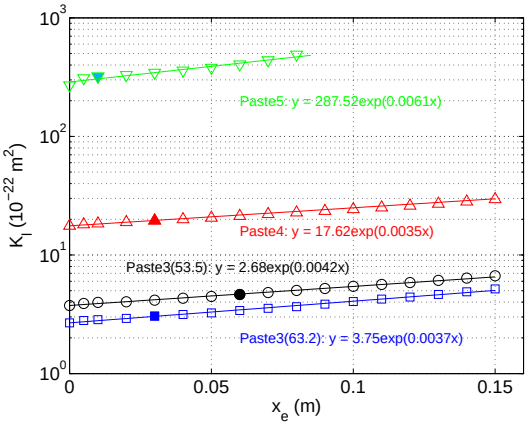

Figure 6.12: Relationship between x_e and K_l for the studied materials. Paste3(53.5) represents experiment at $RH^e = 53.5\%$ and Paste3(63.2) represents experiment at $RH^e = 63.2\%$. Highlighted (solid) symbols are determined by using the flux boundary condition.

Figure 6.12 shows that a very good relation between x_e and K_l for all the studied materials. The K_l values at $x_e = 15$ cm are around two times larger than values at $x_e = 0$ cm, but they are still in the same order of magnitude. Hence, the differences between K_l values calibrated by the first type and the diffusive boundary conditions are not so large.

In Fig. 6.12, K_l values determined by the flux boundary condition are highlighted. These values are located in the figure between $x_e = 0$ to 6 cm. In our experiments, the distance between the salt solution surface and samples is between 5 to 15 cm. Even if the maximum value of $x_e = 15$ cm is chosen, K_l values in Fig. 6.12 are still very close to K_l values determined by using the flux boundary condition. The comparison is able to conclude that the inverses analysis method using these three different boundary conditions (first type, flux and diffusive) can show good agreements in terms of fitted K_l values. This may indicate that the inverse determination of K_l is quite reliable and shows very small influence of the type of boundary condition.

6.2.4 Partial conclusion

In this section, a coupled model has been used to simulate moisture transport in the mass boundary region and in the material. This model only considers vapour diffusion in the MBR according to our experimental conditions. The main conclusions are:

1) If the same K_l combining with different values of x_e is used, the coupled model provides quite similar mass loss curves as in the case using the flux boundary condition.

2) The relationship between x_e and K_l reveals that different x_e values from 0 cm to 15 cm do

not affect moisture transport within the material very much.

3) All results and discussions show that the inverses analysis method using the three usual boundary conditions (first type, flux and diffusive) provide quite similar results of determined K_l values on the basis of drying experiments. Hence, there is no necessity to take into account vapour diffusion in the MBR for determination of K_l in the case of laboratory experimental conditions.

Above observations are restricted to laboratory conditions in which only 1D vapour diffusion is considered. If one wants to study natural conditions, which means that effect of air velocity in the MBR have to be taken into account, a 1D coupled model seems to be not so relevant because the air always flows along the surface of the material rather than in the vertical direction. Although the air does not directly affect moisture transport in the vertical direction, it can certainly increase the drying rates.

6.3 Comparisons of K_l values determined by different methods

Overall, there are nine methods which have been used to determine K_l (see Fig. 6.1). All K_l values corresponding to these methods are presented in Fig. 6.13 for the four studied materials (see Table 3.2). Values for the Katz-Thompson model are taken from the literature [24, 11]. From the second to the fifth methods (red bars in Fig. 6.13), K_l values are calibrated by inverse analysis by fitting drying kinetics. When simulations were performed with the diffusive boundary condition (see Section 6.2.1), the thickness boundary region x_e was adjusted from 0 cm to 15 cm according to our experiments and a series of K_l values has been determined. In Fig. 6.13, only K_l values obtained at $x_e = 10$ cm are presented, which is considered as the most representative thickness. From the sixth to the ninth methods (blue bars), K_l values are determined by fitting measured apparent diffusivity D_a for desorption.

Notice that the newly proposed FXMa and FXMb for fitting D_a seem not as stable as VGMa and VGMb because they present larger K_l value variations. More clearly, FXMb illogically provides a smaller K_l value for Paste4 than Paste3. This is quite unusual because a more porous material (like Paste4) should have a larger permeability than a less porous material (like Paste3). Thus, methods based on FXMa and FXMb will not be compared below.

Roughly speaking, for each material, K_l values indicate that there are two groups for all methods. The first group with higher K_l values consists of the Katz-Thompson model and

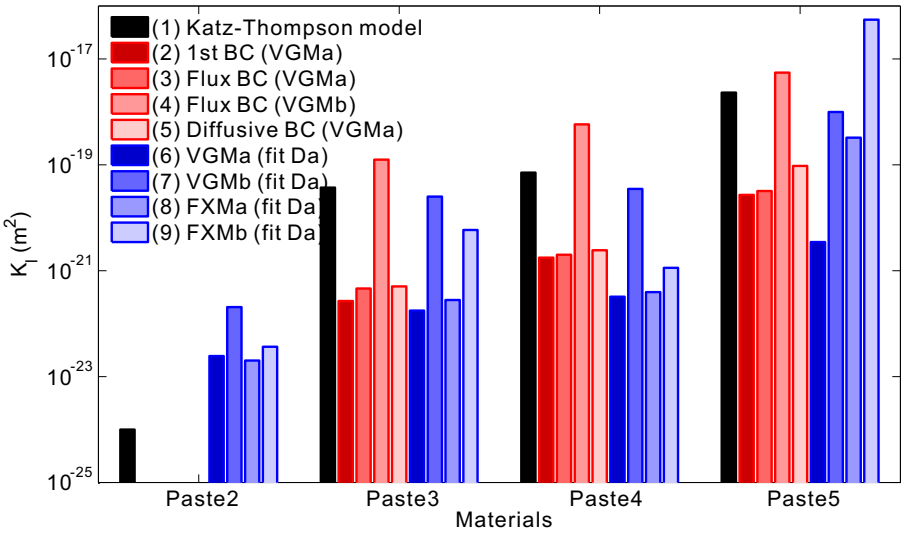

Figure 6.13: Comparisons of K_l values determined by different methods for the studied materials.

methods related to Mualem model-b used to assess k_{rl} [128], including inverse analysis and fitting D_a using VGMb model (methods 1, 4 and 7 in Fig. 6.13). Methods in the other group with smaller K_l values are related to Mualem model-a used to assess k_{rl} [89] (methods 2, 3, 5 and 6 in Fig. 6.13).

If the Katz-Thompson model is considered as the benchmark, methods related to Mualem model-b [128] obviously provide more relevant results than methods related to Mualem model-a [89]. However, as it has been emphasised, Mualem model-b is more difficult to use for numerical modelling and it needs more experimental data (both main sorption curves) than Mualem model-a. Mualem model-b yields much smaller k_{rl} than Mualem model-a. This is the main reason why Mualem model-b provides closer K_l values to the Katz-Thompson model. This may indicate that a modification to Mualem model-a is needed to obtain smaller k_{rl}. This kind of consideration will be included in the further work.

Chapter 7

Conclusion and perspectives

7.1 General remarks

In this study, modelling of drying and wetting cycles in the case of cementitious materials has been described with comprehensive verifications by experimental data. This section highlights the main conclusions of this work, which are shown in the sequence of chapters.

7.1.1 Modelling of isothermal drying

For modelling of drying and wetting cycles, models initially developed to simulate moisture transport under periodic boundary conditions were reviewed firstly. Three methods were summarised: using separate transport coefficients for drying and wetting, non-hysteresis modelling and hysteresis modelling. The literature [14, 15, 16] has pointed out that taking into account hysteresis can improve the simulation results. However, there were no further experimental data to consolidate this conclusion, neither in-situ nor laboratory data. Therefore, this study is devoted to modelling moisture transport with hysteretic effects and to providing experimental data to verify the modelling results and relevancy.

The second step is to find a sufficient moisture transport model. On the basis of previous studies [74, 77, 42, 78, 34], a sophisticated multiphase model, which is able to describe moisture transport through advection of liquid-water, advection of gas-phase and diffusion of water vapour and dry air, was recalled. In experimental verifications, two methods to calculate the relative permeabilities of liquid-water and gas-phase were compared. Both methods can provide good simulation results compared with experimental data. The only difference can be found in the

values of the liquid-water intrinsic permeability K_l and the gas-phase intrinsic permeability K_g validated by these two methods.

Theoretically, K_l and K_g should be the same because there correspond to intrinsic properties of the material and only dependent on the pore structure. However, measurements of K_g show that K_g is much larger than K_l [84, 85, 142]. Hence, both cases ($K_l = K_g$ or $K_l \ll K_g$) were considered in this study. According to the asymptotic analysis, it was able to distinguish quite permeable and weakly permeable porous materials. For the case of cementitious materials, the use of $K_l = K_g$ implies that cementitious material can be considered as weakly permeable media, while materials are apt to show quite permeable behaviour if $K_l \ll K_g$. Gas pressure variations, including overpressure and underpressure, were observed for weakly permeable materials. But for quite permeable materials, gas pressure in the material always remains constant (equal to the atmospheric pressure). If further neglecting advection of gas-phase, a diffusion-like equation only with liquid-water transport can be obtained for the case $K_l = K_g$ [88, 42]. But for the case $K_l \ll K_g$, if advection of gas-phase is negligible as well, a simplified model with advection of liquid-water and vapour diffusion is obtained. This simplified model was used to simulate moisture transport under drying and wetting cycles conditions in Chapter 5.

Different transport modes were investigated for transport both at the boundary and in the material. In the high water content range, advection of liquid-water is predominant, while in the low water content range, vapour transport plays a main role. These different transport modes are related to the material properties, initial and boundary conditions. For natural conditions, two transport modes generally occur simultaneously.

7.1.2 Modelling of drying and wetting cycles

The third step for modelling is to find an appropriate hysteresis model. Thus, detailed comparisons of hysteresis models have been conducted, which include models for the fitting of the main sorption curves, for the prediction of the main adsorption curve based on the known desorption curve, and for the simulation of scanning loops. Quantitative criteria were used to evaluate the relevancy of the fitting. Comparisons showed that most hysteresis models taken from soil science can be used for cementitious materials.

Among the selected main curves fitting equations, the three-parameter models showed better results than the two-parameter models. Models selected for predicting one main isotherm based on the other main isotherm seem not relevant. Concerning hysteresis models, the empirical ones

showed a slight better prediction for the first scanning curves than the domain theory models, but the pumping effect remains a big issue for the empirical model. The domain theory models can avoid this non-physical behaviour and can provide closed scanning loops. This is one of the main advantages to use conceptual models.

After comparisons of hysteresis models, a new method to determine the main desorption and main adsorption curves by using the fewest experimental data was proposed. To predict both desorption and adsorption isotherms, five points with suggested positions (three for the main desorption curve and two for the main adsorption curve) are enough for ordinary cementitious materials. For some high performance materials, the use of one or more points in the low RH range can greatly improve the fitting accuracy.

The fourth step for modelling of drying and wetting cycles is to prepare the input data for modelling and experimental data for verification. Experimental investigations about effects of varying RH at the boundary on moisture distribution within cementitious materials were carried out. Measurements of mass loss curves and saturation profiles were carried out during drying, wetting and re-drying. Comparisons of mass loss curves calculated based on data from gamma-ray attenuation method and measured by weighing showed that gamma-ray attenuation technique can provide very reliable results to assess the repartition of moisture within the material.

Water vapour sorption isotherms for various cement pastes were measured by using a dynamic vapour sorption instrument (DVS). Weibull's equation [191] was used to extrapolate the mass loss curve measured by DVS. This equation can yield very good fitting results. In DVS measurements, the main adsorption isotherms were not measured. Hence, the method proposed in Chapter 3 was employed to estimate the main adsorption curve thanks to the measured main desorption curve and the first adsorption scanning curve. Results showed that this method can provide satisfactory shapes of the main adsorption curves.

The fifth step for modelling is to couple hysteresis models with a moisture transport model. The proposed method, involving two hysteresis indexes to implement hysteresis models into moisture transport models, showed a high applicability. The method can be used for both conceptual and empirical hysteresis models. Comparisons with measured mass loss curves and saturation profiles concluded that modelling taking into account hysteresis explicitly provides better results than non-hysteresis modelling. It is principally because hysteresis models can provide a more relevant RH-S relation at the boundary. Among hysteresis models, because improved Rubin's model (an empirical model) [177, 144] yields non-physical scanning loops,

characterised by "pumping errors", this model did not provide as good results as Mualem Model II (a conceptual model) [53]. Therefore, Mualem Model II is considered as the one recommended for modelling of moisture transport under varying boundary conditions.

Comparison of different forms of Richards' equation revealed that the mixed form, using ∇P_c as the driving force, is a better choice which provides better simulation results than the form using ∇S as the driving force.

Comparisons with different cycle durations showed that smaller cycle durations and boundary RH amplitude cause smaller errors for non-hysteresis modelling. The errors increase with the cycle duration and boundary RH amplitude. For long term simulations, different initial steps (initial drying and initial wetting) did no show significant differences in mass loss curves and saturation profiles. Furthermore, experimental verifications showed that it is not necessary to consider hysteresis in relative permeability to liquid-water $k_{rl}(S)$.

From a practical point of view, one important factor is the moisture penetration depth x_p which can be defined under periodic boundary conditions. For non-hysteresis modelling, this study confirmed that x_p is related to the cycle duration and the RH amplitude, but not to the initial condition. However, for the hysteresis modelling, if the initial saturation is lower than 75% it has a clear influence on x_p. Hence, to estimate x_p with hysteretic effects, our model is more applicable for initial RH values higher than 75%. Comparisons of x_p revealed that the non-hysteresis modelling may overestimate x_p in the case of long cycle durations and large RH amplitudes.

7.1.3 Relevancy of the determination of the liquid-water intrinsic permeability

In the last part of this thesis, two perspectives were introduced to provide more information for the determination of the intrinsic permeability to liquid-water K_l. The first perspective focused on fitting measured apparent diffusivity values to determine K_l. The resistance factor to vapour diffusion can also be assessed by this kind of fitting through the determination of the parameter x_D. Fitting results showed that in the low RH range the use of Knudsen effect can provide more relevant x_D values for cementitious materials. Two groups of materials can be identified corresponding to low ($0.3 < x_D < 0.92$) and high ($2.22 < x_D < 2.83$) x_D values representing respectively high performance and ordinary materials. In the high RH range, fitted K_l values are much lower than those determined by inverse analysis in Chapter 2. This kind of results is mainly

due to the low fitting accuracy and some problems which provide fluctuating experimental data.

The second perspective is to investigate the effect of vapour diffusion in a mass boundary region on determination of K_l by inverse analysis during a drying experiment in laboratory conditions. Coupled simulations have provided the relation between the thickness of the mass boundary region x_e and K_l. This relationship revealed that different x_e values from 0 to 15 cm do not affect moisture transport in the material very much. All comparisons and discussions indicated no necessary to take into account vapour diffusion in the mass boundary region when determining K_l by inverse analysis. It further proved that this kind of inverse determination of K_l can present very stable results for three types of boundary conditions (the first, flux and diffusive boundary conditions).

7.2 Limitations and perspectives for future research

The work conducted in this thesis represents a contribution to the numerical simulation of durability issues concerning concrete structures. Due to knowledge and time limitations, there are several perspectives, which can be proposed for the future research.

1) Gas pressure variations (overpressure and underpressure) have been found in numerical simulations. However, gas pressure variations have not been verified by experimental data. The tentative idea is to pre-deploy pressure sensors when the samples are cast. Hence, during the drying and wetting measurements, gas pressure variations can be measured.

2) When comparing different hysteresis models, the conclusion was that no appropriate model can be used to predict the main adsorption curve only based on the measured main desorption curve. But it still remains interest to carry out further studies on this topic because the main adsorption curve is not easy to measure compared to the main desorption curve. The discussion about reasons of hysteresis showed that different water states can be observed in different pore size. Generally, the main desorption and main adsorption curves are very close in the low RH range because adsorbed water in gel is predominant. This water does not cause significant hysteresis. The "ink-bottle effect" and different contact angles lead to more significant hysteresis in the capillary water dominated range. The main idea is to infer the main adsorption isotherm based on the theoretical relation between two main curves and the measured main desorption isotherm. The relation between two main curves can be established according to reasons of hysteresis such as the "ink-bottle effect" [9], the

assumption of different shapes of pores [17, 233] and the assumption of different levels of connectivity [19]. The measured main desorption will be used to calibrate parameters in the model.

3) In the current research, the proposed modelling method has been verified by experimental data. However, it still lacks the in-situ measured data for verification. Further research needs to find data from literature or to carry out measurements in the field.

4) In this study, the proposed model focuses on moisture transport in the hygroscopic range. But for natural conditions this model needs to be extended to the liquid-water suction range, in which the material is in direct contact with liquid-water. For modelling of this transport process, the modification to the capillary curve ($P_c - S$) is needed. Firstly, measured sorption isotherms should be extended to retention curve range, which is far above the hygroscopic range due to water in large capillary pores or pores connected by microcracks [17, 233]. Secondly, the currently used equations for sorption isotherms (all main curve fitting equations in Chapter 3) are not sufficient because they provide infinite moisture capacity at $S = 1$. Therefore, a new equation which is able to avoid this drawback is needed such as an equation proposed in latest reference [234]. Then, the extended model can be applied to concrete structures under more severe conditions, such as rain-drying weather conditions, tidal zone, groundwater fluctuating zone, etc.

5) It is clear that transport mechanisms in different pore size are different. In gel pores, vapour is transported by surface diffusion, Knudsen diffusion, etc. But in capillary pores, Knudsen diffusion is mixed with ordinary diffusion. Liquid-water can move due to capillary pressure or can condense on pore walls because of adsorption. Thus, the further research has to focus on the integration of these kinds of moisture transport mechanisms for different size of pores in a unique model.

6) When comparing different models to calculate the liquid-water relative permeability, these models were not verified by experimental data due to the difficulty to measure this kind of data. But an indirect method can be used based on the relationship between k_{rg} and k_{rl} indicating in Mualem model-a (see Eq. 2.10) because k_{rg} is much easier to measure. Further work will carry out this kind of research and apply research results to simulate moisture transport.

7) As it has been mentioned in the general introduction, rarely pure water is involved in the degradation processes. Moisture transport is always the essential mechanism able to induce other durability issues for concrete structures; therefore, moisture transport has to be coupled with other transport phenomena (e.g., heat, ions) to study the moisture behaviour in cementitious materials under drying and wetting cycles conditions. Moisture transport under temperature gradients has been widely studied in the literature [73, 235, 99, 223, 16] and it is not difficult to couple with moisture transport. Furthermore, water in cementitious materials is always mixed with chemical components, which can decrease the chemical activity of the liquid-water and further affect liquid-water transport. Therefore, the liquid-water transport potential such as P_c has to be modified according to the change of ions concentration [43, 44]. In experiments, there were no external sources of ions so it was considered that the chemical effect on moisture transport was fully included in the measured sorption data. For each RH value reached in the material during drying or wetting, the effect of the chemical activity is similar as on the position on the sorption curve for the same RH value. Thus, Kelvin's equation for P_c does not need to be modified.

Bibliography

[1] K. L. Scrivener and R. J. Kirkpatrick, "Innovation in use and research on cementitious material," *Cement and Concrete Research*, vol. 38, pp. 128–136, 2008.

[2] R. J. Flatt, N. Roussel, and C. R. Cheesenman, "Concrete: an eco material that needs to be improved," *Journal of the European Ceramic Society*, vol. 32, p. 2787–2798, 2012.

[3] P. K. Mehta and P. J. M. Monteiro, *Concrete - Microstrucure, Properties and Materials (3rd edition)*. New York: McGraw-Hill, 2006.

[4] L.-O. Nilsson, "Water and the hygro-thermal characteristics of hardened concrete," (St-Remy-les-Chevreuse, France), FNB-Collège International des Sciences de la Construction, pages 122 - 138, 1985.

[5] M. J. Cunningham, "The moisture performance of framed structures - a mathematical model," *Building and Environment*, vol. 23, pp. 123–135, 1988.

[6] J. Arfvidsson, "A new algorithm to calculate the isothermal moisture penetration for periodically varying relative humidity at the boundary," *Nordic Journal of Building Physics*, vol. 2, 1999.

[7] J. Arfvidsson and J. Claesson, "Isothermal moisture flow in building materials: modelling, measurements and calculations based on Kirchhoff's potential," *Building and Environment*, vol. 35, pp. 519–536, 2000.

[8] A. Anderberg, "Moisture properties of self-levelling flooring compounds," tech. rep., Report TVBM 3120, Division of Building Materials, Lund Institute of Technology/Lund University, Sweden, 2004.

[9] R. M. Espinosa and L. Franke, "Inkbottle pore-method: Prediction of hygroscopic water content in hardened cement paste at variable climatic conditions," *Cement and Concrete Research*, vol. 36, pp. 1954–1968, 2006.

[10] R. M. Espinosa and L. Franke, "Influence of the age and drying process on pore structure and sorption isotherms of hardened cement paste," *Cement and Concrete Research*, vol. 36, p. 1969–1984, 2006.

[11] V. Baroghel-Bouny, "Water vapour sorption experiments on hardened cementitious materials. Part II: Essential tool for assessment of transport properties and for durability prediction," *Cement and Concrete Research*, vol. 37, pp. 438–454, 2007.

[12] M. S. Åhs, "Sorption scanning curves for hardened cementitious materials," *Construction and Building Materials*, vol. 22, pp. 2228–2234, 2008.

[13] K. Maekawa, T. Ishida, and T. Kishi, *Multi-Scale Modeling of Structural Concrete*. London and New York: Taylor & Francis, 2008.

[14] B. Johannesson and M. Janz, "A two-phase moisture transport model accounting for sorption hysteresis in layered porous building constructions," *Building and Environment*, vol. 44, pp. 1285–1294, 2009.

[15] B. Johannesson and U. Nyman, "A numerical approach for non-linear moisture flow in porous materials with account to sorption hysteresis," *Transp. Porous Med.*, vol. 84, pp. 735–754, 2010.

[16] H. Derluyn, D. Derome, J. Carmeliet, E. Stora, and R. Barbarulo, "Hysteretic moisture behavior of concrete: Modeling and analysis," *Cement and Concrete Research*, vol. 42, pp. 1379–1388, 2012.

[17] H. Ranaivomanana, J. Verdier, A. Sellier, and X. Bourbon, "Toward a better comprehension and modeling of hysteresis cycles in the water sorption–desorption process for cement based materials," *Cement and Concrete Research*, vol. 41, pp. 817–827, 2011.

[18] M. B. Pinson, H. M. Jennings, and M. Z. Bazant, "Hysteresis and percolation in continuum modelling of water transport in cementitious materials," (Guildford, UK), TRANSCEND Conference: Water Transport in Cementitious Materials, November 3-6, 2013.

[19] M. B. Pinson, H. M. Jennings, and M. Z. Bazant, "Inferring pore size and network structure from sorption hysteresis," p. Under review, 2014.

[20] A. H. Thompson, A. J. Katz, and C. E. Krohn, "The microgeometry and transport properties of sedimentary rock," *Advances in Physics*, vol. 36, pp. 625–694, 1987.

[21] V. Baroghel-Bouny, *Characterization of cement pastes and concretes-methods, analysis, interpretations (in French)*. PhD thesis, ENPC (LCPC Publ., Paris), 1994.

[22] V. Baroghel-Bouny, M. Mainguy, T. Lassabatere, and O. Coussy, "Characterization and identification of equilibrium and transfer moisture properties for ordinary and high-performance cementitious materials," *Cement and Concrete Research*, vol. 29, pp. 1225–1238, 1999.

[23] V. Baroghel-Bouny, "Water vapour sorption experiments on hardened cementitious materials. Part I: Essential tool for analysis of hygral behaviour and its relation to pore structure," *Cement and Concrete Research*, vol. 37, pp. 414–437, 2007.

[24] M. Nguyen, *Modélisation des couplages entre hydratation et dessiccation des matériaux cimentaires à l'issue du décoffrage*. PhD thesis, ENPC, September 2009.

[25] M. Delmi, A. Ait-Mokhtar, and O. Amiri, "Modelling the coupled evolution of hydration and porosity of cement-based materials," *Construction and Building Materials*, vol. 20, pp. 504–514, 2004.

[26] K. L. Scrivener, T. Fullmann, E. Gallucci, G. Walenta, and E. Bermejo, "Quantitative study of Portland cement hydration by X-ray diffraction/Rietveld analysis and independent methods," *Cement and Concrete Research*, vol. 34, pp. 1541–1547, 2004.

[27] J. Thomas and H. Jennings, *The Pore System and Classification of Pores*, accessed November 2013. `http://iti.northwestern.edu/cement/monograph/Monograph7_2.html`.

[28] T. C. Powers, "Structure and physical properties of hardened portland cement paste," *Journal of the American Ceramic Society*, vol. 41, pp. 1–6, 1958.

[29] R. F. Feldman and P. J. Sereda, "A new model of hydrated portland cement paste as deduced from sorption - length change and mechanical properties," *Materials and Structures*, vol. 1, pp. 509–519, 1968.

[30] R. F. Feldman and P. J. Sereda, "A new model for hydrated portland cement and its practical implications," *Engineering J.*, vol. 53, pp. 53–59, 1970.

[31] F. H. Wittmann, "Surface tension shrinkage and strength of hardened cement paste.," *Materials and Structure*, vol. 1, pp. 547–552, 1968.

[32] H. M. Jennings, "A model for the microstructure of calcium silicate hydrate in cement paste," *Cement and Concrete Research*, vol. 30, pp. 101–116, 2000.

[33] S. J. Gregg and K. S. W. Sing, *Adsorption, surface area and porosity (2nd ed.)*. London: Academic Press, 1982.

[34] J. Bear and A. H.-D. Cheng, *Modeling Groundwater Flow and Contaminant Transport*. Amsterdam: Springer Netherlands, 2010.

[35] H. Y. Erbil, *Surface Chemistry of Solid and Liquid Interfaces*. New York: Wiley-Blackwell, 2006.

[36] H. Freundlich, "Űber die adsorption in lösungen," *Z. Phys. Chem.*, vol. 57, pp. 385–470, 1909.

[37] I. Langmuir, "The constitution and fundamental properties of solids and liquids. Part I. solids.," *Journal of the American Chemical Society*, vol. 38, pp. 2221–2295, 1916.

[38] S. Brunauer, P. H. Emmet, and E. Teller, "Adsorption of gases in multimolecular layers," *Journal of American Chemical Society*, vol. 60, pp. 309–319, 1938.

[39] R. W. Dent, "A multilayer theory for gas sorption. Part I: Sorption of a single gas," *Textile Research Journal*, vol. 47, pp. 145–152, 1977.

[40] A. Kumar, S. Ketel, K. Vance, T. Oey, N. Neithalath, and G. Sant, "Water vapor sorption in cementitious materials — measurement, modeling and interpretation," *Transport in Porous Media*, vol. 103, pp. 69–98, 2014.

[41] L. Wadsö, "Transcend course 3 at Lund University: Sorption and Transport." Lecture slides, 2011.

[42] M. Mainguy, O. Coussy, and V. Baroghel-Bouny, "Role of air pressure in drying of weakly permeable materials," *Journal of Engineering Mechanics*, vol. 127, pp. 582–592, 2001.

[43] V. Baroghel-Bouny, M. Thiéry, and X. Wang, "Modelling of isothermal coupled moisture-ion transport in cementitious materials," *Cement and Concrete Research*, vol. 41, pp. 828–841, 2011.

[44] V. Baroghel-Bouny, X. Wang, M. Thiéry, M. Saillio, and F. Barberon, "Prediction of chloride binding isotherms of cementitious materials by analytical model or numerical inverse analysis," *Cement and Concrete Research*, vol. 42, pp. 1207–1224, 2012.

[45] W. Haines, "Studies in the physical properties of soil. V: The hysteresis effect in capillary properties, and the modes of moisture distribution associated therewiht," *The Journal of Agricultural Science*, vol. 20, pp. 97–116, 1930.

[46] K. K. Aligizaki, *Pore Structure of Cement-Based Materials Testing Interpretation and Requirements - Modern Concrete Technology*. London: Taylor & Francis, 2006.

[47] R. A. Guyer, H. A. Kim, D. Derome, J. Carmeliet, and J. TenCate, "Hysteresis in modeling of poroelastic systems: quasistatic equilibrium," *Physical Review E*, vol. 83, pp. 1539–3755, 2011.

[48] D. H. Everett, "A general approach to hysteresis - Part 3: a formal treatment of the independent domain model of hysteresis," *Transactions of the Faraday Society*, vol. 50, pp. 1077–1096, 1954.

[49] D. H. Everett, "A general approach to hysteresis - Part 4: an alternative formulation of the domain model," *Transactions of the Faraday Society*, vol. 51, pp. 1551–1557, 1955.

[50] F. Preisach, "Uber die magnetische nachwirkung," *Z. Physik*, vol. 94, pp. 277–302, 1935.

[51] J. D. Mayergoyz, "Hysteresis models from the mathematical and control theory points of view," *Journal of Applied Physics*, vol. 57, pp. 3803–3805, 1985.

[52] Y. Mualem, "Modified approach to capillary hysteresis based on a similarity hypothesis," *Water Resources Research*, vol. 9, pp. 1324–1331, 1973.

[53] Y. Mualem, "A conceptual model of hysteresis," *Water Resources Research*, vol. 10, pp. 514–520, 1974.

[54] Y. Mualem and G.Dagan, "Dependent domain model of capillary hysteresis," *Water Resources Research*, vol. 11, pp. 452–460, 1975.

[55] Y. Mualem, "A modified dependent-domain theory of hysteresis," *Journal of Soil Science*, vol. 137, pp. 283–291, 1984.

[56] R. J. Hanks, A. Klute, and E. Bresler, "A numerical method for estimating infiltration, redistribution, drainage and evaporation of water from soil," *Water Resources Research*, vol. 5, pp. 1064–1069, 1969.

[57] D. Jaynes, "Comparison of soil-water hysteresis models," *Journal of Hydrology*, vol. 75, pp. 287–299, 1984.

[58] P. S. Scott, G. J. Farquhar, and N. Kouwen, "Hysteresis effects on net infiltration," (Hyatt Regency Illinois Center, Chicago, Illinois, USA), Advances in infiltration : proceedings of the National Conference on Advances in Infiltration, 1983.

[59] X. S. Li, "Modelling of hysteresis response for arbitrary wetting-drying paths," *Computers and Geotechnics*, vol. 32, pp. 133–137, 2005.

[60] U. Nyman, P. J. Gustafsson, B. Johannesson, and R. Hagglund, "A numerical method for the evaluation of non-linear transient moisture flow in cellulosic materials," *International Journal for Numerical Methods in Engineering*, vol. 66, pp. 1859–1883, 2006.

[61] C. Wei and M. M. Dewoolkar, "Formulation of capillary hysteresis with internal state variables," *Water Resources Research*, vol. 42, p. W07405, 2006.

[62] E. Mason and A. Malinauskas, *Gas Transport in Porous Media. The Dusty-Gas Model.* Amsterdam: Elsevier, 1983.

[63] K. Higashi, H. Ito, and J. Oishi, "Surface diffusion phenomena in gaseous diffusion, (I) surface diffusion of pure gas," *Journal of the Atomic Energy Society of Japan*, vol. 5, p. 864, 1963.

[64] K. Gudmundsson, "An approach to determining the water vapour transport properties of building materials," *Nordic Journal of Building Physics: Acta Physica Aedificiorum*, vol. 3, 2003.

[65] Y. Xi, Z. Bazant, L. Molina, and H. M. Jennings, "Moisture diffusion in cementitious materials moisture capacity and diffusivity," *Advanced Cement Based Materials*, vol. 1, pp. 258–266, 1994.

[66] S. G. Jennings, "The mean free path in air," *Journal of Aerosol Science*, vol. 19, pp. 159–166, 1988.

[67] M. Iwamatsu and K. Horii, "Capillary condensation and adhesion of two wetter surfaces," *Journal of Colloid and Interface Science*, vol. 182, pp. 400–406, 1996.

[68] M. Tuller and D. Or, "Hydraulic conductivity of variably saturated porous media: Film and corner flow in angular pore space," *Water Resources Research*, vol. 37, pp. 1267–1276, 2010.

[69] F. A. L. Dullien, F. S. Y. Lai, and I. F. Macdonald, "Hydraulic continuity of residual wetting phase in porous media," *Journal of Colloid and Interface Science*, vol. 109, pp. 201–218, 1986.

[70] F. A. L. Dullien, C. Zarcone, I. F. Macdonald, A. Collins, and R. D. E. Bochard, "The effects of surface roughness on the capillary pressure curves and the heights of capillary rise in glass bead packs," *Journal of Colloid and Interface Science*, vol. 127, pp. 362–372, 1989.

[71] E. Buckingham, *Studies on the movement of soil moisture.* Washington, DC.: Washington, Govt. Print. Off., 1907.

[72] L. Richards, "Capillary conduction of liquids in porous mediums," *Physics*, vol. 1, pp. 318–333, 1931.

[73] J. R. Philip and D. A. de Vries, "Moisture movement in porous materials under temperature gradients," *Transactions, American Geophysical Union*, vol. 38, pp. 222–232, 1957.

[74] J. Bear, *Dynamics of Fluids in Porous Media.* New York: Elsevier Publishing Co., 1972.

[75] J. Bear and A. Verruijt, *Modelling of Groundwater Flow and Pollution.* Amsterdam: Reidel Book Co., 1987.

[76] J. Bear and Y. Bachmat, *Introduction to Modeling of Transport Phenomena in Porous Media.* Amsterdam: Kluwer Academic Publ., 191990.

[77] O. Coussy, *Mechanics of porous continua.* New York: Wiley, 1995.

[78] O. Coussy, *Mechanics and physics of porous solids.* United Kingdom: John Wiley & Sons, Ltd, 2010.

[79] Z. P. Bazant and L. J. Najjar, "Nonlinear water diffusion in non-saturated concrete," *Material and Structure*, vol. 25, pp. 3–20, 1972.

[80] J.-F. Daïan, "Condensation and isothermal water transfer in cement mortar. Part I: pore size distribution, equilibrium water condensation and imbibition," *Transport in Porous Media*, vol. 3, pp. 563–589, 1988.

[81] L.-O.Nilsson, "Long-term moisture transport in high performance concrete," *Materials and Structures*, vol. 35, pp. 641–649, 2002.

[82] H. Janssen, B. Blocken, and J. Carmeliet, "Conservative modelling of the moisture and heat transfer in building components under atmospheric excitation," *International Journal of Heat and Mass Transfer*, vol. 50, pp. 1128–1140, 2007.

[83] O. Coussy, *Poromechanics.* New York: John Wiley & Sons, Ltd, 2004.

[84] A. A. Hamami, P. Turcry, and A. Aït-Mokhtar, "Influence of mix proportions on microstructure and gas permeability of cement pastes and mortars," *Cement and Concrete Research*, vol. 42, pp. 490–498, 2012.

[85] H. Loosveldt, Z. Lafhaj, and F. Skoczylas, "Experimental study of gas and liquid permeability of a mortar," *Cement and Concrete Research*, vol. 32, pp. 1357–1363, 2002.

[86] C. Leech, D. Lockington, R. D. Hooton, G. Galloway, G. Cowin, and P. Dux, "Validation of mualem's conductivity model and prediction of saturated permeability from sorptivity," *ACI Materials Journal*, vol. 205, pp. 44–51, 2008.

[87] J. Carmeliet, H. Hens, and S. Roels, "Determination of the liquid water diffusivity from transient moisture transfer experiment," *Journal of Thermal Envelope and Building Science*, vol. 27, pp. 277–305, 2004.

[88] M. Mainguy, *Modèles de diffusion non linéaire en milieu poreux. Application à la dissolution et au séchage des matériaux cimentaires.* PhD thesis, ENPC, September 1999.

[89] Y. Mualem, "A new model for predicting the hydraulic conductivity of unsaturated porous media," *Water Resources Research*, vol. 12, pp. 513–522, 1976.

[90] M. T. van Genuchten, "A closed-form equation for predicting the hydraulic conductivity of unsaturated soils," *Soil Science Society of America Journal*, vol. 44, pp. 892–898, 1980.

[91] J. C. Parker and R. J. Lenhard, "A model for hysteretic constitutive relations governing multiphase flow: 1. Saturation-pressure relations," *Water Resources Research*, vol. 23, pp. 2187–2196, 1987.

[92] L. Luckner, M. T. van Genuchten, and D. R. Nielsen, "A consistent set of parametric models for the two-phase-flow of immiscible fluids in the subsurface," *Water Resources Research*, vol. 25, pp. 2187–2193, 1989.

[93] R. Millington, "Gas diffusion in porous media," *Science*, vol. 130, pp. 100–102, 1959.

[94] C. Li, K. Li, and Z. Chen, "Numerical analysis of moisture influential depth in concrete during drying-wetting cycles," *Tsinghua Science and Technology*, vol. 13, pp. 696–701, 2008.

[95] K. Li, C. Li, and Z. Chen, "Influential depth of moisture transport in concrete subject to drying-wetting cycles," *Cement and Concrete Composites*, vol. 31, pp. 693–698, 2009.

[96] M. J. Cunningham, "Effective penetration depth and effective resistance in moisture transfer," *Building and Environment*, vol. 27, pp. 379–386, 1992.

[97] K. Hong and R. D. Hooton, "Effects of cyclic chloride exposure on penetration of concrete cover," *Cement and Concrete Research*, vol. 29, pp. 1379–1386, 1999.

[98] H. S. Carslow and J. C. Jaeger, *Conduction of heat in solids.* London: Oxford University Press, 1959.

[99] A. Keresteciogl u, M. Swami, and A. Kamel, "Theoretical and computational investigation of simultaneous heat an d moisture transfer in buildings: Effective penetration depth theory," *ASHRAE Transactions.*, vol. 96, pp. 447–454, 1990.

[100] H. J. Steeman, A. Janssens, J. Carmeliet, and M. D. Paepe, "Modelling indoor air and hygrothermal wall interaction in building simulation: Comparison between CFD and a well-mixed zonal model," *Building and Environment*, vol. 44, pp. 572–583, 2009.

[101] M. Steeman, A. Janssens, H. J. Steeman, M. V. Belleghem, and M. D. Paepe, "On coupling 1d non-isothermal heat and mass transfer in porous materials with a multizone building energy simulation model," *Building and Environment*, vol. 45, pp. 865–877, 2010.

[102] H. Janssen and S. Roels, "Qualitative and quantitative assessment of interior moisture buffering by enclosures," *Energy and Buildings*, vol. 41, pp. 382–394, 2009.

[103] M. Woloszyn, T. Kalamees, M. O. Abadie, M. Steeman, and A. S. Kalagasidis, "The effect of combining a relative- humidity - sensitive ventilation system with the moisture-buffering capacity of materials on indoor climate and energy efficiency of buildings," *Building and Environment*, vol. 44, pp. 515–524, 2009.

[104] J. Woods, J. Winkler, and D. Christensen, "Evaluation of the effective moisture penetration depth model for estimating moisture buffering in buildings," tech. rep., Technical Report, NREL/TP-5500-57441. National Renewable Energy Laboratory, Golden, Colorado, USA., 2013.

[105] EnergyPlus, "Engineering reference," tech. rep., Department of Energy, Lawrence Berkeley National Laboratory, 2011.

[106] TRNSYS, "Transient system simulation program, volume 6: Multizone building modeling with type56 and trnbuild," tech. rep., Solar Energy Laboratory, University of Wisconsin-Madison., 2012.

[107] A. S. Kalagasidis and C. E. H. T. Bednar, "Evaluation of the interface moisture conductivity between control volumes – comparison between linear, harmonic and integral averaging," (Clearwater Beach, California, United States), Proceedings of the International Conference on the Performance of Exterior Envelopes of Whole Buildings IX, 2004.

[108] C. Hall, "Water sorptivity of mortars and concretes: A review," *Magazine of Concrete Research*, vol. 147, pp. 51–61, 1989.

[109] K. F. Li and C. Q. Li, "Hydro-ionic transport in concrete near surface under dying-wetting cycles," (Paris, France), Proceedings of Mechanics and Physics of Porous Solids (MPPS) - A tribute to Prof. Olivier Coussy, 2011.

[110] D. Derome, H. Derluyn, W. Zillig, and J. Carmeliet, "Model for hysteretic moisture behaviour of wood," (Copenhagen, Denmark), Proceedings of the Nordic Symposium on Building Physics 2008, C. Rode (ed.), 2008.

[111] K. Maekawa, R. Chaube, and T. Kishi, *Modelling of Concrete Performance: Hydration, Microstructure Formation, and Mass Transport*. London: E. & F.N. Spon, 1999.

[112] A. Hillergorg, "A modified absorption theory," *Cement and Concrete Research*, vol. 15, pp. 809–816, 1985.

[113] S. D. Pont, F. Meftah, and B. A. Schrefler, "Modeling concrete under severe conditions as a multiphase material," *Nuclear Engineering and Design*, vol. 241, pp. 562–572, 2011.

[114] M. Azenha, K. Maekawa, T. Ishida, and R. Faria, "Drying induced moisture losses from mortar to the environment. Part II: numerical implementation," *Transport in Porous Media*, vol. 24, pp. 81–106, 1996.

[115] P. J. Uno, "Plastic shrinkage cracking and evapouration formulas," *ACI Materials Journal*, vol. 95, pp. 365–375, 1998.

[116] T. Ayano and F. H. Wittmann, "Drying, moisture distribution, and shrinkage of cement-based materials," *Materials and Structures*, vol. 35, pp. 134–140, 2002.

[117] Z. Zhang, M. Thiéry, and V. Baroghel-Bouny, "Analysis of moisture transport in cementitious materials and modelling of drying-wetting cycles," (Aix-en-Provence, France), International Conference: Numerical Modeling Strategies for Sustainable Concrete Structures, by The French Association of Civil Engineering (AFGC), 2012.

[118] T. Defraeye, P. Verboven, D. Derome, J. Carmeliet, and B. Nicolai, "Stomatal transpiration and droplet evaporation on leaf surfaces by a microscale modelling approach," *International Journal of Heat and Mass Transfer*, vol. 65, pp. 180–191, 2013.

[119] K. Gustafson and T. Abe, "The third boundary condition - was it Robin's?," *The Mathematical Intelligencer*, vol. 20, pp. 63–71, 1998.

[120] M. Thiéry, V. Baroghel-Bouny, N. Bourneton, G. Villain, and C. Stéfani, "Modélisation du séchage des bétons - Analyse des différents modes de transfert hydrique," *Revue européenne de génie civil*, vol. 11, pp. 541–577, 2007.

[121] V. Papadakis, C. Vayenas, and M. Fardis, "Physical and chemical characteristics affecting the durability of concrete," *ACI Materials Journal*, vol. 8, pp. 186–196, 1991.

[122] X. Wang, *Modélisation du transport multi-espèces dans les matériaux cimentaires saturés ou non saturés et éventuellement carbonatés.* PhD thesis, Paris-Est University/IFSTTAR, April 2012.

[123] A. Morandeau, *Carbonatation atmosphérique des systémes cimentaires à faible teneur en portlandite.* PhD thesis, Paris-Est University/IFSTTAR, Octobre 2013.

[124] T. M. Geffen, W. W. Owens, D. R. Parrish, and R. A. Morse, "Experimental investigation of factors affecting laboratory relative permeability measurements," *Journal of Petroleum Technology*, vol. 3, pp. 99–110, 1951.

[125] J. S. Osoba, J. G. Richardson, J. K. Kerver, J. A. Hafford, and P. M. Blair, "Laboratory measurements of relative permeability," *Journal of Petroleum Technology*, vol. 3, pp. 47–56, 1951.

[126] B. M. Savage and D. J. Janssen, "Soil physics principles validated for use in predicting unsaturated moisture movement in portland cement concrete," *ACI Materials Journal*, vol. 94, pp. 63–70, 1997.

[127] R. J. Lenhard and J. C. Parker, "A model for hysteretic constitutive relations governing multiphase flow: 2. Permeability-saturation relations," *Water Resources Research*, vol. 23, pp. 2197–2206, 1987.

[128] Y. Mualem, "Hysteretical models for prediction of the hydraulic conductivity of unsaturated porous media," *Water Resources Research*, vol. 12, pp. 1248–1254, 1976b.

[129] M. Thiéry, P. Belin, V. Baroghel-Bouny, and M. Nguyen, "Modelling of isothermal drying process in cementitious materials - Analysis of the moisture transfer and proposal of simplified approaches," (Polytech Lille, France), Proceedings of 3rd International Conference on Coupled T-H-M-C Processes in Geo-systems, 571-581, 2008.

[130] G. Villain, V. Baroghel-Bouny, C. Kounkou, and C. Hua, "Mesure de la perméabilité aux gaz en fonction du taux de saturation des bétons," *Revue européenne de génie civil*, vol. 5, pp. 251–268, 2001.

[131] J. P. Monlouis-Bonnaire, J. Verdier, and B. Perrin, "Prediction of the relative permeability to gas flow of cement-based materials," *Cement and Concrete Research*, vol. 34, pp. 737–744, 2004.

[132] M. Thiéry, *Modélisation de la carbonatation atmosphérique des matériaux cimentaires avec prise en compte des effets cinétiques et des modifications microstructurales et hydriques.* PhD thesis, ENPC, Paris, 2005.

[133] O. Coussy, V. Baroghel-Bouny, P. Dangla, and M. Mainguy, "Assessment of the water permeability of concretes from their mass loss during drying (in french)," (Paris), in: V. Baroghel-Bouny (Ed.), Transferts dans les bétons et durabilité, Special issue of Revue Française de Génie Civil, vol. 5, Hermès Science Publications, p.269-284, 2001.

[134] V. Baroghel-Bouny, M. Thiéry, F. Barberon, O. Coussy, and G. Villain, "Assessment of transport properties of cementitious materials. A major challenge as regards durability?," *Revue European de Genie Civil*, vol. 11, pp. 671–696, 2007.

[135] E. J. Garboczi, "Permeability, diffusivity and microstructural parameters: a critical review," *Cement and Concrete Research*, vol. 20, pp. 591–601, 1990.

[136] W. Vichit-Vadakan and G. Scherer, "Measuring permeability and stress relaxation of young cement paste by beam-bending," *Cement and Concrete Research*, vol. 33, pp. 1925–1932, 2002.

[137] G. W. Scherer, J. J. V. II, and G. Simmons, "New methods to measure liquid permeability in porous materials," *Cement and Concrete Research*, vol. 37, pp. 386–397, 2007.

[138] Z. C. Grasley, G. W. Scherer, D. A. Lange, and J. J. Valenza, "Dynamic pressurization method for measuring permeability and modulus: II. cementitious materials," *Materials and Structures*, vol. 40, pp. 711–721, 2007.

[139] O. Coussy and M. Thiéry, "Asymptotic," (Lancaster, USA), Poro-Mechanics IV, Ed. by Hoe I. Ling and Andrew Smyth, Pages:384-389. DEStech Publications, Inc., 2009.

[140] A. H. Thompson, A. J. Katz, and E. C. Krohn, "The microgeometry and transport properties of sedimentary rocks," *Adv. Phys.*, vol. 36, pp. 625–693, 1987.

[141] J. J. Kollek, "The determination of the permeability of concrete to oxygen by the cembureau method—a recommendation," *Materials and Structures*, vol. 22, pp. 225–230, 1989.

[142] Z. A. Kameche, F. Ghomari, A. Khelidj, and M. Choinska, "Measurement of the relative gas permeability of ordinary concrete: influence of saturation degree and the sample size," (Toledo, Spain), VIII International Conference on Fracture Mechanicsof Concrete and Concrete Structures, March 10-14,2013, 2013.

[143] L. J. Klinkenberg, *The permeability of porous media to liquids and gases, in drilling and production practice*. New York: American Petroleum Institute, 1941.

[144] Z. Zhang, M. Thiéry, and V. Baroghel-Bouny, "A review and statistical study of existing hysteresis models for cementitious materials," *Cement and Concrete Research*, vol. 57, pp. 44–60, 2014.

[145] J.-P. Carlier, T. Rougelot, and N. Burlion, "Performance evaluation of models describing sorption isotherm in cementitious materials between saturation and oven dryness," *Construction and Building Materials*, vol. 37, pp. 58–66, 2012.

[146] H. Q. Pham, D. G. Fredlund, and S. L. Barbour, "A study of hysteresis models for soil-water characteristic curves," *Canadian Geotechnical Journal*, vol. 42, pp. 1548–1568, 2005.

[147] A. Maqsoud, B. Bussiere, and M. A. M. Mbonimpa, "Hysteresis effects on the water retention curve: A comparison between laboratory results and predictive models," (Quebec, Canada), 57th Canadian Geotechnical Conference, 2006.

[148] A. Poulovassilis, "Hysteresis of pore water, an application of concept of independent domains," *Soil Science*, vol. 93, pp. 405–412, 1962.

[149] L. Néel, "Theorie des lois d'aimantation de lord rayleigh," *Cahiers de Physique*, vol. 13, pp. 18–30, 1943.

[150] G. C. Topp and E. E. Miller, "Hysteretic moisture characteristics and hydraulic conductivities for glass-bead media," *Soil Science Society of America Journal*, vol. 30, pp. 156–162, 1966.

[151] G. C. Topp, "Soil-water hysteresis: The domain model theory extended to pore interaction conditions," *Soil Science Society of America Journal*, vol. 35, pp. 219–225, 1971.

[152] A. Poulovassilis and E. E. Childs, "The hysteresis of pore water: the non-independence of domains," *Soil Science*, vol. 112, pp. 301–312, 1971.

[153] J. R. Philip, "Similarity hypothesis for capillary hysteresis in porous materials," *Journal of Geophysical Research*, vol. 69, pp. 1553–1562, 1964.

[154] G. Bertotti and I. Mayergoyz, *The Science of Hysteresis. Volume III.* Amsterdam: Elsevier Icn., 2006.

[155] Y. Mualem and E. E. Miller, "A hysteresis model based on an explicit domain-dependence function," *Soil Science Society of America Journal*, vol. 43, pp. 1067–1073, 1979.

[156] P. Lehmanna, F. Staufferb, C. Hinza, O. Durya, and H. Flühlera, "Effect of hysteresis on water flow in a sand column with a fluctuating capillary fringe," *Journal of Contaminant Hydrology*, vol. 33, pp. 81–100, 1998.

[157] B. Johannesson and P. Utgenannt, "Microstructural changes caused by carbonation of cement mortar," *Cement and Concrete Research*, vol. 31, pp. 925–931, 2001.

[158] K. Kosugi, "Lognormal distribution model for unsaturated soil hydraulic properties," *Water Resources Research*, vol. 32, pp. 2697–2703, 1996.

[159] S. Poyet, S. Charles, N. Honoré, and V. L'hostis, "Assessment of the unsaturated water transport properties of an old concrete: Determination of the pore-interaction factor," *Cement and Concrete Research*, vol. 41, pp. 1015–1023, 2011.

[160] M. Feng and D. G. Fredlund, "Hysteretic influence associated with thermal conductivity sensor measurements," (Sask, Canada), The 52nd Canadian Geothechnical Conference, 23-24 October,1999.

[161] D. G. Fredlund and A. Xing, "Equations for the soil-water characteristic curve," *Canadian Geotechnical Journal*, vol. 31, pp. 521–532, 1994.

[162] W. Durner, "Hydraulic conductivity estimation for soils with heterogeneous pore structure," *Water Resources Research*, vol. 30, pp. 211–233, 1994.

[163] H. Q. Pham, D. G. Fredlund, and S. L. Barbour, "A practical hysteresis model for the soil-water characteristic curve for soils with negligible volume change," *Geotechnique*, vol. 53, pp. 293–298, 2003.

[164] W. Brutsaert, "Probability laws for pore-size distribution," *Soil Science*, vol. 101, pp. 85–92, 1966.

[165] R. H. Brooks and A. T. Corey, *Hydraulic properties of porous media.* Colorado State University, Fort Colilins, Colo.: Hydrology paper number 3, 1964.

[166] O. Ippisch, H.-J. Vogel, and P. Bastian, "Validity limits for the van genuchten-mualem model and implications for parameter estimation and numerical simulation," *Advances in Water Resources*, vol. 29, pp. 1780–1789, 2006.

[167] Y. Mualem, "Prediction of the soil boundary wetting curve," *Journal of Soil Science*, vol. 137, pp. 379–390, 1984.

[168] J.-Y. Parlange, "Capillary hysteresis and the relationship between drying and wetting curves," *Water Resources Research*, vol. 12, pp. 224–228, 1976.

[169] R. D. Braddock, J.-F. Parlange, and H. Lee, "Application of a soil water hysteresis model to simple water retention curve," *Transport in Porous Media*, vol. 44, pp. 407–420, 2001.

[170] Y. Mualem, "Extension of the similarity hypothesis used for modelling the soil water characteristics," *Water Resources Research*, vol. 13, pp. 773–780, 1977.

[171] P. Viaene, H. Vereecken, J. Diels, and J. Feyen, "A statistical analysis of six hysteresis models for the moisture retention characteristic," *Journal of Soil Science*, vol. 157, pp. 345–355, 1994.

[172] B. C. Si and R. C. Kachanoski, "Unified solution for infiltration and drainage with hysteresis: Theory and field test," *Soil Science Society of America Journal*, vol. 64, pp. 30–36, 2000.

[173] A. Izady, B. Ghahraman, and K. Davari, "Hysteresis: Phenomenon and modeling in soil-water relationship," *Iran Agricultural Research*, vol. 28, pp. 47–63, 2009.

[174] Y. Dafalias, "Bounding surface plasticity. I: Mathematical foundation and hypoplasticity," *Journal of Engineering Mechanics*, vol. 9, pp. 966–987, 1986.

[175] W. L. Hogarth, J. Hopmans, J.-Y. Parlange, and R. Haverkamp, "Application of a simple soil-water hysteresis model," *Journal of Hydrology*, vol. 98, pp. 21–29, 1988.

[176] H. Huang, Y. Tan, C. Liu, and C. Chen, "A novel hysteresis model in unsaturated soil," *Hydrological Processes*, vol. 19, pp. 1653–1665, 2005.

[177] J. Rubin, "Numerical method for analyzing hysteresis-affected, post-infiltration redistribution of soil moisture," *Soil Science Society of American Process*, vol. 31, pp. 13–290, 1967.

[178] A. D. Werner and D. A. Lockington, "Artificial pumping errors in the kool-parker scaling model of soil moisture hysteresis," *Journal of Hydrology*, vol. 325, pp. 118–133, 2006.

[179] J. Carmeliet and S. Roels, "Determination of the moisture capacity of porous building materials," *Journal of Thermal Envelope and Building Science*, vol. 25, pp. 209–237, 2002.

[180] D. B. Moog and G. H. Jirka, "Analysis of reaeration equations using mean muliplictive error," *Journal of Environmental Engineering Division. American Society of Civil Engineers*, vol. 112, pp. 104–110, 1984.

[181] M. Saillio, *Interactions physiques et chim iques ions - matrice dans les bétons sains et carbonatés. Influence sur le transport ionique*. PhD thesis, Paris-Est University/IFSTTAR, May 2012.

[182] G. Villain and M. Thiéry, "Gammadensimetry: A method to determine drying and carbonation profiles in concrete," *NDT & E International*, vol. 39, pp. 328–337, 2006.

[183] IAEA, *Guidebook on non-destructive testing of concrete structures.* Vienna, Austria: International Atomic Energy Agency, 2002.

[184] S. M. System, *DVS Advantage operation manual*, accessed August 2013. `http://www.thesorptionsolution.com/`.

[185] M. Janz, "Methods of measuring the moisture diffusivity at high moisture levels," tech. rep., Report TVBM 3076, Division of Building Materials, Lund Institute of Technology/Lund University, Sweden, 1997.

[186] B. Johannesson, "Verification of the bet-theory by experimental investigations on the heat of adsorption," tech. rep., Report TVBM 3096, Division of Building Materials, Lund Institute of Technology/Lund University, Sweden, 2000.

[187] M. Janz and B. F. Johannesson, "Measurement of the moisture storage capacity using sorption balance and pressure extractors," *Journal of Thermal Envelope and Building Science*, vol. 24, pp. 316–334, 2001.

[188] P. Arlabosse, E. Rodier, J. H. Ferrasse, S. Chavez, and D. Lecomte, "Comparison between static and dynamic methods for sorption isotherm measurements," *Drying Technology: An International Journal*, vol. 21, pp. 479–497, 2003.

[189] L. Wadsö, K. Svennberg, and A. Dueck, "An experimentally simple method for measuring sorption isotherms," *Drying Technology: An International Journal*, vol. 22, pp. 2427–2440, 2004.

[190] P. Johansson, "Water absorption in two-layer masonry systems - Properties, profiles and predictions," tech. rep., Report TVBM 1024, Division of Building Materials, Lund Institute of Technology/Lund University, Sweden, 2005.

[191] W. Weibull, "A statistical distribution function of wide applicability," *Journal of Applied Mechanics: ASME*, vol. 18, pp. 293–297, 1951.

[192] G. R. Díaz, J. Martínez-Monzó, P. Fito, and A. Chiralt, "Modelling of dehydration-rehydration of orange slices in combined microwave/air drying," *Innovative Food Science & Emerging Technologies*, vol. 4, pp. 203–209, 2003.

[193] G. Dadali, E. Demirhan, and B. Özbek, "Effect of drying conditions on rehydration kinetics of microwave dried spinach," *Food and Bioproducts Processing*, vol. 86, pp. 235–241, 2008.

[194] I. Doymaz, "Evaluation of some thin-layer drying models of persimmon slices (diospyros kaki l.)," *Energy Conversion and Management*, vol. 56, pp. 199–205, 2012.

[195] Z. Zhang, M. Thiéry, and V. Baroghel-Bouny, "Effect of cyclic boundary conditions on moisture transport within cementitious materials," *Cement and Concrete Research*, vol. Under review, 2014.

[196] P. C. D. Milly, "A mass-conservative procedure for time stepping in models of unsaturated flow," *Advances in Water Resources*, vol. 8, pp. 32–36, 1985.

[197] R. G. Hills, D. B. Hudson, I. Porro, and P. J. Wierenga, "Modeling one-dimensional infiltration into very dry soils, 1. Model development and evaluation," *Water Resources Research*, vol. 25, pp. 1259–1269, 1989.

[198] M. R. Kirkland, R. G. Hills, and P. J. Wierenga, "Algorithms for solving richards' equation for variably saturated soils," *Water Resources Research*, vol. 28, pp. 2049–2058, 1992.

[199] M. A. Celia, E. T. Bououtas, and R. L. Zarba, "A general mass-conservative numerical solution for the unsaturated flow equation," *Water Resources Research*, vol. 26, pp. 1483–1496, 1990.

[200] G. A. Williams, C. T. Miller, and C. T. Kelley, "Transformation approaches for simulating flow in variably saturated porous media," *Water Resources Research*, vol. 36, pp. 923–934, 2000.

[201] C. A. B. de Vasconcellos and J. C. C. Amorim, "Numerical simulation of unsaturated flow in porous media using a mass conservative model," (Uberlandia, MG), Proceeding of COBEM. 2001, Fluid Mechanics. Vol. 8, pp. 139-148, 2001.

[202] R. W. Gillham, A. Klute, and D. F. Heermann, "Measurement and numerical simulation of hysteretic flow in a heterogeneous porous medium," *Soil Science Society of America Journal*, vol. 43, p. 1061–1067, 1979.

[203] A. Poulovassilis, "The effect of hysteresis of pore-water on the hydraulic conductivity," *Journal of Soil Science*, vol. 20, pp. 52–56, 1969.

[204] J. Carmeliet, F. Descamps, and G. Houvenaghel, "A multiscale network model for simulating moisture transfer properties of porous media," *Transport in Porous Media*, vol. 35, pp. 67–88, 1999.

[205] A. S. El-Dieb and R. D. Hooton, "A high pressure triaxial cell with improved measurement sensitivity for saturated water permeability of high performance concrete," *Cement and Concrete Research*, vol. 24, pp. 854–862, 1994.

[206] A. S. El-Dieb and R. D. Hooton, "Water-permeability measurement of high performance concrete using a high-pressure triaxial cell," *Cement and Concrete Research*, vol. 25, pp. 1199–1208, 1995.

[207] V. Picandet, D. Rangeard, A. Perrot, and T. Lecompte, "Permeability measurement of fresh cement paste," *Cement and Concrete Research*, vol. 41, p. 330– 338, 2011.

[208] G. W. Scherer, "Bending of gel beams: method of characterizing mechanical properties and permeability," *Journal of Non-Crystalline Solids*, vol. 142, pp. 18–35, 1992.

[209] G. W. Scherer, "Measuring permeability of rigid materials by a beam-bending method: I. theory," *Journal of the American Ceramic Society*, vol. 83, pp. 2231–2239, 2000.

[210] G. W. Scherer, "Measuring permeability of rigid materials by a beam-bending method: Iv. transversely isotropic plate," *Journal of the American Ceramic Society*, vol. 87, pp. 1517–1524, 2004.

[211] G. W. Scherer, H. Hdach, and J. Phalippou, "Thermal expansion of gels: a novel method for measuring permeability," *Journal of Non-Crystalline Solids*, vol. 130, p. 157–170, 1991. Errata, J. Non-Cryst. Solids 194 (1996) 326.

[212] G. W. Scherer, "Measuring permeability by the thermal expansion method for rigid or highly permeable gels," *Journal of Sol-Gel Science and Technology*, vol. 3, pp. 31–40, 1994.

[213] G. W. Scherer, "Thermal expansion kinetics: method to measure permeability of cementitious materials: I, theory," *Journal of the American Ceramic Society*, vol. 83, p. 2753–2761, 2000. Erratum, J. Am. Ceram. Soc. 87 (8) (2004) 1609 –1610.

[214] G. W. Scherer, "Dynamic pressurization method for measuring permeability and modulus: I. theory," *Materials and Structures*, vol. 39, pp. 1041–1057, 2006.

[215] S. Zamani, R. Kowalczyk, and P. J. McDonald, "The relative humidity dependence of the permeability of cement paste measured using garfield nmr profiling," *Cement and Concrete Research*, vol. 57, pp. 88–94, 2014.

[216] B. Bary and A. Sellier, "Coupled moisture—carbon dioxide–calcium transfer model for carbonation of concrete," *Cement and Concrete Research*, vol. 34, p. 1859–1872, 2004.

[217] S. Poyet, "Determination of the intrinsic permeability to water of cementitious materials: Influnece of the water rentention curve," *Cement and Concrete Composites*, vol. 35, pp. 127–135, 2013.

[218] L.-O.Nilsson, "A comparison between different methods to determine moisture transport properties of cementitious materials," tech. rep., Report TVBM 3168, Division of Building Materials, Lund Institute of Technology/Lund University, Sweden, 2013.

[219] K. Malek and M. O. Coppens, "Knudsen self- and Fickian diffusion in rough nanoporous media," *Journal of Chemical Physics*, vol. 119, pp. 2801–2811, 2003.

[220] K. Gertis and U. Wolfseher, "Isothermer gastrasnport in porosen stoffen aus gas kinetischer sicht," *Deustcher Ausschuss fur Stahlbeton*, pp. 36–62, 1976.

[221] R. S. M. J. Hagymassy, S. Brunauer, "Pore structure analysis by water vapor adsorption, I. t-curves for water vapor," *Journal of Colloid Interface Science*, vol. 127, pp. 485–491, 1969.

[222] E. P. Barrett, L. G. Joyner, and P. P. Halenda, "The determination of pore volume and area distributions in porous substances. I. Computations form nitrogen isotherms," *Journal of the American Chemical Society*, vol. 71, p. 373–380, 1951.

[223] C. E. Hagentoft, "Simplified analysis of combined heat, moisture and air transport for one-dimensional cases," tech. rep., Sweden, 1992.

[224] C. E. Hagentoft, "PC-program: 1D-HAM. Notes on heat transfer," tech. rep., Sweden, 1993.

[225] J. B. Laurindo and M. Prat, "Numerical and experimental network study of evaporation in capillary porous media: Phase distributions," *Chemical Engineering Science*, vol. 51, pp. 5171–5185, 1996.

[226] J. B. Laurindo and M. Prat, "Numerical and experimental network study of evaporation in capillary porous media: Drying rates," *Chemical Engineering Science*, vol. 53, pp. 2257–2269, 1998.

[227] A. Erriguible, P. Bernada, F. Couture, and M. Roques, "Simulation of convective drying of a porous medium with boundary conditions provided by CFD," *Chemical Engineering Research and Design*, vol. 84, pp. 113–123, 2006.

[228] H. J. Steeman, B. Blocken, and J. Carmeliet, "Conservative modelling of the moisture and heat transfer in building components under atmospheric excitation," *International Journal of Heat and Mass Transfer*, vol. 50, pp. 1128–1140, 2007.

[229] H. J. Steeman, A. Janssens, J. Carmeliet, and M. D. Paepe, "Modelling indoor air and hygrothermal wall interaction in building simulation: Comparison between CFD and a well-mixed zonal model," *Building and Environment*, vol. 44, pp. 572–583, 2009.

[230] H. J. Steeman, C. T'Joen, M. V. Belleghem, A. Janssens, and M. D. Paepe, "Evaluation of the different definitions of the convective mass transfer coefficient for water evaporation into air," *International Journal of Heat and Mass Transfer*, vol. 52, pp. 3757–3766, 2009.

[231] B. Blocken, T. Stathopoulos, and J. Carmeliet, "CFD simulation of the atmospheric boundary layer: wall function problems," *Atmospheric Environment*, vol. 84, p. 238–252, 2007.

[232] A. G. Yiotis, I. N. Tsimpanogiannis, A. K. Stubos, and Y. C. Yortsos, "Coupling between external and internal mass transfer during drying of a porous medium," *Water Resources Research*, vol. 43, p. W06403, 2007.

[233] H. Ranaivomanana, J. Verdier, A. Sellier, and X. Bourbon, "Prediction of relative permeabilities and water vapor diffusion reduction factor for cement-based materials," *Cement and Concrete Research*, vol. 48, pp. 53–63, 2013.

[234] C. Zhou, "Predicting water permeability and relative gas permeability of unsaturated cement-based material from hydraulic diffusivity," *Cement and Concrete Research*, vol. 58, p. 143–151, 2014.

[235] D. Milly, "Moisture and heat transport in hysteretic, inhomogeneous porous media: a matric head-based formulation and a numerical model," *Water Resources Research*, vol. 18, pp. 489–498, 1982.